2011

# Magnetic micro-confinement of quantum degenerate gases

Ahmed M. Abdelrahman
*Edith Cowan University*

## Recommended Citation

Abdelrahman, A. M. (2011). *Magnetic micro-confinement of quantum degenerate gases*.
https://ro.ecu.edu.au/theses/411

# Magnetic Micro-Confinement of Quantum Degenerate Gases

**Ahmed M. Abdelrahman**

**2011**

**Doctor of Philosophy**

*For further information about Edith Cowan University-Online Dissertation Series, please contact*

**Joondalup Campus Library**
Joondalup Campus
Building 31
270 Joondalup Drive
Joondalup WA 6027
Perth, AUSTRALIA

Telephone: (61 8) 6304 5525
Facsimile: (61 8) 6304 5719
Email: loansjo@ecu.edu.au
URL: `http://www.ecu.edu.au/centres/library-services/overview`

# Magnetic Micro-Confinement of Quantum Degenerate Gases

BY

Ahmed Mohammed Abdelrahman

A THESIS SUBMITTED FOR THE DEGREE OF

**DOCTOR OF PHILOSOPHY**

AT

**ELECTRON SCIENCE RESEARCH INSTITUTE**
**Edith Cowan University**

Principal Supervisor: Prof. **Kamal Alameh**
Electron Science Research Institute (ESRI), Edith Cowan University
Co-Supervisor: Prof. **Peter Hannaford**
Centre for Atom Optics and Ultrafast Spectroscopy (CAOUS) and the ARC Centres of Excellence for Quantum-Atom Optics (ACQAO), Swinburne University

# USE OF THESIS

# DECLARATION

I certify that this thesis does not to the best of my knowledge and belief:

(i) incorporate without acknowledgment any material previously submitted for a degree or diploma in any institution of higher education,

(ii) contains any material that previously published or written by another person except where due reference is made in the text; or

(iii) contains any defamatory material.

I also grant permission for the library at Edith Cowan University to make duplicate copies of my thesis as required.

Signature: **Ahmed Mohammed Abdelrahman**

Date: 08.11.2011

*To my mother:* ***Shaikha A. Abdelkareem****,*

*To my father:* ***Mohammed Abdelrahman*** *(may Allah accept him in his paradises),*

*To all of my brothers, sisters and best friends,*
*To all of my teachers ...*

# Acknowledgments

AT this the very special moment, it is certainly not trivial to find the suitable words that will properly describe my gratefulness to all of those who helped me to reach this level. It is even harder to express my best thanks to my supervisor Prof. Kamal Alameh and to show how his passion to science and support were the great motivations for this work to see the light. It was always very exciting to discuss with him about the project with no fear of tackling any obstacles that often appear in such type of science; and more interesting when we find the joy of talking about life and we can't just prevent ourselves when deeply digging for the sake of its jewels. I learned from him, as a person with a capability of reading between lines, that life sometimes must be taken seriously same as science; courage only is not just enough to have it all dedicated for us. More guts and courage go all the way up together to self discipline ourselves in a moral conduct to get the satisfaction of our actions. His supervision was and still one of the most important ingredient in my life.

It is also a beautiful chance to express my special thanks and gratefulness to Prof. Peter Hannaford and I can't add any more word to describe his reputations in the field of atomic physics as he is well known to those who are involved in this field. With his expertise, his advices were the most important elements for this project to succeed and to gain some respect in the scientific community. He was the first to realize the validity of the proposed method and its applicability to overlap in different branches of atomic physics. Special thanks to him and to Prof. James Wang (for his help in using the magnetic force microscope) in the Center of Atom Optics and Ultrafast Spectroscopy in the University of Swinburne for the grate support and help. The time I spent in that center was very intense and of great benefit to my knowledge but there is a moment that needs to be remembered here: When I went for a coffee break with Prof. Peter, we had a discussion away from science where at that moment I realized how a great person he is, listening carefully to him and learning the most out of life gifted to me melted in a single cup of 'espresso': "One can't just figure out every thing by himself in a moment ... how awkward to forget our commons and concentrate on differences".

Special thanks to Dr. Mikhail Vasiliev for his great help in learning how to operate all of these complicated equipments and understanding the physics behind their operations. I enjoyed working with him and also enjoyed the intensive critical discussions while seriously taking his valuable questions and guidance, it is a real fun to work with him in his laboratories.

Special thanks to Prof. Yong-Tak Lee in the Gwangju Institute of Science and Technology (GIST) and Prof. Hoonsoo Kang in the Advanced Photonics Research Institute (APRI) at GIST for their extreme support and help. I also would like to thank Dr. Sang Youp Yim for his great help in building my experiment in APRI and to all of my office mates there.

Even though he didn't contribute to this work, I find it convenient to acknowledge Dr.

Sreten Askraba for his courage and very useful advices. His great friendly company was another reason to enjoy the environment in our Electron Science Research Institute (ESRI) and to trigger the creativity for most of the postgraduate students. Special thanks to Linda Arthur for her help and her great capacity to accept and tolerate our (students) messy world. Thanks to all of the colleagues and friends in ESRI for the friendly time we spent together, Feng Xiao and his wife Fang Liu, Arie Paap, Hoang Nguyen, Linh Nguyen, Narottam Das, Kavitha Venkataraayan, Valentina Tiporlini, David Michel, Stefan, Nazme , Haithem Mustafa, Ayman Karar and to all of other colleagues. Very special thanks to Mohammad Nur-E-Alam for his help in the lab and to our new administration team Paul and Tiella.

# Abstract

In this dissertation we explore the basic principles of the magnetic micro-confinement of the quantum degenerate gases where the approach of the so-called two-dimensional magnetic lattices has been theoretically and experimentally investigated. In this research a new generation of two-dimensional magnetic lattice has been proposed and considered as a developing phase for the previous approaches. Its advantage relies on introducing a simplified method to create single or multiple micro-traps of magnetic field local minima distributed, at a certain working distance, above the surface of a thin film of permanent magnetic material. The simplicity in creating the magnetic field local minima at the micro-scale manifests itself as a result of imprinting specific patterns through the thin film using suitable and available micro-fabrication techniques. In this approach, to create multiple micro-traps, patterned square holes of size $\alpha_h \times \alpha_h$ spaced by $\alpha_s$ are periodically distributed across the $x/y$ plane taking a two-dimensional grid configuration. These magnetic field local minima are recognized by their ability to trap and confine quantum single-particles and quantum degenerate gases at various levels of distribution in their phase spaces, such as ultracold atoms and virtual quantum particles[1].

Based on the nature of the interaction between the external confining potential fields and the different types of quantum particles, this research is conducted through two separate but not different phases. We performed theoretical and/or experimental investigations, for both phases, at the vicinity of the magnetic micro-confinement and its suitability for trapping quantum particles. A special attention is paid to inspect the coherence in such systems defined in terms of providing an accessible coupling to the internal quantum states of the magnetically trapped particles. Such coherence is considered as one of the important ingredients for simulating condensed matter systems and processing quantum information.

The two-dimensional magnetic lattice is developed, in the first phase of the investigations, to trap paramagnetic atoms and to prepare a suitable environment for achieving a phase transition to the region of ultracold atomic (quantum) degenerate gases, well known as the Bose-Einstein condensation. The trapping mechanism is based on attracting the atoms (usually cold, due to the deceleration in their velocities) to fall in distributed magnetic field local minima in which case the atoms are assumed to be prepared in the so-called magnetic low field seeking states. To create the magnetic field local minima, we realized that by milling a hole through a permanent magnetic thin film a disturbance in the uniformity of the magnetic field occurs and accompanied by two local field minima. These minimum values $B_{min}$ of the magnetic field are found to appear at both ends of the hole and are located at a certain working distance $d_{min}$ that depends on the size of the hole $\alpha_h$ and, in the case of more than one hole, on the holes separating distance $\alpha_s$. It has also been found that, in the proposed

---

[1] The virtuality behavior appears when the particle is itself a metastable composite of quantum particles and lives for very short time, such as excitonic or polaritonic a electron-hole pair composite particle

method, the $B_{min}$ values and the distance $d_{min}$ can both be controlled via the application of external magnetic bias fields as well as choosing suitable values of $\alpha_s$. It is important to choose $B_{min} > 0$ so as to keep the trapped quantum particles away from experiencing the destructive Majorana spin-flip process. Also, by choosing suitable $d_{min}$ values the $B_{min}$ can be located away from the surface of the thin film, hence preventing the Casimir-Polder effect from being developed.

The produced magnetic lattice consists of several magnetic field local minima distributed across a two-dimensional plane and located at $d_{min}$ above the surface of the thin film. These magnetic traps are regarded as the sites for the magnetic lattice. Although the distribution of the sites is symmetric across the $x/y$-planes, this method is also found to produce asymmetrically distributed sites across the $x/z$ and $y/z$ planes. The measured magnetic field of the lattice sites, using Magnetic Force Microscope (MFM), shows that the asymmetrical effect (namely a tilted potential) is always showing large values of $B_{min}$ (i.e. magnetic field values measured at the bottom of the sites) at the center of the lattice when compared to the field minimum values at the edges. The asymmetrical effect was considered, in the early proposals, as a disadvantage for these type of magnetic lattices. However, the theoretical calculations carried in this research have shown that the tilt effect is an essential feature for assisting the tunneling of the trapped quantum particles.

The theoretical approach is based on converting the time-dependent Gross-Pitaevskii equation (GPE), which is the nonlinear Schrödinger equation, to a set of equations denoted by the Boson Josephson Junctions (BJJs) equations for $n$ adjacent magnetic lattice sites in which case the tunneling of the trapped ultracold atoms is assumed to be induced due to the asymmetrical effect and the existence of external bias fields. In the calculations, the wavefunction $\varphi(\mathbf{x}, t)$ is used to roughly describe the macroscopic dynamical oscillations of weakly interacting condensates, at the BEC low temperature, trapped in the magnetic lattice and to obey the time-dependent GPE. The asymmetrical effect is approximated as tilted trapping potentials in the Hamiltonian of the BJJs and the adiabatic tunneling process is controlled via the application of external magnetic bias fields. To identify the dynamical Josephson oscillations of the condensates in the weakly coupled sites of the magnetic lattice, the attention was limited to the localized time-dependent variational ansatz $\varphi(\mathbf{x}, t) = \sum_j^n c_j(t)\chi_j(\mathbf{x})$ (i.e. as superposition states) with $c_j(t) = \sqrt{N_j(t)}e^{i\theta_j(t)}$ and considering the total number of atoms between the adjacent sites to be constant, $\mathcal{N} = \sum_j^n N_j = \sum_j^n |c_j|^2$. The coupling Josephson energy $\Omega^J \simeq -\int[\frac{\hbar^2}{2M}(\nabla\varphi_j\nabla\varphi_{j+1}) + \varphi_j U(\mathbf{x})\varphi_{j+1}]d\mathbf{x}$ is in analogous to the Josephson coupling energy in a Superconducting Josephson Junction (ScJJ) where it has been shown that $\Omega^J$ can be regarded as the two-photon Rabi-like frequency having a coherence that can be described by $N_j = \int d\mathbf{x}\varphi_j^*(\mathbf{x})\varphi_{j+1}(\mathbf{x})$. The oscillating fractional occupations $\widetilde{N}_{j,j+1}(t)$ and the phase amplitudes $\widetilde{\theta}_{j,j+1}(t)$ are found to exhibit an adiabatic Josephson effect in this type of magnetic lattice arising from the superfluidity nature of the trapped condensates when tunneling between the lattice sites.

In the second phase of this research, the magnetic micro-confinement is used to confine metastable particles that formed in quantum heterostructure devices. The purpose of the experimental investigations is to validate whether or not the magnetic micro-confinement is also applicable for trapping virtual quantum particles, namely excitons, when projected into a solid state quantum heterostructure. Excitons can be created in a single (multiple) quantum well(s) of a semiconductor where they exhibit bosonic particles nature and hence they can respond to external confining potential fields in the same way as cold atoms. Using suitable fabrication techniques, the magnetic field local minima are projected into a system of GaAs/AlGaAs multiple quantum wells to confine excitonic particles. In the first attempt a magnetic field cover, of an inhomogeneous spatial distribution, has been projected into the well confining plane by depositing permanent magnetic material on the top of a GaAs/AlGaAs quantum wells heterostructure. The cover creates a weak magnetic field at the center of the sample and, due to the edge effect, the strength of the magnetic field increases towards the edges of the quantum well confining plane when compared to the center. The dispersion surface (curve) of the excitonic particles $E_{ext}(P)$ is found to shift in the $k$-space (i.e. the momentum-space) with respect to the direction of the localized magnetic field. In the perpendicular magnetic field $B_{\perp}$ regions at the center of the $x/y$-plane (since the inhomogeneous field is spatially distributed) the dispersion curve $E_{ext}(P)$ is shifting along the energy direction by $\delta E$ in the $k$-space with no change in the momentum while in the parallel field $B_{\parallel}$ regions at the edges of the $x/y$-plane the dispersion curve shifts along the momentum direction by $\Delta P = -\hbar k \sim \frac{e}{c} B_{\parallel}$. By localizing the inhomogeneous magnetic filed in such a way that it covers the entire $x/y$-planes of the quantum wells, the two formal phenomena, i.e. the $\delta E$ and $\Delta P$ shifts, are both found to simultaneously occur in a one phase distribution. As a consequence, an inhomogeneous depression of the excitons Zeeman splitting has been observed when spatially resolving their recombination rates.

Since the exciton's Bohr radius is known to be comparable to the magnetic length $l_B = \sqrt{\frac{\hbar c}{e B_{\perp}}}$, the lifetime of the excitonic particles is found to vary with respect to the magnitude of the localized field in which case the dispersion surface and the binding energy are also functions of the localized fields such that $E_{ext}(P) = -E_B e^{-\alpha} I_o(-\alpha)$ and $E_B = \frac{\sqrt{\pi}}{2e^2} \frac{1}{l_B}$, respectively, with $\alpha \sim (\delta P l_B)^2$ and $I_o(\alpha)$ being the Bessel function. These behaviors combined together are found to induce an inhomogeneous spatial distribution of the excitonic spin-population, i.e. some regions are populated with spin-up $\mid \uparrow\rangle$ while remaining regions are dominated with the state of spin-down $\mid \downarrow\rangle$. This phenomenon is thought to be of great interest for the field of storing light pulses and processing quantum information.

As described above, by printing a micro-pattern through the magnetic thin film, magnetic field local minima can be created with a sharp trapping field gradient. Through this investigation a simplified method to create such magnetic field local minima, with an absolute control over the minima location within the multiple well confining planes, has been proposed and tested for the first time. This method allows one to precisely locate the field minima at a certain depth into the heterostructure device. As a result, there has been a robust response detected in the excitonic magnetic dipole interaction with the confining low field which assures that these particles are acting as paramagnetic bosons. The detection method is based on measuring the photoluminescence from the recombination of the excitons which is found to be localized at the magnetic trapping region; the high recombination rate indicates that there is an actual accumulation of the excitonic particles due to the acting low magnetic field trapping force. These observations have revealed the following important fact: the magnetic traps can also be implemented into the quantum heterostructure and semiconductor devices and used to confine the excitons or any similar quantum particle, such as micro-cavity polaritons. This type of implementation is expected to enhance the quantum coherence of the interacting particles, whether charge carriers or metastable particles, and more specifically to suppress the phonon interactions and to overcome the crystal fields delocalizations. Moreover, regardless of the simplicity of the method, it was not clear before how to introduce such confining magnetic field local minima across the quantum well (confining) plane.

The magnetic micro-confinement of excitonic particles will open several new research field directions, ranging from field-effect transistors, the coherence in quantum cascade lasers to quantum sensing and beyond. Above all and more importantly, this method might be considered as a possible approach for achieving Bose-Einstein condensation of excitonic particles which still in a long standing debate for the past thirty years. These facts will certainly present this type of trapping mechanism as a promising candidate for the research fields of quantum computing devices and quantum information processing.

The above experimental investigations are being carried using a quantum heterostructure that produces heavy-hole direct-excitons, which are well known to be highly mobilized (hot). Regardless of the fact that the magnetic confinement of the excitonic particles has shown clear evidence of a trapping signature, it was not possible to produce ultracold direct-excitons or at least to approach the phase transition limit. This fact has triggered a very interesting question which certainly needs to have a particular answer in regards to the magnetic micro-confinement of the indirect-excitons.

# Contents

# List of Tables

# List of Figures

# List of symbols

$n$ number of quantum particles such as atoms and excitons.

$\mathcal{U}(\mathbf{r}_{ij})$ general symbol used to describe the interaction potential, e.g. short-range interaction potential between particle $i$ (atoms $i$) and particle $j$.

$r_o$ the radius (or sometime *range*) of the interaction.

$r_{ij}$ relative coordinate between particle $i$ and particle $j$.

$\sigma_c$ the collision cross section.

$\iota_c^{-1}$ the collision rate.

$k_B$ Boltzmann constant.

$T$ for temperate in general.

$\mathbf{p}_i$ the momentum of the particle $i$. Some times written in a vector notation as $\vec{k}$ and used to define the momentum space, i.e. the $k$-space.

$l_{mfp}$ the mean-free-path.

$\zeta(\mathbf{r}, \mathbf{p})$ the total energy distribution in the momentum-space (the $k$-space).

$\vartheta = (1/2\pi\hbar)^3$ phase-space unit volume.

$\boldsymbol{m} = (m_a m_b)/(m_a + m_b)$ the reduced mass of two-body problem, $a$ and $b$.

$\phi_i$ the wavefunction of particle $i$.

$\Phi(\vec{\boldsymbol{r}})$ the total wavefunction of $n$ particle.

$\xi(E, \vec{k}_{int}, \vec{k}_s)$ the scattering amplitude in the scattering direction $\vec{k}_s$.

$\sigma(E)$ the over all intensity of the scattered wave or as well known the *scattering cross section*.

Chapter 1

# INTRODUCTION

> ¶ *To raise new questions, new possibilities, to regard old questions from a new angle, requires creative imagination and marks real advances in science*
>
> **Albert Einstein (1954)**

ONE of the beautiful manifestations for the quantum degenerate gases at very low temperature is the so called Bose-Einstein condensate (BEC). It is a new state of matter named after the prediction of the collapses of the quantum particles into one state as first triggered by the Indian physicist S. Bose for the photon statistics and Planck's radiation distribution in (1924).

S. Bose formulated his idea in a manuscript that came into the hands of Einstein who translated and published it in the German science journal [22]. Einstein generalized the idea to include studies that centered around the statistical mechanics of an ideal monoatomic gases. He justified the use of Bose's photon statistics in describing the distribution function of an atomic gas by citing de Broglie's recently published thesis (1924) on the existence of matter waves[1]. This assumption has led him to formulate the Bose-Einstein statistics.

## 1.1 Fundamental Aspects of Quantum Gases

The following introductory outlines are deliberate attempts to prepare a conceptual approach to the so-called quantum degenerate gases where the mathematical foundation presented in the following chapter is the crucial step towards understanding the physics of the interacting quantum particles.

### 1.1.1 Ideal-gas limits and the confining fields

At the foundation of the kinetic theory, the *mutual interaction* of the quantum particles always comes first even if just at glancing the long list of other classical or quantum interactions, it gives rise to *collisions* in a fashion of binary[2] interactions. Collisions are crucial to maintain the thermal equilibrium and since we are dealing with atomic gases (and virtual quantum particles as discussed later) it is necessary to take into account some collisional parameters that certainly influence the nature of the interaction and consequently the statistical distribution of these quantum particles. For instance, from the collisional *macroscopic* picture at the

---

[1] The Einstein assumption was that if atoms behave like waves, same as photons, then they must obey the same statistics.

[2] Within the range $r_o$ there is a large probability of finding $n = 2$ atoms than that of $n = 3$ atoms.

continuum energy spectrum (as well as at microscopic discrete energy levels) the mean-free-path $l_{mfp} = \frac{1}{n\sigma}$ plays significant role in shaping the macroscopic picture of the gas in regards to its confining volume $V$. It is also useful to calculate the collision cross section $\sigma_c = \pi r_o^2$ and the collision rate $\iota_c^{-1} = n\bar{v}\sigma_c$, assuming that the atomic size is known[3]. Practically, relying on a stable confining method will improve the conditions for studying the quantum gases at a microscopic level. But before we start exploring the interaction nature of a confined gas, it is useful to briefly explain what is meant by the *ideal gas* limit.

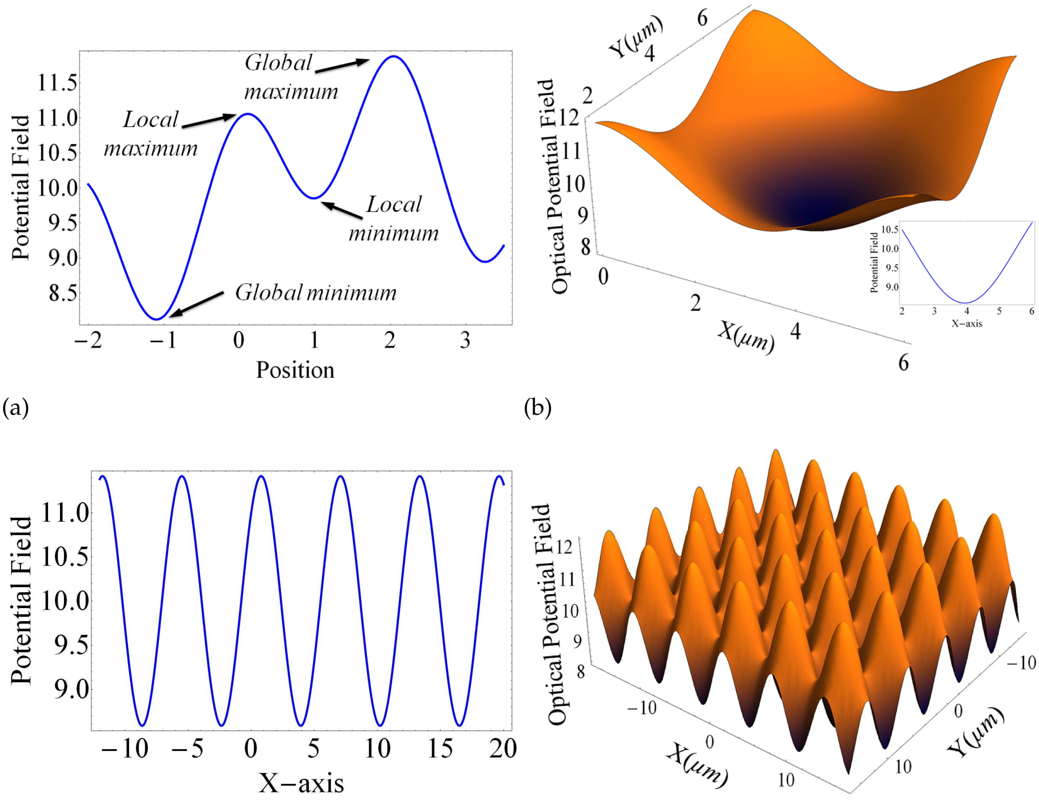

(a) (b)

(c) (d)

***Figure 1.1:*** (a) Disordered potential shows global and local maxima and minima (b-c) Single and periodic electrical trapping potentials, respectively, that can be created by the laser field. (d) The distribution of the confining potential field can also be made in two-dimensional plane.

Classically, the ideal gas assumes no interactions between the particles where the distribution of the total energy $E$ of the gas *cloud* follows the Maxwell-Boltzmann statistics

$$f(E) = C \exp\left(\frac{E}{k_B T}\right) \tag{1.1}$$

where $C$ is a normalization factor and $T$ is the temperature. The statistical approach is important because, in the kinetic space of the gas or the well known *phase space*, it is not possible to determine the energy $\varepsilon_i$ of the single atom $i$ by only specifying its kinetic state $(\mathbf{r}_i, \mathbf{p}_i)$[4]. For such scenario, writing down the system total Hamiltonian, $\mathcal{H} = \sum_i \mathcal{H}^{(i)}$, one often obtains

---

[3] $\bar{v} = \sqrt{\frac{16 k_B T}{\pi m}}$ is the atomic average relative speed.

[4] The kinetic state represents a point $s_i$ in the phase space, $s_i \in \{\mathbf{r}_i, \mathbf{p}_i\}$.

most of the useful information regarding the gas's behavior. For example the *free-particle* Hamiltonian takes into account the kinetic energy and the interaction potential with the condition of the particle-particle interaction is negligible, i.e. $\mathcal{U}(\mathbf{r}_{ij}) \to 0$, such that the Hamiltonian will read

$$\mathcal{H}^{(i)} \qquad \longrightarrow \qquad \mathcal{H}_o(\mathbf{r}_i, \mathbf{p}_i) = \frac{\mathbf{p}_i^2}{2m} + \mathcal{U}(\mathbf{r}_{ij}) \tag{1.2}$$

The Hamiltonian is for free particles with all energy converted into the kinetic energy term $\frac{\mathbf{p}_i^2}{2m}$ leading to the following well known thermal momentum (also known as the thermal velocity) distribution

$$f(\mathbf{p}) = \acute{C}\frac{4\mathbf{p}^2}{m^2}\exp\Big(-\frac{\mathbf{p}^2}{2mk_BT}\Big) \tag{1.3}$$

The *ideal gas regime* is reached when the energy of the interaction is very small compared to the kinetic energy, i.e. $\varepsilon_{int} \ll \varepsilon_{kin}$. However, these interactions are necessary to maintain the thermal equilibrium. This approximation is not always valid, it only applies for a very large space because the integration of the distribution function over the phase space results in the particle number. In such case the space is unbound and thus the integral values are infinitely large.

The above representation takes different shape once the confinement is introduced, the quantum gas behaves differently according to the boundaries exerted by the confining volume in which case its internal interaction becomes rather countable. It is convenient at this stage to emphasize on the mechanism of the *wall-free confinement* due to the supplementary deal it plays in conserving the quantum state of the confined particles. The wall-free confinement is usually created externally by introducing an *inhomogeneous*[5] *potential* field making use of the fact that the quantum states of the particles arrange and characterize themselves due to the *inhomogeneity* inherited in the externally confining potential field. The inhomogeneity in the potential is recognized as global/local maxima and minima that occur in the distribution of the fields and can be seen as a projected pattern that appears at a certain location $\mathbf{r}_{max/min}$ in the physical space. In most cases, static and/or dynamic electromagnetic fields are often used for perusing the external confinement, such as optical traps and magnetic traps as illustrated in Figure (1.1).

In most of the condensed matter and molecular physics calculations, the short-range potential is thought to vanish at large distances, i.e. $\mathcal{U}(\mathbf{r} \to \infty) = 0$. However, we still keep it when writing the total Hamiltonian for such system in which case it reads

$$\begin{aligned}\mathcal{H} &= \sum_i \mathcal{H}_o(\mathbf{r}_i, \mathbf{p}_i) + \sum_{i\neq j} \mathcal{V}(\mathbf{r}_{ij}) \\ &= \sum_i \Big(\frac{p_i^2}{2m} + \mathcal{U}(\mathbf{r}_{ij})\Big) + \sum_{i\neq j} \mathcal{V}(\mathbf{r}_{ij}) \end{aligned} \tag{1.4}$$

The term $\mathcal{V}(\mathbf{r}_{ij})$ denotes the external potential[6] and $p_i = |\mathbf{p}_i|$. Macroscopically, the density of the cloud distributes relative to the inhomogeneity in the potential while microscopically

---

[5] Homogeneous fields can also exhibit a confinement but in very rare cases where the particles are assumed to have less degrees of freedom.

[6] The external potential $\mathcal{V}(\mathbf{r}_{ij})$ is inhomogeneous in all of the theoretical and experimental work carried in this thesis, hence it has a spatial variation, see section (2.3).

the density of the state of the particle (known as the density of state) distributes according to the values of the confining potential. The particles behave as *minimum field point seekers* or *maximum field point seekers* depending on their *kinematic responses* to the minimum/maximum values of the externally confining potential fields. However, for a *central potential* with a single field minimum or single field maximum, as illustrated in Figure 1.1(b), the two cases meet and the density of the cloud drops exponentially inward or outward the center of the potential depending on the particles favor of the quantum state, whether *low-field seeking state* or *high-field seeking state* while for a *periodic potential* the situation is rather complicated as will be described in the following sections.

In general, when comparing the size of the trapped cloud $V$ to the size of the mean-free-path two regimes can be identified:

(i) *The low-density regime where the mean-free-path is very large compared to the cloud size*

$$l_{mfp} \gg V^{1/3} \tag{1.5}$$

*this is the case where the gas is referred to as free-molecular or collisionless.*

(ii) *The high-density regime*

$$l_{mfp} \ll V^{1/3} \tag{1.6}$$

*which known as hydrodynamic gases.*

### 1.1.2 The phase-space distribution

As we briefly described, the general picture of the statistical considerations for the confined gases was essentially glowed by the so-called *quasi-classical behavior* which is a basic concept that lies at the bottom of most of theoretical frames that interpret or explain the behaviors of the quantum gases. In particular, the logic of the quasi-classical behavior extends beyond the statistical foundations to a crucial shaping of the *quantum resolution limits* and most importantly the classical behavior of the quantum gases in the *phase-space* which is referred to as the *quantum degeneracy*. This section and the following section are devoted to explore their properties in relation to the quantum confinement.

### 1.1.3 The quasi-classical behavior

In the ideal limits, the non-interacting one-body Hamiltonian $\mathcal{H}_o(\mathbf{r}_i, \mathbf{p}_i)$ describes the energy of an individual quantum particle at a given kinetic state $s_i = (\mathbf{r}_i, \mathbf{p}_i)$. Since our constrains allow only particles within the ideal gas limits to access to a specific energy state $\varepsilon_s$ out of the total energy $E_{tot}$, then the *probability* $P_s$ of finding a single particle at a given state $s$ for a trapping potential that dominated by a single-component gas is given by[7]

$$P_s = \frac{e^{-\beta\varepsilon_s}}{\sum_s e^{-\beta\varepsilon_s}} \tag{1.7}$$

This is a well known single particle *canonical distribution* with normalization $\sum_s P_s = 1$ and the single particle *canonical partition function* defined as

$$Z = \sum_s e^{-\beta\varepsilon_s} \tag{1.8}$$

---

[7] The discussion at this stage is compact and we refer to any statistical physics book for more details.

Here $\beta$ is a function of the number of the allowed (micro-states) $\mu$-states $\Omega(\bar{E})$ with energy near $\bar{E} = E_{tot} - \varepsilon_s$ in a *canonical ensemble* of $\mu$-states $\{s_i\}$.

It is very clear that the cloud expands to microscopic scale and the spacing between the available energy states is very small (typically at the atomic level) which allows to mathematically play with the summation in the phase-space from discrete to a more convenient phase-space integration, i.e. $\sum_s \to \vartheta \int d\mathbf{p}d\mathbf{r}$ with $\vartheta = (\frac{1}{2\pi\hbar})^3$, the summation runs over all the accessible $s$ energy states which are closely spaced. Therefore, regardless of the fact that we are dealing with a quantum system one finds the energy spectrum is replaced by the so-called *quasi-classical continuum* and the gaseous behavior is identified as a *quasi-classical behavior*.

Turning the attention to the continuum transition and making use of the fact that the non-interacting one-body Hamiltonian in equation (1.4) is continuous with respect to the two dimensions **r** and **p** of the phase-space, the expression of the probability $P_s$ in equation (1.7) can be converted to a *probability density* of finding the quantum particle in the phase-space with a position **r** and momentum **p** and takes the following form

$$P(\mathbf{r}, \mathbf{p}) = \vartheta \Big( \frac{e^{-\mathcal{H}_o(\mathbf{r},\mathbf{p})/k_B T}}{Z} \Big) \tag{1.9}$$

where $k_B$ is the Boltzmann constant. In the quasi-classical limit and with the normalization condition $\int P(\mathbf{r}, \mathbf{p}) d\mathbf{p} d\mathbf{r} = 1$ holds, the single particle canonical partition function takes the form

$$Z = \vartheta \int e^{-\mathcal{H}_o(\mathbf{r},\mathbf{p})/k_B T} d\mathbf{p} d\mathbf{r} \tag{1.10}$$

The quantity $\vartheta$ has a special meaning in the phase-space, it represents the *phase-space occupation* of the state $\{\mathbf{r}, \mathbf{p}\}$ (sometimes known as phase-space point $(\mathbf{r}, \mathbf{p})$) where in our case it deals with the number of the quantum particles occupying, at time **t**, an *elementary volume* $\vartheta$ in the phase space.

In Chapter (2), we will show how the phase space element contributes to the deviation in the behavior of the confined gases from the classical limits to exhibit the so-called *quantum degeneracy*. To this end, it is important to stress on these notations because they make crucial meanings around some phase space points in which case the trapped gases experience the so-called *critical phase transition*, such as the transition to the Bose-Einstein condensate.

## 1.2 The Bose-Einstein Condensation

For tracking down the Einstein generalization principle and the emergence of the condensation state to their origins, our starting point should be the mathematical derivation made by S. Bose[8]. It assumes that the total radiative energy $E$ is to be enclosed in a volume $V$ containing $N^q$ number of the quanta $h\nu^q$ with $q$ the summation index. This makes the total energy to read $E = \sum_q N^q h\nu^q$. Thermodynamically, the second law implies that the system arrange itself to maximize the probability of the distribution of the $N^q$ quanta restricted to the boundary conditions of the energy. Since we started with the Planck's radiation the quanta are forced to remain in a hypersurface in the space due to the following frequency-impulse relation of the photons

$$p_x^2 + p_y^2 + p_z^2 = \frac{h^2\nu^2}{c^2} \tag{1.11}$$

---

[8] We intentionally organize the physics in this overview in a preliminary shape to assure the connectivity of the presented topic back to its origin.

The total number of cells in the phase space, or for a frequency interval $d\nu$, is $8\pi\frac{h\nu^2}{c^3}d\nu$ and we can say that for the frequency interval $d\nu^q$ there are $N^q$ of quanta with $\rho$ number of permutations that distribute the quanta into the cell such that

$$\ln\Big(\rho\Big) = \sum_q 8\pi\frac{h\nu^2}{c^3}d\nu^q \ln\Big(\rho\Big) - \sum_q\sum_p n_p^q ln\Big(n_p^q\Big) \tag{1.12}$$

where $n_p^q$ is the number of cells in the frequency interval in which case each cell contains $p$ photons. Therefore, the total number of quanta reads

$$N^q = \frac{C^q e^{-\frac{h\nu^2}{\beta}}}{1-e^{-\frac{h\nu^q}{\beta}}}, \qquad \text{with} \qquad C^q \equiv 8\pi\frac{h\nu^2}{c^3}d\nu^q \tag{1.13}$$

Inserting the number $N^q$ into the energy expression $E = \sum_q N^q h\nu^q$ one finds that

$$E = \sum_q N^q h\nu^q = \sum_q 8\pi\frac{h(\nu^q)^3 d\nu^q}{c^3}\frac{V}{e^{-\frac{h\nu^q}{\beta}}-1} \tag{1.14}$$

In the attempt to make the previous expression in (1.14) consistent with definition of the entropy, the factor $\beta$ has to read $\beta = k_BT$.

This is exactly the result that S. Bose has succeeded to reach and led him to formulate the concepts of the Planck's radiation. Einstein's role was to extract a more precise ansatz than that of equation (1.11), the well known energy-impulse relation for massive particles of mass $m$ [23, 24]

$$p_x^2 + p_y^2 + p_z^2 = 2mE \tag{1.15}$$

Consequently, Einstein addressed the following important conclusion[9]:

- *" In the theory of the ideal gas, it appears to be a valid demand, that volume and temperature of a gaseous ensemble can be arbitrarily chosen. Theory then allows to calculate energy and pressure of the gas. But the study of the equation of state (...) shows, that at a given number of molecules n and a given temperature T the volume* ***cannot*** *be made arbitrarily small. (...) It follows then, that the number of molecules in such a gas at a given volume V cannot be greater than*

$$n = \frac{\sqrt[3]{2\pi k_BT}}{h^3}V\sum_{\tau}^{\infty}\frac{1}{\sqrt[3]{\tau}} = \frac{\sqrt[3]{2\pi k_BT}}{h^3}V(2.61)... \tag{1.16}$$

*But what happens now, if I let the density of the gas at this temperature of n/V keep growing further, e.g. by iso-thermal compression? I claim, that in this case a growing number of molecules (growing with the overall density) will traverse into the first quantum state, while the remaining ones will redistribute according to unit degeneracy."*

The last point in Einstein's statement above, namely "... *redistribute according to unit degeneracy*" was the precise prediction and the birth of the new state of mater: The Bose-Einstein condensate (BEC).

Laser cooling [1][2][3][4] was used to allow the neutral atoms to be cooled down to very low temperatures which can reach 10 $\mu$K. Temperatures beyond such limit can also

---

[9] Translated by Christian Buggle, **"Collective and Collisional Properties of the Rubidium Quantum Gas"**, Academish Proefschrift, Hannover-Duitsland.

be reached by subsequently trapping the atoms using magnetic fields and force them to be further evaporatively cooled [5][6][7]. In the year 2001, three physicist Eric A. Cornell, Carl E. Wieman and Wolfgang Ketterle were awarded the Nobel prize in physics due to their achievement in demonstrating the first experimental evidence of the Bose-Einstein condensation in dilute alkali gases [8][9][10][11]. Since the first theoretical prediction of the condensate made by Einstein in 1925, achieving the BEC was a long standing goal until the first realization of Bose-Einstein condensation (BEC) in dilute atomic Rb and Na gases in 1995 [10][11]. Since then, this field have witnessed an incredible amount of research activities where the BEC has been observed in many atomic systems, including most alkali atoms, metastable He [12][13], Cs [14], Cr [17], H [18], Yb [15], as well as in the weakly bound dimers of Li [19] and K [20].

### 1.2.1 The Optical Lattices

The field of quantum degenerate gases in periodically distributed microscopic potentials has gained considerable attention over the last decade where it is being explored to unlock the answers to various interesting fundamental questions in physics. In particular, the field of trapped ultracold atoms in optical confining fields, i.e. optical lattices [21], has achieved remarkable results in the simulation of condensed matter systems. Optical lattices are recognized for their ability to coherently transfer cold atoms, via spin-dependent transport, between the lattice sites [41]. Such coherent manipulation has allowed, using trapped low-dimensional quantum gases [42][43], to establish realizable analogies with condensed matter systems [44]. As an example, the Mott-insulator to superfluid transition has been observed using optically trapped Bose-Einstein condensates [45] and, more interestingly, the transition has also been realized using optically trapped ultracold fermionic gases [46] as well as the observation of the Fermi surfaces [47].

In the context of quantum processors using trapped ultracold atoms, it is crucial to satisfy the scalability criterion in order to process quantum information [48]; optical lattices are thought to provide scalable quantum systems where remarkably they have allowed large scale quantum entanglement [49][64] pointing to the possibility of using such ensembles to serve as quantum processing units.

### 1.2.2 The Permanent Magnetic Atom Chips: The Magnetic Lattices

Integrating ultracold atoms with magnetic microstructures [50] and the creation of Bose-Einstein condensates on an atom-chip [51][52][62] have triggered an alternative approach to optical lattices. To realize a magnetic lattice, periodically distributed non-zero magnetic field local minima are created by fabricating microscopic patterns on the surface of permanent magnetic materials [23][24][59] or by using current carrying micro-wires [53]. Magnetic lattices created using permanent magnetic films have very low technical noise and relatively high magnetic field gradients with no resistive heating and offer a highly stable trapping environment for ultracold atoms. It is also possible to construct magnetic lattices in one or two-dimensional configurations where the flexibility of the design and current state-of-the art fabrication technologies allow the implementation of arbitrary trap geometries and scalable lattice spacing [54].

Only atoms (quantum particles) prepared in low field-seeking states are attracted to, and trapped in, the distributed confining magnetic potentials, allowing magnetic-state selectivity as a characteristic identity of the magnetic lattices. This provides a remarkable opportunity to employ on-chip detection and manipulation techniques [55] such as applying radio frequency fields for on-site atomic manipulation [64], evaporative cooling and spectroscopy

[35].

One-dimensional magnetic lattices have been used as magnetic mirrors to reflect atoms in low field-seeking states [56][57][58][63] and, in recent experiments, radial trap frequencies of up to 90 kHz have been measured for $^{87}$Rb atoms trapped at a distance of $\sim 5\ \mu m$ above the surface of a one-dimensional permanent magnetic lattice [59]. Trapped gases with temperatures of T = 2.0 ± 0.3 $\mu K$ have been observed in a permanent 2D magnetic microstructure [35] and coherence times of the order of 1 s have been recorded for cold $^{87}$Rb atoms trapped in two different hyperfine states on an atom-chip [50][60]. A Raman focused laser may be used to selectively drive the cold atoms into highly excited Rydberg states as proposed in [35] which can also lead to the dipole blockade mechanism [66][67], exhibiting a single Rydberg excitation per lattice site. These features have attracted the attention to examine qubit formation and entanglement in magnetic lattices. The internal hyperfine, or Zeeman, magnetic states of the trapped cold atoms can be used to encode the qubit states $|0\rangle$ and $|1\rangle$, where recently a superposition of two hyperfine states with a long coherence lifetime has been demonstrated [60], indicating the possibility of constructing quantum gates with a lifetime longer than the gate operation time [37][61]. This, as well, suggests magnetic lattices to be promising candidates for a scalable quantum processing unit.

Regardless of the above advantages, the permanent magnetic atom chips have some obvious drawbacks. There is no trivial dynamical control available over the distributed trapping potentials where, as a result, up to now all the reported permanent magnetic atom chips rely on using external control bias magnetic fields and current-carrying micro-wires to assist loading the cold atoms into the micro-traps. External bias fields are also used to avoid trapping the atoms very close to the surface because the so-called Casimir-Polder surface potential may ultimately limit the transition to the Bose-Einstein condensate [53]. The ballistic expansion of the cold atomic cloud, before loading into the atom chip, also needs to be carefully addressed for realizing any sophisticated configurations, such as the permanent magnetic 1D and 2D lattices. The Johnson noise in the metal of the atom chip is also known to cause atom loss [52] where metal layer thickness and its conductivity contribute to the loss rate [53, 54, 55]. However, when using permanent magnetic atom chips this problem can be avoided by using thin or poorly conducting films. Another well known problem is the fragmentation of the trapped cloud which arises from the potential corrugation. Due to the deformation of the fabricated patterns the trapping field is also deformed and consequently causes the cloud fragmentation [37, 56, 57, 58]. Carefully designing the atom chip will resolve this technical problem [59, 60, 61].

## 1.3 The Bose-Einstein Condensation of Excitons in Quantum Heterostructure

As well known, in the atomic structure of the semiconductors there are several energy bands available for electrons to occupy but only a few of them are relevant at a particular energy scale, those which have likelihood to be connected via any type of threshold excitations such as *optical excitations*.

In the undoped semiconductor devices, i.e. at the crystallized atomic level, the valence band is completely filled while the conduction band is completely empty. In this type of structures one realizes an *elementary excitation* when an electron become excited and transfered from the valence band into the conduction band by a proper exciting mechanism such as the absorption of a photon. Once an electron gets excited, and thus elevated to a higher energy level, it leaves an empty state behind in the valence band known as *hole* with a positive charge. Consequently, a mutual interaction between the valence band hole and the conduction band electron is created where they stay in a so-called bound state for a short life time, in the order of femto/nano-second, and they both eventually bind to emit a photon.

The mutually interacting electron-hole pair are regarded as a single composite particle in a virtual state in which case the new particle behavior is best described as a hydrogen atom. The name *hydrogenlike particle* has coined to name such quantum objects. The resulting bound state of the *composite electron-hole particle* is known as *exciton*[10]. Exciton energy can be calculated as in the case of the hydrogen atom, with two modifications:

- *The electron-hole pair must be created, i.e., a valence band electron must be given an energy equal to the band gap and transfered. In other words, the excitons must maintain a remaining virtuality.*
- *Both particles, i.e electron and hole mixed to create the exciton, suffer the localized intrinsic crystal potential field. Coulomb interaction is changed due to the presence of the underlying crystal via the potential field.*

Since excitons are created by optical excitations and can convert into photons, exciton motion essentially corresponds to transport of optical energy. Due to the excitonic effective mass these particles move much more slower than the photons and therefore can undergo a spontaneous phase transition to a superfluid state just like condensed atoms. The excitonic condensate can be identified as it corresponds to a spontaneous appearance of optical phase coherence even without lasing, i.e. "coherence without stimulated emission". The phase coherence (the spontaneous appearance) manifests itself as a macroscopic number of excitons that attracted to occupy a single quantum state. This phenomenon, known as "spontaneous symmetry breaking," which leads to the so-called superfluidity, superconductivity, and other fascinating effects.

One way of looking at the (indirect[11]) condensate transition is to create a mixed state of an exciton and a photon to form what is called a polariton [137]. Excitons or polaritons in semiconductors can be created at liquid helium temperatures via an intense, ultrafast (picosecond or femtosecond) laser pulse and the evolution of their momentum distribution and the spatial distribution can be examined by detecting the light they emit. There are several methods that one can use to detect such effect

- either via a time-gated CCD camera with 5 ns resolution,
- time-correlated photon counting with 40 ps resolution,
- a streak camera with 5 ps resolution or
- pulse-probe methods with subpicosecond resolution.

Since these coupled quantum particles, the polaritons, behave more *photon-like* than just simple excitons, the discrimination between the Bose-Einstein condensation of polaritons and lasing[12] is clearly visible; one can call spontaneous coherence in this system a *polariton laser*. So far the confining electric potential field is the only method that being used to trap excitons in GaAs or InGaAs quantum wells, at which an inhomogeneous electric field is applied perpendicular to the plane of the wells. The excitons become polarized and move in response to the gradient in the electric field. In principle, spontaneous coherence of polaritons can occur even at room temperature.

---

[10] Due to extremely short lifetime of the excitons they are regarded as virtual particles.

[11] Purely condensed excitons is not realized yet, however assisted transition, i.e. indirect formation of excitons has been created, such as coupling photon to exciton to form polariton and then condense.

[12] It is a situation where the lowest excitation level is dominated by stimulated emission rather than by spontaneous emission at the output of the laser.

### 1.3.1 Bose-Einstein condensate in solids state mediums

Although the Bose-Einstein condensate of atomic gases has well progressed since 1995 into rather mature sub-discipline of its own, one has to stress on the fact that no clear analogue has been established in solid state systems. This is mainly due to the slow progress in the experimental work to produce high enough density and/or to obtain a clear evidence in spite the complication of solids. Table (1.1) shows some of the parameter comparison for BEC of different quantum particles.

***Table 1.1:*** Comparison of some parameters of Bose-Einstein condensation of different quantum particles.

| System | Atomic gases | Excitons | Polaritons |
|---|---|---|---|
| Effective mass $\frac{m^*}{m}$ | $10^3$ | $10^{-1}$ | $10^{-5}$ |
| Bohr radius $a_B$ | $10^{-1}$ $\mathring{A}$ | $10^2$ $\mathring{A}$ | $10^2$ $\mathring{A}$ |
| Particle spacing: $n^{-1/d}$ | $10^3$ $\mathring{A}$ | $10^2$ $\mathring{A}$ | 1 $\mu m$ |
| Critical temperature $T_C$ | 1 $nK \sim 1$ $\mu K$ | 1 $mK \sim 1$ $K$ | 1 $K \gtrsim 300$ $\mu K$ |
| $\frac{\text{Thermalization time}}{\text{Lifetime}}$ | $\frac{1ms}{1s} \sim 10^{-3}$ | $\frac{10ps}{1ns} \sim 10^{-2}$ | $\frac{1\sim 10ps}{1\sim 10ps} = 0.1 \sim 10$ |

- **BEC of Excitons**

The excitons BEC was first proposed by Moskalenko [124] and Blatt $et.al$ [125] in 1962. Experimentally, in the first conference on BEC held in 1995, the most convincing evidence has been shown in a system for the ortho-excitons in bulk $Cu_2O$ [126]. However, it was found later that the *Auger-recombination* process of excitons has prevented the system from reaching the critical density of BEC [127][128][129]. Butov $et.al$ [130][132] and Snoke $et.al$ [131] have again shown in 2002 a few macroscopic phenomena observed in quantum-well systems and thought to be related to BEC of excitons but more careful analysis concluded later otherwise. However, quantum degeneracy was obtained with no evidence of phase transition within such system, e.g. the coherence properties and momentum distribution of the excitons [132][133].

- **BEC of Polaritons in Bulk and Microcavity**

Another example for the quantum particle in bulk semiconductors is the so-called polariton[13] where in 1968 BEC transition was also proposed to occur with bulk polaritons [134]. However, the bulk polaritons are outside the exciting optical cone (usually very narrow) and hence do not directly couple to light. Their bands minimum energies are the crystal ground state with zero excitation energy and unfortunately the BEC transition occurs only at the bottleneck energy-relaxation. The large degeneracy of these states makes the picture rather complicated.

The scenario is totally different when coupling light fields produced in semiconductor microcavity to the excitons. Due to the full overlap of the cavity and the exciton envelop wavefunctions (both are plane waves), the coupling strength is relatively large, and polaritons are often eigen-modes of the system. Also, due to the tight confinement of the photon in the cavity and the excitons in the quantum well along the growth direction, in which case the translational symmetry is broken in the longitudinal direction, the detection proximity

---

[13] The optical filed, e.g. of a semiconductor microcavity, strongly couples to the excitons in embedded quantum well to produce two normal modes, the lower polariton and the upper polariton. They have various quantum phases including the BEC.

relays only on the transverse wavenumber $k_{||}$ as a good quantum number for microcavity polaritons [135]. The information about the internal polaritons can be directly obtained from the photon emission where the coupling rate is determined by a fixed cavity photon outcoupling rate. The observation of the microcavity polaritons has triggered many reports for the stimulated scattering threshold of polaritons [136][137][138][139] and recently, first-order spatial coherence was studied for the bottleneck polaritons above the stimulated scattering threshold [140].

Through the carried experimental investigations, we introduced a new trapping mechanism which based on using an inhomogeneous confining magnetic field instead of electrical field. To allow such magnetic filed confinement excitons are assumed to interact with the inhomogeneous potential field and seek the field local minima in a similar scenario to that of magnetic trapping of cold atoms prepared in low field seeking-states. The proposed method is based on integrating magnetic material with multiple quantum wells system where we show how to create and to allocate the magnetic field local minima within a plane of spatially distributed excitonic degenerate gas. Excitons stated as bosons and can undergo Bose-Einstein condensation under certain conditions, several attempts have claimed the creation of Bose condensation of exitons in the past ten years, but there is still ongoing debate to clarify these vague claims. Experimentally, it is still not clear how the excitons can maintain a *direct* transition to the Bose-Einstein condense state. The main purpose of the current experiments is to draw the attention to the possibility of using the magnetic micro-traps as a confining mechanism for excitonic particles where this mechanism is assumed to allow employing a further cooling mechanism to achieve the BEC of excitons, such as the evaporative cooling.

Chapter 2

# Quantum Degenerate Gases

> ¶ *If, then, it is true that the axiomatic basis of theoretical physics cannot be extracted from experience but must be freely invented, can we ever hope to find the right way? I answer without hesitation that there is, in my opinion, a right way, and that we are capable of finding it. I hold it true that pure thought can grasp reality, as the ancients dreamed.* ... (*Albert Einstein*, 1954)

## 2.1 Conceptual Approach to the Quantum Degenerate Gases

IN order to understand the underlying physics of the interacting *quantum gases*, whether weak or strong interaction, and to carefully settle the vague awareness of what is meant by the quantum degeneracy, one needs to recall the original theoretical frames that describe such interactions and play the main role in our interpretations for what is observed at the quantum levels.

In regards to the phenomena we are about to explore, it is often convenient to start by looking at the statistical and thermal properties of the *weakly interacting gases* which are referred to as *dilute* gases at low densities. This is a situation where the *quantum particles*, such as *free neutral atoms* and *excitons*[1] in solids, in their ground state mutually interact via isotropic[2] short-range interatomic potential $\mathcal{U}(\mathbf{r}_{ij})$ which vanishes or can be neglected beyond certain limit known as the radius of the interaction $r_o$. This characteristic radius $r_o$ plus the number $n$ of atoms can be used to describe the atomic gas dilutely condition, such that $nr_o^3 \ll 1$.

### 2.1.1 The quantum degeneracy

We start by recalling the quantity *phase-space density* which describes the number of points per unit volume in the phase space for $N$ single-particles. It is an expression that relates the total number of particles $N$ to the probability of finding that phase point, which is written as follows

$$n(\mathbf{r}, \mathbf{p}) = NP(\mathbf{r}, \mathbf{p}) = \vartheta\zeta(\mathbf{r}, \mathbf{p}) \tag{2.1}$$

The phase-space distribution is represented here by the function $\zeta(\mathbf{r}, \mathbf{p})$ where the over all integration leads to total number of particles under the distribution

---

[1] Exciton is a composite particle of electron-hole pair.

[2] $\mathcal{U}(\mathbf{r}_{ij}) \equiv \mathcal{U}(\mathbf{r}_i - \mathbf{r}_j)$ has central symmetry that depends only on the atoms relative distances $r_{ij} = |\mathbf{r}_i - \mathbf{r}_j|$

$$N = \vartheta \int \zeta(\mathbf{r}, \mathbf{p}) d\mathbf{p} d\mathbf{r} \tag{2.2}$$

For inspecting the quantum degeneracy we need to bring the distribution $\zeta(\mathbf{r}, \mathbf{p})$ to its limit, therefore by evaluating the distribution function at the center of the phase space we find that

$$\zeta(0, 0) = \vartheta^{-1} N P(0, 0) = N Z^{-1} \equiv \Theta \tag{2.3}$$

where $\vartheta = (\frac{1}{2\pi\hbar})^3$ and $Z$ as defined in (1.10). Now, the unit volume enters into the playground by maintaining the dimensionless quantity $\Theta$ which represents the number of phase points that belong to each single-quantum particle in the phase space per unit[3].

The importance of the quantity $\Theta$ appears once we start examining the *quantum resolution limits* of the trapped gas in which case the limits are set by the quantum rules, specifically the determination of the smallest possible spatial and momentum resolutions leading to the well known Heisenberg uncertainty principle $\Delta\mathbf{r}\Delta\mathbf{p}_\mathbf{r} \geq \frac{1}{2}\hbar$ with $\mathbf{r} \in \{x, y, z\}$. This is exactly the classical picture of the confined quantum particles which is well known as the *quantum degeneracy effect* with $\Theta$ being the *quantum degeneracy parameter*. More importantly, the above analogue draws the attention to the fact that, at the quantum resolution limits, there are actually a finite number of $\mu$-states at a given distinguishable energy in which case the gas behaves quasi-classically and the phase space density is assumed to be low.

Now we are in a place to extract several useful information regarding the number of particles at specific location having all possible momentum states as well as defining the degeneracy levels of such *quantum gases*. In particular, we can now find a suitable expression for the quantum degeneracy parameter in terms of experimentally accessible factors. But before we do that we need to find a clear answer for an unavoidable question: *What are the quantum gases*?

### 2.1.2 Quantum gases and the characteristic thermal wavelength

Typically, quantum gases appear when the quasi-classical approach breaks down at the quantum resolution limits which is the case when the dimensionless quantum degeneracy parameter $\Theta$ reaches its unity. This limit is attained at very low temperature for a given density, contradicting with the *Van der Waals equation of state* which requires sufficiently high temperature to allow the existence of weakly-interacting quasi-classical gases under equilibrium condition manifesting itself as a gas to liquid phase transition[4].

In the attempt to quantify the quantum degeneracy parameter, we start by calculating the probability of finding a single particle at the position $\mathbf{r}$ which is done by integration over the momentum space

$$\begin{aligned} n(\mathbf{r}) &= \vartheta \int \zeta(\mathbf{r}, \mathbf{p}) d\mathbf{p} \\ &= \Theta e^{-\mathcal{V}(\mathbf{r})/k_B T} \vartheta \int_0^\infty e^{(p/\gamma)^2} 4\pi p^2 dp \end{aligned} \tag{2.4}$$

where $\gamma = \sqrt{2mk_B T}$. It is clear now that we have to take into account the effect and the shape of the external potential $\mathcal{V}(\mathbf{r})$ along with the temperature $T$ where with these consideration the above expression in (2.4) just turned out to be the density distribution of the gas in the

---

[3] Some textbooks refer to the unit cubic Plank constant, though it does not account in the classical limits.

[4] A detailed analysis can be found in F. Reif, *Fundamental of statistical and thermal physics*, McGraw-Hill, Inc., Tokyo 1965 or any recent addition.

configuration space. For simplicity, we introduce the *central density* $n_o$ of the trapped gas written as

$$n_o = n(0) = \Theta\vartheta \int_0^\infty e^{-(p/\gamma)^2} 4\pi p^2 dp \tag{2.5}$$

and by substituting $n_o$ into equation (2.4) will reduce it to the following form

$$n(\mathbf{r}) = n_o e^{-\mathcal{V}(\mathbf{r})/k_B T} \tag{2.6}$$

making use of the Gamma special integration (A.1) to evaluate equation (2.5) to read as follows

$$n_o = \Theta\vartheta \Big( \frac{1}{\vartheta \Lambda^3} \Big) \tag{2.7}$$

where $\Lambda = \sqrt{\frac{2\pi\hbar^2}{mk_BT}}$ is the so-called the *thermal de Broglie wavelength*.

It is clear that we managed to maintain an expression for the quantum degeneracy parameter $\Theta$ which can now be written as

$$\Theta = n_o \Lambda^3 \tag{2.8}$$

If we integrate the density distribution $n(\mathbf{r})$ in equation (2.6) over the same configuration space we obtain the total number $N$ of the trapped particles

$$N = \int n(\mathbf{r}) d\mathbf{r} = n_o \int e^{-\mathcal{V}(\mathbf{r})/k_B T} d\mathbf{r} \tag{2.9}$$

Moreover, one can calculate the *effective volume* $V_e$ of the trapped cloud by evaluating the ratio $V_e \equiv N/n_o$ as follows

$$V_e \equiv \frac{N}{n_o} = \int e^{-\mathcal{V}(\mathbf{r})/k_B T} d\mathbf{r} \tag{2.10}$$

With the aid of the above equation (2.10) we can experimentally estimate the central density $n_o(N,T)$ of the trapped gas by measuring the number of the particles $N$ along with the effective volume $V_e(T)$. We can also use equation (2.10) to relate the single particle canonical partition function $Z$ to the effective volume by rewriting $Z$ from equation (2.3) to read

$$\frac{1}{Z_1} = \frac{n_o}{N} \Lambda^3 \longrightarrow Z = V_e \Lambda^{-3} \tag{2.11}$$

We can now find a qualitative estimate to the quantum resolution limits that we mentioned in section (2.1.1). By recalling one of the elementary quantum physics concepts, the Heisenberg uncertainty principle $\Delta\mathbf{r}\Delta\mathbf{p}_\mathbf{r} \simeq \hbar$ with $\mathbf{r} \in \{x, y, z\}$, we can then make use of the root mean square (rms) fluctuation in the momentum space to be written as

$$\Delta\mathbf{p} = \sqrt{\langle (p - \bar{p})^2 \rangle} \simeq \sqrt{\frac{mk_BT}{2}} \tag{2.12}$$

as well as using the definition of the uncertainty in the position, we find a clear barrier that contains the quantum resolution. This barrier is defined as a limit for such resolution and it become pronounced when $\Delta\mathbf{r}$ reaches the interatomic spacing, such that

$$\Delta\mathbf{r} \simeq \frac{\hbar}{\Delta\mathbf{p}} = \sqrt{\frac{2\hbar^2}{mk_BT}} \simeq \frac{1}{\sqrt[3]{n_o(T)}} \tag{2.13}$$

Apparently, $\Delta\mathbf{r}$ depends on the temperature and therefore it is known as the *thermal wavelength*. The term thermal wavelength is triggered because $\Delta\mathbf{r}$, at a rough estimate, has the same magnitude as the *de Broglie wavelength* of an atom moving with the average momentum of the gas, $\Delta\mathbf{r} \simeq \frac{1}{\pi^2}\Lambda$.

It is clear that the thermal wavelength $\Delta\mathbf{r}$ and the de Broglie thermal wavelength $\Lambda$ coincide within a factor of two which means that at a relatively high temperature $\Lambda$ is small compared to the size of the gas cloud $V^{1/3}$, the average interatomic distance $n^{-1/3}$ or the interatomic potential range $r_o$, in which case the interpretation can mainly be classical.

To conclude, we can now distinguish between two regimes:

- ***Quantum non-degenerate gases***

  *It is a regime where the quantum mechanics manifest itself in a binary scattering events where the temperature is very low and the thermal de Broglie wavelength is large compared to the interatomic potential, i.e.* $\Lambda > r_o$.
  *At* $T = 0$*, the binary interaction energy is positive irrespective of the depth of the interaction potential which also presents a signature of the unbound states. To be precise, the positivity of the binary interaction implies positive pressure in the low-density low-temperature limits where they are also referred to as* ***metastable gaseous states*** *(and this is why it is known as* ***unbound states****). As the density increases the system become unstable with a large chance for the three-body collisions to dominate and hence increased the probability to form molecules and droplets resulting in a liquid or solid.*

- ***Quantum degenerate gases***

  *The overall picture made up to this point shows a scenario of* ***many-body quantum system*** *where the thermal de Broglie wavelength is much larger than the interatomic spacing, i.e.* $n\Lambda^3 > 1$ *in which case the quantum statistics is a mandatory for describing the thermodynamics and the kinetic properties of such system.*

## 2.2 Quantum Gases in Harmonic Traps

As early mentioned, the quantum particles and gases behave differently in a wall-free confinement. Enhanced details regarding the interacting picture and the behavior of the magnetically confined dilute gases will be given in chapter (4) including the adiabatic variations of the confining potential and their effect in the tunneling of the quantum particles, such as the effect of the tilted potential (or as we call it the *asymmetrical effect*) leading to an adiabatically induced tunneling of the quantum degenerate gases.

We are considering the confinement of two types of quantum particles, first we will discuss the magnetic trapping of the *ultracold atoms* in the central and periodical trapping potentials. Second, we will discuss the magnetic confinement of the *electron-hole composite quantum particles* (i.e. the *excitons*). Our dialog is stretched over the conceptual approach of the magnetic local field minima imprinted within a plane of multiple quantum wells system.

### 2.2.1 Modeling the isotropic confining potentials

One of the possible models that has been intensively used to simulate the *free-wall harmonic trapping potential*, described in the Hamiltonian equation (1.4), is the general *power-law* traps [16][21]. It assumes isotropic distribution of the confinement which takes the form

$$\mathcal{V}(r) = \mathcal{V}_o\Big(\frac{r}{r_c}\Big)^{3/v} \equiv \omega_o r^{3/v} \tag{2.14}$$

To configure the potential distribution isotropically, we are specifically picking this model because it accepts different values for the *trap parameter* $v$, the *trap characteristic size* $r_c$ and the *trap coefficient* $\omega_o = \mathcal{V}_o r_c^{-3/v}$ with $\mathcal{V}_o$ being the *trap strength*. For example for the limit $v \to 0$ the model simulates a *spherical square well*, as described in table (2.1).

It is important to find a suitable model for the confining potential that best describes the actual trap in which case several useful information can be extracted when using such model. For example, we can understand the nature of the interaction and phase space occupancy by substituting suitable expression for the external confining potential term in the Hamiltonian (1.4) such as the square well, the effective confining volume $V_e(T) = u_{pl}T^v$ and most importantly the harmonic trapping potential $\frac{1}{2}m\omega^2$, where $\omega$ represents the trapping frequency.

***Table 2.1:*** The isotropic power-law trap can take several shapes of distributions as detailed in this table [16].

| | Square well | Harmonic trap | Linear trap | Square root dimple trap |
|---|---|---|---|---|
| $\omega_o$ | $\mathcal{V}_o r_c^{-3/v}$, $v \to 0$ | $\frac{1}{2}m\omega^3$ | $\mathcal{V}_o r_c^{-1}$ | $\mathcal{V}_o r_c^{-1/2}$ |
| $v$ | 0 | 3/2 | 3 | 6 |
| $u_{pl}$[5] | $\frac{4}{3}\pi r_c^3$ | $\sqrt[3]{\frac{2\pi k_B}{m\omega^2}}$ | $\frac{4}{3}\pi r_c^3 3!\left(\frac{k_B}{\mathcal{V}_o}\right)^3$ | $\frac{4}{3}\pi r_c^3 6!\left(\frac{k_B}{\mathcal{V}_o}\right)^6$ |
| $\varpi_{pl}$ | $\frac{2\sqrt{2}}{3\pi}\left(\frac{\sqrt{m}r_c}{\hbar}\right)^3$ | $\frac{1}{2}\left(\frac{1}{\hbar\omega}\right)^3$ | $\frac{32\sqrt{2}}{105\pi}\left(\frac{\sqrt{m}r_c}{\hbar}\right)^3\mathcal{V}_o^{-3}$ | $\frac{2048\sqrt{2}}{9009\pi}\left(\frac{\sqrt{m}r_c}{\hbar}\right)^3\mathcal{V}_o^{-6}$ |

### 2.2.2 Density of states of the trapped gases

At the quantum level, the confined gases obey specific distribution pattern which is shaped due to the particle favor of the *energy state*. Most of these gases do not rely on the trapping potential space-configuration or the momentum-space to physically orient themselves. Statistically, they rather depend on the *total energy distribution* in which case the phase-space distribution function $\zeta(\mathbf{r}, \mathbf{p})$ is related to the total energy distribution $\zeta(\acute{\epsilon})$, such that

$$\zeta(\mathbf{r}, \mathbf{p}) = \int \zeta(\acute{\epsilon})\delta[\acute{\epsilon} - \mathcal{H}_o(\mathbf{r}, \mathbf{p})]d\acute{\epsilon} \tag{2.15}$$

where $\mathcal{H}_o(\mathbf{r}, \mathbf{p})$ is the single-particle Hamiltonian defined as

$$\mathcal{H}_o(\mathbf{r}, \mathbf{p}) = \frac{p^2}{2m} + \mathcal{U}(\mathbf{r}) \tag{2.16}$$

The definition in (2.15) suggests that certain number of the microstates $\{\mathbf{r}, \mathbf{p}\}$ share same energy $\epsilon$ and occupy $\vartheta$ unit cell in the phase space.[6] Basically, this is the concept of the so-called *density of states* $\varrho(\epsilon)$ defined as

$$\varrho(\epsilon) = \vartheta \int \zeta(\acute{\epsilon})\delta[\acute{\epsilon} - \mathcal{H}_o(\mathbf{r}, \mathbf{p})]d\mathbf{r}d\mathbf{p} \tag{2.17}$$

with $\vartheta = (2\pi\hbar)^{-3}$ is the phase space unit cell as early defined. Quite clear, $\varrho(0)$ reduces to $\vartheta$ and by integrating over the momentum range and making use of the following integral

---

[5] *pl* stands for power law.

[6] Similarly, while still using the phase space analogy one can refer to several phase space points $\big(\mathbf{r}, \mathbf{p}\big)$ within the unit volume $\vartheta$.

$$\int d\mathbf{p} = 4\pi \int p^2 dp = 2\pi \sqrt[3]{2m} \int \sqrt{\frac{p^2}{2m}} d\Big(\frac{p^2}{2m}\Big) \tag{2.18}$$

we find that $\varrho(\epsilon)$ reduces to

$$\varrho(\epsilon) = 2\pi\vartheta \sqrt[3]{2m} \int_{\mathcal{U}(\mathbf{r}) \leq \epsilon} \sqrt{\epsilon - \mathcal{U}(\mathbf{r})} d\mathbf{r} \tag{2.19}$$

Integrating over the momentum space shows the dependency of the density of states on the distribution of the particles interaction potential.

## 2.3 Adiabatic variation of the confining potential field

In practice, to increase the density of the trapped particles a *time-varying potential* is used in most cases where the time-change-rate determines the gain or loss in the number of the trapped particles. For example, suitable changing rate may result in avoiding *inelastic collisions*[7], though collisions are promoted sometime in purpose to induce specific type of interactions, such as to simulate molecular interaction, spinor BECs and $n$-dimensional Fermions.

The *adiabatic process* appears as a consequence to the mechanical work done on the trapped gas due to the variation of the confining potential, the adiabatic notion comes when there is no exchange of heat between the trapped particles and the environment. It is important to show that sufficiently slow change, with a longer time when compared to the collision times, results in a quasi-static change in the temperature and the pressure in which case *reversing* the process is assumed to bring the particles to their original state, this is an important feature for the oscillating trapped gases between two or more quantum sates as will be explained in some details when we investigate the tunneling process of the trapped quantum particles[8].

A particularly interesting result of the slow adiabatic process is that its effect on the quantum degeneracy parameter $\Theta$. We investigate this by using the power-law trapping potential model (2.14) and making use of the thermodynamic properties of the trapped particles in the ideal gas limit where the partition function for the Helmholtz free energy $F$ reads[16]

$$Z = Ne - \Big(1 + \frac{F}{Nk_BT}\Big) \tag{2.20}$$

and the total energy reads

$$E = Nk_BT^2\Big(\frac{\partial lnZ_1}{\partial T}\Big) = Nk_BT\Big(\frac{3}{2} + v\Big) \tag{2.21}$$

we can now rewrite the degeneracy parameter, defined in equation (2.11), to be expressed in a thermodynamical fashion as follows

$$\Theta = n_o\Lambda^3 \longrightarrow \frac{N}{Z_1} = \exp\Big\{\frac{5}{2} + v - \frac{S}{Nk_B}\Big\} \tag{2.22}$$

$S$ here is the entropy of the trapped gas. Clearly, $\Theta$ does not depend on the temperature and for a constant value of $v$ the cloud shape also remains constant, conserving by that the quantum degeneracy of the trapped particles.

---

[7] Inelastic collisions result in heating or loss of particles.

[8] Reversible adiabatic process is assumed to conserve the entropy $S$ of the trapped quantum gas where $dQ = TdS = 0$, these situation are known to be isentropics.

If we let the trap strength parameter changes adiabatically in time $t$, such that $\mathcal{V}(\mathbf{r}) \rightarrow \mathcal{V}(\mathbf{r}, t) = \mathcal{V}_o(t)\left(\frac{r}{r_c}\right)^{3/v}$ then consequently the central density $n_o$ and the effective volume $V_e$ become functions of time and can be written as follows

$$\frac{n_o}{n_o(t)} = \frac{V_e(t)}{V_o} = \left(\frac{T(t)}{T_o}.\frac{\mathcal{V}_o}{\mathcal{V}_o(t)}\right)^{v} \tag{2.23}$$

Substituting this equation into the expression $T(t) = T_o\left[\frac{n_o(t)}{n_o}\right]^{2/3}$ which describes the change in the temperature with respect to the central density and the effective volume we find the following expression

$$T(t) = T_o\left[\frac{\mathcal{V}_o(t)}{\mathcal{V}_o}\right]^{v/(1+\frac{2}{3}v)} \tag{2.24}$$

This equation is important because it describes the so called *adiabatic cooling* in which case reducing the trap strength results in cooling the trapped quantum particles.

In a similar scenario, reversing the process results in an *adiabatic compression* which gives rise to heating and can be shown as a change in the central density, such that

$$n_o(t) = n_o\left[\frac{\mathcal{V}_o(t)}{\mathcal{V}_o}\right]^{v/(1+\frac{2}{3}v)} \tag{2.25}$$

Surprisingly, for harmonic traps the temperature is related to the trapping frequency via the strength of the trap, such that $T \sim \mathcal{V}_o^{1/2} \sim \omega$ and the central density also reads $n_o \sim \mathcal{V}_o^{3/4} \sim \omega^{3/2}$ which shows that the density of the confined particles increases slower than linear.

To conclude, it is very important to notice that by increasing the *trap depth* (strongly related to the trap strength) and assuming that the trap geometry and the size are fixed, i.e. $r_c$ and $v$ are constants, the density of the trapped particles increases. More importantly, the quantum degeneracy of the trapped particles, as defined by the equations (2.8) or (2.22), remains constant as long as the shape ($v$) stay constant. Also, the increase of the density is accompanied by increase of the temperature while still leaves the degeneracy unaffected[9]. In the following sections we will discuss the concepts of the *ultracold quantum particles* and the *cooling* mechanisms.

---

[9] In the square potential well case ($v$ = 0) the density is not affected by increasing $\mathcal{V}_o$.

## 2.4 Schrödinger equation of collisional motion: The phase shift and the characteristic lengths

A convenient way to settle the quantum mechanical analogue of the interacting picture of degenerate gases is to start by briefly describing the basic concepts of the scattering theory and the Schrödinger equation of interacting quantum particles.

Describing the relative motion of quantum particles is typically based on the assumption that they move slowly at large separation and their interaction is mainly due to the Van der Waals elastic interaction potential where the energy is conserved. The interaction range is often ascribed in terms of the de Broglie thermal wavelength[10] defined as $\lambda_{dB}(T) = \sqrt{2\pi\hbar^2/mk_BT}$ in which case three characteristic lengths are used to scale and quantify the effective range of the interaction potential. These three important parameters, evaluated at the limit $k = \frac{\sqrt{2mE}}{\hbar} \rightarrow 0$, are:

- ***The interaction range*** $r_o$ *: The interaction of the particles may be neglected beyond this distance.*
- ***The scattering length*** $a$ *: Determines the collisional cross section and a scale for the interaction strength. It is also denoted by the* $s$*-wave scattering length which is the effective hard sphere diameter. It is an important parameter in the theoretical description of all Bosonic/Fermionic quantum gases where it determines the interaction energy and the kinetic properties.*
- ***The effective range*** $r_e$ *: Describes how the energy dependence of the cross section is affected by the potential.*

At large interatomic separations, the energy is purely kinetic i.e. $E = \hbar^2k^2/2\boldsymbol{m}$, hence the relative motion wavenumber is also conserved. Most importantly, far away from the scattering center the collision affects only the *phase* of the wavefunction and not the wavelength because of that the *phase shift* is considered as a key parameter in shaping the quantum mechanical description of the elastic collisions.

To show the significance of the phase shift we start by writing down the Schrödinger equation for the relative motion of two particles in a central potential[11]

$$\{\frac{1}{2\boldsymbol{m}}\Big(p_{\boldsymbol{r}}^2 + \frac{\mathbf{L}^2}{\boldsymbol{r}}\Big) + \mathcal{U}(\boldsymbol{r})\}\psi(\boldsymbol{r},\theta,\phi) = E\psi(\boldsymbol{r},\theta,\phi) \tag{2.26}$$

where $\boldsymbol{m}$ is the reduced mass of pair of particles and $\mathbf{L} = -i\hbar \times \nabla$ is the angular momentum operator with $\mathbf{L}^2 = L_z^2 + \frac{1}{2}\Big(L_+L_- + L_-L_+\Big)$ satisfying the commutation relation for $L_\pm$, $[L_+, L_-] = 2\hbar L_z$. The eigenfunctions $\psi(\boldsymbol{r},\theta,\phi)$ can be written as $\psi(\boldsymbol{r},\theta,\phi) = R_l(\boldsymbol{r})Y_{lm}(\theta,\phi)$ where the function $Y_{lm}(\theta,\phi)$ is the spherical harmonic and the function $R_l(\boldsymbol{r})$ satisfies the radial wave equation

$$\{-\frac{\hbar^2}{2\boldsymbol{m}}\Big(\frac{d^2}{d\boldsymbol{r}^2} + \frac{2}{\boldsymbol{r}^2}\frac{d}{d\boldsymbol{r}} - \frac{l(l+1)}{\boldsymbol{r}^2}\Big) + \mathcal{U}(\boldsymbol{r})\}R_l(\boldsymbol{r}) = ER_l(\boldsymbol{r}) \tag{2.27}$$

in which case the effective potential is presented by the rotational energy $-l(l+1)\frac{\hbar^2}{2\boldsymbol{m}\boldsymbol{r}^2}$ of the particles pair at a given distance and for a given rotational quantum number $l$ give rise to the a centrifugal force due to the attractive interaction of the pair particles.

---

[10] The de Broglie wave length, defined as above, is best described as the quantum size of a classical object, see after equation (2.7).

[11] Any textbook of elementary quantum mechanics should be sufficient to provide detail analysis for equation (2.26), see e.g. Eugen Merzbacher, *Quantum Mechanics*, JOHN WILEY & SONS, INC.

- **The phase shift of the free-particles motion**

The radial wavefunction equation (2.27) can be simplified by introducing the quantities $\kappa \equiv k^2 = \frac{2mE}{\hbar^2}$ and $\widetilde{\mathcal{U}}(\boldsymbol{r}) = \frac{2m\mathcal{U}(\boldsymbol{r})}{\hbar^2}$ to read

$$R_l'' + \frac{2}{\boldsymbol{r}}R_l' + \{\kappa - \widetilde{\mathcal{U}}(\boldsymbol{r}) - \frac{l(l+1)}{\boldsymbol{r}^2}\}R_l(\boldsymbol{r}) = 0 \tag{2.28}$$

which can also be reduced to a one-dimensional Schrödinger equation by introducing the wavefunction $\varphi(\boldsymbol{r}) = \boldsymbol{r}R_l(\boldsymbol{r})$ such that

$$\varphi_l''(\boldsymbol{r}) + \{\kappa - \widetilde{\mathcal{U}}(\boldsymbol{r}) - \frac{l(l+1)}{\boldsymbol{r}^2}\}\varphi_l(\boldsymbol{r}) = 0 \tag{2.29}$$

For free particles, equation (2.28) has a general solution for the angular momentum $l$, i.e. $R_l(\boldsymbol{r}\sqrt{\kappa}) = C_1 j_l(\boldsymbol{r}\sqrt{\kappa}) + C_2 n_l(\boldsymbol{r}\sqrt{\kappa})$, which is a linear combination of a regular solution that shows no divergence $j_l(\boldsymbol{r}\sqrt{\kappa})$, and an irregular solution $n_l(\boldsymbol{r}\sqrt{\kappa})$, see the Appendix (A.1.2). The constants $C_{1,2}$ are expressed in terms of a dimensionless parameter $\gamma_l$ such that $C_1 = C\cos(\gamma_l)$ and $C_2 = C\sin(\gamma_l)$ with $\gamma_l = \tan^{-1}\left(\frac{C_2}{C_1}\right)$. This yields another form for the general solution, i.e. $R_l(\boldsymbol{r}\sqrt{\kappa}) = C\Big[\cos(\gamma_l)j_l(\boldsymbol{r}\sqrt{\kappa}) + \sin(\gamma_l)n_l(\boldsymbol{r}\sqrt{\kappa})\Big]$ where it is clear at the limit $\gamma_l \to 0$ the general solution reduces to the regular one.

At this point we can find a better interpretation for the dimensionless parameter $\gamma_l$, where at the limit $\boldsymbol{r}\sqrt{\kappa} \to 0$ the general solution reads

$$R_l(\boldsymbol{r}) \underset{\boldsymbol{r}\to 0}{\simeq} \frac{\widetilde{C}_l(\boldsymbol{r}\sqrt{\kappa})}{\boldsymbol{r}} \sin\left(\boldsymbol{r}\sqrt{\kappa} + \gamma_l - \frac{\pi l}{2}\right) \tag{2.30}$$

with $\widetilde{C}_l(\boldsymbol{r}\sqrt{\kappa})$ stands as the normalization constant. In the above equation, for the solution to become for a free particle $\gamma_l$ has to vanish, i.e. $\gamma_l \to 0$. This is in a agreement with the argument that for free particles it is required that $\gamma_l = 0$ for all angular momentum values which leads us to the following important conclusion:

○ *The dimensionless parameter $\gamma_l$ can be interpreted as the asymptotic phase shift.*

The collisional Schrödinger equation (2.29), for sufficiently large values of $\boldsymbol{r}$, reduces to the free particles equation presenting a solution similar to that in equation (2.30), i.e $\lim\limits_{\boldsymbol{r}\to\infty} = \sin\left(\boldsymbol{r}\sqrt{\kappa} + \gamma_l - \frac{\pi l}{2}\right)$. Thus in the presence of the interaction between the quantum particles the distorted wavefunctions $R_l(\boldsymbol{r}) = \frac{1}{\boldsymbol{r}\sqrt{\kappa}}\varphi_l(\boldsymbol{r})$ describes the events near the scattering center bringing another important conclusion:

○ *For $\gamma_l \neq 0$ the interaction is due to a purely collisional effect.*

Because the phase shift $\gamma_l$ is extremely useful in interpreting the collisional events of different types of quantum gases, at different quantum states and possibly mixture of different species, it is convenient to connect $\gamma_l$ to the interaction potential and the general solution of the Schrödinger equation written in an integration form. Following the Wronskian Theorem[12], the phase shift $\gamma_l$ can be written as

$$\sin(\gamma_l) = -\frac{2m}{\hbar^2}\int_0^\infty \mathcal{U}(\boldsymbol{r})\varphi_l(\boldsymbol{r}\sqrt{\kappa})j_l(\boldsymbol{r}\sqrt{\kappa})d\boldsymbol{r} \tag{2.31}$$

---

[12] The Wronskian and the Wronskian theorem can be found in any of the mathematical books that discuss the bounded second-order differential equations.

In the above integral representation of the phase shift the interaction potential takes its original form in which case this reflects the essential feature of the phase shift to determine the nature of the interaction in the trapped quantum gases.

There are several mathematical models used to simulate the interaction potential. However, we concentrate on the *spherical square potential* in following section to find out the importance of the three characteristic parameters, the *scattering length* $a$, the *effective range* $r_e$ and the *interaction range* $r_o$.

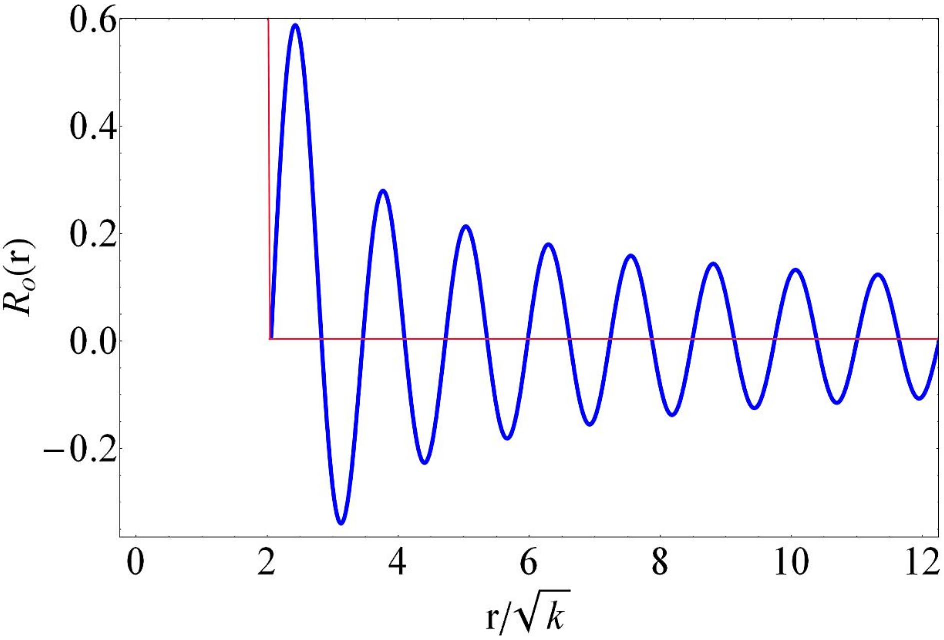

***Figure 2.1:*** The Schrödinger radial wavefunction solution for the hard sphere model. The boundary conditions are fixed by the limits that the wavefunction vanishes at the edge of the hard sphere, i.e. $R_o(\boldsymbol{r}, \sqrt{\kappa}) = 0$.

- **The phase shift related characteristic parameters $a$, $r_e$ and $r_o$ in the low-energy limits**

○ ***Spherical square well model: The scattering length and the bound $s$ state at zero-momentum*** $(l = 0)$

It is convenient now to test the phase shift argument for the spherical square well potential, where our attempt from the start is to relate the phase shift to the characteristic lengths. To start we rewrite equation (2.29) as a one-dimensional Schrödinger equation such that

$$\varphi_0''(\boldsymbol{r}) + \{\kappa - \widetilde{\mathcal{U}}(\boldsymbol{r})\}\varphi_0(\boldsymbol{r}) = 0 \qquad \text{with solutions} \qquad \varphi_0(\boldsymbol{r}) = \begin{cases} \mathcal{C}\sin(\boldsymbol{r}\bar{\kappa}_+) & \text{For } \boldsymbol{r} \leq r_o \\ \mathcal{C}\cos(\boldsymbol{r}\bar{\kappa}_+ + \gamma_o) & \text{For } \boldsymbol{r} \geq r_o \end{cases} \tag{2.32}$$

The wave number $\bar{\kappa}$ is restricted for the particles inside the well and given by

$$\bar{\kappa}_+ = \frac{\sqrt{2\boldsymbol{m}[E - E_{\min}]}}{\hbar^2} = \sqrt{\kappa_o + \kappa} \tag{2.33}$$

The energy of the continuum state is given by $\epsilon = \kappa = K^2$ while for the bound state the energy is $\epsilon_b = -\kappa^2$.

The boundary condition at the point $\boldsymbol{r} = r_o$ is given by $\sqrt{\kappa}\cot(r_o\sqrt{\kappa}+\gamma_0) = \bar{\kappa}_+\cot(r_o\bar{\kappa}_+)$. The special case appears at the zero potential with $\kappa_o \to 0$ in which case the boundary $\bar{\kappa}_+\cot(r_o\bar{\kappa}_+) \to \sqrt{\kappa}\cot(r_o\sqrt{\kappa})$ shows zero phase shift $\gamma_0 = 0$.

From the above analogue we can now relate the *effective hard sphere diameter* $a$ to the phase shift with boundary conditions $\sqrt{\kappa} \to 0$ and $\bar{\kappa}_+ \to \kappa_0$, such that

$$\frac{1}{\kappa_0\Big(r_o - a\Big)} = \cot\Big(r_o\kappa_0\Big) \longrightarrow a = r_o\Big(1 - \frac{\tan\Big(r_o\kappa_0\Big)}{r_o\kappa_0}\Big) \tag{2.34}$$

It is clear that $a \in \{-\infty, +\infty\}$ as shown in Figure (2.2). It purely depends on the potential well depth $\kappa_0^2$ in which case the characteristic length $a$ determines the strength of the interaction potential and it is commonly denoted by the *scattering length*. It is more important to show here the case of the *shallow* potential which is best described by the *near resonances* at $r_o\kappa_0 = (n+\frac{1}{2})\pi$ with $n$ an integer and $a \to 0$.

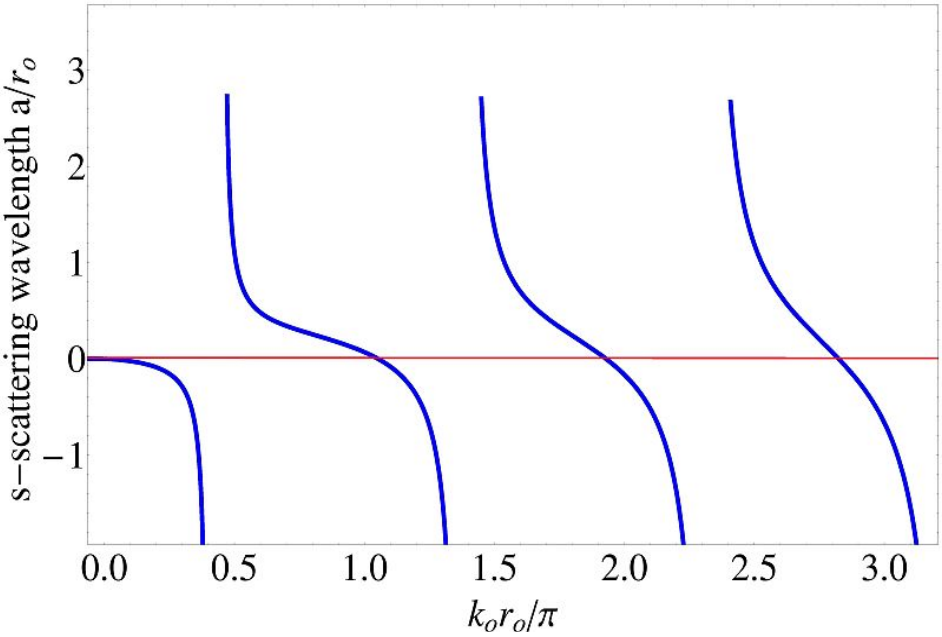

***Figure 2.2:*** The $s$-wave scattering length a normalized on $\boldsymbol{r}$ as a function of the depth of a square potential well as $a$ described in equation (2.34).

The appearance of the so-called ***bound*** $s$ ***states*** inside the potential well is one of the important manifestations of the interacting quantum gases. Regardless it appears at certain circumstances most of the recent experimental efforts rely on these bound $s$ states to simulate or demonstrate specific fundamentals concepts in the broaden field of quantum physics. To briefly describe the appearance of the bound $s$ state, we start by rewriting the radial wave equation in the form of the one-dimensional Schrödinger equation

$$\varphi_0''(\boldsymbol{r}) + \{-\kappa - \widetilde{\mathcal{U}}(\boldsymbol{r})\}\varphi_0(\boldsymbol{r}) = 0 \qquad \text{with solutions} \qquad \varphi_0(\boldsymbol{r}) = \begin{cases} \mathcal{C}\sin(\boldsymbol{r}\bar{\kappa}_+) & \text{For } \boldsymbol{r} \le r_o \\ \acute{\mathcal{C}}\exp\Big(\boldsymbol{r}\bar{\kappa}_+\Big) & \text{For } \boldsymbol{r} \ge r_o \end{cases} \tag{2.35}$$

with the corresponding radial wavefunction $R_0(\boldsymbol{r}) = \acute{\mathcal{C}}\frac{1}{\boldsymbol{r}}\exp(\boldsymbol{r}\bar{\kappa}_+)$ where $\mathcal{C}$ and $\acute{\mathcal{C}}$ are the normalization constants. The reason why we recall the equation (2.35) is to justify the resonance condition for this special case where the boundary condition at the point $\boldsymbol{r} = r_o$ (similar to the above effective range discussion) is determine by resolving the continuity of the logarithmic derivative $\frac{\varphi_0'(r)}{\varphi_0(r)}$, such that

$$-\kappa = \bar{\kappa}_- \cot\Big(r_o - \bar{\kappa}_-\Big) \qquad \text{with} \qquad \bar{\kappa}_- = \frac{\sqrt{2\boldsymbol{m}\Big(E - E_{\text{min}}\Big)}}{\hbar} = \sqrt{\kappa_0 - \kappa} \tag{2.36}$$

At the limits $\kappa \rightarrow 0$ and $\bar{\kappa}_- \rightarrow \kappa_0$ the bound $s$ state appears in which case its appearance coincides with the resonance condition $r_o\kappa_0 = (n + \frac{1}{2})\pi$ and equation (2.36) reduces to $r_o\kappa_0 cot(r_o\kappa_0) = 0$.

There is another (experimentally) attractive feature exist in the bound $s$ level, the so-called *halo states* which are weakly bound $s$ levels. They are well known by their large and positive scattering lengths, i.e. $a \gg r_o$ where at the boundary $\sqrt{\kappa} \rightarrow 0$ the approximation of equation (2.36), $-\kappa = \bar{\kappa}_- \cot(r_o - \bar{\kappa}_-) \rightarrow \kappa_0 \cot(r_o\kappa_0)$, is to rewrite the equation (2.34) at the boundary $0 < r_o\kappa_0 \ll 1$ in the following form

$$a = r_o\{1 - \Big(\frac{1}{r_o\kappa_0}\Big)\tan(r_o\kappa_0)\} \simeq \frac{1}{\kappa} \tag{2.37}$$

We can also relate the energy of the weakly bound states in terms of the scattering length using the above equation (2.37) and the fact that the (normal) bound $s$ level has an energy $\epsilon_b = -\kappa^2$. Thus, the energy of the weakly bound $s$ states reads

$$E_b = -\frac{\hbar^2\kappa^2}{2\boldsymbol{m}} \underset{\kappa\rightarrow 0}{\simeq} -\frac{\hbar^2}{2\boldsymbol{m}a^2} \tag{2.38}$$

The reason why the name halo is triggered for the weakly bound $s$ states is because their probability is found to exist outside the potential well for $r_o\kappa_0 \ll 1$. This is an important point because these states surround the scattering center like a halo in which case this can be used to simulate tunning many parameters in condensed matter systems, such as *Feshbach resonance*. Feshbach resonance is beyond the scope of this dissertation, but it worth mentioning that due to its importance it is currently being under intensive theoretical and experimental investigations [121][122][123].

- ***Spherical square well model: The effective range and the scattering resonance*** $(l = 0)$

As we described early in this section, we would like to relate the energy to the phase shift which is best described using one of the characteristic lengths; we formulate this connection using the *effective range*. In general, the so-called background contribution $\gamma_{bgr}$ adds up to the resonance $\gamma_{res}$ in the phase shift giving a rise to linear phase development and modifies the boundary condition $\sqrt{\kappa}\cot(r_o\sqrt{\kappa} + \gamma_0) = \bar{\kappa}_+ \cot(r_o\bar{\kappa}_+)$ at $\boldsymbol{r} = r_o$ into the following general form of the phase shift

$$\begin{aligned}\gamma_o &= \gamma_{bgr} + \gamma_{res} \\ &= -r_o\sqrt{\kappa} + \tan^{-1}\Big(\frac{r_o\sqrt{\kappa}}{r_o\bar{\kappa}_+\cot(r_o\bar{\kappa}_+)}\Big)\end{aligned} \tag{2.39}$$

In reality (i.e. in the experiment), potential wells typically have many bound levels, namely $r_o\kappa_0 \gg 1$ and the resonance contribution is small for a wide rang of $\sqrt{\kappa}$ which is due to the condition $r_o\bar{\kappa}_+ = \sqrt{\kappa_0 + \kappa} > r_o\kappa_0 \gg 1$. However, the resonance gains its pronounced signature at the point of the phase shifts over $\pi$ which is the same resonance condition as before, $r_o\bar{\kappa}_+ = (n+\frac{1}{2})\pi$, telling us that the scenario here is a typical generalization for which it includes the shallow potential[13].

With some mathematical manipulation to the right-hand-side of equation (2.39), namely applying the angle-addition formula to the tangent and expanding $\tan(r_o\sqrt{\kappa})$ in odd powers of $\sqrt{\kappa}$ we arrive to expression that contains the even powers of $\sqrt{\kappa}$ for $r_o\kappa\cot(\gamma_o)$ such that

$$\kappa\cot(\gamma_o) = \frac{r_o\bar{\kappa}_+\cot(r_o\bar{\kappa}_+) + r_o^2\kappa + ...}{1-\Big(1+\frac{1}{3}r_o^2\kappa + ...\Big)r_o\bar{\kappa}_+\cot(r_o\bar{\kappa}_+)} \tag{2.40}$$

At the limit $\sqrt{\kappa}\to 0$ mathematically the equation above (2.40) reduces to the scattering length $a$ in equation (2.37). Dividing both sides of equation (2.40) by $r_o$ it will reduce to the so-called *effective range expansion*

$$r_o\sqrt{\kappa}\cot(\mu_o) = -\frac{1}{a}+\frac{1}{2}\kappa r_e \tag{2.41}$$

where $r_e$ is one of the main characteristic lengths denoted by the *effective range* and defined as

$$r_e = r_o\Big(1-\frac{3ar_o + r_o^4\kappa_0^2}{3(r_o\kappa_0 a)^2}\Big) \tag{2.42}$$

The effective range shows a dependency on the values of $\sqrt{\kappa}$ through the scattering length $a$, therefore to discuss the scattering resonance it is convenient to rewrite the scattering length as a function of $\sqrt{\kappa}$ as follows

$$\begin{aligned} a(\sqrt{\kappa}) &= -\frac{1}{r_o\sqrt{\kappa}\cot(\gamma_o)} \\ &= \frac{a(0)}{1-\frac{1}{2}r_e\kappa a(0)} \end{aligned} \tag{2.43}$$

For the special case where $a = r_o$, we find that $r_e \simeq \frac{2}{3}r_o$, and $\sqrt{\kappa}$ becomes important for the values $r_o\sqrt{\kappa} \gtrsim 1$ while for $r_o\sqrt{\kappa} \ll 1$ the effective range may be neglected as long as the value of $|a|$ is not too large. As we explained early, the typical experimental situation is a potential well with many $n$ bound levels for $r_o\kappa_0 \gg 1$ and their binding energies $\epsilon_b = -\kappa_n^2$ where the last level $\kappa_n = \kappa$ is a weakly-bound $s$ level with $r_o\kappa \ll 1$.

For the resonance enhancement of the weakly-bound $s$ level to exist the scattering length has to be large and positive, i.e. $a = \frac{1}{\kappa}$, thus equation (2.43) reads

$$a(\sqrt{\kappa}) = \frac{1}{\kappa - \frac{1}{2}r_e\kappa} \tag{2.44}$$

The above expression describes the situation of the scattering length when it is resonantly enhanced by the presence of the weakly-bound $s$ levels. Best two famous examples for this case are the deuteron which is a weakly-bound state of a proton and neutron with parallel spins and, for quantum gases, the double spin-polarized $^{133}$Cs atoms where $a \approx 2400a_o$ and $r_o \approx 101a_o$ with $r_o\kappa_b \approx 0.042$ [26].

The scattering resonance expression $a(\sqrt{\kappa})$ accepts negative values which results in an *almost-bound state* with $a = -\frac{1}{\acute{\kappa}}$. Such state is denoted by the *virtual bound state* with energy $\acute{\kappa}$ and the scattering length reads

---

[13] See after equation (2.34)

$$a(\sqrt{\kappa}) = -\frac{1}{-\acute{\kappa} - \frac{1}{2} r_e \kappa} \tag{2.45}$$

which leads to the following phase shift to read

$$\gamma_o \simeq -r_o\sqrt{\kappa} + \tan^{-1}\left(\frac{\sqrt{\kappa}}{\acute{\kappa}}\right) \tag{2.46}$$

Experimentally, the virtual bound state is realized in the collision of a neutron and a proton with opposite spins where $a = -2.38 \times 10^{-14} m$ and $r_e = 2.67 \times 10^{-15} m$ with $-r_e \kappa_b = 0.11$ [27]. For quantum gases the virtual bound state appears in the doubly-polarized $^{85}$Rb where $a \approx -369 a_0$ and $r_o \approx 83 a_0$ with $-r_o \kappa_b \approx 0.22$ [28].

- ***Spherical square well model: The effective range and the phase shift in the presence of an external power-law potential***

The design of most of the experimental setups for trapping the quantum gases relies on the power-law trap model because it is easy to use for modeling the behavior of the trapped gases, capturing the major features of their interparticles interactions and most of their characteristic parameters. We use this model here to examine the effect of an existing external confining field on the effective interaction range and the phase shift where we show the existence of a finite range and how to determine a value for $r_o$.

Recalling the simplified power-law model described in equation (2.14), $\mathcal{V}(\boldsymbol{r}) = -\mathcal{V}_o(\frac{r}{r_c})^x$, where $r_c$ is the trap characteristic size, $x$ is the trap parameter ($x \equiv 3/v$) and $\mathcal{V}_o \equiv |\mathcal{V}(\boldsymbol{r})|$ which represents the trap depth. Then the radial wave equation takes the following form

$$R_l'' + \frac{2}{\boldsymbol{r}} R_l' + \{\kappa + \widetilde{\mathcal{V}_o}\Big(\frac{r}{r_c}\Big)^x - \frac{l(l+1)}{\boldsymbol{r}^2}\} \tag{2.47}$$

with $\widetilde{\mathcal{V}_o} = 2\boldsymbol{m}\frac{\mathcal{V}_o}{\hbar^2}$. The simplest scenario of the equation above (2.47) is to be solved analytically at the limit $\sqrt{\kappa} \to 0$ in which case the potential $\mathcal{V}(\boldsymbol{r})$ reaches its minima and can be neglected, thus solving the equation (2.47) to obtain a value for $r_o$. However, the situation is rather complicated because the current form of this equation needs to be reshaped into a well-known differential one, to do that we replace the radial wave function $R_l(\boldsymbol{r})$ using some transformations to arrive at the Bessel differential equation[14]. This procedure leads us to a definition for the range $r_o$ as a function of the external potential such that

$$r_o = r_c\{\frac{\widetilde{\mathcal{V}_o} r_c^2}{(x-2)^2}\}^{1/(x-2)} \tag{2.48}$$

The phase shift in the presence of an external power-law potential experiences two angular momentum boundary limits, in the first limit, i.e. $l < \frac{1}{2}(x-3)$, the range $r_o$ is well defined in which case the short-range seems to be applicable

$$\tan(\gamma_l) \underset{\boldsymbol{r}\sqrt{\kappa}\to 0}{\simeq} -\frac{2l+1}{[(2l+1)!!]^2}\left(\sqrt{\kappa} a_l\right)^{2l+1} \tag{2.49}$$

At the limits $l \geq \frac{1}{2}(x-3)$ where the potential is not neglected the radial wave function $R_l(\boldsymbol{r}, \sqrt{\kappa})$ is slightly perturbed by the presence of the confining field, i.e. $R_l(\boldsymbol{r}, \sqrt{\kappa}) \to j_l(\boldsymbol{r}, \sqrt{\kappa})$ where the phase shift can be calculated in the limit $\sqrt{\kappa} \to 0$ by replacing $\varphi_l(\boldsymbol{r}\sqrt{\kappa})$ by $\sqrt{\kappa}\boldsymbol{r} j_l(\boldsymbol{r}\sqrt{\kappa})$ in the integral form of the phase shift in equation (2.31). Thus the phase shift within a power-law confining field reads

---

[14] We skip the mathematical derivations for this case.

$$\sin(\gamma_l) \simeq \frac{\pi}{2}\int_0^\infty \widetilde{\mathcal{V}}_o\Big(\frac{r}{r_c}\Big)^x \{J_{l+\frac{1}{2}}(\boldsymbol{r}\sqrt{\kappa})\}^2 r dr \tag{2.50}$$

where $J_{l+\frac{1}{2}}(\boldsymbol{r}\sqrt{\kappa})$ is the Bessel function as described in the appendix (A.1.2). The above integration (2.50) can be evaluated by setting suitable limits on $x$, namely $1 < x < 2l+3$ to yields a phase shift $\gamma_l$ that depends on all the values of $\sqrt{\kappa} > \frac{1}{2}(x-3)$, i.e the well-known $k$-dependency of $\gamma_l$ within a confining field.

## 2.5 Interaction Dynamics of Quantum Gases at Cold and Ultracold Limits

As mentioned early, collisions between the confined quantum particles is an unavoidable process. The Bose-Einstein theory implies that the condensation is in the ideal gas limit which in practice strictly never realized, in fact the collisions at room temperature can be described classically. Contrarily, at low temperature the collisional events, such as low relative velocities and scatterings, show significantly different behavior that require only quantum physics in order to be interpreted [25].

- ***Overview: Simplified frame for the interacting quantum particles and the induced energy shift***

We start by setting up a simplified theoretical frame for two interacting quantum particles, non-identical and identical particles, by writing down the Hamiltonian of a two-body system, but first we discuss how the presence of the interaction affects the total energy and causes the *energy shift*[15]. The reduced mass particles are assumed to be in a spherical box of radius $\widetilde{\boldsymbol{r}} \gg |a|$ around the potential center where the particles wave functions vanish at the surface of the sphere; it is a traditional way to analyze the boundary conditions. For free particles the wave function behaves according to the following boundary condition

$$R_o(\widetilde{\boldsymbol{r}}) = \frac{\mathcal{C}}{\widetilde{\boldsymbol{r}}}\sin\Big(\widetilde{\boldsymbol{r}}k\Big) = 0 \tag{2.51}$$

$\mathcal{C}$ is the normalization constant and for convenient we set $\sqrt{\kappa} \equiv k = \frac{\pi}{\widetilde{\boldsymbol{r}}}n$ with $n \in \{1, 2, ...\}$.

The total energy shift can be examined by comparing the free particle energy within the boundary above (2.51) and with the one experiences the presence of the interaction. The radial wavefunction of the interacting particles confined in such central confinement reads

$$R_o(\widetilde{\boldsymbol{r}}) \underset{\widetilde{\boldsymbol{r}}\to\infty}{\simeq} \frac{1}{\widetilde{\boldsymbol{r}}}\sin\Big([\widetilde{\boldsymbol{r}} - a]\acute{k}\Big) = 0 \tag{2.52}$$

where $\acute{k} = \frac{\pi}{\widetilde{\boldsymbol{r}}-a}n$. By letting $n = 1$, the induced change in the total energy due to the interaction can be written as follows

$$\begin{aligned}\delta E &= \frac{\hbar^2}{2\boldsymbol{m}}\{\acute{k}^2 - k^2\} \\ &= \frac{1}{\boldsymbol{m}}\Big(\frac{\hbar\pi}{\widetilde{\boldsymbol{r}}}\Big)^2\{1 + 2\frac{a}{\widetilde{\boldsymbol{r}}} + ... - 1\} \to \\ &\underset{a\ll\widetilde{\boldsymbol{r}}}{\simeq} \frac{\hbar^2\pi^2}{\boldsymbol{m}\widetilde{\boldsymbol{r}}^3}a\end{aligned} \tag{2.53}$$

---

[15] Which is basically the interaction energy of the pair.

From this point we can distinguish two barriers, for $a > 0$ the total energy increases due to the effective repulsion interaction while for $a < 0$ the total energy of the interacting pair seems to decrease due to the effective attractive interaction in which case one can conclude that the energy shift $\delta E$ depends on the value of the scattering parameter $a$.

A more general model for the energy shift can be obtain via the pseudo potential which replaces the above model due to its disadvantages. At the core where only one particle can be considered at the center of the quantizing volume and only spherical volume can be used. The pseudo potential uses the unperturbed relative wavefunction $\varphi(\boldsymbol{r}) = \mathcal{C} Y_0^0(\widehat{\boldsymbol{r}}) j_0(\boldsymbol{r}k)$ where $Y_0^0(\widehat{\boldsymbol{r}}) = \frac{1}{2\sqrt{\pi}}$ is the lowest order harmonic and $\widehat{\boldsymbol{r}} = \frac{\boldsymbol{r}}{|\boldsymbol{r}|}$ is the unit vector in the $(\theta, \phi)$ radial direction. The energy shift reads

$$\begin{aligned}\delta E &= \frac{\langle \varphi_k | \mathcal{U}(\boldsymbol{r}) | \varphi_k \rangle}{\langle \varphi_k | \varphi_k \rangle} \to \underset{k \to 0}{\simeq} \frac{2a\pi\hbar^2}{\boldsymbol{m}} \int \delta(\boldsymbol{r}) \varphi_k^2(\boldsymbol{r}) d\boldsymbol{r} \\ &= \frac{a\hbar^2}{2\boldsymbol{m}} \mathcal{C}^2 \left[ \frac{\sin^2(\boldsymbol{r}k)}{\boldsymbol{r}^2 k^2} \right] = \frac{\hbar^2 \pi^2}{\boldsymbol{m}\widetilde{\boldsymbol{r}}^3} a \end{aligned} \tag{2.54}$$

agreeing with equation (2.53).

To reach the point where we can use the *many-body problem* to describe the condensed state of the quantum particles and to be able to show a detail picture for the quantum field Hamiltonian of such systems, we start by recalling the two-body Hamiltonian. The model describes the interaction between two quantum particles in a cubic box of length $L$ and a volume of $V = L^3$ where the particles interact via central potential $\mathcal{U}(\mathbf{r})$, such that

$$\widehat{\mathcal{H}} = -\Big( \frac{\hbar^2}{2m_1} \nabla_1^2 + \frac{\hbar^2}{2m_2} \nabla_2^2 \Big) + \mathcal{U}(\mathbf{r}) \tag{2.55}$$

If the pair behaves with no interaction then its total wavefunction comes as a product of two particles wavefunctions, such as

$$\psi_{\mathbf{k}_1, \mathbf{k}_2}(\boldsymbol{r}_1, \boldsymbol{r}_2) = \frac{1}{V} e^{-i\mathbf{k}_1 . \boldsymbol{r}_1} e^{-i\mathbf{k}_2 . \boldsymbol{r}_2}, \qquad k_i = \frac{2\pi}{L} n_i \tag{2.56}$$

Using the first-order perturbation theory we can calculate the energy shift for a *delta function* potential $\mathcal{U}(\mathbf{r}) = \mathfrak{g}\delta(\mathbf{r})$ as follows

$$\delta E = \frac{\langle \mathbf{k}_1, \mathbf{k}_2 | \mathcal{U}(\mathbf{r}) | \mathbf{k}_1, \mathbf{k}_2 \rangle}{\langle \mathbf{k}_1, \mathbf{k}_2 | \mathbf{k}_1, \mathbf{k}_2 \rangle} = \frac{\mathfrak{g}}{V}, \qquad \mathbf{r} = |\boldsymbol{r}_1 - \boldsymbol{r}_2| \tag{2.57}$$

where we used the fact that $|e^{-i\mathbf{k}_1 . \boldsymbol{r}_1}|^2 = |e^{-i\mathbf{k}_2 . \boldsymbol{r}_2}|^2 = 1$ and $|e^{-i(\mathbf{k}_1 + \mathbf{k}_2) . \boldsymbol{r}_1}|^2 = 1$ which yields $\langle \mathbf{k}_1, \mathbf{k}_2 | \mathcal{U}(\mathbf{r}) | \mathbf{k}_1, \mathbf{k}_2 \rangle = \mathfrak{g}/V$ with $\mathfrak{g} = \frac{4\pi\hbar^2}{m} a$.

○ ***Identical Bosons***

Considering the two particles to be in the same state, i.e. $\mathbf{k} = \mathbf{k}_1 = \mathbf{k}_2$, then this yields $\langle \mathbf{k}, \mathbf{k} | \mathbf{k}, \mathbf{k} \rangle = 1$ with wavefunction same as that in equation (2.56) having $\mathbf{k}_1 = \mathbf{k}_2$. The interaction energy reads $\delta E = \mathfrak{g} \langle \mathbf{k}, \mathbf{k} | \mathbf{k}, \mathbf{k} \rangle = \mathfrak{g}/V$. If the particles are in different states, i.e. $\mathbf{k}_1 \neq \mathbf{k}_2$ then their energy eigenfunctions must be either symmetric or antisymmetric under the exchange of the particles, such that

$$\psi_{\mathbf{k}_1, \mathbf{k}_2}(\boldsymbol{r}_1, \boldsymbol{r}_2) = \frac{1}{\sqrt{2}V} \{ e^{-i\mathbf{k}_1 . \boldsymbol{r}_1} e^{-i\mathbf{k}_2 . \boldsymbol{r}_2} \pm e^{-i\mathbf{k}_1 . \boldsymbol{r}_2} e^{-i\mathbf{k}_2 . \boldsymbol{r}_1} \} \tag{2.58}$$

Using the norm $\langle \mathbf{k}_1, \mathbf{k}_2 | \mathbf{k}_1, \mathbf{k}_2 \rangle = 1$ and approximate it up to the first-order in the perturbation theory, the energy shift reads

$$\begin{aligned}\delta E &= \langle \mathbf{k}_1, \mathbf{k}_2 | \mathbf{k}_1, \mathbf{k}_2 \rangle \\ &= \frac{\mathfrak{g}}{2V^2} \int \int_V \delta(\boldsymbol{r}_1 - \boldsymbol{r}_2) | e^{-i\mathbf{k}_1 . \boldsymbol{r}_1} e^{-i\mathbf{k}_2 . \boldsymbol{r}_2} + e^{-i\mathbf{k}_1 . \boldsymbol{r}_2} e^{-i\mathbf{k}_2 . \boldsymbol{r}_1} |^2 d\boldsymbol{r}_1 d\boldsymbol{r}_2 \\ &= \frac{2\mathfrak{g}}{V} \end{aligned} \tag{2.59}$$

The best conclusion one can draw here is that, the bosonic particles when in the same state have less energy than when in a different states which shows the Einstein's argument in different fashion, putting the particles with their repulsive interaction in the same state minimizes the interaction energy.

### 2.5.1 The condensation state of ideal gases in harmonic traps

The early investigations of the trapped quantum particles were limited to the noninteracting gases where it has been found by Bagnato and Kleppner [29] that there is a *macroscopic* finger print of the Bose-Einstein condensate (BEC) of the harmonically trapped ideal two-dimensional Bose gas that belongs to the occupation of the ground state below a critical temperature[16]. In this section we describe the thermodynamical properties of the ideal one and two-dimensional (1D & 2D) ideal bosonic gases trapped in a harmonic confining external field where we show the thermodynamic averages for the grand canonical ensemble assuming that the system has a fixed *chemical potential* $\mu$, fluctuating number of particles $N$ and in thermal equilibrium at temperature $T$.

- ***Thermal properties of the condensed quantum gases: Ideal Bose gas***

As mentioned in section (1.1.3), the trapped quantum gases are characterized by a set of eigenenergies $\{\epsilon_j\}$ for each individual $j$ particle in an arbitrary trap of any dimension. Relating the total number of particles to the temperature and the chemical potential can be described as

$$N = \sum_j N\Big(\frac{1}{k_B T}(\epsilon_j - \mu)\Big) \tag{2.60}$$

The $n_j$ particles occupy the $j$ single-particles motional state of the trap where the occupation number of these states add up to the above equation (2.60) and given by the Bose-distribution

$$\langle n_j \rangle = \frac{1}{e^{(\epsilon_j - \mu)/k_B T} - 1} = \sum_{j=1}^{\infty} e^{-j(\epsilon_j - \mu)/k_B T} \tag{2.61}$$

For a given temperature the chemical potential $\mu$ is fixed by $N = \sum_j \langle n_j \rangle$ and as the gas cooled down the chemical potential approaches the ground state energy $\epsilon_o = 0$ until it reaches the condition $\mu = \epsilon_o$ at the critical temperature $T_C$. The ground state population at that point is given by

$$N_o = \frac{1}{e^{(-\mu)/k_B T} - 1}, \qquad \text{with} \qquad \epsilon_o = 0 \tag{2.62}$$

At the $T_C$ temperature and for a given large but finite $N$ particles in a trap the occupation number of the ground state $N_o$ becomes a *macroscopic fraction* of the total number of particles

---

[16] A temperature that depends on the number of particles and the trapping frequencies in which case the BEC phase transition occurs at such temperature.

and with a continues cooling to $T \to 0$ all the particles will occupy the ground state and hence crossing over to a regime where the phenomena of the Bose-Einstein condensate is observed having a small but finite chemical potential $\mu$.

- ***Trapped 1D ideal Bose gas***

Starting with a one-dimensional Bose gas we determine the temperature of the BEC crossover by first recalling the density of state $\varrho(\epsilon)$ in equation (2.19) where for 1D Bose gas with energy spectrum $\epsilon_n = \hbar\omega n$ the density of states reads

$$\varrho(\epsilon) = 2\pi\vartheta\sqrt[3]{2m}\int_{\mathcal{U}(\mathbf{r})\leq\epsilon}\sqrt{\epsilon-\mathcal{U}(\mathbf{r})}d\mathbf{r} \qquad \longrightarrow \qquad \varrho(\epsilon) = \frac{1}{\hbar\omega} \tag{2.63}$$

where $\omega$ is the trapping frequency. To calculate the total number of particles the sum in equation (2.60) transforms into integral form due to the fact that the relative contribution of several low-energy states is negligible and thus reads

$$N = N_o + \Big[\int_0^\infty N\Big(\frac{1}{k_BT}(\epsilon-\mu)\Big)\varrho(\epsilon)d\epsilon\Big]_{\hbar\omega\ll T} \tag{2.64}$$

The above integral (2.64) fails as it diverges for $\frac{\mu}{k_BT} \to 0$ which makes no harm in taking the lowest energy levels [30]. In the limits $\{-\mu, \hbar\omega\} \ll T$ equation (2.60) reads, by letting $k_B \to 1$

$$N = N_o + \frac{T}{\hbar\omega}\sum_{n=1}^{\upsilon}\frac{1}{n-\frac{\mu}{\hbar\omega}} + \sum_{n=\upsilon+1}^{\infty}\frac{1}{e^{(\hbar\omega n-\mu)/T}-1} \qquad \text{with} \qquad 1 \ll \upsilon \ll \frac{T}{\hbar\omega} \tag{2.65}$$

Using the digamma function $\bar{\psi}(x)$, in the Appendix (A.1.3), the first sum in the above equation reads as follows

$$\begin{aligned}\frac{T}{\hbar\omega}\sum_{n=1}^{\upsilon}\frac{1}{n-\frac{\mu}{\hbar\omega}} &= \frac{T}{\hbar\omega}\Big\{\bar{\psi}\Big(\upsilon+1-\frac{\mu}{\hbar\omega}\Big)-\bar{\psi}\Big(1-\frac{\mu}{\hbar\omega}\Big)\Big\} \\ &\approx \frac{-T}{\hbar\omega}\Big\{\bar{\psi}\Big(1-\frac{\mu}{\hbar\omega}\Big)+\ln\Big(\upsilon-\frac{\mu}{\hbar\omega}\Big)\Big\}\end{aligned} \tag{2.66}$$

while the second sum in equation (2.65) transforms into the following integral

$$\begin{aligned}\sum_{n=\upsilon+1}^{\infty}\frac{1}{e^{(\hbar\omega n-\mu)/T}-1} &\approx \frac{T}{\hbar\omega}\int_{\hbar\omega/T}^{\infty}\frac{1}{e^{x-\mu/T}-1}dx \\ &\approx \frac{-T}{\hbar\omega}\ln\Big(\frac{\hbar\omega[\upsilon-\frac{\mu}{\hbar\omega}]}{T}\Big)\end{aligned} \tag{2.67}$$

When the chemical potential reaches the level $-\mu \approx \frac{T}{N_o}$ (basically we are eliminating the potential), then equation (2.65) reduces to

$$N - \frac{T}{\hbar\omega}\ln\Big(\frac{T}{\hbar\omega}\Big) = N_o - \frac{T}{\hbar\omega}\bar{\psi}\Big(1+\frac{T}{\hbar\omega N_o}\Big) \tag{2.68}$$

- ***Trapped 2D ideal Bose gas***

For the case of a two-dimensional Bose gas confined in a circularly symmetric trap, the distribution of the energy depends on a pair of quantum numbers $\{n_x, n_y\}$ such that the energy is defined as $\epsilon_{n_x,n_y} = \hbar\omega(n_x + n_y)$ and the density of the states reads $\varrho(\epsilon) = \epsilon/\hbar^2\omega^2$. For a large population of the ground sate equation (2.62) reads $-\mu/T \approx 1/N_o$ and thus the integration of equation (2.64) can be written in the following form

$$\frac{1}{(\hbar\omega)^2}\int_0^\infty N\Big(\frac{(\epsilon-\mu)}{T}\Big)\epsilon d\epsilon \approx \Big(\frac{T}{\hbar\omega}\Big)^2\Big[\frac{\pi^2}{6} - \frac{1+\ln N_o}{N_o}\Big]_{k_B\to 1} \tag{2.69}$$

From the above expression (2.69) we can now relate the number of the particle to the critical temperature $T_C$ by introducing the frequency and number of particle dependent term $T_C = \sqrt{\frac{6N}{\pi^2}}\hbar\omega$, such that

$$N\Big[1-\Big(\frac{T}{T_C}\Big)^2\Big] = N_o - \frac{1}{N_o}\Big(\frac{T}{\hbar\omega}\Big)^2\Big[1+\ln N_o\Big] \tag{2.70}$$

In the above equation (2.70) we notice that below the $T_C$ the last term is negligible and we can then find the occupation of the ground state to read $N_o \approx N\Big[1-\Big(\frac{T}{T_C}\Big)^2\Big]$ which is a consequence of the sharp crossover to the BEC regime as $T \approx T_C$ [29, 31]. Contrarily, above the $T_C$ the first term in the r. h. s. of the above equation (2.70) can be neglected compared to the second one. It is also important to notice that at $T_C$ the de Broglie wavelength[17] of the particles $\Lambda \sim \sqrt{\frac{\hbar^2}{mT_C}}$ becomes comparable to the mean interparticles separation which reads $\sim \sqrt{\frac{T_C}{Nm\omega^2}}$ in which case the width to the crossover region can be estimated as $\frac{\triangle T}{T_C} \sim \sqrt{\frac{\ln N}{N}}$.

Similarly in the 1D case, there are two regimes defined by a border of $N \approx \frac{T_C}{\hbar\omega}\Big[\ln\Big(\frac{T_C}{\hbar\omega}\Big) + 0.577\Big]$ at the critical temperature $T_C$. Below the $T_C$ the first term in the r. h. s. of equation (2.68) greatly exceeds the second one which leads the ground state population to behave as $N_o \approx N - \frac{T}{\hbar\omega}\ln\Big(\frac{T}{\hbar\omega}\Big)$ in which case that for large number of particles the width is pretty small and means that an ordinary BEC transition occurs in ideal gas harmonically trapped.

- ***Trapped 3D ideal Bose gas: Typical experimental analogy***

For the 3D case we will relate the previous concepts to a real experimental setup that uses a large scale magnetic traps based on the so-called *Ioffe-quadrupole configuration*[18]. It is an integration of the simplest trapping geometry that uses a pair of anti-Helmholtz coils which produce a static spherical quadrupole field [32, 33]. We assume magnetic fields generated inside a coil assembly [35, 36] and represented by the cylindrical coordinates as

$$\begin{aligned} B_\rho(\rho,\phi,z) &= -\alpha\rho\sin(2\phi) - \frac{1}{2}\beta\rho(z-z_o) \\ B_\phi(\rho,\phi,z) &= -\alpha\rho\cos(2\phi) \\ B_z(\rho,\phi,z) &= B_o + \frac{1}{2}\beta(z-z_o)^2 - \frac{1}{4}\beta\rho^2 \end{aligned} \tag{2.71}$$

which gives a magnetic field of magnitude

---

[17] See below equation (2.7).

[18] We will discuss the magnetic trapping techniques which was used for the first observation of BEC in rubidium atoms [34].

$$|\mathbf{B}(\rho,\phi,z)| = \sqrt{\Big[B_o + \frac{1}{2}\beta(z-z_o)^2\Big]^2 + \Big[\alpha^2 + \frac{\beta}{2}B_o + \alpha\beta(z-z_o)\sin(2\phi)\Big]\rho^2 + \frac{\beta^2\rho^4}{16}}$$

$$\text{(Close to the center for}\frac{\Big(B_\rho(\rho,\phi,z)-B_o\Big)}{B_o}\text{the field is approximated to)} \rightarrow$$

$$B(\rho,z) = B_o + \frac{1}{2}\Big(\frac{\alpha^2}{B_o} - \frac{\beta}{2}\Big)\rho^2 + \frac{1}{2}\beta z^2 \tag{2.72}$$

In general, the trapping frequencies are given by

$$\omega_k \cong \frac{1}{2\pi}\sqrt{\mu_B g_F m_F \frac{\partial^2 B}{\partial k^2}} \qquad\qquad k \in \{x,y,z\} \tag{2.73}$$

with $\omega_z = \sqrt{\omega_x^2 + \omega_y^2}$. The factor $g_F$ is known as the Land$\acute{e}$ $g$-factor, $\mu_B$ is the Bohr magneton of the quantum particles, and $m_F$ is the magnetic quantum number of their hyperfine state. For the cylindrical coordinate representation, the field amplitude differentiate with respect to the cylindrical coordinates $\rho$, $\phi$ and $z$.

If we assume that close to the trap center the field magnitude is approximated as it appears in equation (2.72), then the trapping frequencies read as follows

$$\omega_z = \sqrt{\frac{\mu_B g_F m_F}{m}\beta} \tag{2.74}$$

$$\omega_\rho = \sqrt{\frac{\mu_B g_F m_F}{m}\Big(\frac{\alpha^2}{B_o} - \frac{\beta}{2}\Big)} \tag{2.75}$$

The trapping frequency equation (2.75) is a straight demonstration for how to experimentally access to the trapping parameter. This famous example shows that for a strong radial confinement the radial frequency is dominated by the term $\frac{\alpha^2}{B_o}$ in which case the confinement strength can be adjusted by varying $B_o$ using compensation coils.

In the 3D trapped case, the particles occupy the single-particle motional states and experience the external potential $\mathcal{V}(\boldsymbol{r})$ and their occupation number is given by the Bose-distribution in equation (2.61). The total number in the *excited states* is given by, using equation (2.64)

$$N - N_o = \int_0^\infty \frac{\varrho(\varepsilon)}{e^{(\varepsilon-\mu)/k_B T} - 1} d\varepsilon \tag{2.76}$$

where $\varrho(\varepsilon)$ as defined in equation (2.63). In such experiment a typical density distribution $n(\boldsymbol{r})$ of the trapped cloud of particles, before the phase transition, can be estimated as $N = \int n(\boldsymbol{r})d\boldsymbol{r}$ and by using the poly-logarithm function $g_\nu(x) = \sum_{j=1}^\infty \frac{x^j}{j^\nu}$ it can be written as

$$n(\boldsymbol{r}) = \frac{1}{\Lambda^3} g_{3/2}\Big(\bar{f} e^{\mathcal{V}(\boldsymbol{r})/k_B T}\Big) \tag{2.77}$$

The term $\bar{f} = e^{\mu/k_B T}$ determines the so-called the *fugacity* of the trapped quantum gases. The condition for the BEC to occur is at the center of the trap is that the degeneracy parameter in equation (2.8) must reach the following critical value

$$\Theta \rightarrow n(0)\Lambda^3 = g_{3/2}(1) = 2.612... \tag{2.78}$$

which is exactly the same value obtained by Einstein in equation (1.16) assuming that measurement is precisely done at the center of the trap. Here the poly-logarithmic function takes the value $g_\nu(1) = \zeta(\nu)$ where $\zeta(\nu)$ is the Riemann's $\zeta$-function, see Appendix (A.1.4). Equation (2.78) means that the BEC occurs when the thermal wavelength of the quantum particles becomes on the order of the separation between the particles.

The example above is a type of an harmonic trap which is quite common technique in almost all the BEC existing experiments. In the Ioffe-quadrupole trap [34] the density of states reads $\varrho(\varepsilon)\frac{\varepsilon^2}{2(\hbar\varpi)^3}$ where $\varpi$ is the mean trapping frequency defined as $\varpi = \sqrt[3]{\omega_\rho^2\omega_z}$, therefore using equation (2.76) we calculate the number of particles in the excited states to be

$$N - N_o = g_{3/2}(1)\left[\frac{k_B T}{\hbar\varpi}\right]^3 \tag{2.79}$$

At the phase transition the occupation number of the ground state $N_o$ of the trap becomes equal to zero, $N_o = 0$, and hence we can estimate the critical temperature to read

$$T_C = \frac{\hbar\varpi}{k_B}\sqrt[3]{\frac{N}{g_{3/2}(1)}} \approx 0.94\frac{\hbar\varpi}{k_B}\sqrt[3]{N} \tag{2.80}$$

## 2.6 Reaching the Ultracold Limits of the Magnetically Confined Quantum Gases

When the confined gas experiences any change in its volume whether a compression or an expansion, resulted from a reduction or an increase in the trap size, the effect of such variation extends to reach the internal states of the trapped particles. To explain and carefully address such argument it is best to navigate throughly for the conditions which limit the particles behavior, because these limiting boundaries are more likely to be exposed to any small variation in the external confining field assuming that the background noise is greatly expelled out of the maintained environment. In this section we intend to show the effect of the adiabatic change of the confining potential fields, as discussed in section (2.2.2), on the trapped gas and their thermal properties where the particles are known to exhibit sever transitional behaviors at such fragile level.

### 2.6.1 The adiabatic compression

The classical limit in the trapped particles is recognized by the negative chemical potential $\mu < 0$ where $|\mu| \gg k_B T$. This creates a fugacity with the condition $\bar{f} \ll 1$ where we find from equation (2.77) at the trap center that the particle density reads

$$n(0) = \frac{1}{\Lambda^3} g_{3/2}\left(\bar{f}\right) \approx \frac{1}{\Lambda^3}\left(\bar{f}\right) \tag{2.81}$$

The equation above (2.81) tells us that the thermal wavelength in the classical regime is much smaller than the separation between the particles and the number of particles can be estimated as $N = n(0)\Lambda^3 Z_1$ as described in equation (2.11).

As mentioned in section (2.2.1), the power-law trapping potentials is used in many cases of the magnetic trapping potentials which can be written as $\mathcal{V}(\boldsymbol{r}) \propto |x|^{1/v_1} + |y|^{1/v_2} + |z|^{1/v_3}$ with $v = \sum_i v_i$, see Table (2.1) for different cases [21]. The partition function for the single quantum particle, using the power-law potential, takes the form

$$Z^v = \mathcal{C}_{pl}^v\left[k_B T\right]^{v+\frac{3}{2}}\Gamma\left(v + \frac{3}{2}\right) \tag{2.82}$$

The constant $\mathcal{C}^{v}_{pl}$ depends on the strength of the potential trap and $\Gamma(x)$ is the Euler gamma function. We can use the above equation (2.82) to describe the single-particle partition function for the Ioffe-quadrupole trap $Z_{Igt}$ such that

$$\begin{aligned} Z_{Igt} &= Z^{3/2} + Z^{5/2} \\ &= 6\mathcal{C}_{Iqt}\Big[k_B T\Big]^4 \Big\{1 + \frac{2\mathcal{V}_o}{3k_B T}\Big\} \end{aligned} \tag{2.83}$$

where $\mathcal{V}_o = \mu_B g_F m_F B_o$. The constant $\mathcal{C}_{Iqt}$ is defined as follows

$$\mathcal{C}_{Iqt} = \frac{(2\pi^2 m)^{3/2}}{(2\pi\hbar)^3(\mu_B g_F m_F)^{3/2}\sqrt{\frac{\beta}{2}\alpha}} \tag{2.84}$$

using equation (2.77) and the fact that $N = n(0)\Lambda^3 Z$, the classical limit signature appears as the following *Gaussian shape* distributed density profile

$$n(\boldsymbol{r}) = \frac{N}{\pi^{3/2}\prod_i r_{o,i}} e^{-\sum_i \left(\frac{r_i}{r_{o,i}}\right)^2} \tag{2.85}$$

in which case the cloud radius is estimated as $1/e$-radius in each confining $i$-direction depending on the trapping frequencies, i.e $r_{o,i} = \frac{1}{\omega_i}\sqrt{\frac{2k_B T}{m}}$.

As we mentioned early in this section, the adiabatic change of the trap size also affects the internal energy assuming that the entropy $\mathcal{S}$ and the atom number are conserved quantities. The internal energy is written in terms of the temperature, the particles number and the effective trapping volume, which changes adiabatically, as follows

$$E = Nk_B T\Big(\frac{3}{2} + \tau\Big), \text{where} \qquad \tau \equiv \frac{T}{V_e}\frac{\partial V_e}{\partial T} \tag{2.86}$$

We can write the degeneracy parameter in terms of the adiabatic measure and the entropy[19] $\tau$ as [37]

$$n(0)\Lambda^3 = \exp\Big\{\frac{5}{2} + \tau - \frac{\mathcal{S}}{Nk_B}\Big\} \tag{2.87}$$

For power-law potential in the classical regime we find that $\tau = v$ while for the Ioffe-quadruple potential $\tau = \left(\frac{3}{2} + \frac{15k_B T}{4\mathcal{V}_o}\right)\left(1 + \frac{3k_B T}{2\mathcal{V}_o}\right)^{-1}$. It is clear that the degeneracy parameter stays constant unless $\tau$ is changed by varying the shape of the confining potential field. It was experimentally approved by Pinkse *et al.*, that the change of the degeneracy parameter is reversible by changing the shape of a magnetic trapping potential for Hydrogen atoms [37].

The adiabatic change of the confining potential before the reversibility point can be described by an initial and final states for several characteristic parameters, such as initial and final degeneracy, initial and final trapping frequencies as well as temperature states. The change results in either compression or expansion, most of the magnetic trapping techniques rely on the adiabatic compression to prepare for the BEC transition level. For the case of the Ioffe-quadruple traps the initial and the final states of degeneracy can be described by ratio

$$\frac{n_f(0)\Lambda_f^3}{n_i(0)\Lambda_i^3} = \exp\Big\{\tau_{\text{Iqt},f} - \tau_{\text{Iqt},i}\Big\} \tag{2.88}$$

---

[19] The free energy is expressed in terms of the entropy $F = E - T\mathcal{S}$.

The above equation (2.88) can be solved numerically to find the final state of the temperature and the density. On the other hand, the density of state in the harmonic traps remain unchanged during the adiabatic compression in which case the *adiabaticity* scenario remain still if the limit $\frac{d\omega}{dt} \ll \omega^2$ is reached [38]. In chapter (4) we present a comprehensive discussion of the adiabatic change of the confining potential field at the $\mu$-scale (microscale) and the possibility of simulating condensed matter systems using such technique.

### 2.6.2 The evaporative cooling

In most of the experiments of the quantum gases, in which case BEC is created, the evaporative cooling is an essential ingredient that works as a final stage for cooling and brining the quantum gases to the ultracold degenerate level. It is now visible that the reliability of this technique has greatly amended the approaches to the BEC stage overtaking by that the optical cooling technique which exhibits some technical limitations, such as the Doppler-limit and the recoil-limit. Evaporative cooling was first implemented by Hess $et\ al.$, in an experiment of trapped Hydrogen gas [39]. More details about evaporative cooling can be found in the Ketterle $et\ al.$, [40] and Walraven [41] reviews.

As the name of this technique stands, the cooling process is based on the discriminatory removal of particles labeled with energies above a certain *truncation energy level* $\epsilon_t$ from the confining field that externally altered at its potential barriers and consequently rethermalizes the quantum gas by the elastic collisions [41][42]. If the truncation barrier $\epsilon_t$ held constant, then the process is a plain evaporative cooling in which case the elastic collisions bring some particle to gain energies that lie beyond the truncation barrier. These particle have the capability to escape the potential barrier and hence *evaporate* from the trap with evaporation rate per single particle that expressed as follow

$$\frac{1}{t_{\text{ev}}} = \frac{1}{N}\frac{dN_{\text{ev}}}{dt} = n(0)\bar{v}_{\text{th}}\sigma\frac{V_{\text{ev}}}{V_e}e^{-\gamma} \tag{2.89}$$

where $\gamma = \frac{\epsilon_t}{k_B T}$ is the *truncation parameter*, $\bar{v}_{\text{th}} = \sqrt{\frac{8k_BT}{\pi m}}$ is the mean thermal velocity, $\sigma = 8\pi a^2$ = 7.9 $\times 10^{-16} m^2$ is the elastic collisional cross section and $V_{\text{ev}} \approx V_e$ is effective evaporative volume. The evaporation of the particles out of the trap causes a reduction in the mean energy per particle resulting in a reduction in the gas temperature which is technically termed as cooling. To keep cooling down the trapped gas, the truncation barrier must be reduced, however as the temperature decreases the truncation parameter increase and the evaporation rate is exponentially suppressed. This is known as the *forced evaporative cooling* in which case the truncation barrier can be maintained to stay constant.

For forced evaporative cooling the temperature is related to the number of particles as $T \propto N^{\delta_{\text{ev}}}$ where the efficiency parameter $\delta_{\text{ev}} = d\ln(T)/d\ln(N)$ only depends on the value of truncation parameter $\gamma$. The effective volume also appears as a function of the temperature $V_e \sim T^v$ where the value of $v = 5/3$ describes the Ioffe-quadruple trap at high temperature exhibiting linear limit while for low temperature when the Ioffe-quadruple trap acts as a harmonic trap $v$ takes the value $v = 3/2$.

I find it very interesting to emphasize on the following arguments, the behavior of the central density of the particles precisely obeys the Einstein prediction[20], in spite of the huge loss in the number of the trapped particles, the density $n(0)$ in the trap center can remain constant or even increases assuming that $v \geq 1/\delta_{\text{ev}}$ and $V_e \equiv \frac{N}{n(0)}$ which brings another argument in Einstein's statement, i.e.: *But the study of the equation of state (...) shows, that at a given number of molecules $n$ and a given temperature $T$ the volume* ***cannot*** *be made arbitrarily small.* To

---

[20] See the Einstein comments in section (1.2).

experimentally realize an increased density it is important to slow the evaporation by allowing large value for the truncation parameter $\gamma$. However, by increasing the density another disadvantage appears when reaching the regime of the so-called *runaway evaporative cooling*, identified by the condition $\frac{d\ln(n\sqrt{T})}{d\ln(N)} = 1 - 2\delta_{\text{ev}} < 0$, and that is because of the increased elastic collisions rate in which case $t_{\text{el}}^{-1} \sim n(0)\bar{v}_{\text{th}} \sim n(0)\sqrt{T}$ regardless of the decrease in the temperature.

The efficiency of the evaporative cooling is maintained via a large evaporation rate $Q_i$ which dominates the loss rate, this is known as the *ratio of good to bad collisions* which is expressed as follows

$$Q_i \equiv \frac{dN_{\text{ev}}}{dt}\frac{dt}{dN_i} = \frac{n^2(0)\bar{v}_{\text{th}}\sigma e^{-\gamma}}{L_i}\frac{V_{\text{ev}}}{V_{\text{ie}}} \tag{2.90}$$

The subscript $i$ in the number of particles $N_i$ and the loss rate constant $L_i$ indicates the $i$-body recombination loss where it is common to have two and three-body recombination loss. The reference volume for the $i$-body collisions $V_{ie}$ is defined as $V_{\text{ie}} \equiv \int \left(\frac{n(\boldsymbol{r})}{n(0)}\right)^i d\boldsymbol{r}$. Numerical calculations of the parameters $\delta_{\text{ev}}$ as a function of $\gamma_{\text{ev}}$ and the ratio in the r. h. s. of equation (2.90) for the Ioffe-quadruple trap is detailed in [43].

The listed above parameters, have direct links to the BEC experiment and it is worth mentioning here some of the relevant details. The main goal at the runaway barrier, i.e. the runaway threshold, is to keep the number of the cooled particle as high as possible where it has been realized that the timing of triggering the different phases during the experiment is crucial to reach this goal, such as choosing an optimized time dependence of $\gamma(t)$ to achieve maximum $\delta_{\text{ev}}$. Consequently, the transition to the BEC via the evaporative cooling is found to occur experimentally within a few seconds.

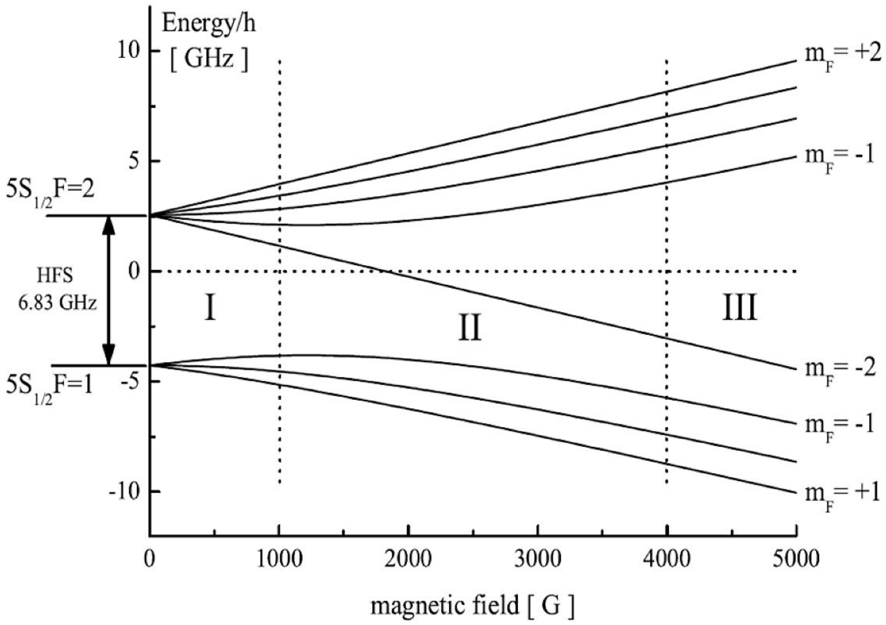

***Figure 2.3:*** The splitting of the energy levels for the $^{87}$Rb atoms showing the states $5S_{1/2}$ $F = 1$ and $5S_{1/2}$ $F = 2$ where three zones are distinguishable, i.e zone **I** for the Zeeman region, zone **II** for the transitional region and zone **III** of the Paschen-Back region.

### 2.6.3 The Radio-Frequency evaporative Cooling

As well known most of quantum particles with magnetic dipole moments, magnetic neutral atoms in particular, experience splittings of their energy levels under when magnetic field is applied. The splitting of the energy levels of the $^{87}$Rb atoms when exposed to external magnetic field is shown in Figure (2.3). Technically, the implementation of the *forced evaporative cooling* requires to introduce a radio-frequency (RF) field to transfer the trapped quantum particles from specific magnetic quantum state to another, such as transferring the atoms from the trapping state $|F = 2, m_F = 2\rangle$ into another untrapping state, i.e into one of the magnetic states $|F = 2, m_F = 0, -1, -2\rangle$. The transfer occurs at the resonance frequency $\omega_{\mathrm{RF}}$ which is defined as

$$\omega_{RF} = \frac{\mu_B g_F}{\hbar}|\mathbf{B}(\boldsymbol{r})| \tag{2.91}$$

where the frequency range of the oscillating field is from $500kHz$ to $50MHz$. The gradient of the magnetic field shows a real correspondence to the experimental values required to maintain the different transitions between the zones.

In general for particles in magnetic field the interaction energy is given by $E = -\bar{\mu}.\mathbf{B}(\boldsymbol{r})$ where $\bar{\mu} = \mu_B g_F m_F \frac{\mathbf{F}}{\hbar}$ with **F** represents the total angular momentum of the atom.

The magnetic moments of the particles orient themselves according to the direction of the external magnetic field which is best described as quantized. By polarizing the particles in a certain Zeeman-state $m_F$ , they will be driven towards either high magnetic fields, where particles are labeled as as *high field seekers*, or low magnetic fields as the *low field seekers*, and depending on the sign of the gyromagnetic factor $g_F$, if $m_F \neq 0$. In the case of the external low magnetic field, the Zeeman shift is to a good approximation linear which means that each Zeeman-state $m_F$ is coupled to all other states and thus transforming the low field seekers with $m_F = 2$ to high field seekers with $m_F = -2$ maintaining by that the $RF$-evaporation process.

As we describe in the evaporative cooling part, particles must approach the truncation barrier in order to evaporatively escape the trap. Therefore, once the resonance frequency $\omega_{\mathrm{RF}}$ is known we can relate *truncation energy* $\epsilon_t$ to an experimental parameter. This relation is defined as follows

$$\epsilon_t = m_F\hbar\Big(\omega_{\mathrm{RF}} - \frac{\mu_B g_F}{\hbar}|\mathbf{B}(0)|\Big) \tag{2.92}$$

the term $\frac{\mu_B g_F}{\hbar}|\mathbf{B}(0)|$ in the above equation (2.92) defines the resonance frequency at the center of the trap $\omega_o$. Because the thermal motion of the particles across the trap center is random, only those with trajectories towards the region of the magnetic potential, which meet with the resonance condition in equation (2.91), experience the evaporation. Two cases appear due to the random distribution of the thermal velocities: First, in the case of low velocities and high amplitudes of the $RF$-magnetic field the particles can adiabatically be transferred to the untrapping states. In the other case with opposite conditions the particles remain in the trapped states after passing with high velocities via the resonance region.

Clearly, the transition probabilities to the untrapped states depend on the amplitude of the $RF$-magnetic field and the speed of the passing atoms through the $\omega_{\mathrm{RF}}$ region leading to undesirable experimental situations such as a BEC with very small number of particles. The overcome of this obstacle was achieved in a two-level atom by calculating the transition probability in a Landau-Zener frame [44, 45]. From Figure (2.3), the Rubidium atoms have 5 Zeeman levels $|F = 2, m_F = -2, -1, 0, +1, +2\rangle$ at the state $F = 2$ where the trapping state is the low field seekers of the state $|F = 2, m_F = +2\rangle$, and if we assume that the state is polarized, then an oscillatory field of amplitude $B_{\mathrm{RF}}$ with linear polarization along the horizontal axis, say $x$-axis, and perpendicular to the trapping field $B(t)$ will add up to the total amplitude as follows

$$\mathbf{B}(t) = B(t)\hat{\mathbf{e}}_z + B_{\mathrm{RF}} \cos(\omega_{\mathrm{RF}} t)\hat{\mathbf{e}}_x \tag{2.93}$$

and the energy term $E$ will extend to a time dependent Hamiltonian that includes the well known two-level Rabi frequency $\omega_R = \frac{\mu_B g_F}{2\hbar} B_{\mathrm{RF}}$, such that

$$E = -\bar{\mu}.\mathbf{B}(\boldsymbol{r}) \longrightarrow \widehat{\mathcal{H}}(t) = \frac{\mu_B g_F}{\hbar} B(t)\mathbf{F}_z + 2\omega_R \cos(\omega_{\mathrm{RF}} t)\mathbf{F}_x \tag{2.94}$$

where diagonalizing $\widehat{\mathcal{H}}(t)$ leads to the *dressed states*. The spatial distribution of the magnetic field $B$ is described in the Landau-Zener frame in terms of the Landau-Zener parameter $\Gamma_{\mathrm{lz}}$ as follows

$$\frac{dB}{dr} = \frac{\hbar \omega_R^2}{\mu_B g_F 2\bar{v}_{\mathrm{th}}} . \frac{1}{\Gamma_{\mathrm{lz}}} \tag{2.95}$$

The saturation of the transition amplitude to almost unity occurs at a certain amplitude of the $RF$-magnetic field, for example for $\Gamma_{\mathrm{lz}} = 1$ the particles are removed from the trap with a probability of 95%.

Quite obviously, the $RF$-magnetic field amplitude is of much concern and it is best to inspect the boundaries under which an efficient evaporation occurs. The excess of the $RF$-power results in only power broadening of the resonance condition (2.91) and at high truncation energies the quadratic Zeeman effect leads to an incomplete evaporation [46]. Therefore, setting some boundary conditions for the $RF$-amplitude is rather suitable which can be done by inspecting the upper and lower limits, for example by expressing the energy of the trapped state in a second order of the static magnetic field we can find the effective trap frequency $\omega_i^{\mathrm{eff}}$ for $i$-direction for a given $\omega_{\mathrm{RF}}$ and $\omega_R$, such that

$$\omega_i^{\mathrm{eff}} = \omega_i \left[ \left( \frac{\omega_R}{\omega_o - \omega_{\mathrm{RF}}} \right)^2 + 1 \right]^{-1/4} \tag{2.96}$$

In the low detuning limit from the trap center, the $\omega_i^{\mathrm{eff}}$ can be reduced assuming that the Rabi frequency is large.

Chapter 3

# MAGNETIC MICRO-CONFINEMENT OF QUANTUM DEGENERATE GASES

> ¶ *The greatest change in the axiomatic basis of physics - in other words, of our conception of the structure of reality - since Newton laid the foundation of theoretical physics was brought about by Faraday's and Maxwell's work on electromagnetic field phenomena.* ... (Albert Einstein, 1931)

## 3.1 Overview

THE field of quantum degenerate gases in periodically distributed microscopic potentials has gained considerable attention over the last decade where it is being intensively explored to answer various interesting fundamental questions in physics. In particular, the field of trapped ultracold atoms in optical confining fields, i.e. optical lattices [55], has achieved remarkable results in the simulation of condensed matter systems. Optical lattices are recognized for their ability to coherently transfer cold atoms, via spin-dependent transportation, between the lattice sites [56]. Such coherent manipulation has allowed, using trapped quantum degenerate gases [57][58], to establish a realizable analogue to condensed matter systems [59]. As an example, the Mott-insulator to superfluid transition has been observed using optically trapped Bose-Einstein condensates [60] and, more interestingly, the transition has also been realized using optically trapped ultracold fermionic gases [61] as well as the observation of the Fermi surfaces [62].

Trapped ultracold atoms are considered as a promising candidate for quantum computers; however, in order to process quantum information it is crucial for such systems to satisfy the scalability criterion [63]; optical lattices are thought to provide scalable quantum systems where remarkably they have allowed multiple particle quantum entanglement [64][65] pointing to the possibility of using such ensembles to serve as quantum processing units.

Integrating ultracold atoms with magnetic microstructures [66] and the creation of Bose-Einstein condensates on an atom-chip [67][68][69] have triggered an alternative approach to optical lattices. To realize a magnetic lattice, periodically distributed non-zero magnetic field local minima are created by fabricating microscopic patterns on the surface of permanent magnetic materials [51][52][54][71][74] or by using current carrying micro-wires [70]. Magnetic lattices created using permanent magnetic films are recognized by the low technical noise and relatively high magnetic field gradients with no resistive heating and offer a highly stable trapping environment for ultracold atoms. It is also possible to construct magnetic lattices in one or two-dimensional configurations where the flexibility of the design and current state-of-the art fabrication technologies allow the implementation of arbitrary trap geometries and scalable lattice spacing [71][72].

Only atoms prepared in low field-seeking states are attracted to, and eventually trapped in, the distributed confining magnetic potentials above the surface, allowing magnetic-state selectivity as a characteristic identity of magnetic lattices. This provides a remarkable opportunity to employ on-chip detection and manipulation techniques [73] such as applying radio frequency fields for on-site atomic manipulation [65], evaporative cooling and spectroscopy [74].

One-dimensional magnetic lattices have been used as magnetic mirrors to reflect atoms in low field-seeking states [75][76][77][78] and, in recent experiments, radial trap frequencies of up to 90 kHz have been measured for $^{87}$Rb atoms trapped at a distance of $\sim 5\ \mu m$ over the surface of a one-dimensional permanent magnetic lattice [48]. Trapped gases with temperatures of T = 2.0 $\pm$ 0.3 $\mu K$ have been observed in a permanent 2D magnetic microstructure [74] and coherence times of the order of 1 second have also been recorded for cold $^{87}$Rb atoms trapped in two different hyperfine states on an atom-chip [66][79]. Recently, Deutsch et. al. set a new remarkable record of coherence times of 58 $\pm$ 12 seconds on an atom chip [80]. A Raman focused laser may be used to selectively drive the cold atoms into highly excited Rydberg states as proposed in [74] which can also lead to the dipole blockade mechanism [81][82], exhibiting a single Rydberg excitation per lattice site.

This has attracted the attention to examine qubit formation and entanglement in magnetic lattices. The internal hyperfine, or Zeeman, magnetic states of the trapped cold atoms can be used to encode the qubit states $|0\rangle$ and $|1\rangle$, where recently a superposition of two hyperfine states with a long coherence lifetime has been demonstrated [79][80], indicating the possibility of constructing quantum gates with a lifetime longer than the gate operation time [83][84]. This suggests that magnetic lattices can be considered as a promising candidate for a scalable quantum processing unit.

In this Chapter, we present a simple method to create a two-dimensional magnetic lattice to microscopically confine ultracold quantum degenerate gases. The proposed magnetic lattice shows asymmetrical feature which can be used to simulate condensed matter systems [85] where the asymmetrical effect introduces a tilt in the magnetic potential similar to the potential tilt in optical lattices [86][87]. It also introduces what we call *gravitational offset* along the gravitational field axis [88].

◇ **Related publications to this Chapter:** A. Abdelrahman, M. Vasiliev, K. Alameh and P. Hannaford, *"Asymmetrical two-dimensional magnetic lattices for ultracold atoms,"* Phys. Rev. A **82**, 012320 (2010).

## 3.2 The $\mu$-Scale Magnetic Confinement

### 3.2.1 The one-dimensional magnetic lattice

The one-dimensional magnetic lattice is the simplest manifestation of the periodically distributed magnetic $\mu$-confinement. It has been intensively studied and developed by Saeed Ghanbari, Mandip Singh and Peter Hannaford in [48][50][51][52]. For the sake of consistency, we give here a brief review for the one-dimensional (1D) magnetic lattice where we use the magnetic field equations presented in [49] as seed equations to create analytical expressions for the magnetic field components along the $x$, $y$ and $z$ directions, i.e. $B_x$, $B_y$ and $B_z$.

A single infinite periodic array of parallel, rectangular, long magnets having a thickness of $\tau$ are arranged in such a way that a periodic gap of width of $\alpha_h$ exists between each two magnets of width $\alpha_s$ (later $\alpha_h$ is considered to represent holes in the case of the $2\times2$ magnetic

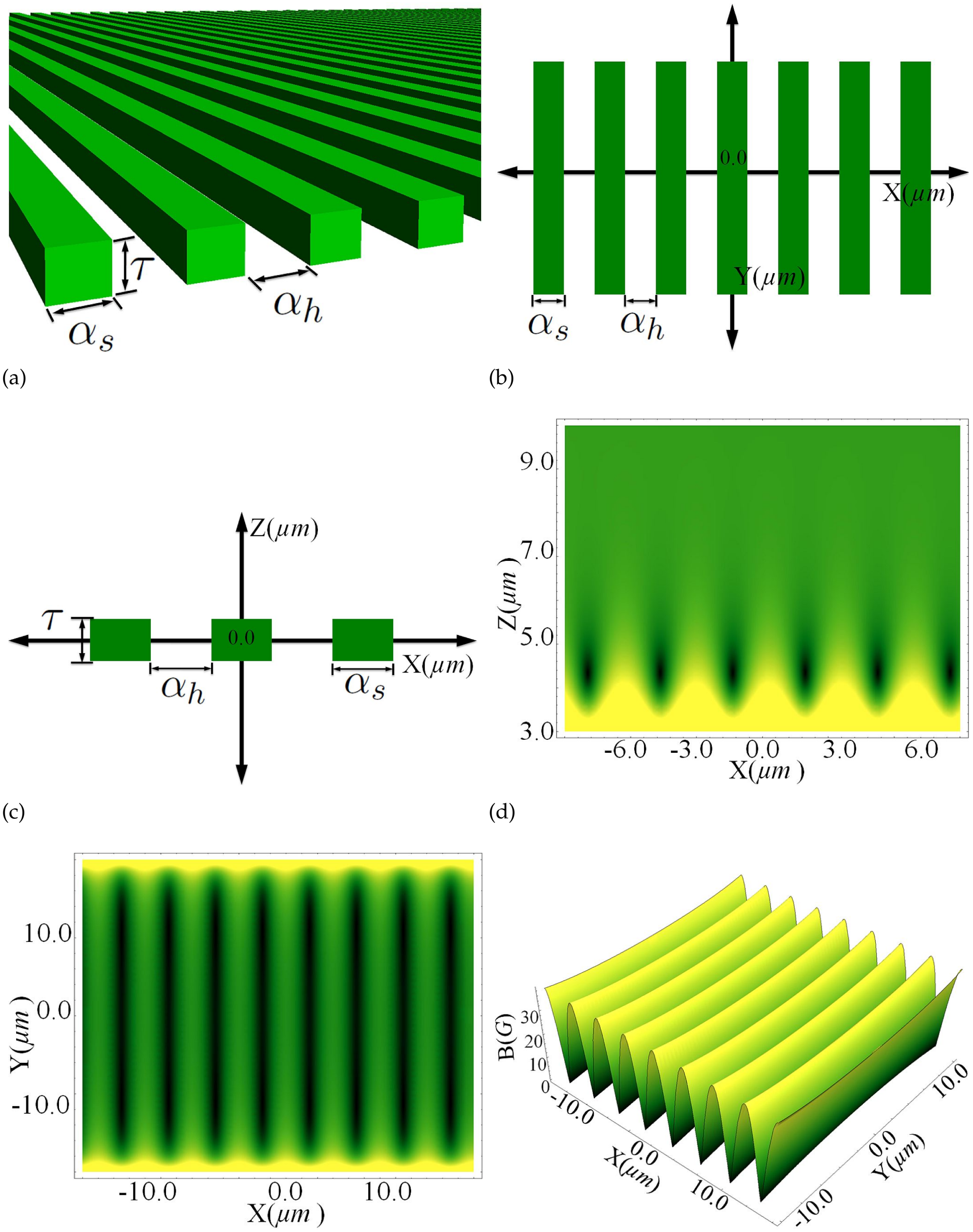

(a) (b) (c) (d) (e) (f)

***Figure 3.1:*** (a-c) Schematic diagram representation of a one-dimensional magnetic lattice showing the important configuration parameters, i.e. the size of the magnetic bars $\alpha_s$ ($\mu$m), the periodicity gap between the magnetic bars $\alpha_h$ ($\mu$m) and the thickness of the thin film $\tau$ ($\mu$m). (d-e) The distribution of the magnetic field local minima $B_{\text{min}}$(G) is shown across the $x/z$-plane and the $x/y$-plane respectively. (f) 3D plot of the magnetic field at the $B_{\text{min}}$ (G) located at $d_{\text{min}}$ ($\mu$m) from the surface of the thin film.

lattice). The analytical expressions of the components of the magnetic fields describe an array of magnets that are assumed to be magnetized along the $z$-axis perpendicularly to their surfaces in which case these expressions are derived in a way that accepts terms for uniform magnetic bias fields, $B_{\text{x-bias}}$, $B_{\text{y-bias}}$ and $B_{\text{z-bias}}$. Thus, we write the spatial magnetic field components $B_x$, $B_y$ and $B_z$ as a combination of a field decaying with distance from the surface of the traps in the $z$-direction and as a periodically distributed magnetic field in the $x - y$ plane produced by the magnetic induction, $B_o = \mu_o M_z/\pi$, at the surface of the magnetized thin film. In the following equations the periodicity extends along the $x$-axis, such that

$$B_x = B_{\text{ref}} \times e^{-\beta[z-\tau]} \sin(\beta x) - \frac{B_{\text{ref}}}{3} \times \sin(3\beta x) e^{-3\beta[z-\tau]} + \ldots + B_{\text{x-bias}} \tag{3.1}$$

$$B_y = B_{\text{y-bias}} \tag{3.2}$$

$$B_z = B_{\text{ref}} \times e^{-\beta[z-\tau]} \cos(\beta y) - \frac{B_{\text{ref}}}{3} \times e^{-3\beta[z-\tau]} \cos(3\beta y) + \ldots + B_{\text{z-bias}} \tag{3.3}$$

We define a surface reference magnetic field as $B_{\text{ref}} = B_o(1 - e^{-\beta\tau})$, where $\beta = \pi/\alpha$, and a plane of symmetry is assumed at $z = 0$. To simplify the mathematical derivations, we also assume the infinite lattice to have separation widths equal to the magnets' width such that $\alpha_h = \alpha_s \equiv \alpha$. The above equations show that there are corrugations corresponding to the third-order spatial harmonic with period $\alpha$ [49] which can be seen at distances very close to the surface of the magnetic thin film, i.e. $d_{\text{min}} \ll \alpha/2\pi$, in which case this situation only happens when there is no magnetic bias field is applied.

In the previous set of equations (3.1), (3.2) and (3.3) the *higher order spatial harmonics* disappear at the trapping working distances $d_{\text{min}}$ which are usually required to be relatively large such that $d_{\text{min}} > \alpha/2\pi$. Therefore, considering this important argument, the axes' field components reduce to the followings set of equations

$$B_x = B_{\text{ref}} \times e^{-\beta[z-\tau]} \sin(\beta x) + B_{\text{x-bias}} \tag{3.4}$$

$$B_y = B_{\text{y-bias}} \tag{3.5}$$

$$B_z = B_{\text{ref}} \times e^{-\beta[z-\tau]} \cos(\beta y) + B_{\text{z-bias}} \tag{3.6}$$

Schematic representations of the 1D magnetic lattice are shown in Figure 3.1(a-c) and numerical simulation of the magnetic field across the $x/z$- and the $x/y$-plane are shown in Figure 3.1(d) and 3.1(e), respectively. The field minima exist at the effective distances $d_{\text{min}}$ located above the separating gaps between the magnets. As shown in Figure 3.1(e-f), the reason this array of traps is called a one-dimensional magnetic lattice is because the trapped quantum particles, after they get trapped, accumulate along the one trapping axis creating adjacent cigar-like shape micro-confined quantum gases.

It is worth mentioning here that the minima levels, i.e. the value of $d_{\text{min}}$ and $B_{\text{min}}$, can be increased by applying the external magnetic bias fields. The permanent one-dimensional magnetic lattices have been successfully integrated into the so called *Atom Chip* [54].

### 3.2.2 The two-dimensional magnetic lattice

There are several approaches to create a two-dimensional array of microtraps for cold and ultracold quantum degenerate gases where a new class of magnetic lattice has been reported in [51][52] while the first experimental realization of the trapped cold atoms in a two-dimensional array of microtraps has recently appeared in [74]. Creating a two-dimensional magnetic lattice using crossed two layers of one-dimensional array of magnets, as proposed in [51][52], requires extreme mechanical stability when considering rotating the two perpendicular layers while keeping the quantum states of the particles remain maintained at certain phase-space points. The difficulty to fabricate the previous two dimensional approach has motivated the development of such type into the a new consistent model.

The proposed structure to generate a magnetic lattice is realized by milling a $n \times n$ array of square holes of width $\alpha_h$, separated by $\alpha_s$, in a magneto-optic thin film of thickness $\tau$ deposited onto a suitable substrate, where $n$ represents the number of holes as illustrated in Figures 3.2(a,b). The depths of all holes are equal and the holes extend through the thin film down to the surface of the substrate. The presence of the holes results in a magnetic field distribution having local minima located at effective z-distances, $d_{\text{min}}$, from the top of the holes.

- ***The Mathematical Model***

The structure generates periodically distributed two-dimensional magnetic field minima above the surface of the thin film in which case the distribution creates a magnetic lattice with $n \times n$ sites or potential wells. The magnetic device is in its remanently magnetized state with magnetization $M_z$ perpendicular to the surface plane. We also noticed that this structure is a special case of the class of magnetic lattices proposed in [54], with $t_1 = t_2$ and $t_3 = 0$. We also include in the analysis of the two-dimensional lattice the external magnetic bias field components, $B_{\text{x-bias}}$, $B_{\text{y-bias}}$ and $B_{\text{z-bias}}$, which can be produced by the microfabricated configuration. The analytical expressions that describe the non-zero local minima are derived and simplified to the following set of equations

$$B_x = B_{\text{ref}} \times \sin(\beta x)e^{-\beta[z-\tau]} - \frac{B_{\text{ref}}}{3} \times \sin(3\beta x)e^{-3\beta[z-\tau]} + \ldots + B_{\text{x-bias}} \tag{3.7}$$

$$B_y = B_{\text{ref}} \times \sin(\beta y)e^{-\beta[z-\tau]} - \frac{B_{\text{ref}}}{3} \times \sin(3\beta y)e^{-3\beta[z-\tau]} + \ldots + B_{\text{y-bias}} \tag{3.8}$$

$$B_z = B_{\text{ref}} \times \Big[\cos(\beta x) + \cos(\beta y)\Big]e^{-\beta[z-\tau]} - \frac{B_{\text{ref}}}{3} \times \Big[\cos(3\beta x) + \cos(3\beta y)\Big]e^{-3\beta[z-\tau]} + \ldots + B_{\text{z-bias}} \tag{3.9}$$

The higher order terms in the above equations can be neglected because atoms prepared in low field-seeking states are trapped in local magnetic minima located at $d_{\text{min}} > \alpha/2\pi$. Thus Equations (3.7) to (3.9) reduce to the following

$$B_x = B_o\left(1 - e^{-\beta\tau}\right)e^{-\beta[z-\tau]} \times \sin(\beta x) + B_{\text{x-bias}} \tag{3.10}$$

$$B_y = B_o\left(1 - e^{-\beta\tau}\right)e^{-\beta[z-\tau]} \times \sin(\beta y) + B_{\text{y-bias}} \tag{3.11}$$

$$B_z = B_o\left(1 - e^{-\beta\tau}\right)e^{-\beta[z-\tau]} \times \Big[\cos(\beta x) + \cos(\beta y)\Big] + B_{\text{z-bias}} \tag{3.12}$$

Using Equations (3.10) to (3.12), the magnitude $B$ of the magnetic field above the thin film surface can be written as

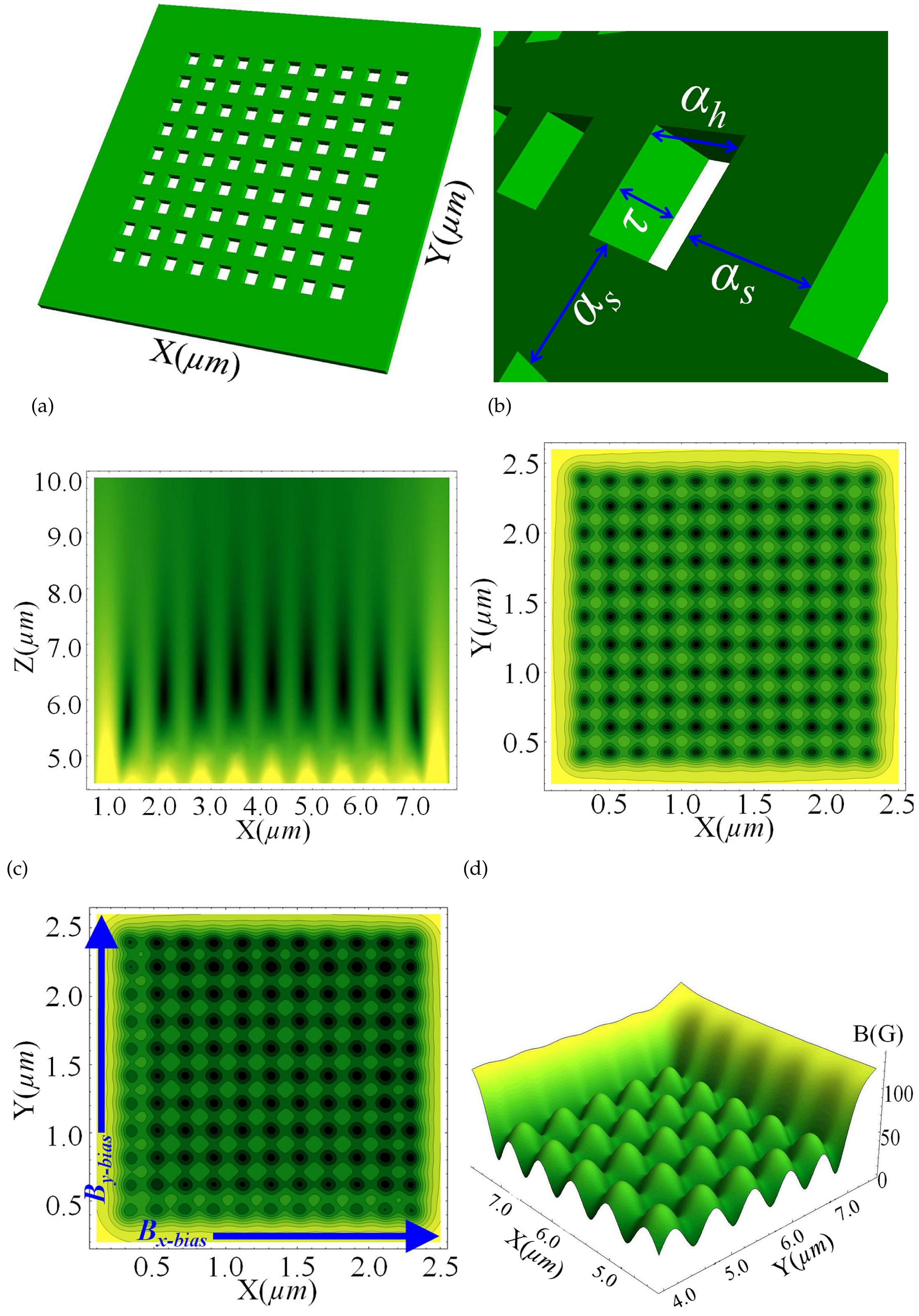

(a) (b) (c) (d) (e) (f)

***Figure 3.2:*** (a) Schematic representation of a two-dimensional magnetic lattice generating structure. (b) The magnetic lattice parameters are specified by the hole size $\alpha_h(\mu m) \times \alpha_h(\mu m)$, the separation between the holes $\alpha_s$ ($\mu$m) and the magnetic film thickness $\tau$ ($\mu$m). (c) Magnetic density plot of the simulated finite magnetic lattice sites in the $z/x$-plane across the center of the lattice. The traps are located at an effective $z$-distance, $d_{\text{min}}$ ($\mu$m), above the holes. (d-e) Contour plots of the distributed lattice sites across the $x/y$-plane (d) without and (e) with application of bias fields of $B_{\text{x-bias}}$ = $B_{\text{y-bias}}$ = 10 $G$. (f) 3D plot of the magnetic field of the distributed sites across the $x/y$-plane at $d_{\text{min}}$. The field is displayed from the center sites to the edge sites. The simulation results in the Figures (c)-(f) are numerically calculated using the following simulation input parameters: $\alpha_s = \alpha_h$ = 1 $\mu m$, $M_z$ = 3 $kG$ and $\tau$ = 2 $\mu m$ [Ref: A. Abdelrahman, *et. al.*, Phys. Rev. A **82**, 012320 (2010)].

$$
\begin{aligned}
B(x,y,z) = \Bigg[& B^2_{\text{x-bias}} + B^2_{\text{y-bias}} + B^2_{\text{z-bias}} + 2B^2_{\text{ref}} \times \Big(1 + \cos(\beta x)\cos(\beta y)\Big) e^{-2\beta[z-\tau]} + \\
&+ 2B_{\text{ref}} \times e^{-\beta[z-\tau]} \Bigg( \sin(\beta x) B_{\text{x-bias}} + \sin(\beta y) B_{\text{y-bias}} + \\
&+ \Big[ \cos(\beta x) + \cos(\beta y) \Big] B_{\text{z-bias}} \Bigg) \Bigg]^{1/2}
\end{aligned}
\tag{3.13}
$$

Simulated maps of the magnetic field strength distribution using numerical calculations across the $x/y$-plane located at an effective $z$-distance above the magnetized thin film surface are shown in Figures 3.2(d,e). Contour plots are shown for a finite magnetic lattice, Figure 3.2(d), in the initial magnetic state formed by $B_{\text{ref}}$ only while, as shown in Figure 3.2(e), with the application of external bias fields $B_{\text{x-bias}}$ and $B_{\text{y-bias}}$.

### ◦ *The Periodically Distributed Non-Zero Magnetic Field Local Minima*

The distribution of the non-zero local minima is periodic and the magnetic field minima $B_{\text{min}}$ are located in the real space at points defined by the coordinates $(x_{\text{min}}, y_{\text{min}}, d_{\text{min}})$. In this type of finite magnetic lattices, e.g. $n = 11$, the $B_{\text{min}}$ takes non-zero values when the external magnetic bias fields are applied. The location of the minima along the $x$, $y$ and $z$ axes for an infinite magnetic lattice can be written as

$$x_{\text{min}} = n_x \alpha, \qquad n_x = 0, \pm 1, \pm 2, \cdots \tag{3.14}$$

$$y_{\text{min}} = n_y \alpha, \qquad n_y = 0, \pm 1, \pm 2, \cdots \tag{3.15}$$

$$d_{\text{min}} \approx \frac{\alpha}{\pi} \ln\Bigg( B_{\text{ref}} \Bigg) \tag{3.16}$$

$$B_{\text{min}} \approx \frac{\sqrt{2}}{B_{\text{ref}}} |B_{\text{ref}} B_{\text{y-bias}} - B_{\text{ref}} B_{\text{x-bias}}| \tag{3.17}$$

The parameters $d_{\text{min}}$ and $B_{\text{min}}$ can significantly influence the lifetime of the trapped cold atoms making it crucial to choose suitable $B_{\text{min}}$ and $d_{\text{min}}$ initial values when micro-fabricating the magnetic lattice structure. As is clear the periodicity can extend from a finite number of lattice sites to a very large number, i.e. an infinite magnetic lattice. This has triggered the idea of creating multiple magnetic lattices in which case this option allows to have $m \times m$ blocks of $n \times n$ magnetic lattice. As will be explained later, it is useful to have several sets of *entangled* magnetic lattices while still being able to maintain the transfer of the quantum states among the lattices sites.

### ◦ *The Confining Magnetic Field Gradient and The Trapping Frequencies*

Each individual potential well, i.e. lattice site, creates its confinement through the magnetic barrier height $\Delta B(\mathbf{x})$ which is determined by

$$\Delta B(\mathbf{x}) = |B_{\text{max}}(\mathbf{x})| - |B_{\text{min}}(\mathbf{x})|, \qquad \mathbf{x} \equiv (x, y, z) \tag{3.18}$$

The magnetic fields around the local minima have symmetrically distributed gradients across the $x/y$-plane. These curvatures along the $x$ and $y$ axes are given by

$$\frac{\partial^2 B}{\partial x^2} = -\beta^2 e^{\beta[z-\tau]} B_{\text{ref}} \times \left[ \frac{\cos(\beta x)\cos(\beta y)}{\sqrt{2+2\cos(\beta x)\cos(\beta y)}} + \frac{\cos^2(\beta y)\sin^2(\beta x)}{[2+2\cos(\beta x)\cos(\beta y)]^{3/2}} \right] \tag{3.19}$$

$$\frac{\partial^2 B}{\partial y^2} = -\beta^2 e^{\beta[z-\tau]} B_{\text{ref}} \times \left[ \frac{\cos(\beta x)\cos(\beta y)}{\sqrt{2+2\cos(\beta x)\cos(\beta y)}} + \frac{\cos^2(\beta x)\sin^2(\beta y)}{[2+2\cos(\beta x)\cos(\beta y)]^{3/2}} \right] \tag{3.20}$$

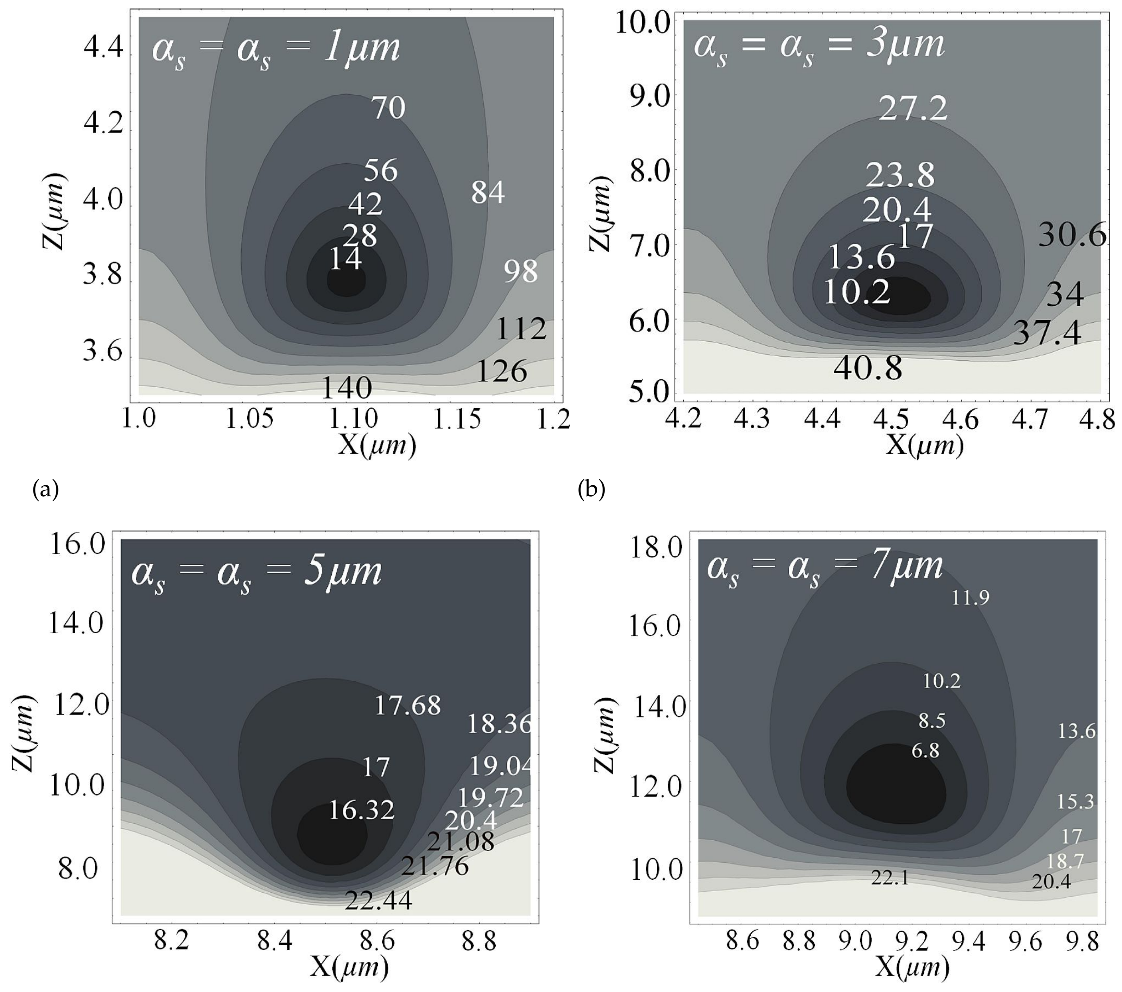

(a) (b)

(c) (d)

***Figure 3.3:*** (a-d) Contour plots of different magnetic field gradients for different sizes of a single magnetic potential well simulated using different values of hole size $\alpha_h$. The simulation is carried out using the parameters $M_z$ = 2.8 $kG$, $\tau$ = 2 $\mu m$ and with external bias fields $B_{\text{x-bias}} = B_{\text{y-bias}}$ = 1.5 $G$. The different values of the hole size are $\alpha_h = \alpha_s$ = (a) 1 $\mu m$, (b) 3 $\mu m$, (c) 5 $\mu m$ and (d) 7 $\mu m$[Ref: A. Abdelrahman, *et. al.*, Phys. Rev. A **82**, 012320 (2010)].

Due to the $x/y$-symmetry for an unbiased magnetic lattice, we find at the centers of the traps that the condition $\frac{\partial^2 B}{\partial x^2} = \frac{\partial^2 B}{\partial y^2}$ holds. The curvature of the trapping magnetic field at each individual site is of particular importance when loading the cold atoms into the magnetic lattice. Lattice sites with a steeper gradient may develop a *destructive Majorana spin-flip process*. To avoid the situation of the Majorana spin-flip it is crucial for the magnetic field local minima to have *non-zero* values. In such scenario, it is best for this type of magnetic lattices to have small number of sites, e.g. $5 < n < 15$, so that edge-effects are important. Moreover, by choosing suitable periodicities and applying the external magnetic bias fields the local filed minima can reach suitable trapping values, i.e. $B_{\text{min}} \gg 0$. Figures 3.3(a-d) show the dependence of the magnetic field gradient on $\alpha_h$ and $\alpha_s$.

The curvatures along the confining directions determine the trapping frequencies $\omega_{x,y,z}$ which depend on the Zeeman sub-levels. For the case of harmonic potentials they are given by

$$\omega_k = \frac{\beta}{2\pi}\sqrt{\mu_B g_F m_F \frac{\partial^2 B}{\partial k^2}} \qquad\qquad k = x, y, z \tag{3.21}$$

and $\omega_z = \sqrt{\omega_x^2 + \omega_y^2}$, where $g_F$ is the Landé $g$-factor, $\mu_B$ is the Bohr magneton, and $m_F$ is the magnetic quantum number of the hyperfine state.

The non-zero local minimum values determine the depth of the harmonic potential traps. For an external trapping magnetic field $B \ll \frac{\hbar \triangle\eta}{\mu_B g_F m_F}$, in which case the hyperfine splitting $\triangle\eta$ is larger than the Zeeman splitting, the depth $\Lambda_{\text{depth}}$ of an individual trap (in units of temperature) can be expressed as

$$\Lambda_{\text{depth}}(\mathbf{x}) = \frac{\mu_B g_F m_F}{k_B} \Delta B(\mathbf{x}) \tag{3.22}$$

where $k_B$ is the Boltzmann constant.

There is no difference between the general definition of the power-law potential and the magnetic field potential for each individual site of the magnetic lattices; however, here we define the magnetic potential as

$$\mathcal{V}(\mathbf{x}) = \mu_B g_F m_F B \tag{3.23}$$

with the potential barrier heights in the $k$-direction given by

$$\begin{aligned}\Delta\mathcal{V}^k(\mathbf{x}) &= \mathcal{V}^k(\mathbf{x})_{\text{max}} - \mathcal{V}^k(\mathbf{x})_{\text{min}} \\ &= \mu_B g_F m_F \Delta B^k(\mathbf{x}) = k_B \Lambda_{\text{depth}}(\mathbf{x})\end{aligned} \tag{3.24}$$

where the potential maxima and minima are calculated in a similar way to equation (3.23) such that

$$\mathcal{V}^k(\mathbf{x})_{\text{max}} = \mu_B g_F m_F B_{\text{max}} \tag{3.25}$$

$$\mathcal{V}^k(\mathbf{x})_{\text{min}} = \mu_B g_F m_F B_{\text{min}} \tag{3.26}$$

As an example, we show in the following lines a rough description of how the above calculations can be related to experimental data:

- *For $^{87}$Rb atoms in a low magnetic field seeking state with $F = 2$ and $m_F = +2$, the potential barrier heights along the $x$, $y$ and $z$-axes are $\frac{\Delta\mathcal{V}^x}{k_B} \approx 184\ \mu K$, $\frac{\Delta\mathcal{V}^y}{k_B} \approx 186\ \mu K$ and $\frac{\Delta\mathcal{V}^z}{k_B} \approx 122\ \mu K$, respectively, where $\triangle B^x$ = 2.74 G, $\triangle B^x$ = 2.78 G and $\triangle B^z$ = 1.83 G.*
  *The lattice parameters are $\alpha_h = \alpha_s$ = 3.5 $\mu m$, $\tau$ = 2 $\mu m$, $M_z$ = 3.80 kG, $B_{\textit{x-bias}}$ = -5 G, $B_{\textit{y-bias}}$ = -4.22 G and $B_{\textit{z-bias}}$ = -1.87 G.*

### 3.2.3 Characteristic parameters of the two-dimensional magnetic lattice: The asymmetrical and symmetrical lattices

In this section we give a brief summary for the magnetic lattice characteristic parameters that need to be carefully addressed in the experiment where tuning these parameters to the right values may lead to an accurate interpretation for the collected experimental data.

- ***The Asymmetrical and the Symmetrical Two-Dimensional Magnetic Lattices***

The lifetime of the ultracold quantum gases trapped in the two-dimensional magnetic lattice and the coherence of the computational bases of the $n \times n$ qubits, when considering quantum particles in the lattices sites to form qubits, are strongly influenced by the characteristic parameters of the magnetic lattice. In Table (3.2) we show some of the important parameters, in particular the value of the magnetic filed minimum $B_{\text{min}}$ and effective distances $d_{\text{min}}$. As mentioned, small values of $B_{\text{min}}$, i.e. values close to zero magnetic field, robustly increase the chances of developing the destructive Majorana spin-flip and consequently destroying the computational bases of the qubits. As shown in Table (2), applying external magnetic bias fields, $B_{\text{x-bias}}$ and $B_{\text{y-bias}}$, increase the values of $B_{\text{min}}$ at the center and the edge lattice sites which keeps the cold atoms away from the Majorana limits.

We simulated the effect of changing the dimensions $\alpha_s$ and $\alpha_h$ on the characteristic parameters of the magnetic lattice, specially the location of the non-zero local minima, their size and the curvature of the magnetic field across each individual lattice site. A shallower or steeper magnetic potential can be realized by choosing suitable values of $\alpha_s$ and $\alpha_h$. Increasing the separation $\alpha_s$ between the holes raises the value of the non-zero local minimum by several Gauss above the zero threshold, as shown in Figure 3.5(b), thereby eliminating the Majorana spin-flips.

***Table 3.1:*** Simulation parameters used to produce the non-zero local minima $B_{\text{min}}$ with their effective distances $d_{\text{min}}$. The magnetic walls are produced by the condition $\tau_{\text{wall}} \geq \tau_{\text{btm}}$.

| Simulation parameters | $m \times m$ | $n \times n$ | $M_z$ | $\tau_{\text{btm}}$ | $\tau_{\text{wall}}$ | $\alpha_h$ | $\alpha_s$ |
|---|---|---|---|---|---|---|---|
| Input values | $1 \times 1$ | $11 \times 11$ | $3\,kG$ | $2\,\mu m$ | $1\,\mu m$ | $3.5\,\mu m$ | $3.5\,\mu m$ |

***Table 3.2:*** Characteristic parameters describing the suitability of the magnetic lattice to host the cold atoms. Simulation input as shown in Table (3.1).

| Magnetic lattice parameters | $B_{\text{x-bias}} = B_{\text{y-bias}}$ | $B_{\text{min}}^{\text{Center}}$ | $B_{\text{min}}^{\text{Edge}}$ | $d_{\text{min}}^{\text{Center}}$ | $d_{\text{min}}^{\text{Edge}}$ |
|---|---|---|---|---|---|
| Simulation output | $0\,G$ | $0.002\,G$ | $0.0\,G$ | $2.3\,\mu m$ | $2.7\,\mu m$ |
| | $2.3\,G$ | $1.02\,G$ | $0.65\,G$ | $1.7\,\mu m$ | $1.6\,\mu m$ |

The simulation results show that the unperturbed film area, of thickness $\tau_{\text{wall}}$, surrounding the $n \times n$ matrix ($n$ = 11) affects the bottoms of most of the potential minima at the center of the magnetic lattice. The effect of $\tau_{\text{wall}}$ (magnetic wall effect) on the magnetic lattice sites introduces pronounced changes in the values of $B_{\text{min}}$ and $d_{\text{min}}$ at the edge and center lattice sites. This is because the magnetic walls effect acts as in-situ sources for the magnetic bias fields for a finite magnetic lattice. To describe the influence of the magnetic walls on some of the characteristic lattice parameters, such as the magnetic barrier heights $\Delta B$ and the effective working distance $d_{\text{min}}$, we simulate the trapping magnetic field of the lattice with

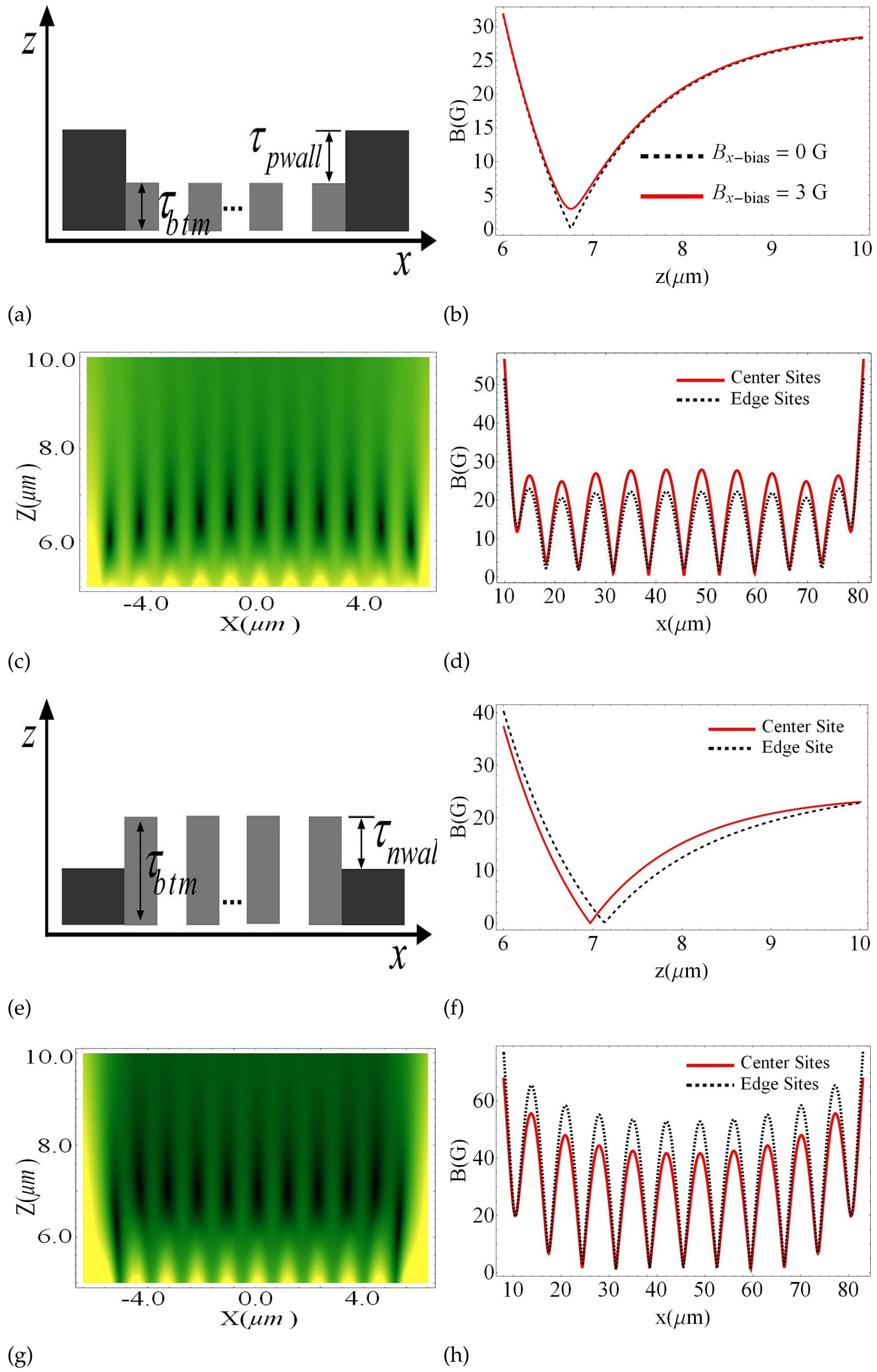

(a) (b) (c) (d) (e) (f) (g) (h)

***Figure 3.4:*** (a) Schematic diagram of a positive wall, $\tau_{\text{p-wall}} > \tau_{\text{btm}}$. (b) Density plot representation of the simulation results of applying the condition $\tau_{\text{p-wall}} = 0.7\mu m$ ( $\tau_{\text{p-wall}} > \tau_{\text{btm}}$) for an $11 \times 11$ magnetic lattice which causes reductions in the tilting magnetic potential between the lattice sites. (c) Comparing the magnetic minima locations between the center site and the edge site along the z-axis. (d) Magnetic lattice simulation using the $\tau_{\text{p-wall}} = 0.7\mu m$ constraint. (e) Schematic diagram of a negative wall, $\tau_{\text{n-wall}} < \tau_{\text{btm}}$, where (f) the density plot representation shows the effect of the condition $\tau_{\text{n-wall}} = -0.7\mu m$ on the locations of the sites across the $z/y$-plane, and (g) the magnetic minimum of the center and edge sites. (h) Magnetic field distribution along the $x$-axis using $\tau_{\text{n-wall}} = -0.7\mu m$. Simulation parameters are Mz = 2.8 $kG$, $\tau_{\text{btm}}$ = 2 $\mu m$, $\alpha_h$ = $\alpha_s$ = 10 $\mu m$, and no external bias fields.

different values of $\tau_{\text{wall}}$. The terms positive wall, negative wall and surface-equal wall are introduced to denote the conditions $\tau_{\text{p-wall}} > \tau_{\text{btm}}$, $\tau_{\text{n-wall}} < \tau_{\text{btm}}$ and $\tau_{\text{surf}} = \tau_{\text{btm}}$, respectively, as shown in Figure (3.4).

It is crucial to keep the working distance $d_{\text{min}}$ between the bottoms of the magnetic sites and the surface of the thin film large enough ($d_{\text{min}} \gtrsim 2\ \mu m$), because small values of $d_{\text{min}}$ bring the ultracold quantum gases, specially ultracold atoms, close to the surface of the film and hence allowing the Casimer-Polder potential to take place. The Casimer-Polder interaction introduces degrees of decoherence which strongly couple the spin of the cold atoms to the surface environment leading to a destructive event in the qubit formation. The proposed method shows that it is possible to maintain suitable values of $d_{\text{min}}$. Large separation values, $\alpha_s \gtrsim 2.5\ \mu m$, cause the magnetic minima to occur far from the surface, Figures 3.5(a-b), which helps to keep the atoms away from Casimir-Polder interactions.

Applying external magnetic bias fields, namely $B_{\text{x-bias}}$ and $B_{\text{y-bias}}$, will maintain symmetrically distributed lattice sites across the $x/z$ and $y/z$-planes. This is very useful when using the 2D magnetic lattices as magnetic mirrors or as condensed matter system simulators.

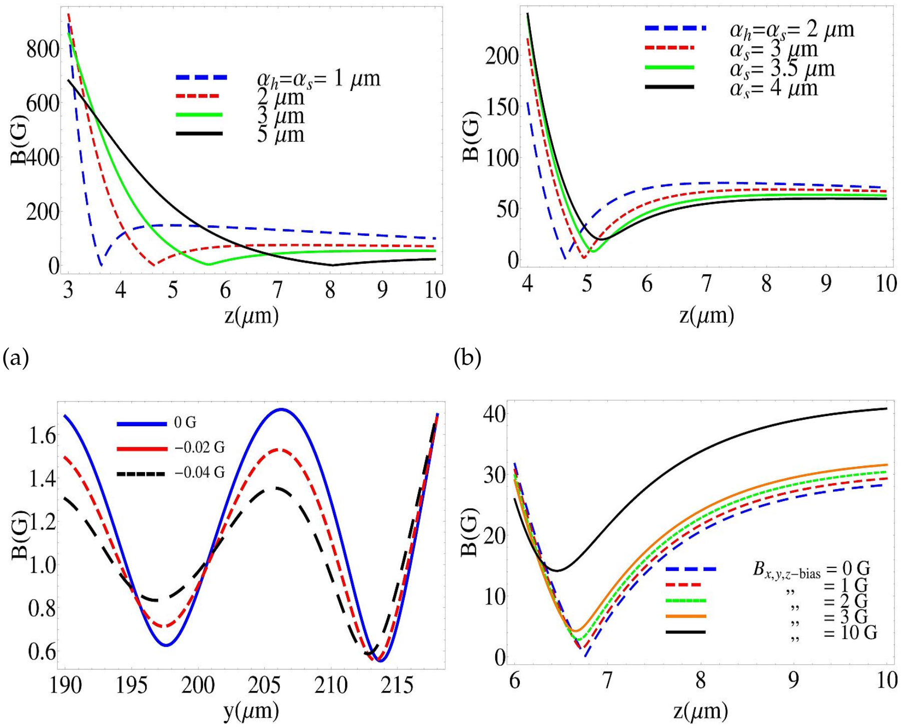

(a)

(b)

(c)

(d)

*Figure 3.5:* (a) Effect of changing the period, $\alpha_h$, on the location of the magnetic field local minima along the $z$-axis at $d_{\text{min}}$ above the holes of the thin film, and (b) effect of changing the separation of the holes, $\alpha_s$, across the $x/y$-plane. (c) Simulation result of varying the barrier heights $\Delta B_y$ by applying a negative external $B_{\text{z-bias}}$ magnetic field, and (d) $B_{\text{x-bias}}$, $B_{\text{y-bias}}$ and $B_{\text{z-bias}}$ effects on the gradient of the magnetic sites near the local minima along the $z$-axis . A film thickness of $\tau$ = 2 $\mu m$ with $M_z$ = 3 $kG$ is used in the above simulation results.

### 3.2.4 Magnetic band gap structures in the asymmetrical two-dimensional magnetic lattices

An important characteristic behavior in the two-dimensional magnetic lattice is also identified for small $n$. There is a pronounced *asymmetrical distribution*[1] of the magnetic local minima across the $x/z$, $y/z$-planes, as shown in Figures 3.4(c)(g); each two adjacent lattice sites, i.e. site ($i$) and site ($i+1$), are displaced along the $z$-axis and differ from one another by a tilting potential $\Delta\mathcal{V}_i^{i+1}$. We regard the magnetic lattice exhibiting such asymmetrical behavior as a simulator for the *magnetic band gap structure* of ultracold quantum gases, similar to the energy band gap structure in semiconductor devices. This may allow the simulation of condensed matter systems using trapped degenerate quantum gases. Figures (3.5)(a,b) summarize the simulation results of changing the hole size and the separating distance, and Figures (3.5)(c,d) show the effect of applying external magnetic bias fields on the height of the magnetic barrier and the amount of potential tilt between each two adjacent lattice sites, along the $y$-axis and $z$-axis, respectively.

An asymmetrical magnetic lattice set (with small $n$) at the reference magnetic field $B_{\text{ref}}$ with no external bias fields creates a magnetic confinement with $B_{\text{min}}$ close to zero. Using only the magnetic induction at the surface of the permanently magnetized thin film in the $z$-direction, in the case of an infinite magnetic lattice, leads to a *symmetrical distribution* of the potential wells in the $x/y$-plane (with $B_{\text{min}} = 0$) and *asymmetrical distribution* of the sites across the $x/z$ and $y/z$-planes. This effect is simulated by applying the constraint $B_{\text{x-bias}} = B_{\text{y-bias}} = B_{\text{z-bias}} = 0$ and $B_o \approx \mu_o M_z/\pi$, where the dominant factor is the surface reference magnetic field $B_{\text{ref}}$. Thus, equation (3.13) reduces to

$$B(x,y,z) = B_{\text{ref}} e^{-\beta[z-\tau]} \sqrt{2\Big(1 + 2\cos(\beta x)\cos(\beta y)\Big)} \tag{3.27}$$

As mentioned above, the critical values of $B_{\text{min}}$, i.e. $B_{\text{min}} \to 0$, can be avoided by changing the separation $\alpha_s$ between holes to be larger than the size of the holes $\alpha_h$ or by applying external magnetic bias fields for a finite $n$ magnetic lattice.

It is best to describe the magnetic band gap structure by what we call the *pyramid-like distribution* in which case the sites in the center of the magnetic lattice exhibit the highest magnetic minima compared to other sites (excluding the far edge-sites), where the magnetic minima values are distributed in the space (in $x/y$-planes along $z$-axis) downward to the edges of the lattice. The distribution takes a pyramid shape in the $x/y$-planes in which case each level has its own $B_{\text{z-min}}$ value and spaced along the $z$-axis by the over all sites tilting potential $\delta B_l^{l+1}$ where $l$ is the band index. The amount of the potential tilt creates a gap between each two sets of magnetic minima distributed in two adjacent bands. This configuration exhibits a scenario similar to that of the energy band gap structure in semiconductor devices.

## 3.3 The Asymmetrical Effect in the 2D Magnetic Lattice: Experimental Realizations

The method of producing the two-dimensional magnetic lattice is applicable to a variety of permanent magnetic materials. For example the permanent magnetic material **GdTbFeCo** is used by the Swinburne center for creating the atom chips[2]. In our experiments we have

---

[1] This effect is the reason for this type of lattices being named by the *asymmetrical two-dimensional magnetic lattices*.

[2] More information can be found in "*http://www.swinburne.edu.au/engineering/caous/*"

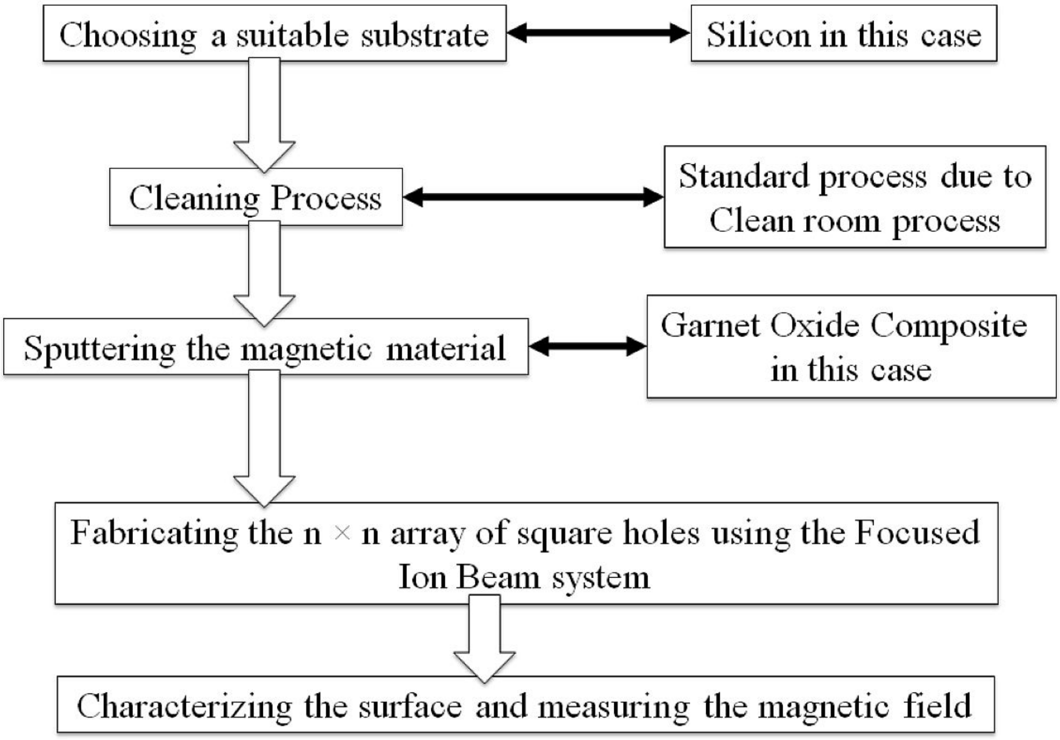

***Figure 3.6:*** Preparation procedure for the two-dimensional magnetic lattice sample.

fabricated the magnetic lattice device by using the $\mathbf{Bi_2Dy_1Fe_4Gd_1O_{12}}$ permanent magnetic material. The fabrication processes is described in the following section.

### 3.3.1 Sample Preparations: The Two-Dimensional Magnetic Lattice

The details of the fabrication process for the two-dimensional magnetic lattice are shown in Figure (3.6) and explained as below.

- **The substrate**

Depending on the purpose of the experiment and its configurations, the substrate can be chosen to be glass, silicon or Gadolinium Gallium Garnet (GGG, $Gd_3Ga_5O_{12}$) which is a synthetic crystalline material of the garnet group that has a good mechanical, thermal, and optical properties. In our case, silicon material is used as a substrate for the two-dimensional magnetic lattice.

- **The cleaning process**

The substrate was first cleaved to different small sizes between 5 mm to 10 mm. The substrate is then rinsed with clean water produced by a "*Ibis technology, Water Purification and Filtration* " machine and then immersed in an acetone solvent and set in an ultrasonic cleaner, "*Sharpertek Digital XP Pro*" at a temperature 15$^o$C for 10 mins. The last step was repeated using isopropanol, methanol and water.

- **The sputtering and the fabrication**

The "*Korea Vacuum Tech., LTD, R.F Magnetron Sputtering System, KVS. T4065*" is used to deposit the $Bi_2Dy_1Fe_4Ga_1O_{12}$ permanent magnetic material. The sputtering conditions are as follows

- Vacuum pressure of $10^5$ mTorr,
- Stage rotation speed of 7 rpm and temperature $23^o$C,
- Argon gas at plasma state generated by a rf-field.

The two-dimensional microstructure which generates the two-dimensional magnetic lattice is then created using the "*Focused Ion Beam, Fei Dual Beam 820*[3]" FIB/SEM workstation and magnetized along the $z$-axis.

- **Characterization**

For characterization, the external magnetic field is measured at the location of the magnetic field local minima, i.e. $d_{\text{min}}(\mu m)$ using the "*NT-MDT Solver P7LS scanning probe microscope*" set at both the "*Atomic Force Microscope*" AFM and the "*Magnetic Force Microscope*" MFM modes. The $d_{\text{min}}$ point is estimated from the condition $d_{\text{min}} > \alpha/2\pi$ where $\alpha$ = 10 $\mu m$.

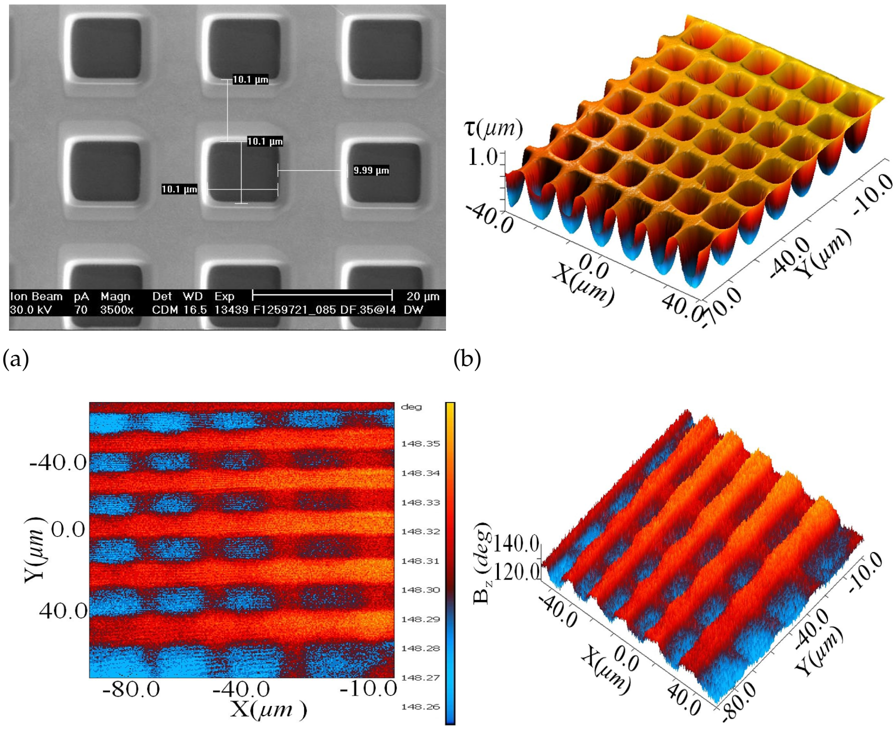

(a) (b)

(c) (d)

***Figure 3.7:*** (a) Scanning electron microscope and (b) atomic force microscope topological images of a fabricated two-dimensional magnetic lattice. (c-d) 2D and 3D images of the $z$-component of the magnetic field measured using the magnetic force microscope at the field local minima space-point. The fabricated samples contains 10 × 10 holes with $\alpha_h = \alpha_s$ = 10 $\mu m$, a thin film of thickness $\tau$ = 1 $\mu m$ sputtered onto a silicon substrate of thickness of 5 $\mu m$.

Figure 3.7(a) shows a 2D image of the structure generated by **Scanning Electron Microscope** (**SEM**) and Figure 3.7(b) shows a topological 3D image of the structure generated by using an **Atomic Force Microscope** (**AFM**). The Figures 3.7(c-d) shows the magnetic field $z$-component of the asymmetrical magnetic lattice which is measured using a magnetic force microscope where the MFM is set at the effective working distance $d_{\text{min}}(\mu m)$. In the Figures

---

[3] Fei is the name of the manufacturer, please see "*http://www.fei.com/default.aspx*"

(3.8) the measured $z$-components of the magnetic field show how the gradients of the field propagate with a tilting potential. The local minima $B_{\text{min}}$ in Figure 3.8(a) show asymmetrical behavior inherited in the lattice sites and extend, as numerically calculated, from the center of the lattice to the edges, i.e. from the right side of the Figures to the left side. Also Figure 3.8(b) shows the same behavior exhibited by the local maxima of the field $B_{\text{max}}$. In Figure 3.8(d) we show the amount of the magnetic tilt between two adjacent sites along the $x$-axis i.e. $\Delta B^{i,i+1}_{\text{min}}(x) = B^{i}_{\text{min}}(x) - B^{i+1}_{\text{min}}(x)$, and in Figure 3.8(e) we show the difference of the field maxima, i.e $\Delta B^{i,i+1}_{\text{max}}(x) = B^{i}_{\text{max}}(x) - B^{i+1}_{\text{max}}(x)$.

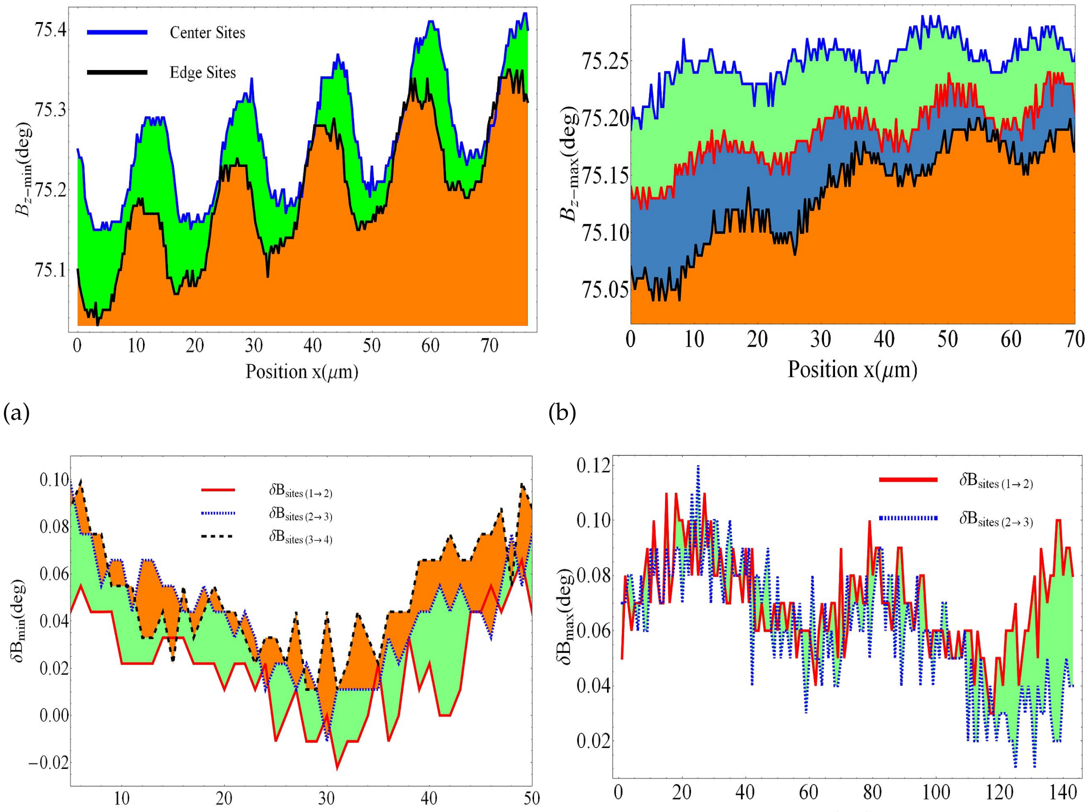

(a) (b)

(c) (d)

***Figure 3.8:*** (a) Measurements results of $z$-component of the magnetic field at the $B_{\text{min}}$ location. The results show the value of the $B_{\text{min}}$ at the center and at the edge of the lattice. (b) The measurement of the field local maxima $B_{\text{max}}$ measured from the center to the edge. (c-d) Show the values of $\Delta B^{i,i+1}_{\text{min}}(x) = B^{i}_{\text{min}}(x) - B^{i+1}_{\text{min}}(x)$ and $\Delta B^{i,i+1}_{\text{max}}(x) = B^{i}_{\text{max}}(x) - B^{i+1}_{\text{max}}(x)$, respectively. The experimental conditions as described in Figure (3.7).

During the fabrication process, it is important to pay attention to annealing temperature and the composition of the garnet material. Bad annealing temperature, dusty surface and surface roughness lead to a propagation of micro-cracks across the surface of the magnetic lattice. The existence of the micro-cracks results in destroying the magnetic field local minima. In Figures 3.9(a-b) we present an example for micro-cracks that resulted from the dust between two adjacent holes regardless of the solid state lattice configuration of the annealed magnetic material is perfectly matching the silicon substrate lattice with a minimum mismatching as shown in Figure 3.9(d). The magnetic field measured using the magnetic force microscope images shown in Figures 3.10 shows a clear evidence for destroying the magnetic

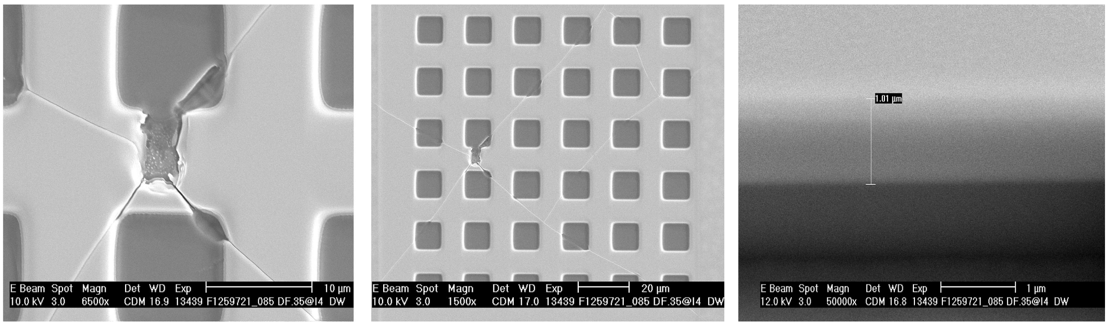

(a) (b) (c)

***Figure 3.9:*** (a-b) Micro-cracks ($\mu$-cracks) propagating across the surface of thin film result in deformation of the magnetic field local minima regardless of the perfect lattice matching as shown in (c).

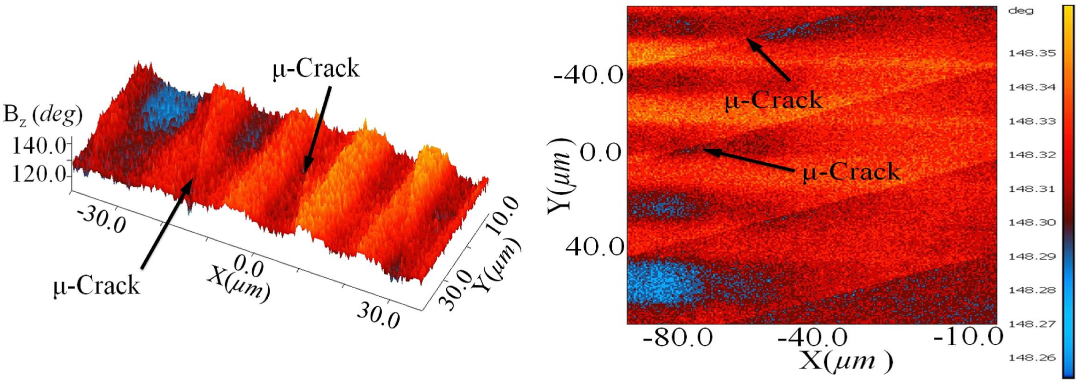

(a) (b)

***Figure 3.10:*** (a-b) 3D and 2D images of the magnetic field microscope show the deformed magnetic lattice sites due to a propagated micro-cracks across the surface of the thin film.

lattice sites due to the propagation of the micro-cracks across the surface of the thin film.

## 3.4 The Tunneling Mechanism of the Ultracold Quantum Gases

The tunneling of the trapped ultracold quantum gases across the magnetic lattice sites can *adiabatically* be controlled by applying external $z$-bias magnetic field, $B_{\text{z-bias}}$[4]. The quantum particles are confined individually in each lattice site allowing the quantum states to be *addressed selectively* at the center or at the edge of the magnetic lattice depending on the chosen configuration of the magnetic lattice. The addressing of the quantum state can be achieved via laser, ultra-short laser and/or rf-fields. There are two possible configurations as shown in Figure (3.4) which can easily be created using the current fabrication technology.

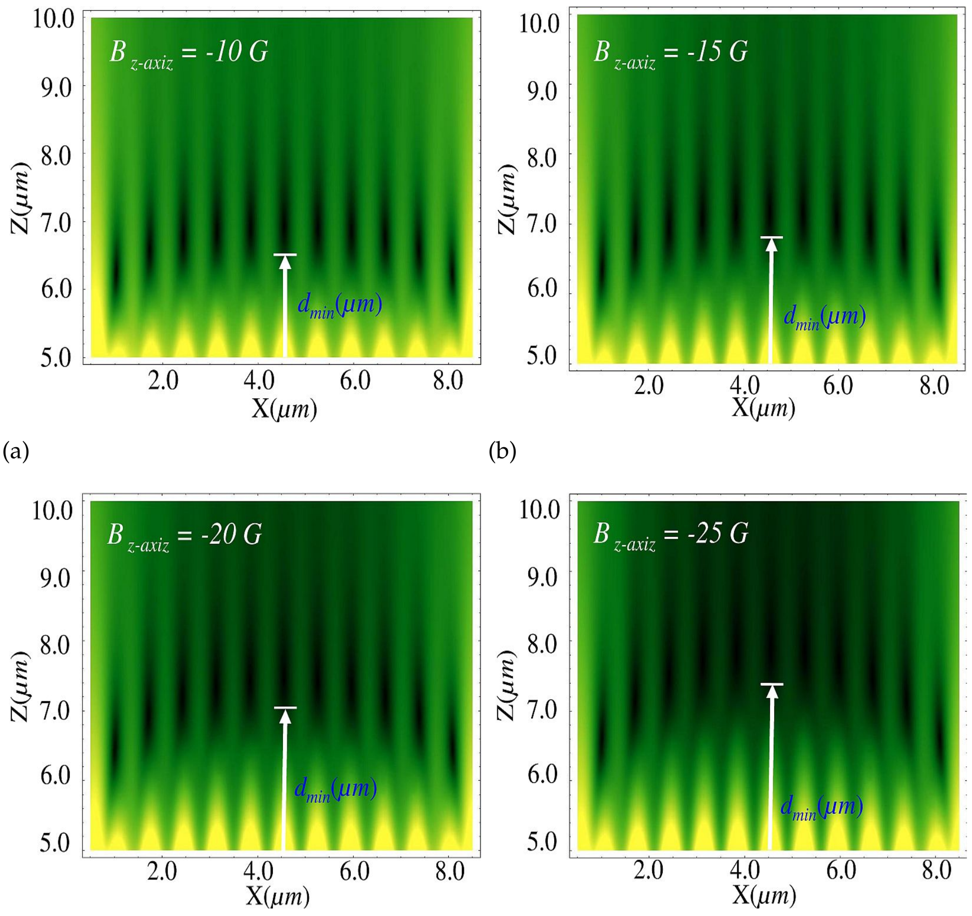

(a) (b) (c) (d)

*Figure 3.11:* (a-d) Effect of increasing a $B_{\text{z-bias}}$ field, along the negative direction of the $z$-axis, on the magnetic barriers $\Delta B_y$(G), $\Delta B_z$(G) and the non-zero magnetic local minima. Enhanced asymmetrical effect and $d_{\text{min}}(\mu\text{m})$ values are realized for different values of $B_{\text{z-bias}}$ field. Simulation input parameters: $n$ = 11 sites, $\alpha_s = \alpha_h$ = 3.5 $\mu m$ $M_z$ = 2.8 $kG$ and $\tau$ = 2 $\mu m$.

Figure (3.11) shows simulation results of the effect of applying different values of $B_{\text{z-bias}}$ in which case the external bias field acts as a tunneling controller that minimizes the mag-

---

[4] The adiabaticity of the tunneling points to a whole new type of research related to condensed matter system simulation. This is mentioned in some detail in Chapter (4).

netic tunneling barrier $\Delta B$[5]. The effect appears as increases in the values of $B_{\text{min}}$ and $d_{\text{min}}$ which allows the quantum particles to tunnel from the center of the magnetic lattice to the edge sites. One can emphasize the importance of increasing the value of $B_{\text{min}}$, due to the application of $B_{\text{z-bias}}$, by mentioning that the tunneling of the quantum particles can be assisted by the *gravitational field* along the negative direction of the $z$-axis.

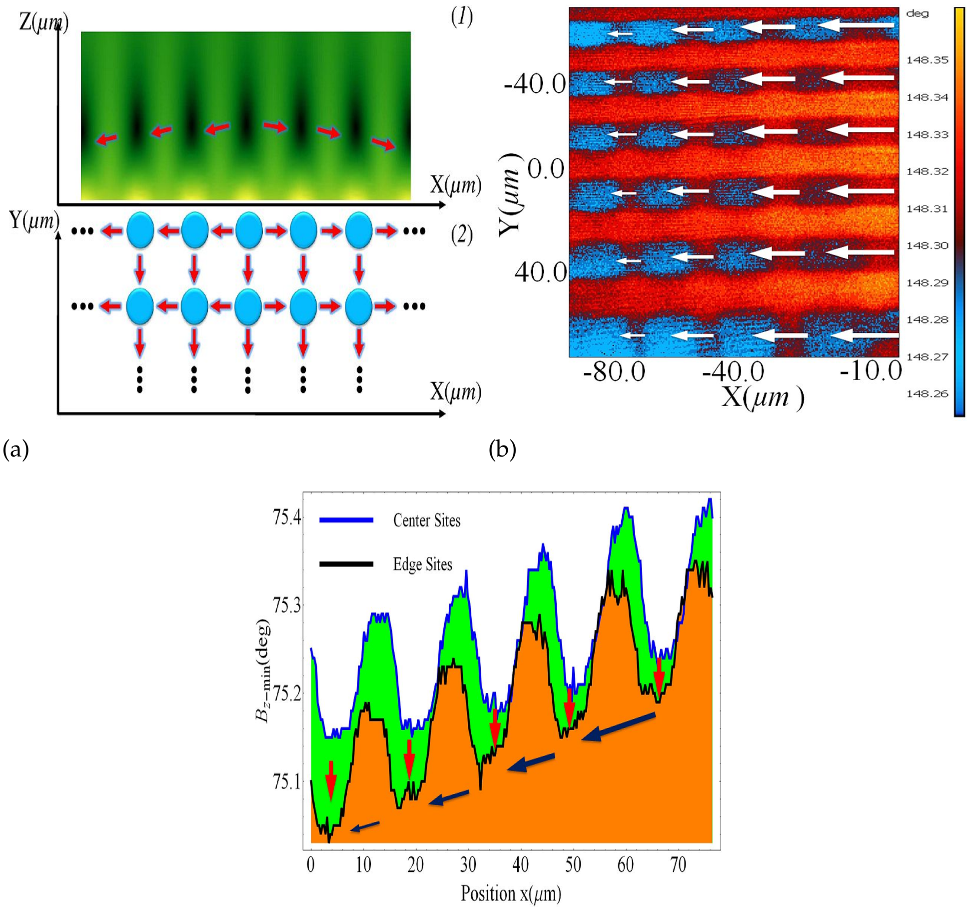

(a) (b)

(c)

***Figure 3.12:*** (a-d) Effect of a $B_{\text{z-bias}}$ field, along the negative direction of the $z$-axis, on the magnetic barriers $\Delta B_y$, $\Delta B_z$ and the non-zero magnetic local minima. Enhanced asymmetrical effect and $d_{\text{min}}$ values are realized for different values of $B_{\text{z-bias}}$ field. Simulation input parameters: $n$ = 11 sites, $\alpha_s = \alpha_h$ = 3.5 $\mu m$ $M_z$ = 2.8 $kG$ and $\tau$ = 2 $\mu m$. Figure (b) and (c) show experimental measurements.

In Figure 3.12(a), we schematically represent the possible tunneling direction and its mechanism across the two-dimensional magnetic lattice. The experimental results shown in Figure 3.12(b-c) show smaller values of $B_{\text{min}}$ concentrated at the edges of the lattice in which case the quantum degenerate gases migrate from the center to the edge with a loss in their density (compared to the original density at the center) as schematically represented by the arrows' thicknesses. The two-dimensional magnetic lattice in Figure 3.12(b) is a special case for an externally biased lattice; this is why the sites periodicity appears in one direction. In the ideal situation, as shown in Figure 3.12(c), the quantum particles are expected to tunnel across the $x/y$-plane of the magnetic lattice, starting from the center to the edges. These

---

[5] As an interesting application of such action is to consider the (adiabatic) magnetic control mechanism as an operation control for the quantum gates.

directions are schematically represented in the same Figure 3.12(c) by the vertical (red color) and horizontal (dark blue color) arrows.

Chapter 4

# SIMULATING CONDENSED MATTER USING QUANTUM DEGENERATE GASES

> ¶ *We are at the very beginning of time for the human race. It is not unreasonable that we grapple with problems. But there are tens of thousands of years in the future. Our responsibility is to do what we can, learn what we can, improve the solutions, and pass them on.* ... (Richard P. Feynman)

## 4.1 Overview

As explained in the previous chapters, ultracold atoms and Bose-Einstein condensates (BECs) prepared in the so-called low magnetic field seeking-states can be trapped in the periodically distributed magnetic local minima to create the magnetic lattices configurations [48][74]. The magnetic lattices are recognized as quantum devices with abilities to coherently access and manipulate the quantum states of the trapped ultracold atoms in a similar scenario to optical lattices [192]. These advances in the field of ultracold atoms have opened a wide gate to investigate and study many interesting fundamental problems in different area of physics such as condensed matter [193] and quantum information processing [192]. Magnetic lattices created by trapping ultracold atoms can be used to simulate such environments and critical quantum phase transitions because they can provide adiabatic control over interesting quantum phenomena such as quantum tunneling, superfluidity and formation of bound states of long lived quasi-particles, such as excitons condensation in solids [194][195]. Bound states are naturally hard to detect and it is difficult to access their individual quantum states due to the short lifetime and the fragility of their coupling to a desirable environment [132][196]. One of the interesting problems is to detect and manipulate the phase coherence signature in a macroscopic quantum system. A well known example of the direct manifestation of a macroscopic phase coherence is the Josephson effect between two superfluids or two superconductors [197][198]. Theoretically, the use of trapped ultracold atoms in varying periodically distributed potential fields has been proposed to simulate the Josephson effect [107][113][199][200] and experimentally has been realized [87][201][202]. The new approach of the asymmetric two-dimensional magnetic lattice will allow the trapped ultracold atoms to simulate collective excitations similar to those formed in condensed matter systems. The ultracold atoms can be trapped to maintain an asymmetric two-dimensional lattice with magnetic band gap-like structure similar to that in semiconductor devices. We also show the possibility of using this type of 2D magnetic lattice to simulate the adiabatically controlled oscillations of collective excitations such as the discharging Josephson states and the exciton-Mott quantum phase transition formed by coherent tunneling of cold atoms across the lattice sites.

We need to recall some primary details regarding the ideal Bose gas so as we can arrive at a simplified model for describing the *Interacting Quantum Degenerate Gases*. In this overview, we briefly describe the classical limits in the ideal Bose gas and show a necessary condition for the critical temperature not to depend on the trap shape within the degeneracy limits, i.e. $1 \lesssim \vartheta < 2.612$. We also show the fully degenerate Bose gases with and without the Bose-Einstein condensation from a statistical prospective. All these point together will add up to explain what is meant by the *Macroscopic Quantum Phase Transition* exhibited by the degenerate gases at certain conditions.

We regard the contest of the overview as a continuity for the section (2.5.1) "The condensation state of ideal gases in harmonic traps". In particular, to emphasize the classical regime ($n_o\Lambda^3 \ll 1$) we recall the degeneracy parameter in Equation (2.78) and we rewrite that expression at the trap minimum point, i.e for the single lattice site at a magnetic bottom with small field value, but not close to zero, and with the Majorana spin-flip is assumed to be suppressed to its minimal effect[1]

$$\Theta \to n'(0)\Lambda^3 = g_{3/2}(\bar{f}) = \sum_{j=1}^{\infty} \frac{\bar{f}^j}{j^{v=3/2}} \tag{4.1}$$

The l. h. s. of the above equation (4.1) entails a monotonically decrement in its values as the temperature increases with a fixed number of particles $n'_o$. We investigate the boundaries here to analyze under what circumstances the classical limits appear, considering the minimum limit of the degeneracy parameter, i.e $\Theta \to 0$. We find that the corresponding fugacity also has become smaller which allows only the first terms in the summation in equation (4.1) to contribute, that is $\sum_{j=1}^{\infty} \frac{\bar{f}^j}{j^{v=3/2}} \simeq \bar{f}$.

The above analysis gives an interesting conclusion; the condition for the classical limits assumes that at $n'_o = n_o$ the fugacity and the degeneracy parameters both coincide such that

$$\bar{f} \underset{T\to\infty}{\simeq} n_o\Lambda^3 \Longleftrightarrow \mu = k_B T \ln\left[n_o\Lambda^3\right] \tag{4.2}$$

which shows that the chemical potential in the classical limits must have large negative values for the atoms (with a reasonably large number) to undergo the Bose-Einstein distribution.

Apparently, inspecting the fugacity limits will eventually lead us to quantify the deviation of the gas behavior from the classical statistics. In other words, from the above equation (4.2) the presence of the quantum degeneracy robustly maintain a realizable signature when the fugacity expansion reaches its convergence limit, i.e. $\bar{f} \to 1$. Thus decreasing the temperature of the trapped gas results in increasing of the chemical potential in which case the fugacity convergence occurs at the critical temperature $T_C$ and the density profile shapes in the following fashion

$$n(\boldsymbol{r}) = \frac{1}{\Lambda^3} \sum_{j=1}^{\infty} \frac{1}{j^{3/2}} e^{-j\mathcal{V}(\boldsymbol{r})/k_B T_C} \tag{4.3}$$

If one would argue the above equation (4.3) mathematically, the following conclusions are drawn in consistence with the experimental discussion in section (2.5.1) on the "Trapped 3D

---

[1] Majorana spin-flip is one of the limiting processes for creating Bose-Einstein condensation; it is an unavoidable destructive process when the value of magnetic bottom of the trap approaches the zero value.

ideal Bose gas: Typical experimental analogy": First, at the trap center all the terms of the expansion contribute to the density while away from the center the higher order terms are exponentially suppressed compared to the lower ones. Second, it is also in agreement with Einstein's argument that the favorable state is the mostly occupied by the particles which purely reflects the Bose statistics. Third, at the trap center the quantum degeneracy merely converts to the value $\Theta \approx 2.612...$, agreeing with equation (2.78) and the critical temperature $T_C$ only depends on the density of the particles at the trap center and not on the trap shape, such that $k_B T_C \simeq 3.31 \frac{\hbar^2}{m} n_o^{2/3}$.

- ***The Chemical Potential***

Before we describe the interacting picture of the quantum particles, it is important to show the boundary limits of the so-called *chemical potential* $\mu$. It is an important scale that relates the degeneracy parameter to the critical temperature as well as determining the conversion point to the BEC state. For a precise description of the chemical potential limits, it has to be evaluated close to the critical temperature:

- ○ For $T \lesssim T_C$; the chemical potential $\mu$ is always close to zero and the Bose function is best represented by the following expansion in the degenerate regime

$$N = \frac{k_B T}{-\mu} + \frac{V}{\Lambda^3}\Big[\zeta(3/2) + \zeta(1/2)\sqrt{\frac{-\mu}{k_B T}} + ...\Big] \tag{4.4}$$

- ○ For $T \gtrsim T_C$; where $\frac{1}{N} \lll \frac{-\mu}{k_B T} \ll 1$, the chemical potential is expressed as

$$\mu = -k_B T\Big[\frac{\zeta(3/2) - n_o\Lambda^3}{\zeta(1/2)}\Big]^2 \tag{4.5}$$

  From the above expression (4.5), the condition $\mu \lesssim k_B T$ shows a non-classical behavior and for $\mu \ll k_B T$ the fugacity expansion approaches its convergence limits where the thermal term in equation (4.4) is no longer counted for all atoms [16].

- ○ For $T = T_C$; and for a large number of atoms ($N \ggg 1$), the chemical potential has a small but finite negative value and the expansion in (4.4) extends to the following

$$N = \frac{k_B T}{-\mu} + \frac{V}{\Lambda_C^3}\Big[\zeta(3/2) + \zeta(1/2)\sqrt{\frac{-\mu}{k_B T_C}} + ...\Big] \simeq \frac{V}{\Lambda_C^3}\zeta(3/2) \tag{4.6}$$

  Clearly, this expression is valid at $T_C$, therefore by lowering the temperature below $T_C$ (as Einstein suggested and predicted) the ground state occupation grows exponentially from $N_o = -\frac{k_B T}{\mu} \ll N$ to macroscopic values that are best described as a Bose-Einstein condensate. It is important to show that below the $T_C$ the *non-condensed fraction* is given by $\frac{N'}{N} = \frac{\zeta(3/2)}{n_o\Lambda^3} = \Big[\frac{T}{T_C}\Big]^{3/2}$.

The previous expressions are for the homogeneous case of a fully degenerate gas and Bose-Einstein condensate. For a non-homogeneous gas and for an analytical expression for the chemical potential far below the critical temperature we refer to [16].

◇ **Related publications to this Chapter:**

1 A. Abdelrahman, P. Hannaford and K. Alameh *"Adiabatically Induced Coherent Josephson Oscillations of Ultracold Atoms in an Asymmetric Two-Dimensional Magnetic Lattice,"* Optics Express **17**, 24358 (2009).

2 A. Abdelrahman, K. Alameh and M. Vasiliev, *"The macroscopic quantum phase of ultracold degenerate gases in the asymmetrical two-dimensional magnetic lattice,"* Solid State Communications, **151**, 859 (2011).

3 A. Abdelrahman, M. Vasiliev, K. Alameh, P. Hannaford, Yong-Tak Lee, Byoung S. Ham, *"Towards Bose-Einstein condensation of excitons in an asymmetric multi-quantum state magnetic lattice"*, Numerical Simulation of Optoelectronic Devices (NUSOD) (2009).

4 A. Abdelrahman, K. Alameh and P. Hannaford, *"Adiabatic coherent quantum tunneling of ultracold atoms trapped in an asymmetrical two-dimensional magnetic lattices"*, 6th International Symposium on High-Capacity Optical Networks and Enabling Technologies (HONET) (2009).

In this Chapter, we considered weakly coupled microscopic clouds of BECs, with a small number of trapped ultracold atoms allowed to tunnel between sites via the adiabatic control of the hopping strength of the adjacent magnetic bands. The adiabatic control can be induced through application of external magnetic bias fields applied along the negative direction of the z-axis. Atoms tunnel through the magnetic barriers from the highest magnetic band to the neighboring lowest magnetic band following the pyramid-like distribution of energy levels in which case the gap can also be regarded as the difference between the magnetic height of the two sites' magnetic hight.

## 4.2 The Interacting Quantum Degenerate Gases

The interaction of the quantum particles within the above special circumstances, is usually described within the frame of the *self-consistent nonlinear Schrödinger equation* which is also known as the *Gross-Pitaevskii equation* (**GPE**). Detailed derivation of the **GPE** can be found in [16]. For a trapped $d$-dimension *interacting Bose gas* that interacts via the interatomic potential $\mathcal{U}(\boldsymbol{r})$ and externally confined by the confining field $\mathcal{V}(\boldsymbol{r})$ the Hamiltonian of the system in the second quantization reads as follows[2]

$$\widehat{\mathcal{H}} = \int_{\boldsymbol{r}} \widehat{\Psi}^{\dagger}(\boldsymbol{r})\Big[-\frac{\hbar^2\nabla^2}{2m} + \mathcal{U}(\boldsymbol{r})\Big]\widehat{\Psi}(\boldsymbol{r}) + \frac{1}{2}\int\int_{\boldsymbol{r},\boldsymbol{r}'} \mathcal{V}(|\boldsymbol{r}-\boldsymbol{r}'|)\widehat{\Psi}^{\dagger}(\boldsymbol{r})\widehat{\Psi}^{\dagger}(\boldsymbol{r}')\widehat{\Psi}(\boldsymbol{r})\widehat{\Psi}(\boldsymbol{r}') \tag{4.7}$$

where $\widehat{\Psi}(\boldsymbol{r})$ and $\widehat{\Psi}^{\dagger}(\boldsymbol{r})$ are the boson field operators which satisfy the commutation relation $[\widehat{\Psi}(\boldsymbol{r}), \widehat{\Psi}(\boldsymbol{r}')] = 0$ and $[\widehat{\Psi}(\boldsymbol{r}), \widehat{\Psi}^{\dagger}(\boldsymbol{r}')] = \delta(\boldsymbol{r}-\boldsymbol{r}')$. The boson field operators are also expressed in the *density-phase* representation such that

$$\widehat{\Psi}(\boldsymbol{r}) = \sqrt{\hat{n}}e^{i\hat{\phi}}, \qquad \widehat{\Psi}^{\dagger}(\boldsymbol{r}) = \sqrt{\hat{n}}e^{-i\hat{\phi}} \tag{4.8}$$

where the density operator $\hat{n}(\boldsymbol{r})$ and the phase operator $\hat{\phi}(\boldsymbol{r})$ are real and satisfy the commutation relation $[\hat{n}(\boldsymbol{r}), \hat{\phi}(\boldsymbol{r})] = i\delta(\boldsymbol{r}-\boldsymbol{r}')$.

In the Heisenberg representation the action of the time-operator $i\hbar\frac{\partial}{\partial t}$ on the Boson field operator $\widehat{\Psi}(\boldsymbol{r})$ leads to the following commutation relation

$$i\hbar\frac{\partial\widehat{\Psi}}{\partial t} = -\Big[\widehat{\mathcal{H}}, \widehat{\Psi}\Big] = \Big(-\frac{\hbar^2\nabla^2}{2m} + \mathcal{U}(\boldsymbol{r}) + \int_{\boldsymbol{r}'} \mathcal{V}(|\boldsymbol{r}-\boldsymbol{r}'|)\widehat{\Psi}^{\dagger}(\boldsymbol{r}')\widehat{\Psi}(\boldsymbol{r}')\Big)\widehat{\Psi} \tag{4.9}$$

The above equation (4.9) can be rewritten, using the commutation relation of the boson field operators, as follows

---

[2] This is a many-body problem [89], also see after section (2.5).

$$i\hbar\frac{\partial\widehat{\Psi}}{\partial t}+\mathcal{V}(0)\widehat{\Psi}=-\frac{\hbar^2\nabla^2}{2m}+\mathcal{U}(\boldsymbol{r})\widehat{\Psi}+\widehat{\Psi}\int_{\boldsymbol{r}'}\mathcal{V}(|\boldsymbol{r}-\boldsymbol{r}'|)\widehat{\Psi}^{\dagger}(\boldsymbol{r}')\widehat{\Psi}(\boldsymbol{r}') \tag{4.10}$$

The term $\mathcal{V}(0)\widehat{\Psi}$ is trivially eliminated by the substitution of the central confinement time-dependent boson field operator $\widehat{\Psi}\rightarrow\widehat{\Psi}\exp\left(i\frac{\mathcal{V}(0)t}{\hbar}\right)$. Substituting the density -phase representation into the above equation (4.10) we get the following system of continuity equations[3]

$$-\hbar\frac{\partial\hat{n}}{\partial t}=\frac{\hbar^2}{m}\nabla(\nabla\hat{\phi}\hat{n}) \tag{4.11}$$

$$-\hbar\frac{\partial\hat{\phi}}{\partial t}=\frac{\hbar^2}{2m}\Big[(\nabla\hat{\phi})^2-\frac{\nabla^2\sqrt{\hat{n}}}{\sqrt{\hat{n}}}\Big]+\mathcal{U}(\boldsymbol{r})+\int_{\boldsymbol{r}'}\mathcal{V}(|\boldsymbol{r}'-\boldsymbol{r}|)\hat{n}(\boldsymbol{r}') \tag{4.12}$$

In the short-range interatomic potential for the dilute ultracold weakly interacting gas, the integral in the r. h. s. of equation (4.12) can be reduced to an expression that includes only the mean-field coupling constant $g$ and the density $\hat{n}(\boldsymbol{r})$ such that

$$\int_{\boldsymbol{r}'}\mathcal{V}(|\boldsymbol{r}'-\boldsymbol{r}|)\hat{n}(\boldsymbol{r}')\approx g\hat{n}(\boldsymbol{r}) \tag{4.13}$$

It is well known that the problem of $N$ interacting bosons is a very complicated task where the dynamical evolution of the system is described by the $N$ body wavefunction. However, great simplifications to this problem can be obtained at the level of sufficiently dilute gas and the occurrence of the Bose-Einstein condensate in which it is possible to estimate the interaction potential using the Born approximation represented as in the above equation (4.13) or as $g|\Psi|^4$. It is also important to mention that the coupling constant $g$ is related to the $s$-wave scattering length, see section (2.4) after "***Spherical square well model: The scattering length and the bound $s$ state at zero-momentum*** ($l=0$)".

The wavefunction $\widehat{\Psi}(\boldsymbol{r})$ is in fact a time-dependent *macroscopic wavefunction* $\widehat{\Psi}(\boldsymbol{r},t)$ which also obeys the Gross-Pitaevskii equation [90] that can be rewritten, under the above circumstances, as follows

$$i\hbar\frac{\partial}{\partial t}\widehat{\Psi}(\boldsymbol{r},t)=-\frac{\hbar^2}{m}\nabla^2\widehat{\Psi}(\boldsymbol{r},t)+\Big[\mathcal{V}(\boldsymbol{r},t)+g|\Psi(\boldsymbol{r},t)|^2\Big]\widehat{\Psi}(\boldsymbol{r},t) \tag{4.14}$$

where the coupling constant $g$ is as described after equation (2.57), i.e. $g=\frac{4\pi\hbar^2 a}{m}$, where $a$ is the atomic $s$-wave scattering length and $m$ is the atomic mass. The nonlinearity arises from the interaction in the form of the self-consistent field $g|\widehat{\Psi}(\boldsymbol{r})|^2$ in which case this term is directly linked to the dynamical properties of the BEC such as the spatial distribution of the condensate which can change drastically with respect to the non interacting ground state of the Gaussian shape.

In relation to the theoretical investigations presented in this chapter, it is important to emphasize the following argument

- *In an inhomogeneous and finite system the condensed state wavefunction clearly can be determined through the* ***diagonalization of the one-body density matrix***

  $$\langle\widehat{\Psi}^{\dagger}(\boldsymbol{r}',t)|\widehat{\Psi}(\boldsymbol{r},t)\rangle \tag{4.15}$$

  *in correspondence to the eigenfunction that exhibits the largest eigenvalue. These eigenvalues are directly related to the* ***condensate fraction*** $n_o$ *[91].*

---

[3] Also known as Euler hydrodynamic equations.

- ***Linearizing the Gross-Pitaevskii equation: The Bogoliubov approximation***

The **GPE** is very useful for presenting an appropriate description of the *low energy elementary excitations at zero temperature*; this is a precise description for the type of interactions that occur in the condensate of the alkali gases. The elementary excitations appear as small oscillations around the ground state of the condensate where the frequency of these oscillations can be obtained by linearizing the **GPE** which is known as the Bogoliubov de-Gennes approximation. In that sense, the wavefunction is expanded in terms of the small perturbation $\delta\widehat{\Psi}(\boldsymbol{r},t)$ such that

$$\widehat{\Psi}(\boldsymbol{r},t) = \exp\Big[-\frac{i\mu_o t}{\hbar}\Big]\Big(\widehat{\Psi}_o(\boldsymbol{r}) + \delta\widehat{\Psi}(\boldsymbol{r},t)\Big) \tag{4.16}$$

which is still a solution for the **GPE** to the first order in $\delta\widehat{\Psi}(\boldsymbol{r},t)$ but only if this perturbation satisfies the equation

$$i\hbar\frac{\partial}{\partial t}\delta\widehat{\Psi}(\boldsymbol{r},t) = -\frac{\hbar^2}{m}\nabla^2\widehat{\Psi}(\boldsymbol{r},t) + \Big[\mathcal{V}(\boldsymbol{r}) - \mu_o\Big]\delta\widehat{\Psi}(\boldsymbol{r},t) + 2g|\Psi_o(\boldsymbol{r})|^2\delta\widehat{\Psi}(\boldsymbol{r},t) + g|\Psi_o(\boldsymbol{r})|^2\delta\widehat{\Psi}^*(\boldsymbol{r},t) \tag{4.17}$$

In our scenario, the external potential $\mathcal{V}(\boldsymbol{r},t)$ can change with time to induce tunneling in which case the approximation still suffers extra nonlinearity; therefore the time dependency of the confining field has been eliminated, i.e. $\mathcal{V}(\boldsymbol{r},t) \to \mathcal{V}(\boldsymbol{r})$, as required by the approximation. The solution for the above equation (4.17) can be written in the form

$$\delta\widehat{\Psi}(\boldsymbol{r},t) = u(\boldsymbol{r})e^{-i\nu t} - v^* e^{+i\nu t} \tag{4.18}$$

Substituting the above solution (4.18) in equation (4.17) it will take the following form of system of equations

$$\hbar\omega\begin{pmatrix} u(\boldsymbol{r}) \\ -v(\boldsymbol{r}) \end{pmatrix} = \begin{bmatrix} \widehat{\mathcal{H}}_o - \mu_o + 2g|\Psi_o(\boldsymbol{r})|^2 & -g|\Psi_o(\boldsymbol{r})|^2 \\ -g|\Psi_o(\boldsymbol{r})|^2 & \widehat{\mathcal{H}}_o - \mu_o + 2g|\Psi_o(\boldsymbol{r})|^2 \end{bmatrix}\begin{pmatrix} u(\boldsymbol{r}) \\ v(\boldsymbol{r}) \end{pmatrix} \tag{4.19}$$

where $\widehat{\mathcal{H}}_o = -\frac{\hbar^2}{2m}\nabla^2 + \mathcal{V}(\boldsymbol{r})$. Each elementary excitation is associated with its own energy $\varepsilon$ that corresponds to the frequency $\nu$ of the relative oscillation around the ground state, i.e. $\varepsilon = \hbar\nu$.

Since the elementary excitations have small amplitudes we simplify the equations (4.11)-(4.12) for small fluctuations of densities. Thus following the same procedure as above we linearize the equations (4.11)-(4.12) with respect to $\delta\hat{n}$ and $\nabla\hat{\phi}$ by representing the density operator as $\hat{n} = n_o(\boldsymbol{r}) + \delta\hat{n}(\boldsymbol{r})$ and shifting the phase by an amount of $-\mu t/\hbar$ around the stationary solutions $\hat{n} = n_o$, $\nabla\hat{\phi} = 0$. Then the zero-order terms allow the **GPE** to be written in the following form for $n_o$

$$-\frac{\hbar^2}{2m}\frac{\nabla^2\sqrt{n_o}}{\sqrt{n_o}} + \mathcal{U}(\boldsymbol{r}) + gn_o = \mu \tag{4.20}$$

while the first-order terms provide equations for the density and phase fluctuations as follows

$$\hbar\frac{\partial}{\partial t}\Big(\frac{\delta\hat{n}}{\sqrt{n_o}}\Big) = 2\Big[-\frac{\hbar^2}{2m}\nabla^2 + \mathcal{U}(\boldsymbol{r}) + gn_o - \mu\Big]\sqrt{n_o}\hat{\phi} \tag{4.21}$$

$$-\hbar\frac{\partial}{\partial t}\Big(\sqrt{n_o}\hat{\phi}\Big) = \frac{1}{2}\Big[-\frac{\hbar^2}{2m}\nabla^2 + \mathcal{U}(\boldsymbol{r}) + 3gn_o - \mu\Big]\frac{\delta\hat{n}}{\sqrt{n_o}} \tag{4.22}$$

The solutions for the above equations (4.21)-(4.22) represent the elementary excitations and can be written in terms of $\delta\hat{n}$ and $\nabla\hat{\phi}$ as follows

$$\delta\hat{n}(\boldsymbol{r}) = \sqrt{n_o(\boldsymbol{r})}\sum_j i\psi_j^-(\boldsymbol{r})e^{-i\varepsilon_j t/\hbar}\hat{a}_j + H.c. \tag{4.23}$$

$$\hat{\phi}(\boldsymbol{r}) = \frac{1}{\sqrt{4n_o(\boldsymbol{r})}}\sum_j i\psi_j^+(\boldsymbol{r})e^{-i\varepsilon_j t/\hbar}\hat{a}_j + H.c. \tag{4.24}$$

Thus we can write the Bogolyubov approximation for the eigenenergies $\varepsilon_j$ and the eigenfunctions $\psi_j^{\pm}$ as follows

$$\begin{bmatrix} \left(-\frac{\hbar^2}{2m}\nabla^2 + \mathcal{U}(\boldsymbol{r}) + gn_o - \mu\right) & -\varepsilon_j \\ -\varepsilon_j & \left(-\frac{\hbar^2}{2m}\nabla^2 + \mathcal{U}(\boldsymbol{r}) + 3gn_o - \mu\right) \end{bmatrix} \begin{pmatrix} \psi_j^+ \\ \psi_j^- \end{pmatrix} = \begin{pmatrix} 0 \\ 0 \end{pmatrix} \tag{4.25}$$

The functions $\psi_j^{\pm}$ are related to the well-known Bogolyubov functions $u$ and $v$ as $\psi^{\pm} = u \pm v$. We arrive at the following crucial conclusions

- *The Bogolyubov spectrum of the excitation is not related to the presence or the absence of a true condensate for small density fluctuations [92].*
- *Magnetic lattice sites show small densities; therefore it is applicable to use the Bogolyubov approximations.*

## 4.3 The Quantum Degenerate Gases Simulator of Condensed Matter Systems

The macroscopic quantum phase signature exhibited by quantum degenerate gases at low temperature, such as Bose-Einstein condensates (BECs), has remarkably presented a detectable inherited coherence [203]. Such existing macroscopically pronounced quantum coherence has triggered an intensive search to identify critical phase transitions. Consequently, it is now feasible to detect the interference patterns, i.e. accessible interference fringes of overlapped quantum degenerate gases [204][205][206]. The coherent coupling allowed close investigations of strongly interacting condensates using traditional spectroscopic techniques, such as Bragg spectroscopy [207]. The macroscopic quantum phase is also used to classically map the rich interacting nature of weakly coupled reservoirs of ultracold quantum degenerate gases, e.g. BECs in double wells [203][208]. An environment with such signature provides a unique analogy to condensed matter systems with a capability to adiabatically control critical phase transitions, such as superconductivity [209] and superfluidity [210]. This made it possible to simulate a diverse range of interesting phenomena, for example the Josephson effect [211][212], the de Broglie wave interference [204] and Feshbach resonance [215] . The essential underlying physics of the macroscopic finger print in such systems can be understood by studying a simplified model of a double potential well BEC with an adiabatically controlled barrier height using the well known quantum two-mode approximation, i.e. the Bose-Hubbard model [213][214].

### 4.3.1 Bose-Hubbard model and the macroscopic quantum phase

Due to the tight magnetic confinement of the lattice sites there are several quantum energy levels available in each site allowing the *two-state approximation* to be considered for studying the number occupations, the spin-spin interaction of the trapped quantum particles and above all to create qubits for quantum information processing. We ignore in our approximation the higher energy levels of each site [93] and describe our system by considering the two-level quantum system configuration where at each individual $i$-th site there is a vibrational ground state $\phi_i^g$ and vibrational excited state $\phi_i^e$, where $i \in \{1, 2, ..., n\}$ is the site index starting from the center site. These two modes are in a linear superposition when we adiabatically induce the tunneling, and hence the interaction, between each two adjacent sites that exist in two different adjacent magnetic bands. Such a superposition describes the many Schrödinger cat-state which can be written, for simplicity, as one-directional transitions.

For the $n \times n$ asymmetric magnetic lattice with $n$ magnetic bands and no tunneling between sites, i.e. the case of uncoupled magnetic bands, the individual lattice site $i$ of the two energy levels $k \in \{0, 1\}$ allows a localized single wave function of the condensate to be in the ground state, taking the form

$$\phi_i^{[k,m]}(\mathbf{x} - \mathbf{x}_i) = \langle \mathbf{x} | i, k, m \rangle \tag{4.26}$$

which can be approximated by the eigenfunction of an isotropic simple harmonic oscillator. The superscript $m$ accounts for the quanta of angular momentum in the $z$-direction, where the value of the index $m$ depends on the value of $k$ such that for $k = 0$ there is no angular momentum $m = 0$ and for $k = 1$ $m \in \{-1, 0, 1\}$ in the three dimensions [97][98]. In the following, we give a general description for the Hamiltonian and the state vectors in such a way that it can also be used to describe a spinor Bose-Einstein condensate or ultracold fermions. The coupling is between the $i$-th site ground state and the $(i + 1)$-th excited state and the one-directional transition can be generalized to describe the superposition of all sites in the two-dimensional magnetic lattice.

We consider the two lowest energy states, $\phi_i^g$ and $\phi_i^e$, in each individual potential well (site), are closely spaced and sufficiently separated from the other higher levels within the well, permitting the two-mode approximation of the many-body problem in our proposed magnetic lattice [94]. The Bose-Hubbard model describes the bosons-bosons interaction of the on-site, or the self-trapped ultracold quantum particles, and intra-site tunneling process [95]. The general second-quantized Hamiltonian, in terms of the bosonic creation field operator $\widehat{\Phi}^\dagger(\mathbf{x})$ and the bosonic annihilation field operator $\widehat{\Phi}(\mathbf{x})$, with $\mathbf{x} \in \{x, y, z\}$, for a system of $N$ interacting bosons of mass $m$ confined by an external time varying magnetic field $B(\mathbf{x}, t)$ at zero temperature is given by

$$\begin{aligned}\widehat{H} = \sum_{i\neq j} \int d^3\mathbf{x}\widehat{\Phi}_i^\dagger(\mathbf{x})\Big[-\frac{\hbar^2}{2m}\nabla^2 + B(\mathbf{x},t)\Big]\widehat{\Phi}_i(\mathbf{x}) + \\ + \sum_i^n \int d^3\mathbf{x}\, d^3\acute{\mathbf{x}}\, \widehat{\Phi}_i^\dagger(\mathbf{x})\widehat{\Phi}_{i+1}^\dagger(\acute{\mathbf{x}})U_{i,i+1}(\mathbf{x},\acute{\mathbf{x}})\widehat{\Phi}_{i+1}(\acute{\mathbf{x}})\widehat{\Phi}_i(\mathbf{x})\end{aligned} \tag{4.27}$$

where

$$\widehat{\Phi}(\mathbf{x}) = \sum_{i=1}^n \widehat{a}_i \phi_i(\mathbf{x}), \qquad \widehat{\Phi}^\dagger(\mathbf{x}) = \sum_{i=1}^n \widehat{a}_i^\dagger \phi_i^*(\mathbf{x}) \tag{4.28}$$

The trapped cold particles tunnel, through a quantum cold collision process, within the usual $s$-wave scattering length, $a_s$, described by the interaction potential $U_{i,i+1}(\mathbf{x}, \acute{\mathbf{x}})$ in the second term of the above Hamiltonian, equation (4.27), such that

$$U_{i,i+1}(\mathbf{x},\acute{\mathbf{x}}) = g\int d\mathbf{x} \mid \phi_i^g(\mathbf{x}) \mid^2 \mid \phi_{i+1}^e(\acute{\mathbf{x}}) \mid^2 \longrightarrow \frac{4\pi\hbar^2 a_s^{i,i+1}}{m}\delta^4(\mathbf{x}-\acute{\mathbf{x}}) \tag{4.29}$$

which reduces to the coupling strength $g$ between the two states $\phi_i^g$ and $\phi_{i+1}^e$, in the $s$-wave scattering range. When tunneling is allowed, the coupling between the two modes is described by rewriting the Hamiltonian for the Bose-Hubbard model (4.27) in terms of the hopping (tunneling) strength $J_{i,i+1}(\mathbf{x},\acute{\mathbf{x}})$ between the adjacent magnetic bands in which case the tunneling of the ultracold particles between the sites is also affected by the tilting magnetic field $\delta B$.

The lowest mode $\phi_i^{[0,m]}$ is essentially symmetric and the second mode $\phi_i^{[1,m]}$ is antisymmetric, due to the initially tilted $n$ potential wells, the tunneling of the condensate causes a superposition of the higher magnetic band ground state mode $\phi_i^{[0,m]}$ and the adjacent lowest band excited mode, $\phi_j^{[1,m]}$. The superposition amplitude strongly depends on the spatial separation of the wells which is determined by $\alpha_s$ where $\Delta B^i = B^i_{max} - B^i_{min} \approx \alpha^2/2$ [99].

Dynamically interacting bosonic cold atoms in $n$ potential wells with tight $B(\mathbf{x})$ magnetic field confinement can be described by generalizing, for $n$ sites, the *quantized Josephson* or a *two-mode Bose-Hubbard Hamiltonian*. Assuming that the site number distribution starts from the center of the magnetic lattice, then one can write the above Hamiltonian in equation (4.27) as follows

$$\begin{aligned}\widehat{H}_{BH} = &-\sum_{j\neq i=1}^{n} J_{i,j}^{[k,m]}\Big(\widehat{\mathbf{b}}_i^{\dagger}\widehat{\mathbf{b}}_j + \widehat{\mathbf{b}}_j^{\dagger}\widehat{\mathbf{b}}_i\Big) + \sum_{j\neq i=1}^{n}\frac{U_{i,j}^{[k,m]}}{2}\Big(\widehat{\mathbf{n}}_i[\widehat{\mathbf{n}}_i-1] + \widehat{\mathbf{n}}_j[\widehat{\mathbf{n}}_j-1]\Big) + \\ &+\delta B\sum_{i\neq j}\Big(\widehat{\mathbf{b}}_i^{\dagger[k,m]}\widehat{\mathbf{b}}_j^{[k',m]} + \widehat{\mathbf{b}}_j^{\dagger[k',m]}\widehat{\mathbf{b}}_i^{[k,m]}\Big), \qquad k\neq k'\in\{0,1\}\end{aligned} \tag{4.30}$$

where $\hat{\mathbf{b}}_{i,j}^{\dagger}$ and $\hat{\mathbf{b}}_{i,j}$ are the bosonic creation and annihilation operators obeying the canonical commutation rules, $\hat{n}_{i,j} = \hat{\mathbf{b}}_{i,j}^{\dagger}\hat{\mathbf{b}}_{i,j}$ is the boson number operator and $\delta B$ is the amount of tilt in the magnetic potential. $J_{i,j}^{[k,m]}$ and $U_{i,j}^{[k,m]}$ are the tunneling and the inter-lattice site boson-boson interaction parameters, respectively, defined as

$$J_{i,i+1}^{[k,m]}(\mathbf{x},\acute{\mathbf{x}}) = \int d\mathbf{x}\phi_{i,i+1}^{*[k,m]}(\mathbf{x}-\acute{\mathbf{x}})\left[\frac{\hbar^2}{2m}\nabla^2 + B(\mathbf{x},t)\right]\phi_{i,i+1}^{[k,m]}(\mathbf{x}-\acute{\mathbf{x}}) \tag{4.31}$$

$$U_{i,i+1}^{[k,m]}(\mathbf{x},\acute{\mathbf{x}}) = \frac{3g}{8}\int d\mathbf{x} \mid \phi_{i,j}^{[0,0]}(\mathbf{x}-\acute{\mathbf{x}}) \mid^4 \tag{4.32}$$

When $\delta B = 0$ the Bose-Hubbard Hamiltonian describes the noninteracting magnetic bands where the condensate is assumed to occupy the ground state $\phi_{i,i+1}^{[0,0]}$ of an individual lattice site in each magnetic band with a single-mode one-level configuration regardless of the existence of the excited mode. This is because the no-tunneling condition results in inter-site many boson interaction which creates a lattice structure described in the Fock regime.

Using the Hamiltonian (4.30), we can describe two well known regimes formed in this type of magnetic lattice [96], as schematically represented in Figure (4.1):

- *In case of self-trapping, where the condition $U_{i,i+1} \gg J_{i,i+1}$ holds, the ground state $\phi_i^g$ of each site is assumed to be equally occupied by a certain number of cold atoms or a single atom. The self-trapping in the lattice can be addressed in the Fock regime in which case its ground state is the Mott insulator state.*

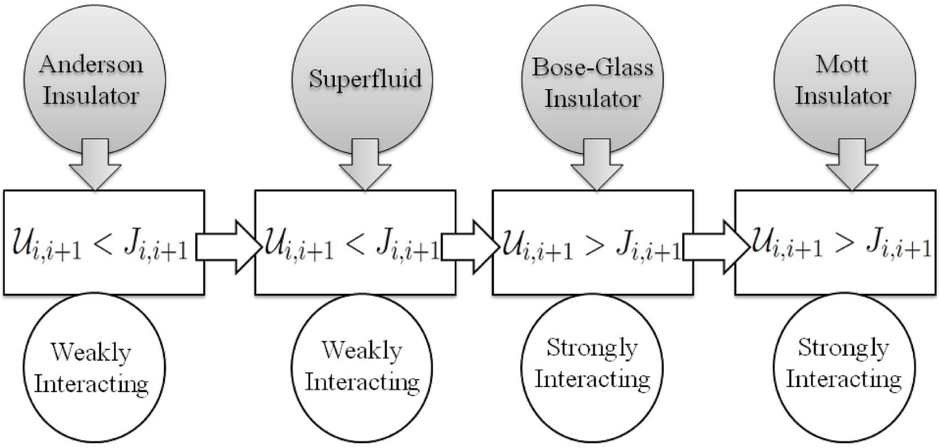

***Figure 4.1:*** (a) Schematic representation describes the possible interacting pictures depending on the relation between the interaction potential $U_{i,i+1}$ and the tunneling parameter $J_{i,i+1}$. As explained in the text, the phase transition is also a function of these two parameters where it spans from an Anderson insulator to a Mott insulator transition phase.

- ○ *Tunneling is allowed when the condition $U_{i,i+1} \ll J_{i,i+1}$ is met. In the case of magnetic lattice the scenario is similar to an optical lattices where the hopping strength $J_{i.i+1}$ is adiabatically controlled via the application of an external magnetic bias field, such as $B_{z-bias}$ applied along the negative direction of the $z$-axis. It is known as the Josephson regime because the tunneling of cold atoms between sites simulates the induced Josephson current (both $ac$ and $dc$ can be simulated) with adiabatically controlled flow as will be explained in the following section.*

Since our attention is limited to the adiabatically induced transition process, we only summarize the case where the trapped ultracold atoms exhibit a superposition between the vibrational ground state $\phi_i^{[0,m]}$ of a localized quantum well in the magnetic band $i$ and the vibrational excited state $\phi_j^{[1,m]}$ of a quantum well localized in the magnetic band $j$.

### 4.3.2 Josephson oscillations and the exciton Mott phase transitions

The two well known regimes, the Josephson regime and the Fock regime can be considered in our approach as a description to the outcome of the tunneling process of the trapped ultracold atoms [100]. Regardless of the asymmetrical effect in the two-dimensional magnetic lattice, one can still describe the transitions between the lattice sites as an induced Josephson current, i.e. the *superfluid phase transition*, between two states recognized as the Mott insulator state and the discharging Josephson state in which case the *adiabatically controlled Josephson current oscillation* depends on the coupling values. In the followings, we briefly describe the required conditions for such transitions.

- ***Mott Insulator State***

In the non-interacting regime where the first-mode $\phi_{i,j}^{[0,m]}$ is regarded as the ground state and as a solution for the Schrödinger equation with negligible inter-site interactions regardless of the existence of the excited mode $\phi_{i,j}^{[1,m]}$ , the condensate is said to have an individual mode solution of the form $\phi_{i,j}^{g} = \phi_{i,j}^{[0,m]}(\mathbf{x} - \acute{\mathbf{x}})$ [93]. Initially, there is an approximately equal number of atoms in each site $N_s \approx N/n$, where this number is fixed until the tunneling is allowed. The atoms are completely localized at the lattice site where we assume that the coupling strength between the two levels is very weak such that

$$N_s \mid U^{[0,0]}_{i,i+1}(\mathbf{x}, \acute{\mathbf{x}}) \mid \ll \Delta E^{[k,m]}_{i,i+1} = 2\Big[E^{[1,m]}_{i,i+1} - E^{[0,m]}_{i,i+1}\Big] = \hbar m \tag{4.33}$$

where $\Delta E^{[k,m]}_{i,i+1}$ is the energy difference. Localization in our scenario means that the first symmetric mode $\phi^{g}_{i,j}$ is dominating over all lattice sites and the expansion of the excited mode $\phi^{e}_{i,j}$ between each two adjacent magnetic bands is negligible. This condition can be thought of as the Fock regime where the on-site interaction is greater than the hopping strength $U^{[0,m]}_{i} \leftrightarrow U^{[1,m]}_{i} \gg J^{[0\to 1,m]}_{i\leftrightarrow j}$. This is a signature of the Mott insulator where all particles are localized in the ground state, with a negligible excited level, and a defined number of atoms at each site exhibiting no coherence or a macroscopic wavefunction. It permits a one-level approximation and a one-level Bose-Hubbard Hamiltonian for the $n \times n$ asymmetric magnetic lattice of the form

$$\widehat{H}_{1BH} = -\sum_{j\neq i=1}^{n} J^{[0,0]}_{i,j}\Big(\widehat{\mathbf{b}}^{\dagger}_{i}\widehat{\mathbf{b}}_{j} + \widehat{\mathbf{b}}^{\dagger}_{j}\widehat{\mathbf{b}}_{i}\Big) + \sum_{j\neq i=1}^{n} \frac{U^{[0,0]}_{i,j}}{2}\Big(\widehat{\mathbf{n}}_{i}[\widehat{\mathbf{n}}_{i} - 1] + \widehat{\mathbf{n}}_{j}[\widehat{\mathbf{n}}_{j} - 1]\Big) \tag{4.34}$$

where $\delta B = 0$ and $\widehat{H}_{1BH}$ describes a finite number of sites. In the case of an infinite number of sites, equation (4.34) describes the single-band Bose-Hubbard Hamiltonian for weakly interacting bosons in the symmetric magnetic lattice, i.e. $\widehat{H}_{1BH} \to \widehat{H}_{BH}$. Note that the operators $\widehat{\mathbf{b}}^{\dagger}_{i,j}$, $\widehat{\mathbf{b}}_{i,j}$ and $\widehat{\mathbf{n}}_{i,j}$ are for the case of $k = m = 0$. The Fock space state vector takes the form

$$|\phi\rangle = \sum_{n_i,j=0}^{N+1} c^{[0,0]}_{i,j}|\widehat{\mathbf{n}}_{i}, \widehat{\mathbf{n}}_{j}\rangle \tag{4.35}$$

Here the size of the Hilbert space is roughly estimated to $(N + 1)$ and $c^{[0,0]}_{i,j}$ represents the ground state amplitude.

- ***Exciton Mott Quantum Phase Transition via the Induced Josephson Atomic Current***

The situation where the hopping strength is adiabatically increased can typically be described using the self-consistent nonlinear Schrödinger equation, i.e. the Gross-Pitaevskii equation (4.14)

$$i\hbar\frac{\partial}{\partial t}\phi_i(\boldsymbol{x}, t) = \Big[-\frac{\hbar^2}{2m}\nabla^2 + B(\boldsymbol{x}, t) + g||\Psi(\boldsymbol{x}, t)\,||^2\,\Big]\phi_i(\boldsymbol{x}, t) \tag{4.36}$$

which represents the nonlinear generalization of the *sinusoidal Josephson oscillation* which occurs in superconducting junctions, described in some detail in [92, 95, 100, 101]. It also allows the scenario of the generalized tunneling mechanisms of the condensate between two sites to be applied to the $n$ asymmetric magnetic bands where the field operator is expanded in terms of the static ground state solution $\phi^{g}_{i/j}$ of the GPE equation (4.36) for each individual uncoupled lattice site, and in terms of the amplitude of the relative population $N_s \equiv N^{s}_{i/j}$ expressed as $\psi_{i/j}(\boldsymbol{x}, t) = \sqrt{N^{s}_{i/j}}e^{\theta_{i/j}(t)}$, where $\theta_{i/j}(t)$ is the corresponding phase in the lattice site $i$ or $j$ [102]. Thus, we expand the field operator as

$$\phi_{i/j}(\boldsymbol{x}, t) = \sqrt{N}\sum_{i/j=1}^{n}\psi_{i/j}(\boldsymbol{x}, t)\phi^{g}_{i/j} \tag{4.37}$$

Hence the evolution of the ultracold atoms' population $N_i^s(t)$ of the $n$ sites can be obtain by integrating over the spacial distributions $\phi_{i/j}(\boldsymbol{x}, t)$ to get the following time dependent equation

$$i\hbar \frac{\partial}{\partial t}\psi_i(\boldsymbol{x}, t) = \Big[\Omega_{i,j}(\boldsymbol{x}, t) + U_{i,j}^{[0,m]} N \mid \psi_i \mid^2 \Big]\psi_i(\boldsymbol{x}, t) - \sum_{i \neq j}^{n} J_{i,j}^{[0,m]}(\boldsymbol{x}, t)\psi_j \tag{4.38}$$

where

$$\Omega_{i,j}(\boldsymbol{x}, t) = \int d\boldsymbol{x} \Big[\frac{\hbar^2}{2m} \mid \nabla \phi_{i/j}^{*g} \mid^2 + \phi_{i/j}^{*g} B(\boldsymbol{x}, t) \phi_{i/j}^{g}\Big] \tag{4.39}$$

Equation (4.38) is well known as the *Bose Josephson junction* (**BJJ**) tunneling equation which can be re-derived in terms of the phase differences and the fractional population differences between the lattice $n$ sites. A similar case of a double well is discussed in [93]. The transition from self-trapping to Josephson oscillating states [103, 104] is possible in this type of asymmetrical magnetic lattice having several uncoupled magnetic bands which can be coupled via the induced Josephson current or it can be described as a *Josephson discharging state* created via quantum cold collisions, as described in the following section.

The quantum state of the asymmetrical magnetic lattice at this point of transition belongs to the so-called Josephson regime, where the on-site (inter-well) many boson interaction of the two energy states $k = 0$ and $k = 1$ is very small compared to the on-site many boson interaction which is described by the condition

$$U_{i,i+1}^{[0,m]}(\mathbf{x}, \acute{\mathbf{x}}) \leftrightarrow U_{i,i+1}^{[1,m]}(\mathbf{x}, \acute{\mathbf{x}}) \ll J_{i \leftrightarrow j}^{[0 \to 1,m]} \tag{4.40}$$

The dominant transition at the critical number of atoms is the *$n$ magnetic band one-directional Josephson transition* $\phi_i^{[0,m]} \to \phi_i^{[1,m]}$. Oscillating bound states will be created in both situations in and between sites leading to exciton Mott multiple transitions. The on-site bound state is created between the ground state and the excited state, e.g. two different components of a spinor BEC trapped in a single site. This is due to the dipole interaction which occurs when the condensate in the excited state periodically couples to the oscillating ground state at each individual site. The number of atoms may play an important role in such a scenario where it might be required to have an equal number of atoms in both modes. The fragmented condensate in the ground state of each site couples periodically via the Coulomb potential to the excited state in the neighboring site exhibiting a recombination rate between two different adjacent magnetic bands with plasma oscillation frequency relative to the strength of the Coulomb interaction which is experimentally realized in a *single bosonic Josephson junction* [104]. This can also be thought of as a difference in the chemical potential between sites in the case of trapped ultracold fermions.

### 4.3.3 Adiabatically oscillating Josephson discharging state

As previously detailed, the transition from self-trapping to Josephson oscillating states occurs in this type of asymmetrical magnetic lattice when several magnetic bands are instantly coupled via the *induced Josephson current* in which case the transition state, created via quantum cold collisions, is described as the *Josephson discharging states*.

It is possible to simulate this effect by studying the physics of the Josephson junctions in the same scenario as before where we regarded the $n$-weakly coupled macroscopic wavefunctions of the $n$ lattice sites to be separated by a magnetic potential barrier $\Delta B$ with a barrier hight given by

$$\Delta B^i = B^i_{max} - B^i_{min} = \frac{\alpha_s^2}{2} \tag{4.41}$$

the holes' separation is estimated to be $\alpha_s = \frac{\hbar^2}{M\kappa}$, where $\kappa$ is a function of the trap frequency $\omega_t$ and defined as $\kappa = \hbar/2M\omega_t$. The local mode states $\varphi_i(\mathbf{x}, t)$ are Gaussian and hence enables solving the self-consistent nonlinear Schrödinger equation ( the GPE) [105]. The transition from self-trapping to Josephson oscillation is described by the GPE (4.36)

$$i\hbar \frac{\partial \varphi_i(\mathbf{x}, t)}{\partial t} = \left[ -\frac{\hbar^2}{2M} \bigtriangledown^2 + \mathbf{B}(\mathbf{x}, t) + g \mid\mid \varphi_i(\mathbf{x}, t) \mid\mid^2 \right] \varphi_i(\mathbf{x}, t) \tag{4.42}$$

The process is a purely weakly interacting system in the $s$-wave scattering range governed by the inter-atomic scattering pseudo potential $g = \frac{4\pi\hbar^2 a_s}{M}$ of scattering length $a_s$. The set of $n$ equations in (4.42) represent the nonlinear generalization of the sinusoidal Josephson oscillations occurring in superconducting junctions [106]. The Gaussian states have uniform amplitudes $\varphi_i(\mathbf{x}, t) = \sqrt{N_i} e^i \theta_i$, where $N_i$ and $\theta_i$ are the number of cold quantum particles and the phase in each individual lattice site, respectively. We introduce the phase difference $\zeta_i = \theta_i - \theta_{i+1}$ and the fractional population $-1 < \gamma = \sum_i^n (N_i - N_{i+1})/N < 1$, with $N$ is the total number of cold atoms, to write the $n$ Gross-Pitaevskii equations in terms of the $\zeta$ and $\gamma$ as follows

$$\dot{\gamma}(\mathbf{B}, t) = -\sqrt{1-\gamma^2} \sin(\zeta(\mathbf{B}, t)) \tag{4.43}$$

$$\dot{\zeta}(\mathbf{B}, t) = \chi\gamma + \frac{\gamma(\mathbf{B}, t)}{\sqrt{1-\gamma^2(\mathbf{B}, t)}} \cos(\zeta(\mathbf{B}, t)) + \left[ J_1 - J_{i+1} \right] \tag{4.44}$$

where $\chi = N^2 U/4K$, and $U$ is as defined in equation (4.29) and $K$ is defined as follows

$$K = -\int d\mathbf{x} \left[ \frac{\hbar^2}{2M} \prod_{i=1}^{n} \bigtriangledown \phi_i + \mathbf{B}(\mathbf{x}, t) \prod_{i=1}^{n} \phi_i \right] \tag{4.45}$$

The above set of equations (4.43) to (4.44) represent the nonlinear generalization of the *sinusoidal Josephson oscillations* in the $n$ sites of the asymmetric magnetic lattice similar to superconducting junctions in which case a simple mechanical analogue can be mapped to describe the system as a non-rigid pendulum.

Based on the above facts, at a critical phase difference and fractional population the system maintains the Josephson oscillation between the *self-trapping* and *Josephson discharging state*, where the discharging current represented as a superconducting state induced by the tunneled quantum particles which is known as *plasma oscillations* and was experimentally realized in [104]. An interesting different dynamical phenomenon arises if the initial population imbalance is not equal to the critical value. We simulate this effect in section (4.4.2).

By setting (via fabrication) the relevant value of $\alpha_s$, one can induce the $dc$ Josephson current adiabatically between the lattice site by applying a $B_{\text{z-bias}}$. Ultracold atoms tunnel between sites starting from the center of the magnetic lattice to the edges due to the variation of the magnetic values of $B_{\text{min}}$ between magnetic bands. Higher values of $B_{\text{min}}$ exist at the center.

### 4.3.4 First Brillouin zone dimensionality and Bloch interacting wavefunctions

The number of sites $n$ has a special feature in the asymmetric two-dimensional $n \times n$ magnetic lattice. When $n$ is odd, $n = 3, 5, 7...$, only one center site is created and screened by the surrounding four sites taking a molecule-like configuration, as depicted in Figure 4.2(a). If

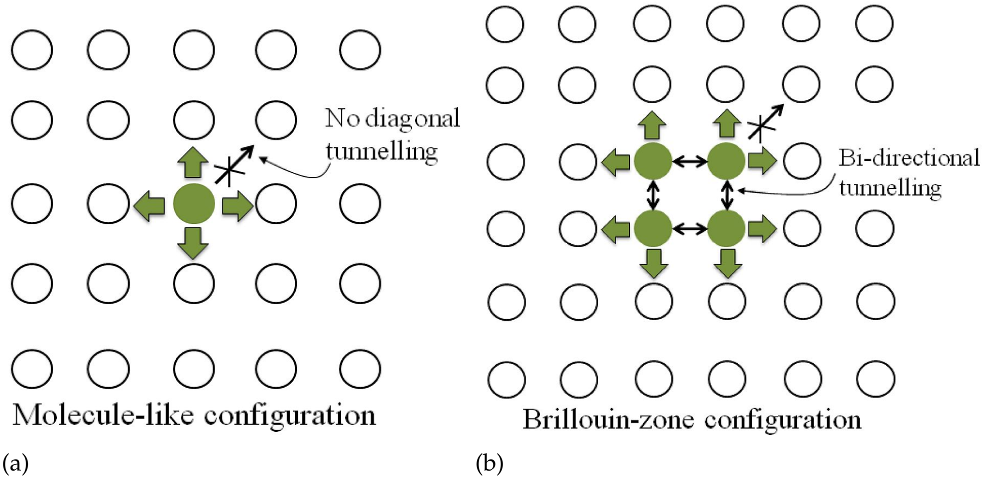

***Figure 4.2:*** (a) Schematic representation of a magnetic lattice with an odd number of sites (odd magnetic lattice). In the case of $n$ taking an odd value there is only one center site linked to the surrounding sites and it has a molecule-like configuration. (b) $n$ takes an even value (even magnetic lattice) where there are always 4 sites at the center of the asymmetrical magnetic lattice. The 4 sites are symmetric and tunneling between them is critical due to this symmetry.

the coupling between these sites is equal, $J_1 \equiv J^x_{1,2} = J^x_{1,-2} = J^y_{1,2} = J^y_{1,-2}$, this creates a binding potential between the center site and the other four sites.

In the case of an even number of sites, $n = 2, 4, 6, ...$, there are always four symmetrical sites in the center of the magnetic lattice as schematically represented in Figure 4.2(b). They exhibit a first Brillouin zone dimensionality and hence have Bloch interacting wavefunctions with the field operator expanded in terms of the localized single-particle wave functions taking the following form

$$\widehat{\Phi}(\mathbf{x}) = \sum_{i=1}^{4} \widehat{a}_i^\kappa \phi_1^\kappa(\mathbf{x}) \tag{4.46}$$

$\phi_1^\kappa(\mathbf{x})$ is the Bloch wave function (the ground state mode of the four center sites, $\phi_1^g$) with $\kappa$ the wave vector in the first Brillouin zone [31]. Thus the tunneling mechanism between the four sites involves the standard eigenvalue problem

$$\left[ -\frac{\hbar^2}{2M} \nabla^2 + \Delta B(\mathbf{x}, t) \right] \phi_1^\kappa(\mathbf{x}) = E_1^\kappa(\mathbf{x})\phi_1^\kappa(\mathbf{x}) \longrightarrow J_1^\kappa \phi_1^\kappa(\mathbf{x}) = E_1^\kappa(\mathbf{x})\phi_1^\kappa(\mathbf{x}) \tag{4.47}$$

assuming that $\int d^3\mathbf{x} \phi_1^{*\kappa}(\mathbf{x})\phi_1^\kappa(\acute{\mathbf{x}}) \approx \delta(\mathbf{x} - \acute{\mathbf{x}})$. Clearly, there is no tilting magnetic potential between the four sites, $\delta B = 0$, and tunneling only occurs when the magnetic barriers, $\Delta B$, are minimized.

## 4.4 The Macroscopic Quantum Phase of Ultracold Degenerate Gases

- ***Overview***

The classical coherent mapping of the trapped low-dimensional quantum gases has enabled the simulation of several critical phase transitions of condensed matter systems such as the Mott-insulator-to-superfluid transition by using both trapped BECs and trapped ultracold fermionic gases. Integrating ultracold atoms with a magnetic microstructure and the creation of a Bose-Einstein condensate on-atom-chip have triggered an alternative approach to adiabatically inducing an identity for macroscopic quantum phases. In the following theoretical attempt we try to emphasize on the possibility of realizing the macroscopic quantum phase signature in this new type of magnetic traps.

### 4.4.1 Bosonic Josephson junctions in the two-dimensional magnetic lattice

The wavefunction $\varphi(\mathbf{x}, t)$ is used to roughly describe the *macroscopic* dynamical oscillations of weakly interacting condensates at low temperature trapped in magnetic lattice obeying the time-dependent Gross-Pitaevskii equation (GPE)

$$i\hbar\partial_t\varphi(\mathbf{x},t) = \Big[ - \frac{\hbar^2}{2m}\nabla^2 + U(\mathbf{x}) + g_o|\varphi(\mathbf{x},t)|^2 \Big]\varphi(\mathbf{x},t) \tag{4.48}$$

where $g_o = \frac{4\pi\hbar^2 a_s}{m}$ is the inter-atomic scattering pseudo potential with $a_s$ the s-wave scattering length and $m$ the particle mass. The external harmonic potential $U(\mathbf{x})$ is written as

$$U(\mathbf{x}) = \frac{1}{2}M \sum_{k\in\{x,y,z\}} \omega_k^2 k^2 + \delta z \tag{4.49}$$

where $\delta z$ determines the amount of tilt introduced in the potential $U(\mathbf{x})$ along the $z$-axis and $\omega_k$describes the trapping frequencies which are calculated using Equation (2.73) with the external magnetic field $B$ as described in Equation (3.13), with $k \in \{x, y, z\}$.

Since the two-dimensional magnetic lattice contains $n\times n$ sites then the interaction picture of the trapped BECs considers allowed tunneling between all sites in which case each single lattice site is connected to all four neighbor sites. However, for simplicity we consider in the present work the interaction between only two adjacent lattice sites. For two adjacent lattice sites, described as in section (4.3.2) by the Boson Josephson Junctions (BJJs) [106, 107], the system of time-dependent Schrödinger equations can be described by the following Hamiltonian matrix

$$\widehat{\mathcal{H}} = \begin{pmatrix} E_1^o + \Gamma_1 N_1 & -\Omega^J \\ -\Omega^J & E_2^o + \Gamma_2 N_2 \end{pmatrix} \tag{4.50}$$

where $E_{1,2}^o$ are the zero-point energies in each individual lattice site defined as

$$E_i^o = \int \Big[\frac{\hbar^2}{2M}|\nabla\varphi_i|^2 + |\varphi_i|^2 U(\mathbf{x})\Big] d\mathbf{x} \tag{4.51}$$

and the atomic self-interaction energy is determined by

$$\Gamma_i = g_o \int |\varphi_i|^4 d\mathbf{x} \tag{4.52}$$

and $\Omega^J$ describes the Josephson energy. Since Our interest is to identify the dynamical Josephson oscillations of the condensates in the weakly coupled sites of the magnetic lattice, we thus limit our attention to the localized time-dependent variational ansatz

$$\varphi(\mathbf{x},t) = c_1(t)\chi_1(\mathbf{x}) + c_2(t)\chi_2(\mathbf{x}) \tag{4.53}$$

with

$$c_{1,2}(t) = \sqrt{N_{1,2}(t)} e^{i\theta_{1,2}(t)} \tag{4.54}$$

and consider the total number of atoms between the adjacent sites $\mathcal{N} = N_1 + N_2 = |c_1|^2 + |c_2|^2$ to be constant. To define the spatial dependence of $\chi_{1,2}(\mathbf{x})$ we use the exact symmetric $\chi_+(\mathbf{x})$ and antisymmetric $\chi_-(\mathbf{x})$ stationary eigenstates of the GPE in which case $\chi_{1,2}(\mathbf{x})$ can be defined as follows

$$\chi_1(\mathbf{x}) = \frac{\chi_+(\mathbf{x}) + \chi_-(\mathbf{x})}{2} \tag{4.55}$$

$$\chi_2(\mathbf{x}) = \frac{\chi_+(\mathbf{x}) - \chi_-(\mathbf{x})}{2} \tag{4.56}$$

having both the orthogonality and the normalization conditions fulfilled. The wavefunctions are in a superposition state for the two adjacent sites ($1 \leftrightarrow 2$) and therefor we write the coupling Josephson energy as

$$\Omega^J \simeq -\int \Big[\frac{\hbar^2}{2M}(\nabla\varphi_1\nabla\varphi_2) + \varphi_1 U(\mathbf{x})\varphi_2\Big] d\mathbf{x} \tag{4.57}$$

which is analogous to the Josephson coupling energy in a Superconducting Josephson Junction [86][112][113].

Taking a two-component BEC as an example in which case the BEC is magnetically trapped and prepared in different hyperfine states, experimentally $\Omega^J$ can also describe driving such a system by a two-photon pulse in which $\Omega^J$ is regarded as the two-photon Rabi-like frequency with a coherence described by [108]

$$N_{12} = \int d\mathbf{x}\varphi_1^*(\mathbf{x})\varphi_2(\mathbf{x}) \tag{4.58}$$

Also, using the Hamiltonian in Equation (4.50) one can obtain the equation of motion for the populations as will be shown in the following section. This frame work can be generalized to include the interaction of $n \times n$ magnetic lattice sites; however the discussion here is limited to only two traps.

### 4.4.2 The dynamical Josephson oscillations and the Rabi-like oscillations

The general occupation and localized phases obey the following two-mode dynamical BJJs equations

$$i\hbar\partial_t c_1(t) = \big[E_1^o + \Gamma_1 N_1\big]c_1(t) - \Omega^J c_2(t) \tag{4.59}$$

$$i\hbar\partial_t c_2(t) = \big[E_2^o + \Gamma_2 N_2\big]c_2(t) - \Omega^J c_1(t) \tag{4.60}$$

where in the two-mode approximation of the quantum system the eigenstates are always symmetric with a large lifetime that scales exponentially with the populations imbalance. Therefore the ground state of the BJJs equations is a symmetric eigenfunction of the GPE and can describe the population oscillating imbalance [107][109].

The Dirac action principle leads to a classical expression of the system Hamiltonian for two variational parameters described as the fractional population at each lattice site

$$\widetilde{N}(t) = \frac{N_1(t) - N_2(t)}{\mathcal{N}} \tag{4.61}$$

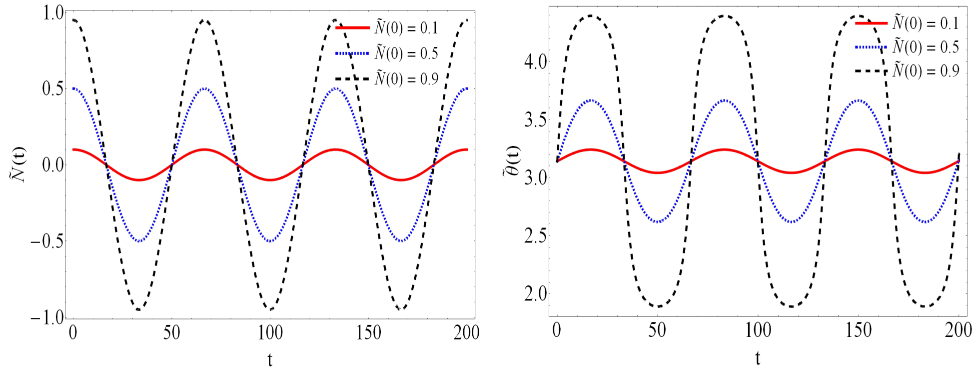

(a) (b)

***Figure 4.3:*** (a) Fractional population difference $\widetilde{N}(t)$ and (b) phase difference $\widetilde{\theta}(t)$ per site evaluated as a function of a rescaled time using different initial values of $\widetilde{N}(t)$ and a fixed initial value of $\widetilde{\theta}(0)$ = $\pi$. Lattice parameters are $\delta = 0$, $B_{\text{z-bias}}$ = 0, $\tau$ = 2 $\mu m$ and $\alpha_s = \alpha_h$ = 3.5 $\mu m$.

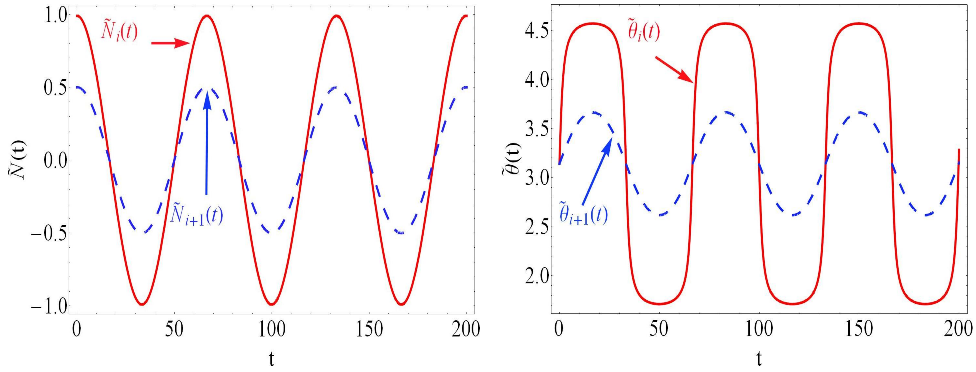

(a) (b)

***Figure 4.4:*** (a) $\widetilde{N}_i(t)$ and $\widetilde{\theta}_i(t)$ evaluated with time and (b) $\widetilde{N}_{i+1}(t)$ and $\widetilde{\theta}_{i+1}(t)$ with initial values for the ($i$)-site fractional population $\widetilde{N}_i(0)$ = 0.99 and for the ($i+1$)-site $\widetilde{N}_{i+1}(0)$ = 0.5, while the initial phase differences in both sites are equal, $\widetilde{\theta}_i(0) = \widetilde{\theta}_{i+1}(0) = \pi$. Lattice parameters are $\delta = 0$, $B_{\text{z-bias}}$ = 0, $\tau$ = 2 $\mu m$ and $\alpha_s = \alpha_h$ = 3.5 $\mu m$.

and the phase difference

$$\widetilde{\theta}(t) = \theta_1(t) - \theta_2(t) \tag{4.62}$$

where both variables are canonical conjugates [92]. The time-dependent variational two-mode approximation can be used to describe the interaction dynamics in this type of magnetic lattice where the set of trail wavefunctions $\chi_i(t)$ in the order parameter $\varphi(\mathbf{x}, t) = \sum_i^n c_i(t)\chi_i(\mathbf{x})$ span a subspace that constrains the system. Using the phase space conserved coordinates $c_1(t)$ and $c_2(t)$, where $|c_1(t)|^2 + |c_2(t)|^2 = 1$, one realizes that the two variational parameters $\widetilde{N}(t)$ and $\widetilde{\theta}(t)$ are actually the principal variables of the following Hamiltonian in the non-interacting limit

$$\widehat{\mathcal{H}}(\widetilde{N}, \widetilde{\theta}) = E^o + \Omega^J \sqrt{1 - \widetilde{N}^2} \cos\widetilde{\theta} \tag{4.63}$$

where we considered the inter-atomic interactions to be negligible compared to the coupling Josephson energy, i.e. $\Gamma_{1,2} \ll \Omega^J$.

Energy conservation per particle implies that the dynamics of the system is governed by a system of coupled equations which interestingly yields, for an exact solution, a *Rabi-like oscillation*. Thus the system of coupled time-dependent differential equations in the non-interacting limit can be written as[4]

$$\dot{\widetilde{N}} \equiv \partial_{\widetilde{\theta}} \widehat{\mathcal{H}}(\widetilde{N}, \widetilde{\theta}) = \frac{2\Omega^J}{\hbar} \sqrt{1 - \widetilde{N}^2} \sin(\widetilde{\theta}) \tag{4.64}$$

$$\dot{\widetilde{\theta}} \equiv \partial_{\widetilde{N}} \widehat{\mathcal{H}}(\widetilde{N}, \widetilde{\theta}) = \frac{-2\Omega^J}{\hbar} \frac{\widetilde{N}}{\sqrt{1 - \widetilde{N}^2}} \cos(\widetilde{\theta}) \tag{4.65}$$

This system is solved for $\widetilde{N}(t)$ and $\widetilde{\theta}(t)$, with a rescaled time $t \rightarrow \frac{2t}{\hbar}\Omega^J$, in which case the results indicate coherent oscillations in the asymmetrical two-dimensional magnetic lattice and can be identified as the dynamical Josephson oscillations [110]. Figures 4.3(a,b) show the oscillated modes $\widetilde{N}_i(t)$ and $\widetilde{\theta}_i(t)$ per site for different initial values. The oscillating fractional occupations $\widetilde{N}_{i,i+1}(t)$ and the phase amplitudes $\widetilde{\theta}_{i,i+1}(t)$ are shown in Figures 4.4(a,b), respectively, with initial conditions $\widetilde{N}_i(0) = 0.99$, $\widetilde{N}_{i+1}(0) = 0.5$ and $\widetilde{\theta}_i(0) = \widetilde{\theta}_{i+1}(0) = \pi$.

To conclude, an adiabatic Josephson effect may also be realized in this type of magnetic lattice arising from the superfluidity nature of the trapped condensates when tunneling between the lattice sites [111]. Moreover, these oscillations, with a frequency $\omega_R \approx |\Omega^J_{i,i+1}|$, are similar to the dynamical oscillations of single atoms.

---

[4] Here $\partial_{\widetilde{\theta}}$ represents $\frac{\partial}{\partial \widetilde{\theta}}$.

Chapter 5

# QUANTUM COMPUTING WITH ULTRACOLD DEGENERATE GASES

> ¶ *I want to build a billion tiny factories, models of each other, which are manufacturing simultaneously ... The principles of physics, as far as I can see, do not speak against the possibility of maneuvering things atom by atom. It is not an attempt to violate any laws; it is something, in principle, that can be done; but in practice, it has not been done because we are too big.* ... (Richard P. Feynman)

## 5.1 Overview

QUANTUM computation is to device the quantum information in a scalable environment by being able to manipulate and access to their pure and mixed quantum states. Large scale quantum computer is still critical challenge due to several difficulties in controlling large quantum systems which consist of large number of qubits [115]. Ensemble of large number of qubits usually maintains large number of degrees of freedom in their systems's Hilbert complex spaces. Coherently entangling large number of qubits is a key element in fixing and minimizing the large degrees of freedom. Entanglement is an important step towards a nondemolition access to the internal state of the quantum system to encode or read out the qubit states [116]. Optically and magnetically trapped ultracold atoms, prepared in degenerate quantum gases, such as Bose-Einstein Condensate (BEC), have remarkably featured themselves to simulate quantum information [55][117].

There are various approaches to magnetically trap ultracold atoms at the micro-scale, such as current carrying wires and permanently magnetized material atomic traps [51] [54][74]. We adopted the approach of the permanent magnet traps for ultracold atoms where in this chapter we explain how to use our simple method to create the so called magnetic lattice with two different configurations. We also explain the tunneling mechanisms of ultracold atoms between their trapping lattice sites in order to form qubits ensembles. A method for entangling the ultracold atoms trapped in the two-dimensional magnetic lattice is briefly explained.

Long-range entanglement provides coherent coupling between many qubit quantum systems leading to the required long time of coherence to achieve a reasonable number of quantum computing operations. It is also considered as one of the big experimental and theoretical challenges in the field of quantum computing and quantum information processing and communication, where several proposals have been considered to demonstrate the possibility of long-range entanglement of many qubits. Most of these approaches exhibit mixed

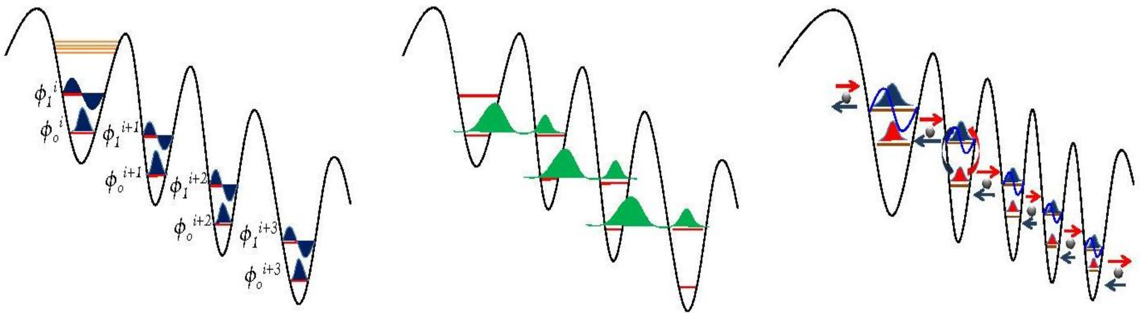

(a) (b) (c)

*Figure 5.1:* (a-b) Josephson current can be realized in the superposition state oscillating between adjacent sites. It is mainly an oscillating ground mode $\phi_i^g$ of the $i$th site to the excited mode $\phi_j^e$ of the adjacent $j$th site. (b-c) Schematic representation of the Josephson oscillation ($ac$ current) and the coupling of $n$-site qubits which can be formed simultaneously in the asymmetrical magnetic lattice using adiabatically induced Josephson oscillations, respectively.

states because of the coupling of the qubit pure quantum state to thermal states. Scaling and quantifying the degree of entanglement (entropy of entanglement) for a mixed state is not uniquely identified. However there are some theoretical frames considered to partially quantify the entanglement of composite quantum states, such as the entanglement distillation method. The crucial point in these approaches is to achieve the long-range entanglement with the lowest possible dimensions of the complex Hilbert space of the system, in particular the requirement for individual local control.

Based on these dynamical facts we propose a quantum device that is capable of providing a suitable environment for a long-range entangled multipartite system (many qubits). They can be created using trapped ultracold atoms in a discrete magnetic bands magnetic lattice where magnetically trapped ultracold atoms represent stable harmonic quantum systems. Atoms are decelerated by means of laser cooling and magnetic trapping and pumped into the so-called low magnetic field seeking state in which case the ultracold atoms tend to settle in the periodically distributed local magnetic minima iwhere they can eventually create degenerate quantum gases, such as Bose-Einstein Condensation and ultracold fermions.

♢ **Related publications to this Chapter:**

1 A. Abdelrahman, P. Hannaford, M. Vasiliev, and K. Alameh, *"Multipartite Entanglement in a Discrete Magnetic Bands Magnetic Lattice"*, Asia Communications and Photonics Conference and Exhibition (ACP) (2009).

2 A. Abdelrahmany, M. Vasiliev and K. Alameh, *"Qubit Formation and Entanglement of Ultracold Atoms Trapped in Two-Dimensional Magnetic Lattice"*, Postgraduate Symposium (PEECS) (2009).

## 5.2 Qubits Formation and Long Range Multipartite Entanglement

The realization of qubits formed using a Bose-Einstein condensate (qubit BEC) is proposed by using two BECs trapped in tilted double potential wells [114]. In order to formulate the qubit state in the case of trapped cold atoms in an asymmetric two-dimensional magnetic lattice, we expand the Heisenberg atomic field operator for the $n$-two localized modes. The

$n$ sites are individually symmetric regardless of the fact that they are asymmetrically distributed. Such an expansion can be written as

$$\widehat{\Phi}(\mathbf{x},t) = \sum_{i=1}^{n} \widehat{a}_i(t)\phi_i(\mathbf{x}-\acute{\mathbf{x}}) \tag{5.1}$$

with the creation $\widehat{a}_j^\dagger(t)$ and annihilation $\widehat{a}_i(t)$ operators satisfy the commutation relation

$$\Big[\widehat{a}_i(t), \widehat{a}_j^\dagger(t)\Big] = \delta_{ij} \tag{5.2}$$

and with

$$\int d^3\mathbf{x}\widehat{\Phi}_i^*(\mathbf{x})\widehat{\Phi}_j(\mathbf{x}) \approx \delta_{ij} \tag{5.3}$$

In a similar way to [114] we substitute the operator (7.1) in the following Hamiltonian (i.e. the Bose-Hubbard model in equation (4.27))

$$\begin{aligned}\widehat{H} = \sum_{i\neq j}\int d^3\mathbf{x}\widehat{\Phi}_i^\dagger(\mathbf{x})\Big[-\frac{\hbar^2}{2m}\bigtriangledown^2 + B(\mathbf{x},t)\Big]\widehat{\Phi}_i(\mathbf{x}) + \\ + \sum_{i}^{n}\int d^3\mathbf{x}d^3\acute{\mathbf{x}}\widehat{\Phi}_i^\dagger(\mathbf{x})\widehat{\Phi}_{i+1}^\dagger(\acute{\mathbf{x}})U_{i,i+1}(\mathbf{x},\acute{\mathbf{x}})\widehat{\Phi}_{i+1}(\acute{\mathbf{x}})\widehat{\Phi}_i(\mathbf{x})\end{aligned} \tag{5.4}$$

so as to write the Hamiltonian of the $n$-two local mode approximation in the following form

$$\widehat{H'} = \sum_{i\neq j}\Big(J_i\widehat{n}_i + J_j\widehat{n}_j\Big) + \sum_{i\neq j}\Big(\widehat{n}_i[\widehat{n}_i - 1] + \widehat{n}_j[\widehat{n}_j - 1]\Big) - \sum_{i\neq j}\Big(\chi\widehat{a}_i^\dagger\widehat{a}_j + \chi^*\widehat{a}_i\widehat{a}_j^\dagger\Big) \tag{5.5}$$

in which case we have ignored the tilting potential in this representation for simplicity and we define $\chi$ as

$$\chi = -\int d^3\mathbf{x}\Big[\frac{\hbar}{2M}\bigtriangledown\phi_i^*(\mathbf{x}).\bigtriangledown\phi_j(\mathbf{x}) + \mathbf{B}(\mathbf{x},t)\phi_i^*(\mathbf{x})\phi_j(\mathbf{x})\Big] \tag{5.6}$$

Since we are considering a one directional tunneling starting from the center sites, the situation is similar to $n$ adjacent double wells separated by a tilting potential. Considering the overall number of trapped cold atoms is conserved, it implies that one can work in a subspace of the form

$$\Big|\frac{m}{\kappa}\Big\rangle \equiv \bigotimes_{i\neq j}\Big|\frac{m_i}{\kappa}, N_s - \frac{m_j}{\kappa}\Big\rangle \tag{5.7}$$

where $N_s = \frac{N}{n}$ and $m_{i,j}$ are the total number of cold atoms in each individual well and the number of atoms left after tunneling in the $i$th (or the $j$th) potential well, respectively. $\kappa$ is the tunneled fraction of atoms with min$\{\kappa\} = 1$. Using this fact it is convenient to mention the following representation written in the above basis in equation (7.6)

$$\widehat{a}_i^\dagger\widehat{a}_j\Big|\frac{m_i}{\kappa}, N_s - \frac{m_j}{\kappa}\Big\rangle = \sqrt{\Big(\frac{m_i}{\kappa+1}\Big)\Big(N_s - \frac{m_j}{\kappa-1}\Big)}\Big|\frac{m}{\kappa+1}\Big\rangle \tag{5.8}$$

allowing us by that to rewrite the Hamiltonian in equation (5.5) in the following form

$$\widehat{H''} = \sum_{i\neq j} U_{i,j}\left[(\widehat{n}_i+\widehat{n}_j)-n_g\right] - nJ\sqrt{N_s(N_s+1)}\sum_{n}\left[\left|\frac{m}{\kappa+1}\right\rangle\left\langle\frac{m}{\kappa}\right| + \left|\frac{m}{\kappa}\right\rangle\left\langle\frac{m}{\kappa+1}\right|\right] \quad (5.9)$$

where $n_g$ is the gate charge [120]. Here one can realize two possible scenarios. The first implies a Mott insulator picture when the Hamiltonian in equation (7.8) is dominated by internal two-mode interactions in which case the charging energy is greater than the Josephson energy

$$U_{i,j} \gg nJ\sqrt{N_s(N_s+1)} \quad (5.10)$$

The second is the possibility of maintaining the $n \times n$ qubit state formed when the Josephson oscillation strongly mixes the two states $\mid m/\kappa\rangle$ and $\mid m/(\kappa+1)\rangle$, namely the two adjacent $i$th ground state modes and the $j$th excited modes, $\phi_i^g$ and $\phi_j^e$, respectively. A schematic representation is shown in Figure (7.1). One can interpret the physical behavior examined here of the connection of the $n$ sites via two types of Josephson currents, so that we can rename the two scenarios as the directional induced $ac$ and $dc$ Josephson currents. The slow flow of the current will transfer the qubits between the sites of the magnetic lattice and hence triggers the gate operations.

Adiabatic control of the tunneling permits a slow flow of the Josephson current which is a specific feature exhibited by the asymmetrical two-dimensional magnetic lattice. Maximal entanglement can be reached when the non-symmetric states $\mid m_i/\kappa, N_s - m_j/\kappa\rangle$ span the whole Fock space including the subspace of the center sites and hence a long-range entanglement can be addressed [118][119]. This is a typical case of a long-range entanglement environment where the one directional Josephson current connects all sites along the tunneling direction. This means qubits are adiabatically transfered from the center sites outward to the edge sites in this type of magnetic lattice, which is a significant feature that can be used in quantum informations processing. Another interesting feature to highlighted here is the possibility of $separably$ addressing quantum states to a subspace of the system, by encoding the center sites only which can be done by entangling the cold atoms in the center site to the environment using light.

### 5.2.1 The Long-range entanglement of multipartite system formed in the two - dimensional magnetic lattice

Ideally, long-range entanglement of several directly coupled qubits can be represented as interacting system chain of harmonic oscillators. A method of entanglement distillation is often used to indirectly quantify the many qubits entanglement; however, entanglement of mixed states is not yet identified. The mechanism we propose offers this feature by selectively assigning a quantum pure state to a specific number of lattice sites, such as creating maximally entangled Bell state pairs, and then dynamically allowing the system to evolve into the regime of long-range entangled multipartite as long as the sites are spatially well separated as required before implementing the entanglement. A smaller number of maximally entangled pairs (2 × 2) can symmetrically be created at the center of the (4 × 4) magnetic lattice. At this stage, the system is an uncoupled harmonic oscillator chain trapped in the indirectly coupled magnetic quantum wells (CMQWs).

To induce long-range entanglement , tunneling between the lattice sites must be allowed which can be done by minimizing the size of the magnetic energy band gap. The tunneling mechanism across the lattice site allows the spatially separated qubits to evolve into interacting multipartite formed in the indirectly CMQWs. It also allows a symmetrical distribution of BECs at the center ($m \times m$) sites through successive tunneling because the CMQWs at the center are symmetrically created. This key element allows minimum individual local control in directly entangled center qubits to the far long-range entangled qubits, where the system can be designed to allow ($n - m \times n - m$ ) sites.

Chapter 6

# MAGNETIC CONFINEMENT OF EXCITONS

## 6.1 Overview

> ¶ *Concepts that have proven useful in ordering things easily achieve such authority over us that we forget their earthly origins and accept them as unalterable givens.* ...
> (Albert Einstein, 1910)

THE magnetic field micro-confinement, is not only limited to trap atoms and accommodate a suitable environment for their phase transitions to a critical limit. In fact, it has a tremendous ability extends beyond the field of atomic physics; for example, the magnetic filed local minima can even be used to confine the bacteria for efficient biological analyses.

In the following experimental studies, we show a clear evidence for magnetically trapped virtual quantum particles, i.e. the magnetic micro-confinement of excitons. But before that, we briefly review related theoretical frames to describe the physics of the excitons and their interaction with external potential fields.

## 6.2 Wannier-Mott excitons

The statistical trend in solid state physics is to treat the ground state of an isolated system as a *quasi-vacuum* and to treat the units of the elementary excitations as *quasi-particles* that weakly interact with each other. More specifically, quasi-vacuum in semiconductor can be thought of as a state with both filled valence band and empty conduction band.

As briefly explained in the overview, exciton is considered as a quasi-particle that consists of an electron and a hole bounded by the Coulomb interaction. The excited *electron*, with negative charge $e^-$, transfers to the empty conduction band leaving behind a quasi-particle with a positive charge $e^+$ recognized as a *hole* the filled valence band with an *effective mass* defined by $-\left(\frac{\partial^2 E}{\partial p^2}\right)^{-1}$. The electron and the hole at a momentum that is close to zero, $p \sim 0$, interact with each other via the Coulomb potential in which case they form a bound pair of the two particles (i.e. composite particle) that defines the *exciton* similar to that of the hydrogen atom. Another reason of this analogue is that the exciton has an envelope wavefunction similar to the hydrogen atom envelop wavefunction, but due to the strong dielectric screening (Coulomb screening) plus the small effective mass ratio of the hole to the electron, the binding energy of an exciton is three orders of magnitude smaller than that of the hydrogen atom, in GaAs is on the order of 10 $meV$. Moreover, the radius of the exciton is about $10^2$ $\mathring{A}$ extending over tens of atomic sites in the crystal where the excitons are denoted by *Wannier-Mott excitons*[1].

The well known Hamiltonian of the electronic system of a direct two-band semiconductor can be written as [141]

$$\widehat{\mathcal{H}} = \int d^3\boldsymbol{r}\widehat{\Psi}^\dagger(\boldsymbol{r})\widehat{\mathcal{H}_o}(\boldsymbol{r})\widehat{\Psi}(\boldsymbol{r}) + \frac{1}{2}d^3\boldsymbol{r}d^3\boldsymbol{r}'\widehat{\Psi}^\dagger(\boldsymbol{r})\widehat{\Psi}^\dagger(\boldsymbol{r}')\mathcal{V}(|\boldsymbol{r}-\boldsymbol{r}'|)\widehat{\Psi}(\boldsymbol{r})\widehat{\Psi}(\boldsymbol{r}') \tag{6.1}$$

where $\widehat{\mathcal{H}_o}(\boldsymbol{r})$ is the single particle Hamiltonian. $\widehat{\Psi}(\boldsymbol{r})$ and $\widehat{\Psi}^\dagger(\boldsymbol{r})$ are the electrons field operators which satisfy the commutation relation $[\widehat{\Psi}(\boldsymbol{r}), \widehat{\Psi}(\boldsymbol{r}')] = 0$ and $[\widehat{\Psi}(\boldsymbol{r}), \widehat{\Psi}^\dagger(\boldsymbol{r}')] = \delta(\boldsymbol{r}-\boldsymbol{r}')$. The potential $\mathcal{V}(|\boldsymbol{r}-\boldsymbol{r}'|)$ is the screened Coulomb potential. The field operators are expanded in terms of the electron eigenfunction $\psi_{\mathbf{k}}(\boldsymbol{r})$ in the conduction and the valence band as

$$\widehat{\Psi}(\boldsymbol{r}) = \sum_{\mathbf{k},j}\widehat{a}_{\mathbf{k}j}\psi_{\mathbf{k}}(\boldsymbol{r}) \tag{6.2}$$

with $j = c, v$ denoting the conduction or the valence band. The electron eigenfunction is defined as

$$\psi_{\mathbf{k}j}(\boldsymbol{r}) = \frac{1}{\sqrt{N}}u_{\mathbf{k}j}(\boldsymbol{r})\exp\Big(i\mathbf{k}.\boldsymbol{r}\Big) \tag{6.3}$$

The Bloch wavefunction is denoted by $u_{\mathbf{k}j}(\boldsymbol{r})$ and the number of unit cells of the lattice is denoted by $N$ and $\widehat{a}_{\mathbf{k}j}$ in equation (6.2) denote the fermionic annihilation operators for the electron. They obey the commutation relations $[\widehat{a}_{\mathbf{k}}, \widehat{a}^\dagger_{\mathbf{l}}] = \delta_{\mathbf{k},\mathbf{l}}$ and $[\widehat{a}_{\mathbf{k}}, \widehat{a}_{\mathbf{l}}] = 0$.

Since the disappearance, via annihilation operator $\widehat{a}_{\mathbf{k}}$, of the electron create a hole then it is theoretically convenient to replace the electron annihilation operator $\widehat{a}_{\mathbf{k}}$ by a hole creation operator $\widehat{b}^\dagger_{\mathbf{k}}$ such that $\widehat{a}_{\mathbf{k}c} \equiv \widehat{b}^\dagger_{\mathbf{k}}$ and $\widehat{a}^\dagger_{\mathbf{k}v} \equiv \widehat{b}_{-\mathbf{k}}$. This can be explained as follows, the annihilation of a valence band electron in a state with a wave vector **k**, spin ↑, negative charge $e^-$ and kinetic energy $-E(k)$ from the top of the valence band is equivalent to the creation of a hole in a state with a wave vector $-$**k** with an opposite spin ↓, positive charge $e^+$ and kinetic energy $E(k)$.

From these simple modification and ignoring the number non-conserving terms, the Hamiltonian in equation (6.1) will read

$$\begin{aligned}\widehat{\mathcal{H}} = &\sum E_e(k)\widehat{a}^\dagger_k\widehat{a}_k + \sum E_h(k)\widehat{b}^\dagger_k\widehat{b}_k \\ &+ \frac{1}{2}\sum\mathcal{V}_{\mathbf{k}_{1c}\mathbf{k}_{2c}\mathbf{k}_{3c}\mathbf{k}_{4c}}\widehat{a}^\dagger_{k1}\widehat{a}^\dagger_{k2}\widehat{a}_{k3}\widehat{a}_{k4} + \frac{1}{2}\sum\mathcal{V}_{\text{-}\mathbf{k}_{1v}\text{-}\mathbf{k}_{2v}\text{-}\mathbf{k}_{3v}\text{-}\mathbf{k}_{4v}}\widehat{b}^\dagger_{k1}\widehat{b}^\dagger_{k2}\widehat{b}_{k3}\widehat{b}_{k4} \\ &- \sum\Big(\mathcal{V}_{\mathbf{k}_{1c}\mathbf{k}_{3v}\mathbf{k}_{2v}\mathbf{k}_{4c}} - \mathcal{V}_{\mathbf{k}_{1c}\mathbf{k}_{3v}\mathbf{k}_{4c}\mathbf{k}_{2v}}\Big)\widehat{a}^\dagger_{k1}\widehat{b}^\dagger_{k2}\widehat{b}_{k3}\widehat{a}_{k4}\end{aligned} \tag{6.4}$$

using the effective mass approximation the electron kinetic energy $E_e(k)$ and the hole kinetic energy $E_h(k)$ are defined as

$$E_k(k) = E_g + \frac{\hbar^2k^2}{2\mathbf{m}_e}, \qquad \mathbf{m}_e \equiv \text{the electron effective mass} \tag{6.5}$$

$$E_h(k) = \frac{\hbar^2k^2}{2\mathbf{m}_h}, \qquad \mathbf{m}_h \equiv \text{the hole effective mass} \tag{6.6}$$

---

[1] A relevant text book is the *"Bose-Einstein Condensation of Excitons and Biexcitons and Coherent Nonlinear Optics with Excitons,"* by S. A Moskalenko & D. W. Snoke, Cambridge University Press (2000).

where $E_g$ is the band gap energy and $\mathcal{V}_{\mathbf{k}_{1c}\mathbf{k}_{3v}\mathbf{k}_{4c}\mathbf{k}_{2v}}$ are the direct exchange interactions among electrons and holes due to the Coulomb interaction potential such that

$$\mathcal{V}_{\mathbf{k}_{1c}\mathbf{k}_{3v}\mathbf{k}_{4c}\mathbf{k}_{2v}} = \langle \mathbf{k}_{1i}, \mathbf{k}_{2j} | \mathcal{V}(|\boldsymbol{r} - \boldsymbol{r}'|) | \mathbf{k}_{3m}, \mathbf{k}_{4n} \rangle \tag{6.7}$$

The Wannier-Mott excitons are known to have slowly varying functions for the Coulomb potential $\mathcal{V}(|\boldsymbol{r} - \boldsymbol{r}'|)$ and plane wave factor in equation (6.3) with small change over one unit cell of the lattice. This leads us to calculate the potential in equation (6.7) by first integrating the Bloch function in a unit cell and then summing over all unit cells (e.g. over the valence band $v_i$)

$$\int_{v_i} d^3\boldsymbol{r} u^*_{\mathbf{k}\approx 0,c}(\boldsymbol{r}) u_{\mathbf{k}\approx 0,c}(\boldsymbol{r}) \approx 1 \tag{6.8}$$

$$\int_{v_i} d^3\boldsymbol{r} u^*_{\mathbf{k}\approx 0,c}(\boldsymbol{r}) u_{\mathbf{k}\approx 0,v}(\boldsymbol{r}) \approx 0 \tag{6.9}$$

And hence the direct exchange interactions among electrons and holes due to the Coulomb interaction potential can be simplified to the following

$$\mathcal{V}_{\mathbf{k}_c\text{-}\mathbf{l}'_v\text{-}\mathbf{k}'_v\mathbf{l}_c} = \frac{1}{V^2} \int d^3\boldsymbol{r} d^3\boldsymbol{r}' e^2 \frac{\exp\left[i(\mathbf{l} - \mathbf{k}).\boldsymbol{r} + i(\mathbf{l}' - \mathbf{k}').\boldsymbol{r}'\right]}{\epsilon|\boldsymbol{r} - \boldsymbol{r}'|} \tag{6.10}$$

### 6.2.1 Wannier equation for excitons

The general wavefunction of the electron-hole pair state can be written in terms of the quasi-vacuum state $|\mathbf{0}\rangle$ in which case one can write the momentum state as

$$|p\rangle = \sum \mathbb{C}_{\mathbf{k}\mathbf{k}'} \widehat{a}^\dagger_{\mathbf{k}} \widehat{b}^\dagger_{\mathbf{k}'} |\mathbf{0}\rangle \tag{6.11}$$

The amplitude $\mathbb{C}_{\mathbf{k}\mathbf{k}'}$ can be obtained from the eigenvalue equation $\widehat{\mathcal{H}}|p\rangle = E|p\rangle$ and hence the amplitude equation is

$$\left[E_e(k) - E_h(k') - E_g\right]\mathbb{C}_{\mathbf{k}\mathbf{k}'} - \sum \left[\mathcal{V}_{\mathbf{k}_c\text{-}\mathbf{l}'_v\text{-}\mathbf{k}'_v\mathbf{l}_c} - \mathcal{V}_{\mathbf{k}_c\text{-}\mathbf{l}'_v\text{-}\mathbf{l}_c\mathbf{k}'_v}\right]\mathbb{C}_{\mathbf{l}\mathbf{l}'} = 0 \tag{6.12}$$

To obtain the Wannier equation for the excitons [142] we take the Fourier transformation for the above equation (6.12) and use the equations (6.7) - (6.10) such that

$$\widehat{\mathcal{H}}_{\text{exc}} \widetilde{\psi}(\boldsymbol{r}_e, \boldsymbol{r}_h) = E \widetilde{\psi}(\boldsymbol{r}_e, \boldsymbol{r}_h) \tag{6.13}$$

where the Wannier Hamiltonian $\widehat{\mathcal{H}}_{\text{exc}}$ reads

$$\widehat{\mathcal{H}}_{\text{exc}} = -\frac{\hbar^2}{2\mathbf{m}_e}\nabla_e - \frac{\hbar^2}{2\mathbf{m}_h}\nabla_h + E_g - \frac{e^2}{\epsilon|\boldsymbol{r}_e - \boldsymbol{r}_h|} \tag{6.14}$$

and the composite particle wavefunction is related to the amplitude $\mathbb{C}_{\mathbf{k}\mathbf{k}'}$ as follow

$$\widetilde{\psi}(\boldsymbol{r}_e, \boldsymbol{r}_h) = \sum \mathbb{C}_{\mathbf{k}\mathbf{k}'} \exp\left[i\mathbf{k}.\boldsymbol{r}_e + i\mathbf{k}'.\boldsymbol{r}_h\right] \tag{6.15}$$

Since the motion of these quantum particles includes the center of mass motion and the relative motion then it is useful to separate them by introducing the following new coordinates

$$\widetilde{\boldsymbol{r}} = \boldsymbol{r}_e - \boldsymbol{r}_h, \qquad \mathbf{R} = \widetilde{\mathbf{m}}_e \boldsymbol{r}_e - \widetilde{\mathbf{m}}_h \boldsymbol{r}_h \tag{6.16}$$

where $\widetilde{\mathbf{m}}_e \equiv \frac{\mathbf{m}_e}{\mathbf{M}}$ and $\widetilde{\mathbf{m}}_h \equiv \frac{\mathbf{m}_h}{\mathbf{M}}$. Then the exciton wavefunction reads

$$\widetilde{\psi}(\boldsymbol{r}_e, \boldsymbol{r}_h) = \frac{1}{\sqrt{V}} \widetilde{\psi}(\widetilde{\boldsymbol{r}}) e^{i\mathbf{K}.\mathbf{R}} \tag{6.17}$$

with an equation for the relative motion written as

$$\Big( - \frac{\hbar^2}{2\mathbf{m}_{\widetilde{\boldsymbol{r}}}} \nabla_{\widetilde{\boldsymbol{r}}} - \frac{e^2}{\epsilon_o \widetilde{\boldsymbol{r}}} + \varepsilon_{\text{exc},n} \Big) \widetilde{\psi}(\widetilde{\boldsymbol{r}}) = 0 \tag{6.18}$$

The above mathematical manipulation has led us to shape the excitonic equation (6.14) into a hydrogen-like atom equation (6.18) with a reduced mass $\mathbf{m}_{\widetilde{\boldsymbol{r}}} = \frac{\mathbf{m}_e \mathbf{m}_h}{\mathbf{M}}$ that normally four order of magnitude less than the hydrogen atom mass. Also in the above equation the Coulomb interaction is screened and reduced by a factor of $\epsilon_o$. Interestingly, excitons with such description have a larger Bohr radius and a binding energy that much weaker when compared to the hydrogen atom. Therefore, the total energy of the exciton is

$$E(k, n) = E_g - \varepsilon_{\text{exc},n} + \frac{\hbar^2 k^2}{2\mathbf{M}} \tag{6.19}$$

and the 1s excitonic binding energy defined as

$$\varepsilon_{\text{exc},1} = \frac{\hbar^2}{2\mathbf{m}_{\widetilde{\boldsymbol{r}}} a_B^2 n^2} \tag{6.20}$$

where $a_B$ is the Bohr radius that takes the following value for 1s

$$a_B = \frac{\hbar^2 \epsilon_o}{e^2 \mathbf{m}_{\widetilde{\boldsymbol{r}}}} \tag{6.21}$$

### 6.2.2 Excitons as Bosons

To examine the bosonic statistical feature on excitons we need to introduce the exciton operators $\widehat{\mathbf{e}}_{\mathbf{K},n}$ and $\widehat{\mathbf{e}}^{\dagger}_{\mathbf{K},n}$ by inserting the equations (6.15) - (6.17) into equation (6.11) and use the momentum state of excitons $|p\rangle = \widehat{\mathbf{e}}^{\dagger}_{\mathbf{K},n} |\mathbf{0}\rangle$ such that

$$\widehat{\mathbf{e}}^{\dagger}_{\mathbf{K},n} = \sum_{\mathbf{k},\mathbf{k}'} \delta_{\mathbf{K},\mathbf{k}+\mathbf{k}'} \widetilde{\psi}_n (\widetilde{\mathbf{m}}_e \mathbf{k} - \widetilde{\mathbf{m}}_h \mathbf{k}') \widehat{a}^{\dagger}_{\mathbf{k}} \widehat{b}^{\dagger}_{\mathbf{k}'} \tag{6.22}$$

The wavefunction $\widetilde{\psi}_n(\widetilde{\mathbf{m}}_e \mathbf{k} - \widetilde{\mathbf{m}}_h \mathbf{k}')$ is the Fourier transform of $\widetilde{\psi}_n(\widetilde{\boldsymbol{r}})$. The commutation relation of the exciton operators read

$$\Big[ \widehat{\mathbf{e}}_{\mathbf{K}',n'}, \widehat{\mathbf{e}}_{\mathbf{K},n} \Big] = 0 \tag{6.23}$$

$$\Big[ \widehat{\mathbf{e}}^{\dagger}_{\mathbf{K}',n'}, \widehat{\mathbf{e}}^{\dagger}_{\mathbf{K},n} \Big] = 0 \tag{6.24}$$

$$\Big[ \widehat{\mathbf{e}}_{\mathbf{K}',n'}, \widehat{\mathbf{e}}^{\dagger}_{\mathbf{K},n} \Big] = \delta_{\mathbf{K}\mathbf{K}'} \delta_{nn'} - O(n_{\text{exc}} a_B) \tag{6.25}$$

From the above commutation rules one immediately realizes that the excitons are acting as bosons in the low density regime under when the condition $n_{\text{exc}} \ll \frac{1}{\sqrt[3]{a_B}}$ is held true or under when the exciton inter-particle spacing is much larger than its Bohr radius.

## 6.3 The Optical Transition of Excitons

As any quantum particles excitons have dipole moments that interact with electromagnetic fields and thus one can obtain an interband optical transition matrix element by using the Fermi's golden rules

$$\mathbb{W}_{cv} = \frac{2\pi}{\hbar} \sum_{f,i} |\langle f|\widehat{\mathcal{H}}_{\text{dipole}}|i\rangle|^2 \delta\Big(E_f - E_i - \hbar\omega\Big) \tag{6.26}$$

The above matrix $\mathbb{W}_{cv}$ calculate the transition between the initial state $i$ of energy $E_i$ and the final state $f$ with energy $E_f$ using the dipole interaction Hamiltonian $\widehat{\mathcal{H}}_{\text{dipole}}$.

Considering an uncorrelated electron-hole pair, the matrix element reads

$$\mathbb{M} = |\langle f|\widehat{\mathcal{H}}_{\text{dipole}}|i\rangle| = \delta_{\sigma,j_e-j_h} \int_V \chi^*_{k_e,c}(\widetilde{\boldsymbol{r}})u^*_{k_e,c}(\widetilde{\boldsymbol{r}})e\widetilde{\boldsymbol{r}}.Eu_{k_h,v}(\widetilde{\boldsymbol{r}})\chi_{k_h,v}(\widetilde{\boldsymbol{r}}) \tag{6.27}$$

where $\chi^*_{k_e,c/v}$ are the envelope functions, $\sigma$ is the polarization of the light, $j_{e/h}$ are the angular momenta of the electron/hole and $u_{k_{e/h},c/v}$ are the Bloch functions.

The volume integration in equation (6.27) can be simplified since the envelope functions $\chi^*_{k_e,c/v}$ have a small amplitude variations and the Bloch functions $u_{k_{e/h},c/v}$ are the same across all the cells. Thus the volume integral can be rewritten as a summation over all cells assuming a unit cell $\Omega_i$, such that

$$\begin{aligned}
\mathbb{M} &\approx \delta_{\sigma,j_e-j_h} \sum_{\mathbf{R}_i} \int_V d\widetilde{\boldsymbol{r}}' \Big[\chi^*_{k_e,c}(\widetilde{\boldsymbol{r}}' - \mathbf{R}_i)u^*_{k_e,c}(\widetilde{\boldsymbol{r}}' - \mathbf{R}_i)e\widetilde{\boldsymbol{r}}.Eu_{k_h,v}(\widetilde{\boldsymbol{r}}' - \mathbf{R}_i)\chi_{k_h,v}(\widetilde{\boldsymbol{r}}' - \mathbf{R}_i)\Big] \\
&\simeq \delta_{\sigma,j_e-j_h} \frac{1}{\Omega} \sum_{\mathbf{R}_i} \Omega\chi^*_{k_e,c}(\mathbf{R}_i)\chi_{k_h,v}(\mathbf{R}_i). \\
&\quad \Big[\int_\Omega d\widetilde{\boldsymbol{r}}' u^*_{k_e,c}(\widetilde{\boldsymbol{r}}')e\widetilde{\boldsymbol{r}}.Eu_{k_h,c}(\widetilde{\boldsymbol{r}}' + e\mathbf{R}_i.E \int_\Omega d\widetilde{\boldsymbol{r}}' u^*_{k_e,c}(\widetilde{\boldsymbol{r}}')u_{k_h,c}(\widetilde{\boldsymbol{r}}')\Big]
\end{aligned} \tag{6.28}$$

The equation above can also be simplified by making use of the facts that for the lowest energy interband transition we find that the Bloch wavefunctions at the conduction band $u_{k_{e/h},c}$ have $s$-wave symmetry while the valence band wavefunctions $u_{k_{e/h},v}$ have a $p$-wave symmetry, see Figure (6.1) and therefore the equation (6.29) reduces to

$$\mathbb{M} \simeq \Big[\int_V d\widetilde{\boldsymbol{r}}\chi^*_{k_e,c}(\widetilde{\boldsymbol{r}})\chi_{k_h,v}(\widetilde{\boldsymbol{r}})\Big]\delta_{\sigma,j_e-j_h}\Big[\frac{1}{\Omega}\int_\Omega d\widetilde{\boldsymbol{r}}' u^*_{k_e,c}(\widetilde{\boldsymbol{r}}')u_{k_h,c}(\widetilde{\boldsymbol{r}}')e\widetilde{\boldsymbol{r}}'.E\Big]\sqrt{\frac{2\pi\omega}{\epsilon\hbar V}} \tag{6.29}$$

Regardless of the fact that we are investigating the magnetically confined excitons, the first term in the above equation (6.29), without confining potential, measures the overlap of the envelope function of an electron and a hole where these envelopes read

$$\chi_{k_e,c}(\widetilde{\boldsymbol{r}}) = e^{i\mathbf{k}_e.\widetilde{\boldsymbol{r}}} \tag{6.30}$$

$$\chi_{k_h,v}(\widetilde{\boldsymbol{r}}) = e^{i\mathbf{k}_h.\widetilde{\boldsymbol{r}}} \tag{6.31}$$

therefore, the overlap term in equation (6.29) reduces to the *momentum conservation* condition where the momentum of the photons is negligible compared to the excitons, such that

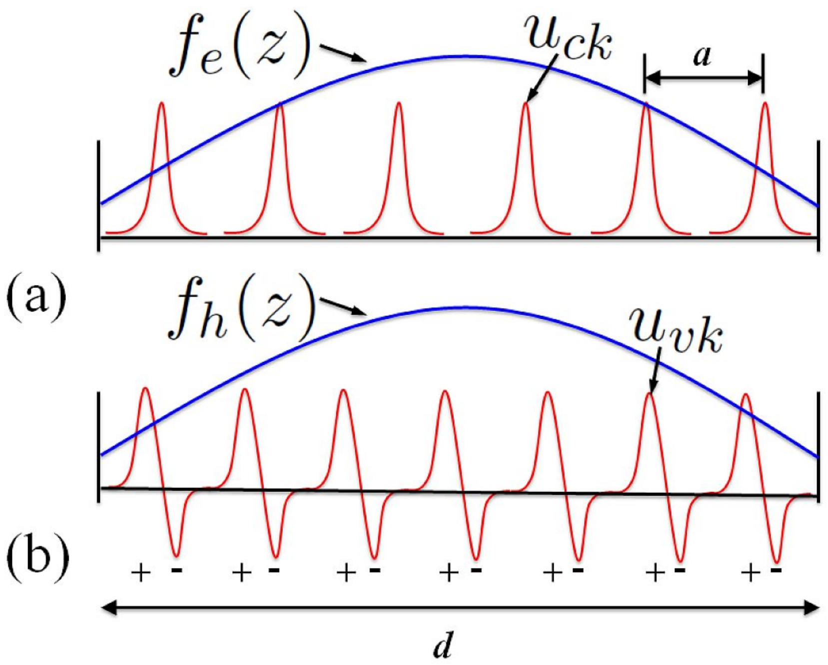

*Figure 6.1:* The Bloch functions $u_{k_{e/h},c/v}(\widetilde{\boldsymbol{r}})$ and the envelope function $f_{e/h,c/v}(z) \equiv \chi_{k_{e/h},c/v}(\widetilde{\boldsymbol{r}})$ in a quantum well.

$$\int_V d\widetilde{\boldsymbol{r}} \chi^*_{k_e,c}(\widetilde{\boldsymbol{r}}) \chi_{k_h,v}(\widetilde{\boldsymbol{r}}) \to \delta(\mathbf{k}_e - \mathbf{k}_h) \tag{6.32}$$

The second term in equation (6.29) represents the *angular momentum conservation* which means that for *heavy holes* (HH) only the pairs with angular momentum $j_{HH} = +\frac{3}{2} \leftrightarrow j_e = +\frac{1}{2}$ and $j_{HH} = -\frac{3}{2} \leftrightarrow j_e = -\frac{1}{2}$ are optically active as shown in Figure (6.3). The third term in equation (6.29) represents the projection of exciton dipole moment on the light polarization.

### 6.3.1 The strength of an excitonic oscillator

The exciton oscillator strength $\mathcal{S}$ is a parameter that characterizes the exciton-photon coupling which is defined in analogue to that of the atomic oscillator strength such that

$$\mathcal{S} = \frac{2\boldsymbol{m}^* V}{\pi \hbar a_B^3} |\langle u_v | \widetilde{\boldsymbol{r}}.E | u_c \rangle|^2 \tag{6.33}$$

It is also possible to express the optical transition matrix $\mathbb{M}$ in equation (6.29) in terms of the oscillator strength as follow

$$\mathbb{M} = \sqrt{\pi e^2 \mathcal{S} \epsilon \boldsymbol{m}^* V \Sigma} \tag{6.34}$$

where $\Sigma$ represent the first three terms in equation (6.29) that depend on the selection rules and the geometric properties of the semiconductor.

- **The Mesoscopic Enhancement**

As mentioned early, the excitonic envelope function consists of a plane wave for the center of mass motion with a momentum $K$ and the bound relative motion. At the momentum conservation condition, $\mathbf{k} = 0$, the overlap integral is enhanced by $\sqrt{\frac{V}{a_B^3}}$. At the excitonic bound state the electron and hole in an exciton move together, unlike an uncorrelated

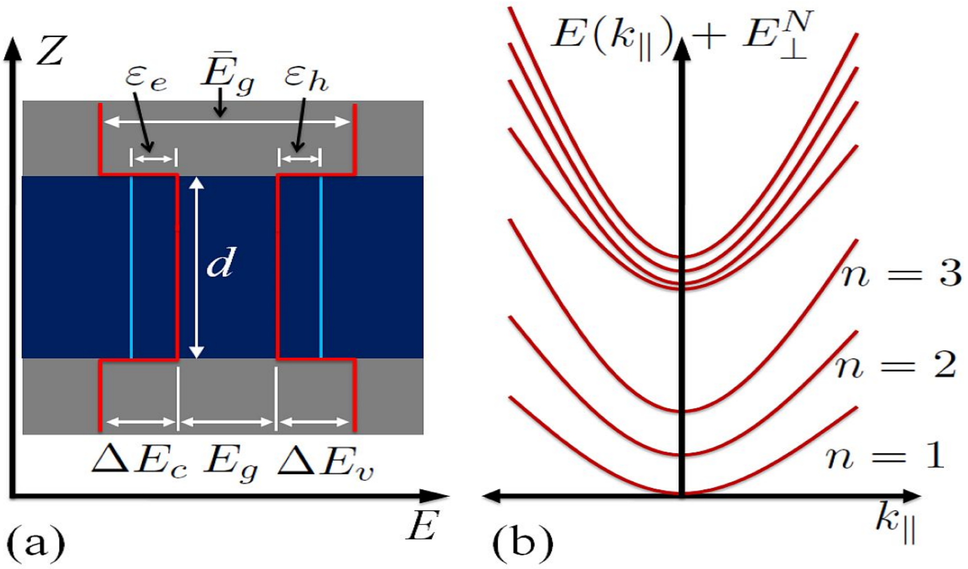

***Figure 6.2:*** (a) The energy band diagram of a confined semiconductor of thickness $d$ along the $z$-axis. The confinement change the band gab energy $\bar{E}_g$ to a less energy gab $E_g$ which result in a conduction $\Delta E_c$ and valence $\Delta E_v$ energy gabs. (b) A discrete energy band in energy-momentum space of a quantum well.

electron-hole pair, with an average relative separation $a_B$ to increase by that the probability of an optical transition. This is called the *mesoscopic enhancement*.

On the other hand, due to the conservation of the angular momentum, only heavy holes excitons (HH-excitons) with $j = \pm 1$ can interact with circularly polarized photons where they are called *bright excitons*. For heavy hole excitons with $j = \pm 2$, the light emission and absorption is forbidden creating by that the so-called *dark excitons*. Dark excitonic state is used to enhance electromagnetic transparency.

### 6.3.2 The Excitons Formation in Quantum Wells

A novel quantum structure, such as quantum heterostructure, can be fabricated at the atomic monolayer precision in semiconductor materials using the state-of-art fabrication technologies. For example, two-dimensional quantum wells (QWs), one-dimensional quantum wires and zero-dimensional quantum dots can be created. As shown in Figure 6.2(a), the quantum well is a thin layer (shown dark blue color) of a narrow bandgap material sandwiched between two barrier layers of a wider bandgap (gray color). The thickness of the quantum well is comparable to the Bohr radius of the excitons in which case the motion of the electrons and the holes is confined perpendicular to the growth direction of the quantum well ($z$-direction $\perp$ QW plane).

Due to the confinement the energy levels are quantized and the particle energy-momentum dispersion consists of set of bands, see Figure 6.2(b). Also, the confinement modifies the valence band structure significantly, in GaAs the hole has a $p$-like wavefucntion having an orbital angular momentum $L = \pm 1$ and spin $S = \pm\frac{1}{2}$. This kind of modification is illustrated in Figure 6.3(a).

One can distinguish the difference between the band structure of the bulk and that of the modified due to the quantum confinement as follows

- **In Bulk**

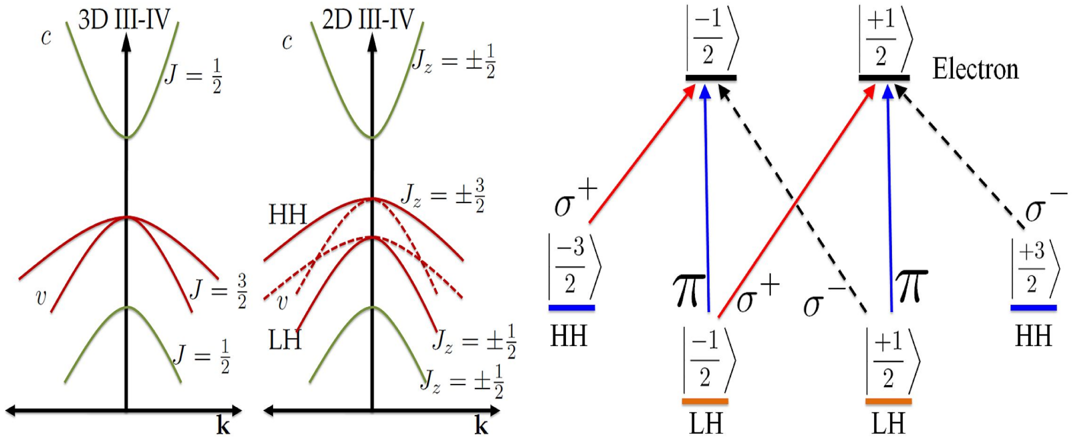

(a) (b)

*Figure 6.3:* (a) Schematic representation of the conduction and valence band states in 3D II-IV bulk (left) and for 2D III-IV quantum well (right). The spin orbit coupling contributes to the formation of the exciton ground state in and 2D structure. (b) Schematic representation of the optical transitions between the electrons energy states and the holes energy states which conserve the total angular momentum. $\sigma^{\pm}$ and $\pi$ denotes the polarization directions of the excitation pulses.

Holes form two degenerate light hole (LH) bands and two degenerate heavy hole (HH) bands, they are four-folds degeneracy at **k** = 0. LHs have a total angular momentum $J = \pm\frac{1}{2}$ and light mass[2] of $m_{LH} = \frac{m_e}{\gamma_1+2\gamma_2}$. The HHs have total angular momentum $J = \pm\frac{3}{2}$ and heavy mass of $m_{HH} = \frac{m_e}{\gamma_1-2\gamma_2}$.

- **In Quantum Well**

  The translation symmetry is broken in the growth direction and the degeneracy of the energy levels between the LH and HH is lifted at **k**=0. In such case, as shown in Figure 6.3(a), the HH bands become closer to the conduction band where the mass is light and given at **k**=0 by $m_{HH} = \frac{m_e}{\gamma_1-\gamma_2}$.

### 6.3.3 The Binding Energy of Excitons in the Quantum Well

At the limits of strong confinement in the quantum wells system the excitonic binding energy increases at the limit of an exact two-dimensional gas where the Bohr radius of an exciton becomes half of that corresponds to the three-dimensional gas value as stated in equation (6.21). The increase in the binding energy is by a factor of four when compared to the 3D value in equation (6.20). As shown in Figure (6.4), the thickness of the quantum well plays an important rule in determining the 2D Bohr radius $a_B^{2d}$ and the 2D binding energy $E_B^{2d}$ [143][144][145].

In perfect situations one normally is interested in strongly confined excitons with a relatively small momenta $p \approx 0$ in which case the following approximations are valid

- The quantum well confining potential accept the square well potential model that confines the electron by $V_e$ and the hole by $V_h$ along the $z$-direction.

---

[2] Mass is written in term of the Luttinger parameters.

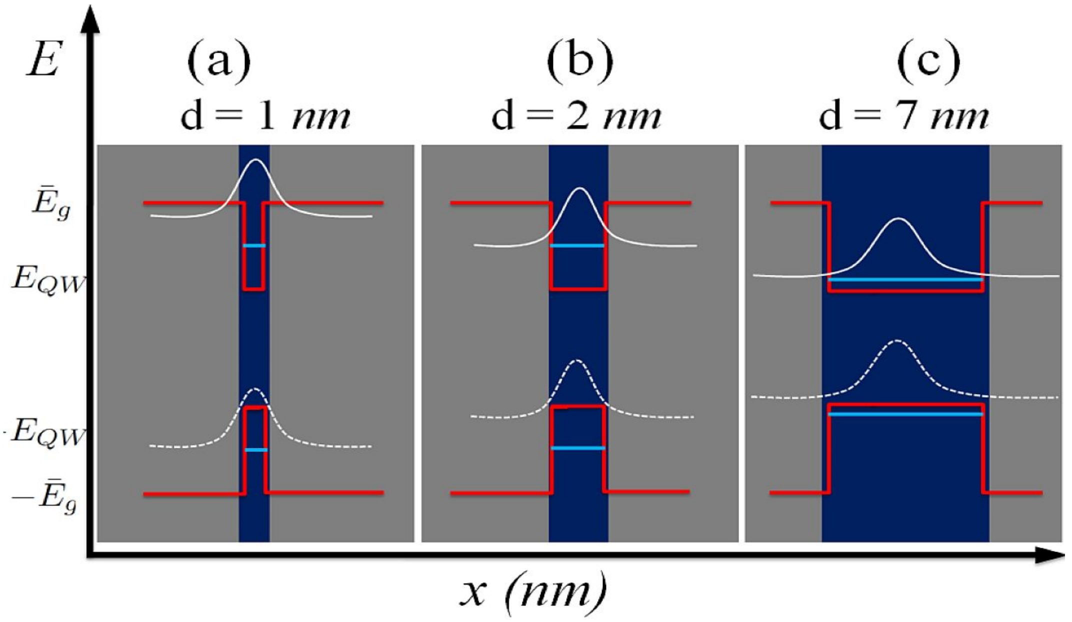

***Figure 6.4:*** Comparison of the electron wavefunction $f_e(z)$ (solid curve) and the hole wavefunction $f_h(z)$ (dashed curve) with respect to the energy gap $\bar{E}_g$ in (a) ultrathin (b) narrow and (c) shallow quantum well.

- Both the conduction and the valence bands can be treated as parabolic.
- There is no sub-band mixing among the electron or the hole bands as well as with high valence bands.

The internal motion of excitons can thus be described by the following decomposed wavefunction

$$\varphi(\boldsymbol{r}_e, \boldsymbol{r}_h) = f_e(z_e) f_h(z_h) p(\widetilde{\boldsymbol{r}}, Z) \tag{6.35}$$

where $Z = |z_e - z_h|$ and $f_e(z_e)$, $f_h(z_h)$ are the electron and hole transverse wavefunctions, respectively. $p(\widetilde{\boldsymbol{r}}, Z)$ is the pair's in-plane wavefunction. The above equation (6.35) satisfies the following set of motion equations

$$\Big[ -\frac{\hbar^2}{2} \frac{d}{dz_e} \Big( \frac{1}{\boldsymbol{m}_{e\perp}} \frac{d}{dz_e} \Big) + V_e(z_e) \Big] f_e(z_e) = \varepsilon_e f_e(z_e) \tag{6.36}$$

$$\Big[ -\frac{\hbar^2}{2} \frac{d}{dz_h} \Big( \frac{1}{\boldsymbol{m}_{h\perp}} \frac{d}{dz_h} \Big) + V_h(z_h) \Big] f_h(z_h) = \varepsilon_e f_e(z_e) \tag{6.37}$$

$$\Big[ -\frac{\hbar^2}{2u_{\|}} \frac{1}{\widetilde{\boldsymbol{r}}} \frac{d}{d\widetilde{\boldsymbol{r}}} \Big( \widetilde{\boldsymbol{r}} \frac{d}{d\widetilde{\boldsymbol{r}}} \Big) - \frac{e^2}{\epsilon_o \sqrt{\widetilde{\boldsymbol{r}}^2 + Z^2}} \Big] p(\widetilde{\boldsymbol{r}}, Z) = \varepsilon_{\widetilde{\boldsymbol{r}}}(Z) p(\widetilde{\boldsymbol{r}}, Z) \tag{6.38}$$

and the binding energy of the excitons is approximated as

$$E_B^{2d} = \int dz_e dz_h |f_e(z_e)|^2 |f_h(z_h)|^2 \varepsilon_{\widetilde{\boldsymbol{r}}}(z_e - z_h) \tag{6.39}$$

where $\varepsilon_{\widetilde{\boldsymbol{r}}}(z_e - z_h)$ is the binding energy of the two-dimensional excitons of lectrons and holes confined along the $z$-axis, $z = z_e = z_h$. The binding energy $E_B^{2d}$ in the above equation is considered to be an average of $\varepsilon_{\widetilde{\boldsymbol{r}}}(z_e - z_h)$ over the $(z_e, z_h)$ configuration space weighted by the probability of electron at $z_e$ and a hole at $z_h$ coordinates[3].

Decreasing the quantum well thickness, as schematically represented in Figure (6.4) for GaAs with AlAs barrier, will tightly confine the electron and holes. However, with very narrow quantum well, i.e. too thin confining layer, the wavefunction start to spread outside of the quantum well and the electrons become much more delocalized than the holes. Using the variational method, the solution to $p(\widetilde{\boldsymbol{r}}, Z)$ can be obtained in which case one can easily use equation (6.39) to calculate the binding energy of the quantum well, as detailed in the article *"Simple method for calculating exciton binding energies in quantum-confined semiconductor structures"* by Leavitt and Little [143]. The results calculated by Green $et.al$ in [145] show that when quantum well thickness is decreased the binding energy $E_B^{2d}$ first increases from the bulk limit to an optimal quantum well thickness, $\sim 3\ nm$, which corresponds to the decrease of Bohr radius with a tighter confinement. In the case of very thin quantum well, as shown in Figure 6.4(a), the overlap between $f_e(z_e)$ and $f_h(z_h)$ decreases while the average $|z_e - z_h|$ increases which results in decreasing binding energy.

### 6.3.4 The Excitonic Optical Transition in the Quantum Well

The $z$-direction motion and the in-plane motion of the electrons and holes are decoupled due to the quantum confinement in which case their envelope wavefunctions become

$$\chi_{k_e,c}(\widetilde{\boldsymbol{r}}) = f_e(z) e^{i\mathbf{k}_{e\parallel}.\widetilde{\boldsymbol{r}}_\parallel} \tag{6.40}$$

$$\chi_{k_h,v}(\widetilde{\boldsymbol{r}}) = f_h(z) e^{i\mathbf{k}_{h\parallel}.\widetilde{\boldsymbol{r}}_\parallel} \tag{6.41}$$

In order to have a momentum conservation condition fulfilled, the optical transition matrix $\mathbb{M}$ in equation (6.29) must have different elements. Using the above equations (6.40)-(6.41) then the first term in equation (6.29) reads

$$\int_V d\widetilde{\boldsymbol{r}} \chi^*_{k_e,c}(\widetilde{\boldsymbol{r}}) \chi_{k_h,v}(\widetilde{\boldsymbol{r}}) = \int_z dz f_e^*(z) f_h(z) \int_S d\widetilde{\boldsymbol{r}}_\parallel \exp\left[i\Big(\mathbf{k}_{h\parallel} - \mathbf{k}_{e\parallel}\Big).\widetilde{\boldsymbol{r}}_\parallel\right] \tag{6.42}$$

The right side of the above equation contains the required information the optical transition of the excitons where the first $z$-integral term show that an optical transition can only take place between the $z$-direction sub-bands of the electrons and holes in which case they have the same parity, such as the two lowest energy bands in the quantum well. The second $S$-integral term requires momentum conservation in the quantum well plane. Since the quantum wells are more optically accessible than the bulk material, it thus turns out from the above analysis that the excitons in quantum wells couple to external electromagnetic fields with the same in-plane wavenumber $\mathbf{k}_\parallel$ and arbitrary transverse wavenumber $\mathbf{k}_\perp$.

Figure 6.3(b) summaries the possible optical transition of excitons that satisfy the angular momentum conservation rules. The heavy holes in quantum wells only have an in-plane orbital angular momenta which means that due to the conservation heavy holes excitons always couple to TE modes. On the other hand light hole excitons have one third of probability coupling to the TE modes while the two third is for TM modes.

An important conclusion one can make here is as the following

---

[3] The solution of the equations (6.36) and (6.37) for $f_e(z_e)$ and $f_h(z_h)$, respectively, can be obtained from any standard quantum mechanics text books.

- *Since the Bohr radius is reduced in the two-dimension compared to three-dimension, as a result the oscillator strength is enhanced. The offset of the enhancement can be described as a reduction in the overlap between the electromagnetic fields (photons) and the exciton which is mainly due to the fact that the longitudinal coherence of the TE-mode photon field is usually large compared to the quantum well thickness. Confining the photon field helps to achieve stronger coupling between the photon and exciton, this can be done by trapping the photon along the $z$-direction in a microcavity.*

### 6.3.5 Photoluminescence and Life Cycle of Excitons

To create the electron-hole pairs, normally one uses an excessive energy excitation, such as an optical excitation. After the creation the thermal equilibrium is restored through the carrier relaxation and exciton formation which eventually recombine giving rise to observable *luminescence*. The electron-hole pairs in a system of quantum wells relax to respective sub-bands via the emission of longitudinal acoustic phonons, longitudinal optical phonons or through carrier-carrier scattering [146]. In some special cases, such as inducing the tunneling of electrons using electric field, relaxation of electrons from the anti-symmetric to symmetric sub-band states through the longitudinal optical phonon scattering is possible when the sub-band transition energy exceeds the longitudinal phonon energy, e.g. $\hbar\omega_{LO} = 36$ meV in GaAs [147]. Time under 10 ps has been predicted for longitudinal optical phonon in quantum well under certain circumstances [148]. Also impurities assisted tunneling between the excited and ground state sub-bands for heavy holes with symmetric quantum wells have shown a 340 ps tunneling time [149].

- **Excitons Emission and Internal Cooling Mechanism**

The formation of excitons is often dominated by the Coulomb attraction force between electrons and holes where the relaxation to the respective ground sub-band states in times of the order of sub-nanoseconds. The created initial excitons are rather energetic (means hot) with a finite momenta $\mathbf{P} = \hbar\mathbf{k} \neq 0$ for their center-of-mass (CM). Internal cooling occurs through the exciton-exciton, exciton-free carrier and exciton-acoustic phonon scattering [146][150] to reach the quasi-thermal equilibrium, that is cold excitons with $k \approx 0$ which eventually annihilate and emit detectable photons in the so-called *photoluminescence*. At low temperature the exciton-longitudinal optical phonons scattering dominates the cooling process exhibiting by that a characteristic sub-nanosecond relaxation time. It is important to mention here that the relaxation time can increase depending on the interface roughness and the de-localization of the crystal potential.

Usually the quantum wells are embedded in a three-dimensional structure which results in a relaxation of the momentum conservation along the quantum wells growth $z$-direction. This makes the cooling of the excitons to the lattice temperature via emission of bulk longitudinal acoustic phonon to be about three orders of magnitude faster than that in bulk [151]. The cooling conserves elastically both the in-plane and the total energy where the energy of a phonon mode with a momentum $\hbar\mathbf{k}_{\|}$ is given by $E_{\text{phon}} = \hbar\mathbf{k}_{\|}v_s$, with $v_s$ is the sound velocity. The free excitons with mass $\mathbf{m}_{\text{exc}}$ and wave vector $K$ can not be scattered into a lower kinetic energy state by a single acoustic phonon as long as the slop of the *exciton energy dispersion* at $K$ is less than $\hbar v_s$, i.e. if $\hbar K < \mathbf{m}_{\text{exc}}v_s$. Hence the bottleneck for cooling by the acoustic phonons scattering occurs at an energy of $\frac{1}{2}\mathbf{m}_{\text{exc}}v_s$ for excitons in which case the low temperature limit for acoustic phonon assisted cooling is then given by $\frac{1}{2k_B}\mathbf{m}_{\text{exc}}v_s \sim 0.1K$.

- **The Lifetime of Excitons**

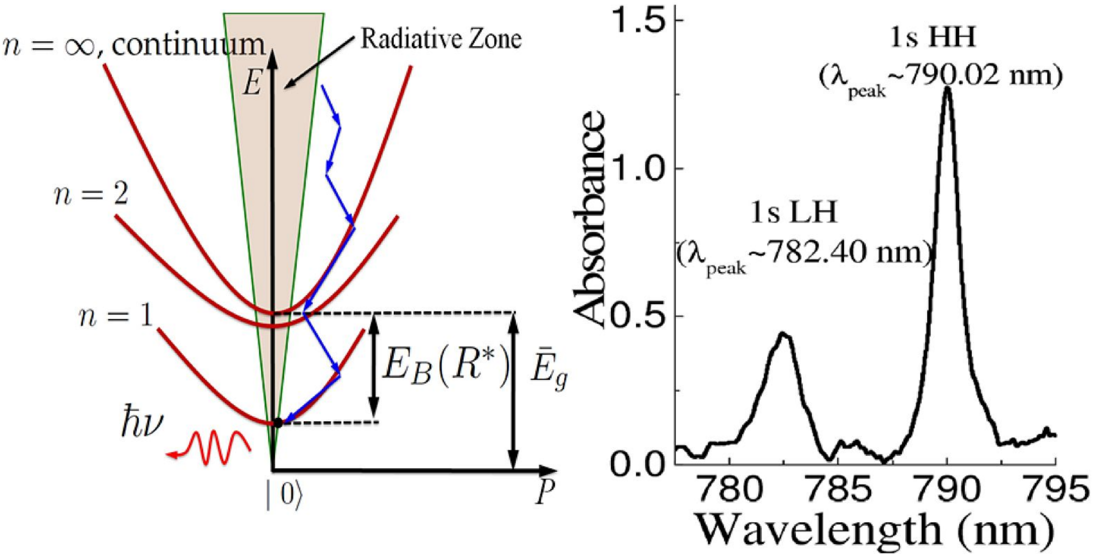

*Figure 6.5:* (Right) Schematic representation of the energy-momentum dispersion with the excitation optical cone (the radiative zone). The difference between the continuum state ($n = \infty$) and the first excited state ($n = 1$) is of the order of the Rydberg energy $R^*$ with $E_B$ the energies of the bound states are given by $E_B = E_g - \frac{R^*}{n^2}$. The arrows represent a life cycle of an exciton (relaxation process). (Left) Typical Absorption (photoluminescence) spectra of the AlGaAs/GaAs multiple quantum wells sample that used in these experiments.

The interaction of the quantum well excitons with the quasi-continuum photon states limit their lifetime. The Fermi Golden Rule gives a radiative lifetime of free excitons proportional to the temperature $T$, by assuming that

- there is a thermal distribution of the in-plane center of mass energy $\frac{\hbar^2 K^2}{2\mathbf{m}_{\text{exc}}}$ and
- only excitons with in-plane wave vector $K$ equal to the photon wave vector $\frac{\hbar\omega n}{c}$ can radiate.

When the excitons are localized and the length of the characteristic coherence length $l_c$ satisfies the condition $\frac{\hbar^2}{2\mathbf{m}_{\text{exc}} l_c^2} > k_B T$, then the picture of free-exciton radiative decay becomes invalid where the localized exciton lifetime becomes temperature independent and generally in the 100 ps range. Moreover, the radiative lifetime decreases with decreasing the well thickness which is due to a better overlapping between the envelope electron and the hole wavefunctions [152]. At room temperature, most of excitons are thermally ionized and the radiative recombination process is essentially dominated by the band-to-band bi-molecule process.

- **Photoluminescence: $k$-selection Rules**

The excitonic states that decay into photon must have a conservation of both energy and momentum where the resulted photoluminescence is coming from the recombination of optically active bound and unbound electron-hole pairs with center-of-mass momenta $\mathbf{P} \approx 0$ [153]. The emitted photoluminescence photons have a momentum with a $z$-component generated from the Fourier components of the quantum confined electron and hole wavefunctions. The in-plane momentum is determined by the excitons center-of-mass momentum.

Excitons with homogeneous *linewidth* $\hbar\Gamma$ (explained in next section) which have states that satisfy the following relationship, become optically active

$$\frac{\hbar^2 K^2}{2\mathbf{m}_{\text{exc}}} \leq \frac{1}{2}\hbar\Gamma \tag{6.43}$$

Optically active excitons constitute only a small fraction of thermally quasi-equilibrium distribution of exciton population. The homogeneous linewidth is on the order of $10^{-8}$ eV for radiative recombination lifetimes on the order of 100 ns in two-level system. This is too small when compared to the thermal energy of the excitons, where the exciton energy is on the order of the spread in the kinetic energy $k_B T \sim \frac{\hbar^2 \Delta K^2}{2\mathbf{m}_{\text{exc}}}$ [154].

- **Photoluminescence: The Linewidth**

The variation in the confining potential of the quantum well is often due to the thickness fluctuations, which is typically in the order of one monolayer when grown using the molecular beam epitaxy. The confining potential variation results in producing an inhomogeneous broadening of the exciton linewidth where the excitons photoluminescence linewidth is better described by the convolution of the homogeneous and inhomogeneous linewidths with the later being the dominant term [155].

The origin of the homogeneous linewidth of the exciton transition in the quantum well system comes form the inelastic electron-phonon scattering process and other scattering processes due to the Coulombic impurities. The homogeneous linewidth is well approximated by

$$\Gamma = \Gamma_o + \gamma T + \Gamma_{LO} \frac{1}{e^{\hbar\omega_{LO}/k_B T} - 1} \tag{6.44}$$

with $\Gamma_o = 0.5 - 1$ meV represents the temperature-independent contribution from defect scattering, $\gamma = 5 - 10$ $\mu$V/K is due to the acoustical phonons scattering and $\Gamma_{LO} = 5$ meV is due to the longitudinal optical phonons ($\hbar\omega = 36$ meV) scattering [156]. At low temperature, the inhomogeneous excitonic linewidth is broadened because of interface roughness.

- **Photoluminescence: The Intensity**

The localization of the excitons occurs due to the presence of the disorder in quantum well system where these localized excitons are mainly a trapped fraction of them in the potential minima depending on the amount of disorder and the lattice temperature. The absolute photoluminescence increases with decreasing temperature as more localized excitons become optically active. At low lattice temperature and hence reduced thermal activation energy available to detrap the excitons, more of them become localized by the disorder where a remarkable conclusion can be made here

- ○ *The excitons with localized wavefunctions are delocalized in momentum space leading to an enhanced radiative recombination.*

The photoluminescence is a measure of the rate of photons emitted at a particular energy $PL_I(\epsilon)$ which can be described by

$$PL_I(\epsilon) \propto \frac{1}{\tau(\epsilon)} \text{DOS}(\epsilon) f(\epsilon) \tag{6.45}$$

where $\tau(\epsilon)$ is the radiative recombination lifetime, DOS($\epsilon$) is the density of the available states and $f(\epsilon)$ is the occupancy of excitonic state.

The density of states is independent of the temperature or the excitonic density and the change in the photoluminescence line shape can thus be determined by measuring the occupancy of the available excitonic states and the kinetic process that repopulate the vacant states.

## 6.4 The Magnetic Potential Cover and the Trapping Field Localized Minima

Our experiments, as detailed in the following chapter, focus in optically determining the exciton-dispersion under when a magnetic field is applied. The application of the magnetic field, namely localized weak fields, is maintained by imprinting a magnetic filed cover and localized field minima within the system of multiple quantum wells. The behavior of the excitons under such circumstances can be understood by considering the usual momentum operator under a magnetic field in which case it commute with the excitonic Hamiltonian and plays the center-of- mass momentum role [157][158] such that

$$\mathbf{P} = \mathbf{m}_{\mathrm{exc}}\vec{v}_{cm} - \frac{e}{c}\vec{B} \times \vec{\tilde{\boldsymbol{r}}} \tag{6.46}$$

where $v_{cm} = \frac{\partial E_{\mathrm{exc}}}{\partial \mathbf{P}}$ is the center-of-mass velocity. Only excitons with momentum $\mathbf{P} \approx 0$ can recombine radiatively and thus an exciton is optically active only when it has a velocity $\vec{v}_{cm} = -\frac{e}{c\mathbf{m}_{\mathrm{exc}}}\vec{B} \times \vec{\tilde{\boldsymbol{r}}}$. Not like in the case of the *indirect-excitons*[4] the separating electron-hole distances of the direct excitons vary with respect to the crystal potential field within the layer; however, if an in-plane magnetic field is applied the exciton states shift rigidly in the $k$-space in the in-plane direction perpendicular to the magnetic field [159]. The in-plane field is expected to tune the recombination lifetime of the excitons at rest to very high values without affecting their binding energy [160] where this mechanism could be used for obtaining a cold excitonic gas in thermodynamic equilibrium.

Figure (6.6) illustrates the underlying coupling mechanisms for varies magnetic fields orientations. Assuming a freely moving exciton in an in-plane with as center-of-mass momentum $\mathbf{P}(x, y)$, a dispersion relation $E_{exc} = E_{\mathrm{exc}}(\mathbf{P})$ and velocity $v_{cm} = \frac{\partial E_{\mathrm{exc}}}{\partial \mathbf{P}}$, then we can determine the excitons dispersion, the binding energy $E_B$ and, in turn, the effective mass $\mathbf{m}_{\mathrm{exc}}$. The important conclusions that can be drawn here are

- $E_B = \sqrt{\frac{\pi}{2}}\frac{e^2}{\varepsilon l_B} \sim \sqrt{B_\perp}$ *where* $B_\perp$ *is the component of the magnetic field perpendicular to the quantum well plane,* $l_B = \sqrt{\frac{\hbar c}{eB_\perp}}$ *is the magnetic length and* $\varepsilon$ *is dielectric constant,*
- $E_{exc} = -E_B e^{-\alpha} I_o(\alpha)$ *where* $I_o(\alpha)$ *is the modified Bessel function and* $\alpha = \left(\frac{\boldsymbol{P} l_B}{2\hbar}\right)^2$*,*
- *At the condition* $\frac{\boldsymbol{P} l_B}{\hbar} \ll 1$ *we find that* $\boldsymbol{m}_{exc} = \frac{\sqrt[3]{2}\varepsilon\hbar^2}{\sqrt{\pi}e^2 l_B} \sim \sqrt{B_\perp}$*,*
- *For excitons with nearly zero momentum* $\boldsymbol{P} \approx 0$ *the magnetic length* $l_B$ *plays the role of the Bohr radius* $a_B$*, and*
- *Excitons with momentum* $\boldsymbol{P}$ *carry an electric dipole in a direction perpendicular to* $\boldsymbol{P}$ *with a magnitude* $\langle \tilde{\boldsymbol{r}} \rangle = \hat{z} \times \frac{\boldsymbol{P} l_B^2}{\hbar}$*.*

---

[4] An indirect-exciton is created when an electron and hole, separated in two different layers, join together in abound state via Coulomb attraction while still confined in the two separate layers. Indirect excitons are outside the focus of this dissertation.

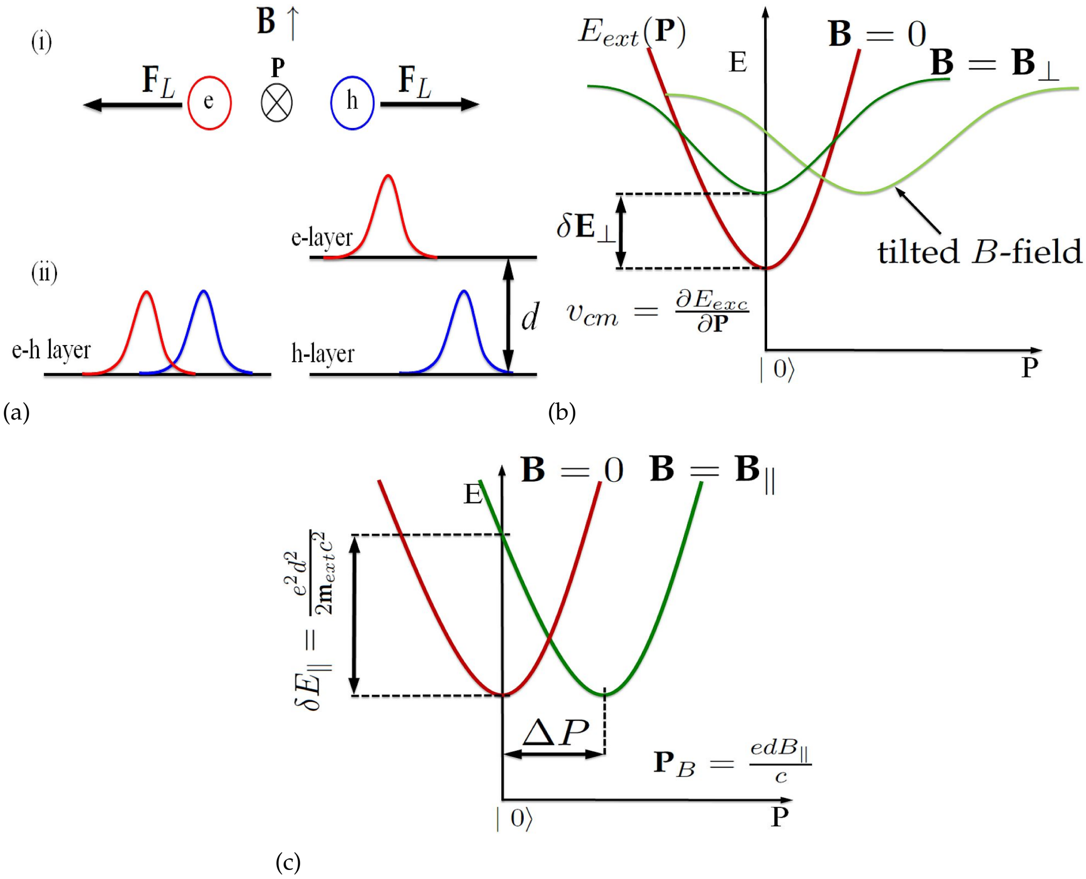

***Figure 6.6:*** (a-i) The force acting between the two charge carriers with (a-ii) the two different configurations of the direct- and indirect-excitons where the dispersion $E_{\text{exc}}(\mathbf{P})$ can be calculated from the Coulomb force between the electron and hole as a function of $\langle\tilde{r}\rangle$. (b-c) The effect of the magnetic field on the dispersion curve across the energy-momentum phase space. Clearly, tilted magnetic filed causes a shift along the energy axis and the momentum axis, simultaneously.

The last expression makes explicitly the coupling between the center-of-mass motion and the internal structure where the coupling results in an interesting property called the *electrostatic analogy*. This property entails that the dispersion $E_{exc}(\mathbf{P})$ can be calculated from the expression of the Coulomb force between the electron and hole as a function of $\langle \widetilde{r} \rangle$ with an important consequence that the exciton mass depends only on $B_\perp$ independent of the electron and hole masses with no scattering rate at zero magnetic field because the electron and hole pairs are in bound states.

The basic features of the direct excitons are determined by the coupling between the internal structure of the excitons and the center-of-mass motion when under the application of magnetic field. Due to the separation between the electrons layer and the holes layer, as shown in Figure 6.6(a), the binding energy and the effective mass of the indirect excitons differ quantitatively from that of direct excitons. The basic features for excitons within weak and strong magnetic field has been greatly investigated in [161].

### 6.4.1 Effects of magnetic $B_\perp$- and $B_\parallel$-fields on Excitons

As the separating distance between the electron and hole decreases, the binding energy increase in same scenario to that of separated layers of electron-hole pairs, i.e. indirect excitons, where $d$ play the same role. The picture might not be typical but the following boundary conditions are assumed to hold particularly at high magnetic fields

- ○ When $d \ll l_B$, $\mathbf{m}^{Bd}_{exc} = \mathbf{m}^{B}_{\text{exc}}\left[1 + \sqrt[3]{2}\left(\frac{d}{\sqrt{\pi} l_B}\right)\right]$ and
- ○ for $d \gg l_B$, $\mathbf{m}^{Bd}_{\text{exc}} = \mathbf{m}^{B}_{exc}\sqrt{\pi}\left(\frac{d^3}{\sqrt[3]{2} l_B^3}\right)$ [161].

Distinguishing the effects of the magnetic field on the excitons basic features mainly depends on the magnetic field direction. We can summaries the two principal directions magnetic $B_\perp$- and $B_\parallel$- directions as follows

- **Excitons under the application of $B_\perp$ magnetic fields**

Applying magnetic field perpendicular to the growth $z$-direction of the multiple quantum wells shifts the energy dispersion curve $E_{\text{exc}}(\mathbf{P})$ along the energy $E$-direction with no change in the excitons momentum causing a binding energy shift of $\delta E_B$, as illustrated in Figure 6.6(b). However, we experimentally demonstrated that a momentum shift can be induced along with the energy shift across the $k$-space by introducing a *tilt* in the magnetic potential as illustrated in the same Figure 6.6(b). The results due to the perpendicular magnetic field $B_\perp$ are concluded early at the beginning of Section (6.4).

- **Excitons under the application of $B_\parallel$ magnetic fields**

Parallel magnetic fields $B_\parallel$, i.e. the in-plane fields, cause the dispersion surface to shift along the momentum **P**-direction by amount of $\Delta\mathbf{P}$ as shown in Figure 6.6(c). As will be shown in the next chapter, increasing the in-plane field will increase the energy of the excitons due to the displacement of the dispersion surface in momentum direction where the results also show that the photoluminescence shift is smaller for the higher perpendicular field component.

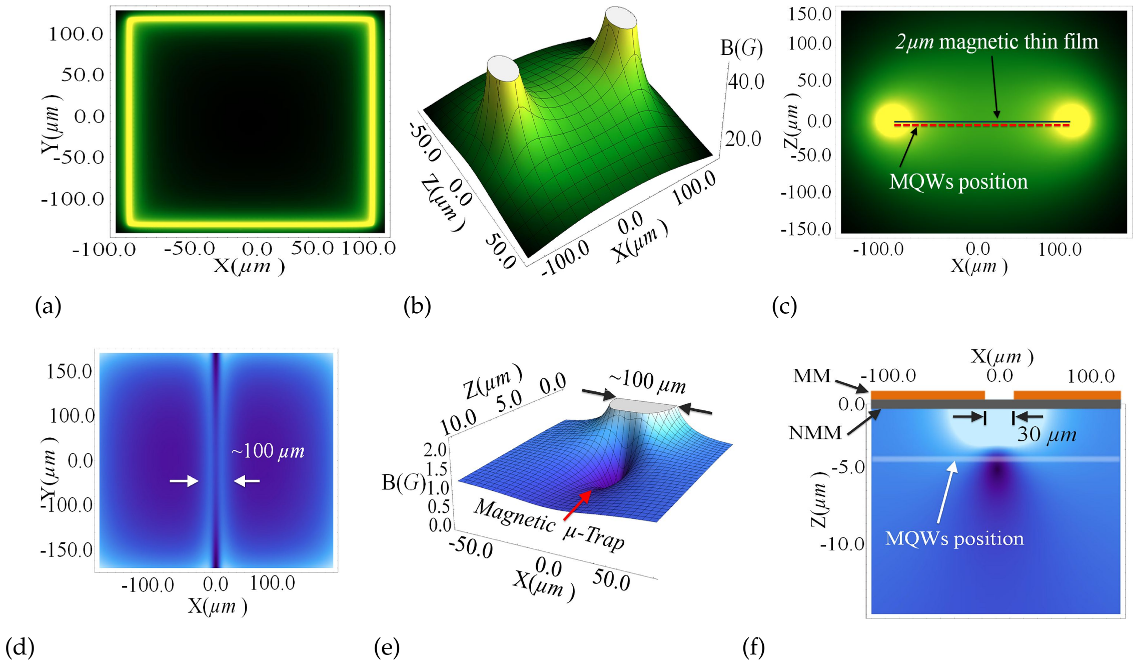

***Figure 6.7:*** The simulation of the magnetic field cover for the two different configurations (a-c) the plane cover with exaggerated high field at the edges and (d-f) the local minima created by the single-slit.

### 6.4.2 Localized magnetic fields and confinement of excitons

As a particular case, we investigated the effect of a localized magnetic field cover introduced by two configurations as shown in Figure (6.7). The configurations maintain nonhomogeneous distributions of the magnetic fields across the plane of the multiple quantum wells and along the growth direction in which case a localized variation of the basic features of excitons is measured. The Figures (6.8) illustrate the fields distributions where these configurations allow the multi-directional fields, i.e. $B_\perp$ and $B_\|$, to be presented along the excitonic motional axes in which case a pronounce photoluminescence shift, as explained above, was clearly visible.

We used the approach of the magnetic fields micro-trap to confine direct excitons in similar scenario to the confinement of ultracold atoms. These types of traps exhibit a sharp inhomogeneous distribution of the field which can be localized accurately within the plane of the quantum wells. Since the exciton are regarded as hydrogen-like atoms, their magnetic dipole moment interact with the magnetic potential fields while experiencing the gradient of the magnetic fields. It is also well known that these type of traps exhibit an exponential field gradient, as illustrated in Figure 6.8(b). Our trail is to examine whether or not the magnetic confinement mechanism is valid to test the hypotheses of the exciton BEC, where we relay on the fact that this approach has never been experimentally implemented. In the following chapter we present an experimental evidence of the magnetically trapped excitons.

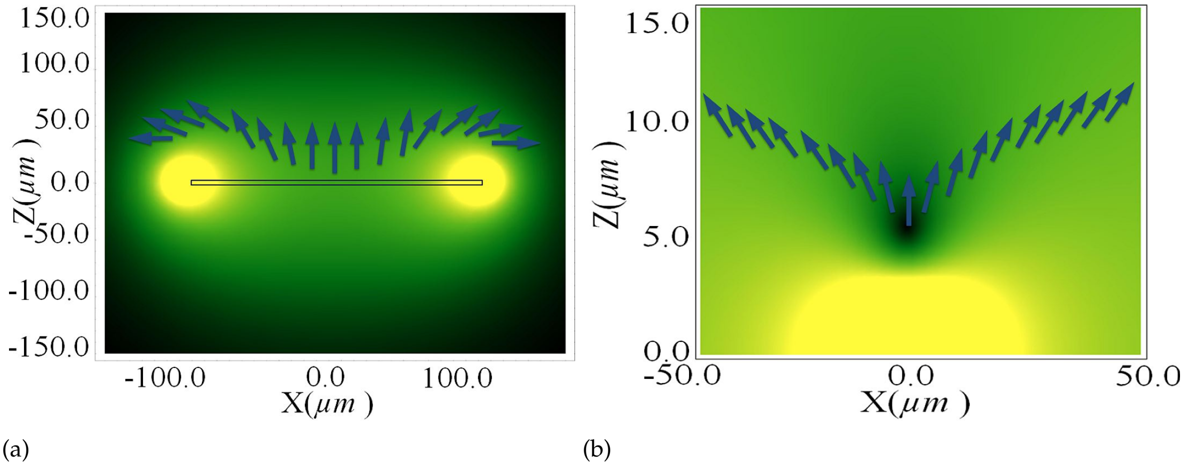

***Figure 6.8:*** Schematic diagrams of the magnetic field direction shows parallel and perpendicular patterns at the center and at the edges of the quantum wells confining plane.

Chapter 7

# EXPERIMENTAL REALIZATIONS OF MAGNETICALLY CONFINED EXCITONS

## 7.1 Overview

Special efforts have been recently paid to investigate the behavior of the excitons in strong magnetic field [162] where very interesting results have been reported such as observing a remarkable enhancement of the magnetic moments of excitons that resulted from their motion in an external uniform magnetic field or more specifically the induced mixing of $nP$ states into the $1S$ which is due to the hydrogenic nature of excitons [163]. Moreover, L. C. Smith *et al* have reported that the Zeeman splittings and the diamagnetism of excitons change as functions of the translational wave vector $K_z$ of the exciton in the growth direction of the well irrespective of the width of the well [164]. Most importantly, they have shown that the splittings of the excitons are found to be strong functions of the direction of the magnetic field as we also demonstrate such observation in this report. Also, L. Butov *et al* have shown strong dependency between the enhancement of the exciton effective mass and the increase of the external perpendicular magnetic field where at high fields it becomes much larger than the sum of electron ($e$) and hole ($h$) masses [165].

Relevantly, combining magnetic material with quantum well system has been theoretically proposed [166][167][168] and experimentally demonstrated aiming towards a localized magnetic field effect on the translational wave vector of the exciton. In particular, J. Leavy *et al* was able to image the influence of the locally disordered magnetic semiconductor heterostructures in the behavior of the excitonic spin [169]. Similarly, through the following experimental works we investigate the *spatial* inhomogeneous depression of the Zeeman splittings of the excitons, with respect to their translational wave vectors, due to the application of an inhomogeneous local magnetic field, e.g. magnetic field local minima, exhibited by a permanent magnetic material integrated with the multiple quantum wells system.

We assume that the magnetic material exhibits a field perpendicular to the growth direction and gradually increases from the center to the edge of the sample. The effect of the magnetic field is thought to enhance the excitons concentration where it was shown by Lerner and Lozovik and Kuramoto and Horie that strong magnetic field perpendicular to the well plane is important to improve the critical conditions for exciton condensation [170].

◇ **Related publications to this Chapter:**

1 A. Abdelrahman, H. Kang, S. Y. Yim, M. Vasiliev, K. Alameh, Y. T. Lee, "*Spatially resolved inhomogeneous depressions of the excitons Zeeman splittings in an integrated magnetic-multiple quantum wells system*," J. Appl. Phys. **110**, 013710 (2011).

2 A. Abdelrahman, H. Kang, M. Vasiliev, and K. Alameh, "*Magnetic micro-trapping of excitons in multiple quantum wells system using local field minima*," **Postdeadline**, the SPIE Photonics West meeting, Proceedings **7937**, 73 (2010).

3 A. Abdelrahman, H. Kang, M. Vasiliev, and K. Alameh, "*Inhomogeneous spin-dependent spatial distribution of excitons in an integrated magnetic-multiple quantum wells system*," **Postdeadline**, the SPIE Photonics West meeting, Proceedings **7937**, 74 (2010).

## 7.2 Sample Structure and Preparations

The GaAs/$Al_{0.35}Ga_{0.65}As$ multiple quantum well system is grown in GaAs substrate using molecular beam epitaxy. As shown in Figure 7.1(b), the sample structure consists of twenty layers of GaAs quantum wells and $Al_{0.35}Ga_{0.65}As$ barrier layers with a thickness of 9 nm and 20 nm, respectively. The permanent magnetic material $Bi_2Dy_1Fe_4Ga_1O_{12}$ is deposited on the surface of the GaAs/$Al_{0.35}Ga_{0.65}As$ multiple quantum wells system using rf-sputtering technique and annealed at 876.15 $K$, then it is permanently magnetized along the $z$-direction which is considered to be perpendicular to the multiple quantum wells growth direction. Figure 7.1(a) shows the integrated magnetic material with the multiple quantum wells structure. This configuration with an inhomogeneous localized magnetic field introduces a significant change in the symmetry of the $x/z$ and $y/z$-planes of distribution of the excitons, causing by that the observed behavior in the spatially resolved exciton concentration, as will be shown in the next sections.

The transmission and reflectivity profiles of the $Bi_2Dy_1Fe_4Ga_1O_{12}$ magnetic material create limits for the excitation pulse to be above the 600 $nm$ when using the magnetic material top side to measure the Photoluminescence signal, Figure (7.2). However, the effect of transmission profile takes no place when using the bottom GaAs substrate side in which case a 200 $\mu m$ thick is removed from the substrate using fine mechanical polishing to avoid the absorption by the GaAs substrate when measuring the photoluminescence signal allowing by that a 400 $nm$ excitation pulse to be used.

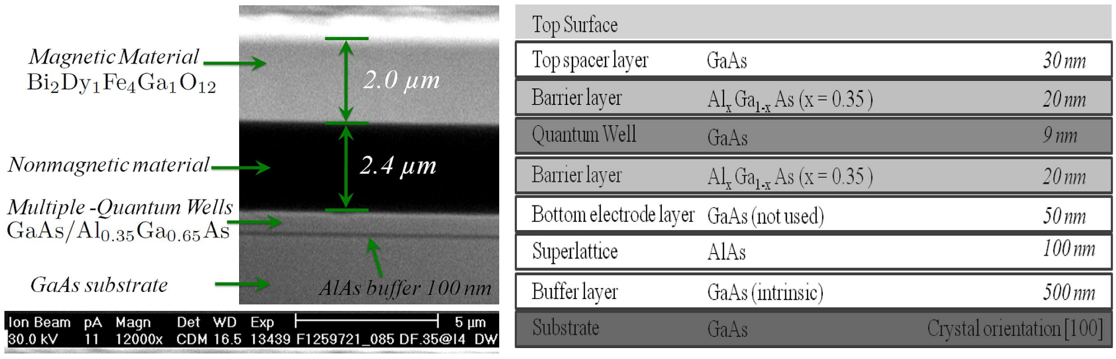

(a) (b)

*Figure 7.1:* (a) A focused ion beam image shows the internal structure of the integrated magnetic-quantum well system. (b) Details illustration of the system of multiple quantum wells, the magnetic material layer is not included in this schematic diagram.

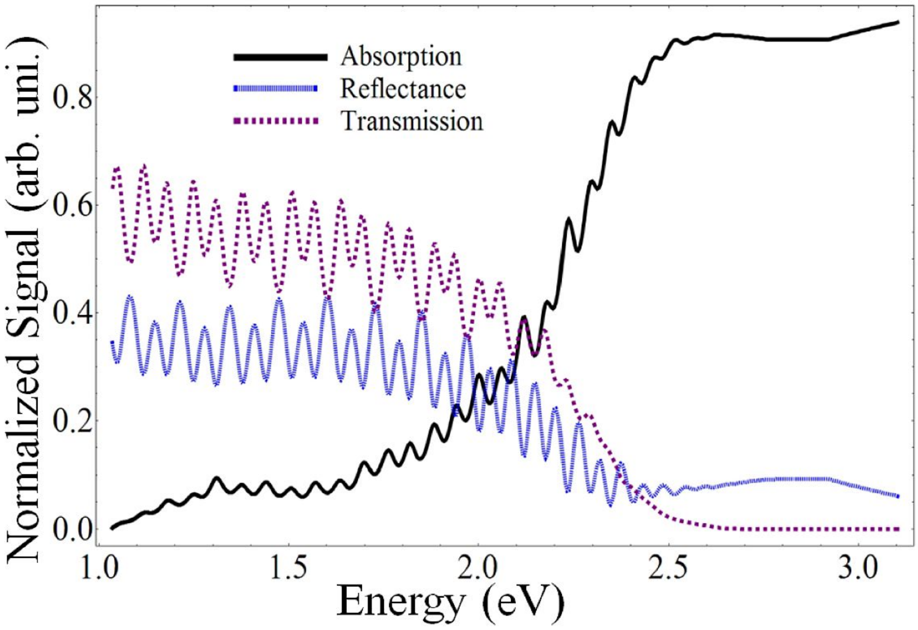

***Figure 7.2:*** Absorption, reflectance and transmission curves of the $\mathrm{Bi_2Dy_1Fe_4Ga_1O_{12}}$ magnetic material. The high absorbency above the 2.0 $eV$ limited the excitation pump to wavelengths above the 600 $nm$ for a high density of excitons.

The integrated magnetic multiple quantum wells sample is placed in an evacuated optical cryostat and cooled down in a helium path to 8 $\sim$ 9 $K$ to suppress the phonons interactions. A detailed schematic diagram of a similar optical cryostat that used in all of our experiments is shown in Figure (7.4) and its functionality is explained in the following section.

## 7.3 Experimental Apparatus and Setups

We performed three experiments regarding the weak magnetic field effect and its confinement on the excitonic quantum degenerate gases where the main equipments used to measure the effects are listed in Table (7.1) and the flow of the data collection is schematically represented in Figure (7.3). The details of the equipments are discussed within the following sections.

In the first experiment we measured the effect of an inhomogeneous magnetic field cover on the spatial distribution of excitons and their Zeeman splittings as explained in some details in section (7.4). In this experiment an evacuated optical cryogenic system is used to cool down the sample to 8 $K$, an automated stage is used to move the excitation beam across the sample $x/y$-plane and a beam of femtosecond ND: YAG Laser is purified before it enters the cryostat. The emitted photoluminescence is then collected and the desired transition energy range is selected via a monochromator where the signal is amplified by photomultiplier tube and presented in a computer screen.

The second experiment is devoted to investigate whether or not the magnetic field minima is suitable to confine the excitons. The $x/y$-plane of the multiple quantum wells system is scanned via the automated stage where an intensified charge-coupled device is used in a conjunction with the monochromator for instantly monitoring the highest transition energy peak, the details of this experiment are shown and discussed in section (7.5). In the third experiment, a similar setup to the first one was used with additionally implementing a Time-Correlated Single-Photon Counting scheme to measure the lifetime of the excitons. The experiment principle is demonstrated in section (7.6).

### 7.3.1 The cryogenic system

The integrated magnetic multiple quantum wells devices were maintained at a constant bath temperature by adjusting the heating power and the flow of helium vapor. The mounted devices were inserted into a socket embedded within a copper block and placed within the optically accessible sample chamber similar to the "Janis Super VariTemp (SVT) cryostat with optical access" shown in Figure (7.4). The chamber we used, shown in the left side of the same Figure, differs from the Janis chamber by not having the radiation shield around the sample holder.

| Device abbreviation | Functionality |
|---|---|
| SGH | Second Harmonic Generation |
| ND Filter | Neutral Density Filter |
| T. E. Cooler | Thermo-Electric Cooler |
| FPD | Fast Photodiode |
| HV/PS | High Voltage/ Power Supply |
| MCP PMT | Microchannel Plate Photomultiplier |
| CFD | Constant Fraction Discriminator |
| FPA | Fast Pre-Amplifier |
| ICCD | Intensified Charge-Coupled Device |
| TCSPC | Time-Correlated Single-Photon Counting |

***Table 7.1:*** Abbreviations list of devices used in all of the three experiments.

The sample is fixed to a die mounted on a flat metal sample holder facing the optical access window. At the thermal equilibrium, the sample position was approximately stable to be within 2 $\mu m$ where a capillary tube connects the sample space to a helium reservoir and helps to maintain thermal balance. The pumping rate was regulated but with no chances to suppress the mechanical vibration and the bottom of the sample cell was filled with superfluid He-3 at a temperature that is maintained to be around 8 $\sim$ 9 $K$. Cryogenics diode sensor attached near the sample which is used to monitor the near sample temperature via a separate digital display and a heater was attached to the sample holder and used to heat the medium to up to 70 $K$ for studying the temperature effect in the photoluminescence. Figure (7.5) shows the temperature effect on the energy peak lines of the exciton transition. The temperature effect is well known to be one of the evidence of the optical transition of the excitons.

### 7.3.2 Excitation sources and laser system

The optical transitions of the excitons were induced using continuous wave diode laser and femtosecond ND: YAG Laser with 150 fs, 76 MHz. These optical fields excitations are used to create the light-hole excitons and the heavy-holes excitons transitions, as shown in Figure (6.3) with a photoluminescence energy peaks as shown in Figure (6.5). In some experiments, specially the one that concerns the population intensities, a purification scheme was introduced in the optical path along with a gradient neutral density filter combined with other neutral density filters inserted to vary the excitation intensity over more than three orders

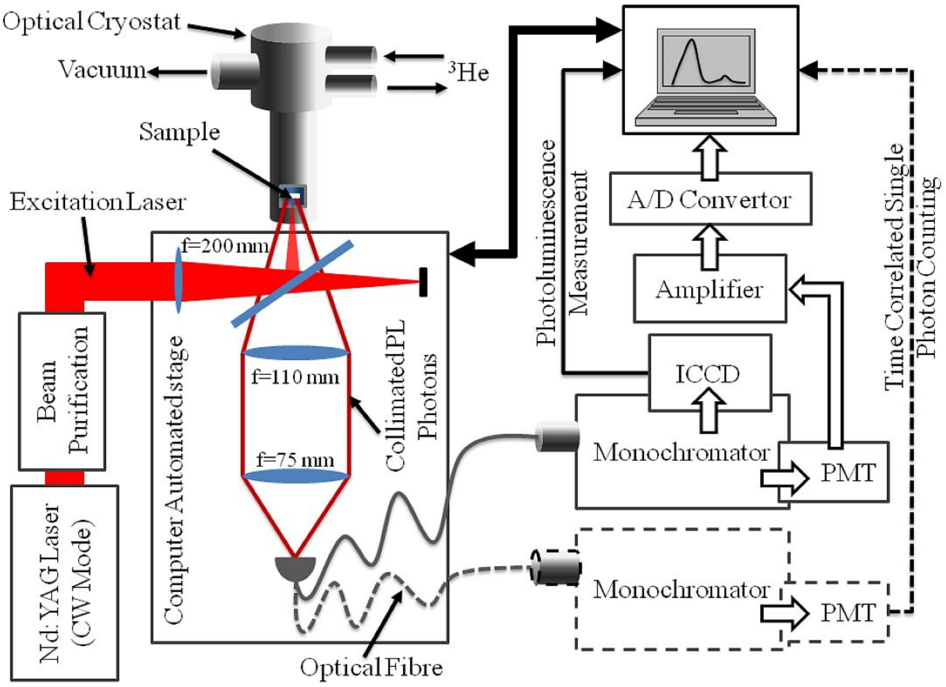

***Figure 7.3:*** Schematic diagram represents the experimental setups. Details of all experiments are shown through this chapter where the dashed line represent the different configuration of the measurement.

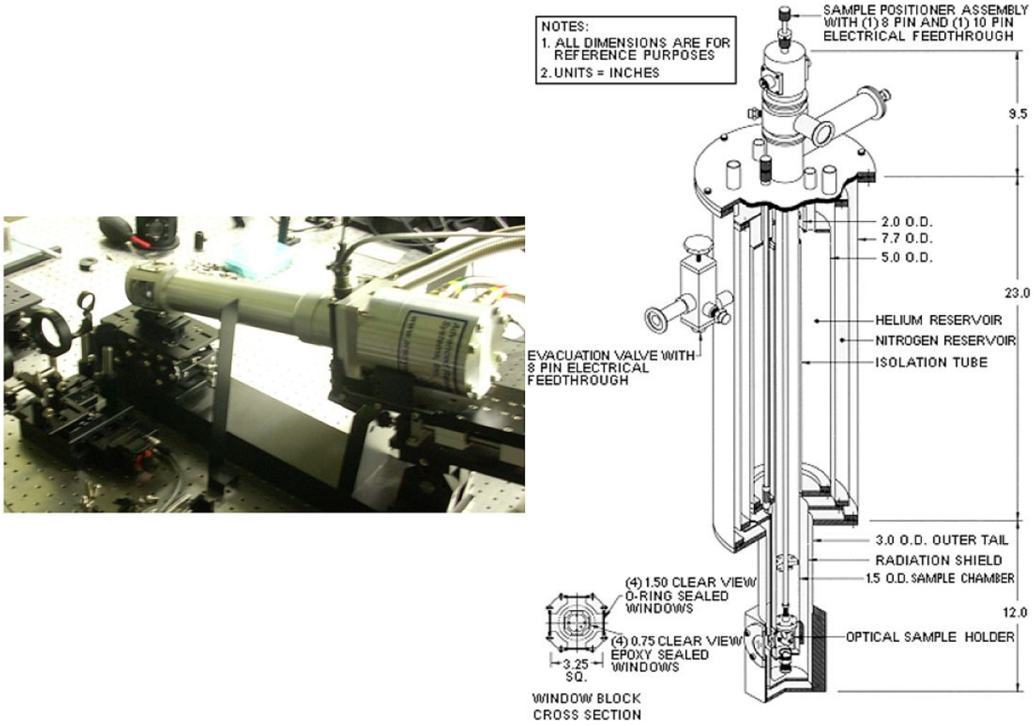

***Figure 7.4:*** (Left) The optical cryostat used in the experiment where the internal structure of the chamber is similar to that of (Right) the "Janis Super VariTemp (SVT)" cryostat with optical access.

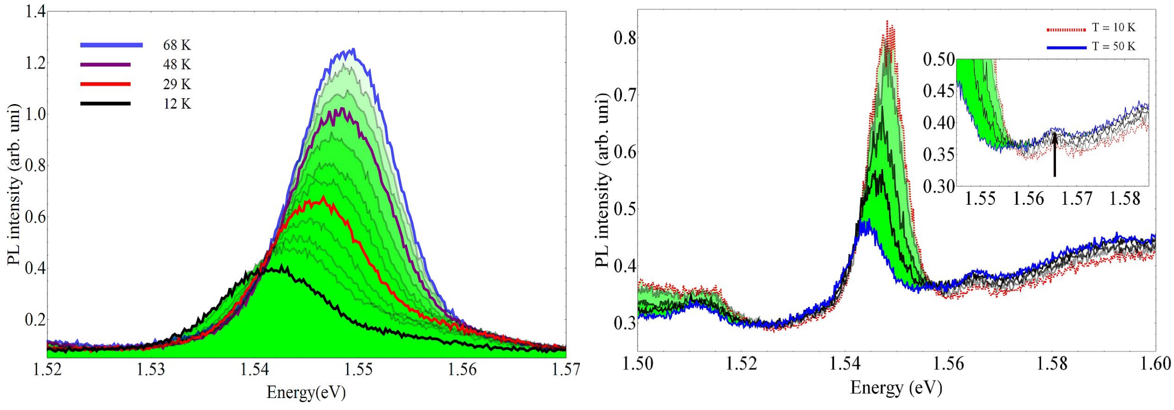

(a) (b)

*Figure 7.5:* Temperature effect on the peak energy of the emitted photon insures that the photoluminescence spectra is coming from the recombination of the HH and LH-exciton, the inset in (b) shows LH thermal shift. The photoluminescence is measured while the sample is magnetized.

of magnitude where they provide high resolution intensity control without introducing a gradient in the intensity distribution. Depending on the type of the experiment and the measurement, the laser beam was defocused by a combination of a lens and rotary holographic diffuser to a spot with a large diameter for uniform excitation and/or focused down to a minimum of 10 $\mu m$ diameter spot for localized excitation and probing.

Both the continuous wave diode laser and the femtosecond laser were set, in some experiments, at the 400 $nm$ excitation wavelength. However the femtosecond laser was also set at 798 $\sim$ 800 $nm$ below the GaAs excitation limits. The laser power was measured by an optical power meter before the laser hits the optical cryostat window in which case the laser power is deposited on the system of multiple quantum wells surface while taking into account the transmission loss in transversing the optical cryostat window.

- **On the photoluminescence measurement**

It is well known that the photoluminescence spectroscopy is highly selective and extremely sensitive when functioning as a probe for several types of critical measurements such as identifying the transition between the discrete electronic states and featuring the emission spectrum of the studied sample as a signal intensity peak energy. Moreover, the linewidths are commonly used in solid state devices to identify surfaces, interfaces, impurity states, gauge alloy disorders and interface roughness as well as determining the sample quality. Figure (7.6) shows the measured photoluminescence emitted from the integrated magnetic-multiple quantum wells sample embedded in a broadening background spectrum. It is important to show that, for pulsed excitation, the transient spectrum provides useful information on the decay process of the excitons, i.e. the lifetime, of non-equilibrium states. In addition, activated processes due to temperature often cause changes in the photoluminescence intensity, the linewidth, and the lifetime as measured from our sample and shown in Figure (7.5). These type of results provide useful information regarding the interactions among excited carriers of the confined quantum state.

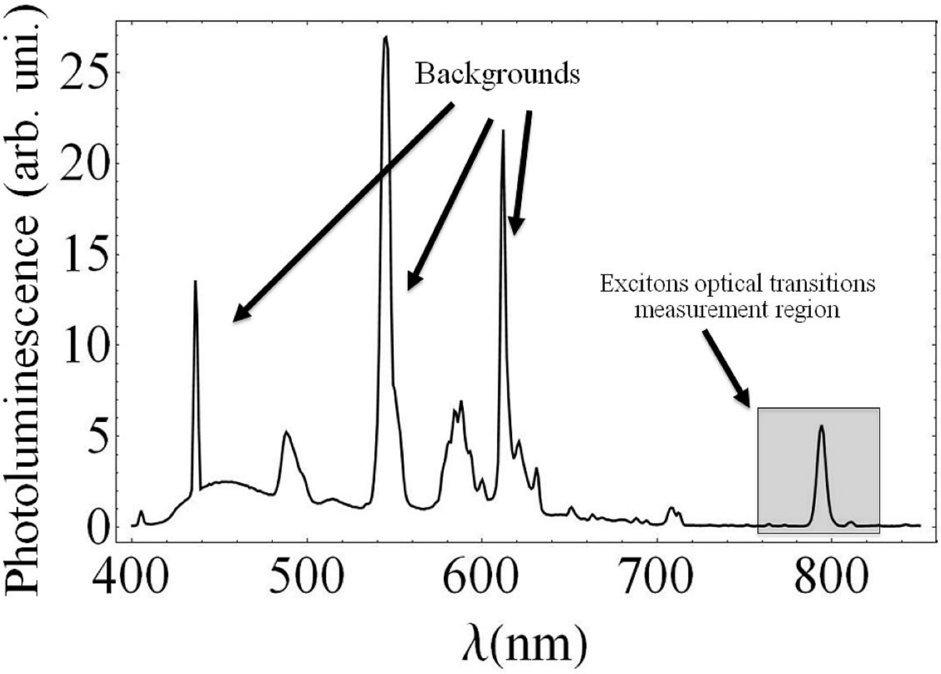

*Figure 7.6:* Measured photoluminescence with a wide detection range, i.e. 400 nm → 860 nm, where this initial scan was used to identify the excitonic transition energy zone and to eliminate the background fields.

## 7.4 Experiment I: Spatially Resolved Inhomogeneous Depressions of Excitonic Zeeman Splittings

### 7.4.1 Magnetic induced shift of the excitons dispersion surface in the $k$-space

As mentioned early in Chapter (6), it is well known that the exciton exhibits a hydrogenlike nature because of its composite particle internal motion where the electron and hole are mutually orbiting each other, plus the translational motion of their center-of-mass. We assume that the ground state of the exciton's two-particle motion has a finite momentum [181][182] and the optically active states are those for free excitons with momentum close to zero. They recombine in a radiative zone defined in the $k$-space by the intersection of the dispersion surface $E_{\text{exc}}(P)$ of the excitons with a photon cone defined as

$$E_{\text{ph}} = \frac{cP}{\sqrt{\epsilon}} \tag{7.1}$$

where $\epsilon$ is the dielectric constant [165][183][184]. A schematic representation of the intersection of the exciton dispersion curve in the momentum-space is shown in Figure 7.7(b). The exciton energy is defined as

$$E_{\text{exc}}(P) = -E_B e^{-\alpha} I_o(-\alpha) \tag{7.2}$$

where $I_o(-\alpha)$ is the modified Bessel function and $\alpha$ defined as

$$\alpha = (\frac{P l_B}{2\hbar})^2 \tag{7.3}$$

with $l_B$ being the magnetic length [185]. The momentum operator **P** of the center-of-mass in a magnetic field **B** is defined as

$$\mathbf{P} = \boldsymbol{m}_{\text{exc}} v_{cm} - \frac{e}{c}\mathbf{B} \times \mathbf{x}_{\text{exc}} \tag{7.4}$$

where $\mathbf{x}_{exc} = \mathbf{x}_e - \mathbf{x}_h$ is the relative coordinate of the excitonic electron-hole motion and $\boldsymbol{m}_{\text{exc}}$ is the effective mass of the exciton and $v_{cm}$ is the center-of-mass velocity.

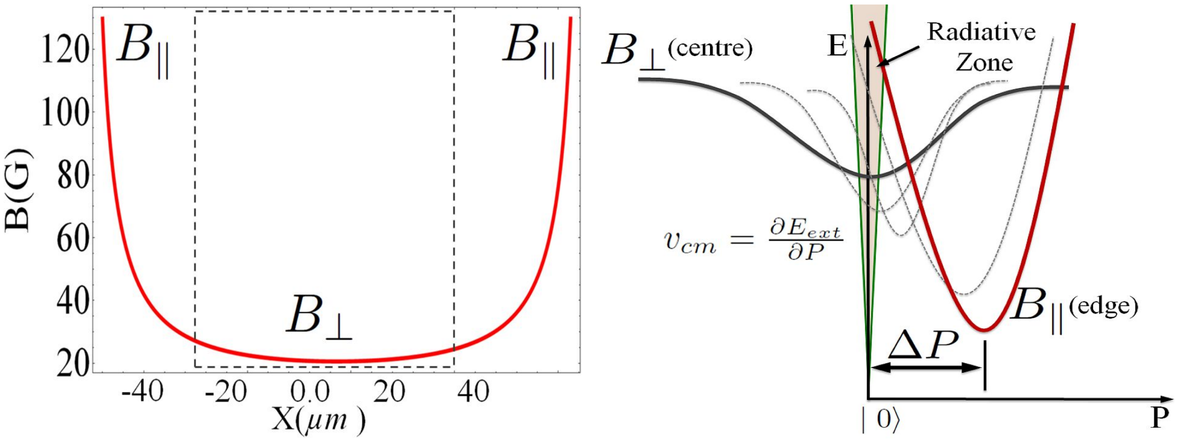

(a)

(b)

*Figure 7.7:* (a) Modeled magnetic field distribution along the x-axis showing the edge effect. (b) Schematic representation of the exciton dispersion curve shift in the $k$-space characterized by the center-of-mass velocity, $v_{cm} = \frac{\partial E_{\text{exc}}}{\partial P}$, where its intersect with the radiative zone (photon cone) also shifts along the energy direction due to the inhomogeneity of the magnetic field across the $x/y$-plane. The localized magnetic field varies from the $B_{\perp}$ field region at the center to the dominated $B_{||}$ field region at the sample edges

In our system, the inhomogeneous magnetic cover is imprinted at the quantum wells level where the field is generated by a semitransparent permanent magnetic material integrated with the multiple quantum wells system. The magnetic material is uniaxially anisotropic and its magnetization vector is perpendicular to the film plane. The inhomogeneity inherited in the field distribution is due to the edge effects where high field values occur at the edges, in which case the magnetic $B_{||}$ field is nearly parallel to the $x/y$-plane, and relatively magnetic $B_{\perp}$ field low values exist at the center where the magnetic field is pointing almost perpendicularly.

Simulated magnetic fields for a 200 $\mu m$ × 200 $\mu m$ and thickness of 2 $\mu m$ permanently magnetized thin film are shown in Figures 7.7(a) where the results show that maximum magnetic field, $B_{\text{max}}$, occurs at the edges of the sample and relatively low field, $B_{\text{min}}$, at the center with $M_z \approx 2.8\ kG$.

At the $B_{\perp}$ field region, the exciton states shift rigidly in $k$-space [186] and the recombination lifetime of the excitons is slightly modified by the localized inhomogeneous magnetic field without affecting their binding energy defined as

$$E_B = \frac{\sqrt{\pi}}{2e^2}/\epsilon l_B \sim \sqrt{B_{\perp}} \tag{7.5}$$

with $l_B$ the magnetic length defined as

$$l_B = \sqrt{\frac{\hbar c}{eB_\perp}} \tag{7.6}$$

Thus the migration of the dispersion surface in $k$-space is a function of the magnetic field and can be observed as changes in the transport properties of excitons. Meanwhile, at the dominated $B_\parallel$ field region, the dispersion curve departs away from the center of the photon cone in the $k$-space by the following shift in the momentum direction [184]

$$\Delta P = -\hbar k = \frac{e}{c} dB_\parallel \tag{7.7}$$

The dispersion curve departure is schematically represented in Figure 7.7(b).

### 7.4.2 The experimental setup

The integrated magnetic multiple quantum wells sample is placed in an evacuated optical cryostat and cooled down to $\sim 9\ K$ in a helium path to suppress the phonon interactions. In this experimental setup, a Ti:sapphire laser pump emitting a linearly polarized continuous wave (CW) with photon energy $\sim$ 1.724 $eV$ is used for excitation and delivered to the sample inside the optical cryostat via an automated pump scanning head.

- **The Automated Pump Scanning Head**

  A computer automated stage is assembled using Newport universal motion controller which is interfaced by a LabView program. The automated stage is fitted with a collimation system where lenses with $f = 110\ mm$ and $f = 75\ mm$ are used to collect the emitted photoluminescence photons from the integrated quantum wells system and focused into an attached optical fiber, as shown in Figure (7.3).

The photoluminescence signal is collected and transferred via an optical fiber to the monochromator which is swept across the transition energy spectral region surrounding the optically active state of interest $E \sim$ 1.547 $eV$. The photoluminescence signal is then fed electronically from a photomultiplier to be amplified and eventually monitored on the computer screen as illustrated in the schematic diagram of experiment's setup shown in Figure (7.8). The scanning head (i.e the automated head) is used to scan lines within the $x/y$-plane with a step size of 2 $\mu m$ by delivering a pump spot focused to a size of $\sim$ 10 $\mu m$ to the sample that mounted into the optical cryostat.

The data is collected by spatially resolving the photoluminescence signal across the $x/y$-plane of the sample, starting from the sample center towards the edges. Figure 7.9(a) shows enhanced emissions around the HH-exciton energy point measured at the $B_\perp$ field region where the intersection of the dispersion curve and the radiative zone is expected to shift in the $k$-space with no change along the momentum direction. However, due to the inhomogeneity of the localized magnetic field a migration of the intersected zone across the $k$-space occurs towards a region where $B_\parallel$ is dominant. This behavior can be identified as a shift in the energy peaks of HH-excitons which occurs due to the depressions in the Zeeman splittings and a reduction in their photoluminescence intensities, as shown in Figure 7.9(b). Meanwhile, as shown in the inset of Figure 7.9(a), a detectable conversion between the HH-excitons and the LH-excitons occurs when scanning the photoluminescence signal across the $x/y$-plane from the center towards the edges.

In general, one would expect the dispersion surface to behave as the exciton Bohr radius changes due to the magnetic field (comparing the e-h relative coordinate to the magnetic

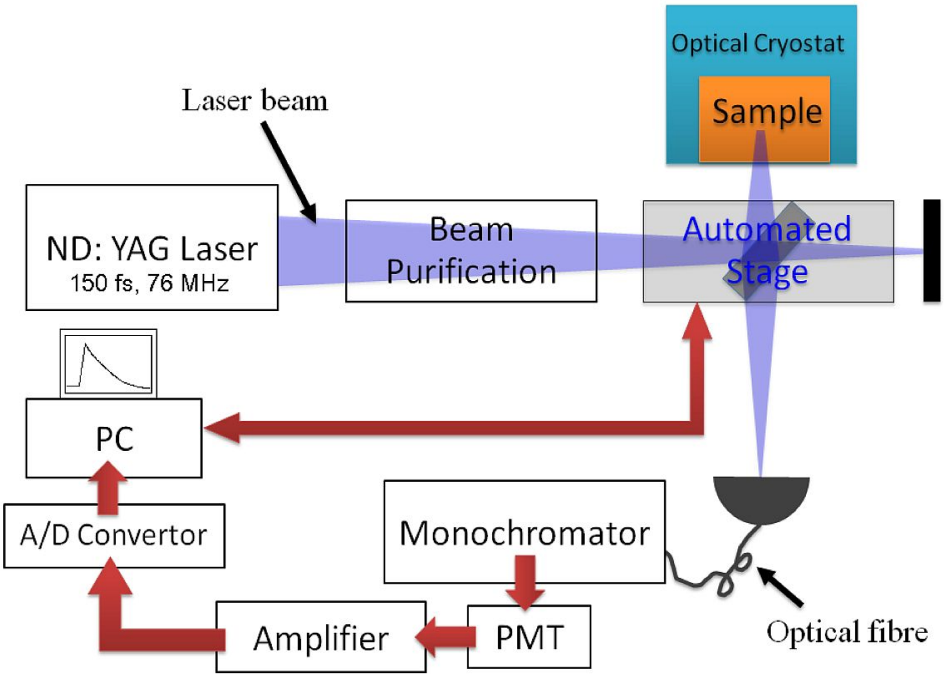

*Figure 7.8:* The setup for Experiment I. The beam purification part consists of the main components a 50/50 beam splitter and a $\lambda/4$ wave plate which is used to purify the degree of polarization for the excitation laser. The automated stage is controlled by a computer LabView interface where the step size of the moving part can be accurate to around 2 $\mu m$ step size.

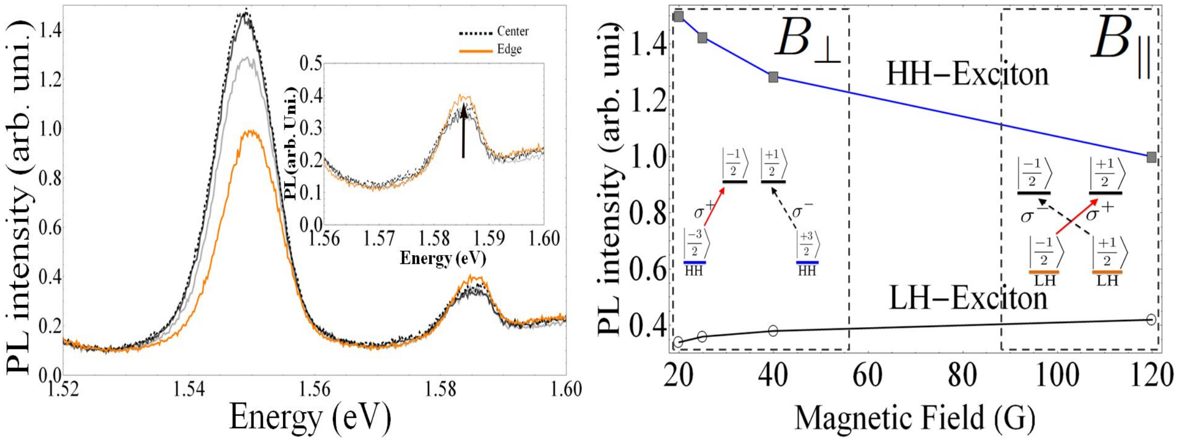

(a)

(b)

*Figure 7.9:* (a) Measured photoluminescence spectra across the $x/y$-plane, starting from the perpendicular magnetic field $B_\perp$ regions at the center towards the parallel $B_\parallel$ field regions at the edges of the sample. A linearly polarized continuous wave (CW) excitation pump of energy $\sim 1.724\ eV$ is used and the emission is probed at $\sim 1.55\ eV$. The inset shows the spatially resolved conversion of the LH-excitons. (b) Extracted photoluminescence maxima (related to peaks energy) (a) which shows two different regions of two different optically active states of HH and LH-excitons.

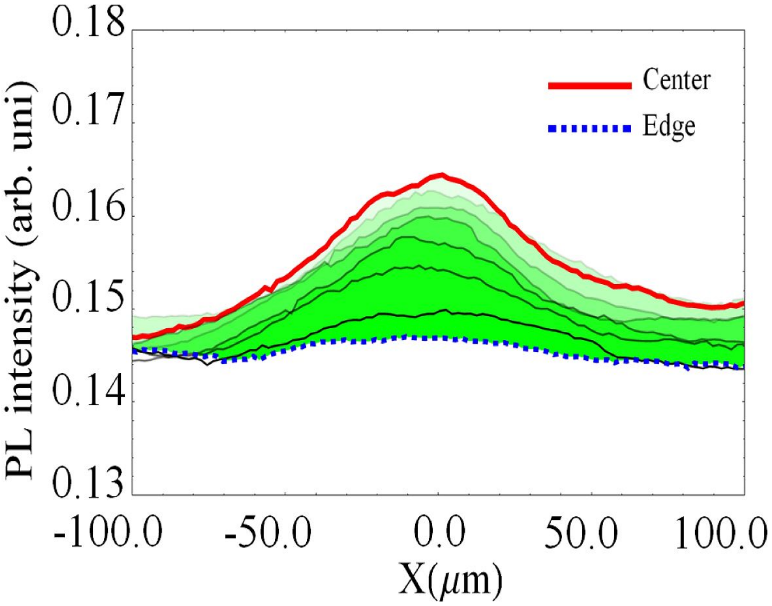

***Figure 7.10:*** Spatially resolved photoluminescence spectra of energy $\sim 1.55\ eV$ corresponding to the optically active $|\frac{\pm 3}{2}, \frac{\mp 1}{2}\rangle$ HH-exciton states. An automated focused-pump scanning head is used to scan the $xy$ plane with steps of $\sim 2.5\ \mu m$ along the $x$-axis and $\sim 10\ \mu m$ along the $y$-axis, using a linearly polarized CW excitation pump of energy $\sim 1.724\ eV$.

length $d \sim l_B$). We believe that the spatial conversion is happening because the optically active states of the HH-excitons $|\frac{\pm 3}{2}, \frac{\mp 1}{2}\rangle$ and these of the LH-excitons $|\frac{\pm 1}{2}, \frac{\mp 1}{2}\rangle$ suffer slightly inverted modifications in their magnetic lengths (thus depression in Zeeman splittings) depending on the value and the direction of the localized magnetic field which itself gradually changes across the $x/y$-plane. The effect of the localized field on the LH-exciton is weak as also reported by J. J. Davies $et\ al.$ [163] using strong magnetic bias fields. Accumulation of the HH-excitons at the center is shown in Figure (7.10) in which case the scanning probe is adjusted to record only the emitted photons with energies surrounding the transition of the HH-exciton states, i.e. $E \sim 1.547\ eV$.

### 7.4.3 Spatial spin-dependent distribution of heavy-hole excitons coherent states

The magnetic field values as depicted above, project an inhomogeneous distributed map of the heavy-hole excitons population across the $k$-space due to their field dependent ground momentum-states. At regions where $B_\perp$ field is dominating in the $k$-space, the intersection of the excitons dispersion curve shows steady energy splitting and presents a longer lifetime than that for excitons at the edges as will be shown in section (7.6). Meanwhile, the Zeeman splittings of the excitons suffer a depression at the edges, where the magnetic $B_\|$ field is dominant. In other words, the Bohr radius of the excitons becomes a field dependent and can be characterized by the magnetic length $l_B = \sqrt{\frac{c\hbar}{eB_\perp}}$. As shown in Figures 7.11(c-d), the energy gap between the two spin states $|\uparrow\rangle$ and $|\downarrow\rangle$ is large at the $B_\perp$ field regions (at center) and gradually changes to small at the dominated $B_\|$ field regions (at edges). These results show that the spin-state of the exciton depends on the field strength and its direction. It also indicates that the exciton magnetic dipole moment seems to have inhomogeneous localization influenced by the inhomogeneity in the magnetic field distribution. Figures 7.11(a), shows the magnetic field-dependent population after resolving the photoluminescence spectra at

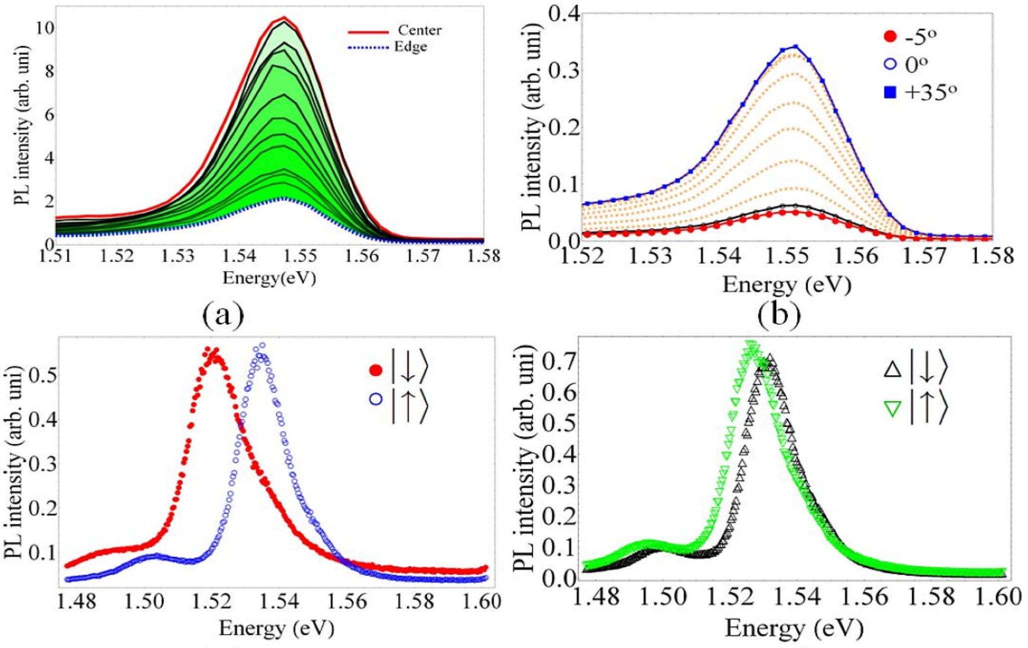

(a) (b)

(c) (d)

***Figure 7.11:*** (a) Spatially resolved photoluminescence spectra at the populated two magnetic field regions, $B_{\perp}$-field at the center and $B_{\parallel}$ field at the edge and (b) the PL intensity (population density) dependence on the degree of the polarization ($\sigma^{+}$ in this case). (c-d) A large energy splitting occurs between the two optically active states $\sigma^{+} \equiv |\uparrow\rangle$ and $\sigma^{-} \equiv |\downarrow\rangle$ at the two fields regions, (c) $B_{\perp}$ and (d) $B_{\parallel}$.

the two regions (center and edge) and Figures 7.11(b) shows the polarization $\sigma^{+}$ dependency.

## 7.5 Experiment II: Magnetic Micro-Confinement of Excitons

In quantum heterostructure, the presence of a confining potential along certain direction causes the motion of excitons to be quantized along that direction in discrete levels in which case the quantized motion of the electron-hole composite can be, adiabatically, restricted to two dimensions, allowing by that to introduce an inhomogeneous in-plane stress and gain an *additional* degree of confinement [177][178][179]. Due to the former observations, special attention has been recently paid to investigate the confinement of excitons using inhomogeneous magnetic fields [166][168][180], making use of the fact that in weak magnetic fields the trapping energy of the exciton is positive and the excitonic states are unbound states with large parts of their center-of-mass wavefunctions sufficiently extend in the confining space [168].

After tremendous theoretical [171][172][173][174] and experimental [132][175][176][165] efforts, it is now obvious that the two-particle composite (exciton) shows two extreme cases of behavior based on the system dimensionality $d$, the number of excitons $n$ and their Bohr radius $a_B$. At the limits $na_B^d \ll 1$, excitons form a dilute gas of rigid Bosons that undergoes Bose-Einstein condensation (BEC), while at the boundaries $na_B^d \gg 1$ the phase signature belongs to the BCS superconducting state, though the excitons still, under certain circumstances, maintain a smooth transition to the BEC state [171].

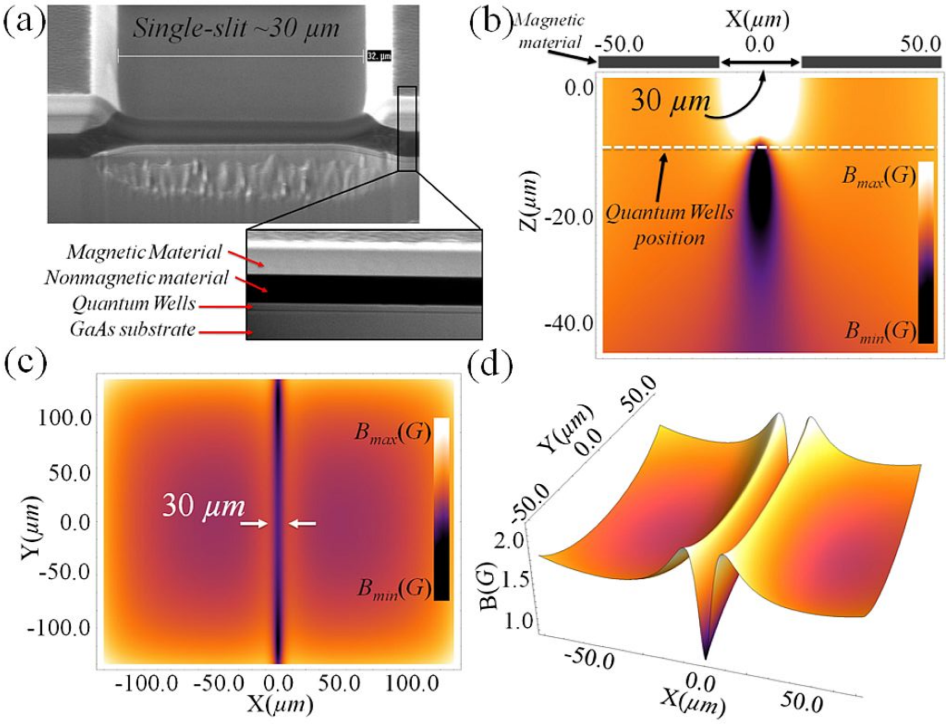

*Figure 7.12:* (a) A focused ion beam image of the internal structure of the integrated magnetic multiple quantum wells system. (b) Density plot representation of the magnetic field local minima simulated across the $x/z$-plane. The dotted line shows the location of the multiple quantum wells system. (c) Density plot and (d) 3D plot of the magnetic field simulated at the position of the multiple quantum wells.

Through this experiment we propose a simple method to create and to position magnetic field local minima within a system of multiple quantum wells. The quantum wells are integrated with a permanently magnetized material and the localized magnetic field minimum is a projection of a specifically patterned structure through the magnetic material. The projected local minimum is used to magnetically confine a two-dimensional Bosonic gas of excitons allowing by that to consider the proposed method as a possible pathway for achieving Bose-Einstein condensate of excitons.

- **Projected magnetic field local minima within multiple quantum wells system**

As demonstrated in the early chapters, the magnetic field local minima $B_{\text{min}}$ is realized by milling a specific pattern in a magneto-optic thin film of thickness $\tau$ in which case the pattern extends through the thin film down to the surface of the underlying layers. The presence of the pattern(s) disturbs the magnetic field distribution resulting in local field minima that appears, at an effective $d_{min}$ distance, above the top side and beneath bottom side of the pattern(s). The region of the local $B_{\text{min}}$ is surrounded by magnetic barriers $\Delta B(\mathbf{x})$ that define the space of the confinement and determined by

$$\Delta B(\mathbf{x}) = |B_{\text{max}}(\mathbf{x})| - |B_{\text{min}}(\mathbf{x})| \tag{7.8}$$

with $\mathbf{x} \equiv (x, y, z)$. The trapped excitons experience transverse trapping frequencies $\nu_{x,y}$ that depend on the gradients of the magnetic field along the confining directions and on the Zeeman (sub) levels of the excitons. For the case of a harmonic potential the trapping frequency is given, same as in the case of cold atoms, by

$$\nu_k \approx \sqrt{\mu_B g_F m_F \frac{\partial^2 B}{\partial k^2}} \tag{7.9}$$

where $k = x, y$, $g_F$ is the Landé g-factor, $\mu_B$ is the exciton Bohr magneton, and $m_F$ is the magnetic quantum number of the exciton (hyperfinelike) state. The depth of the harmonic potential trap, $\Lambda_{\text{depth}}$, is determined by the values of the magnetic local minimum and expressed as

$$\Lambda_{\text{depth}}(\mathbf{x}) = \frac{\mu_B g_F m_F}{k_B} \Delta B(\mathbf{x}) \tag{7.10}$$

with $k_B$ is the Boltzmann constant. Simulated maps of the magnetic field local minima are shown in Figure 7.12(b-d) for a magnetized sample of size 200 $\mu m \times$ 200 $\mu m$ with a single-slit of sizes 30 $\mu m \times$ 150 $\mu m$ patterned at the center. The magnetization is simulated to be perpendicularly pointing to the growth direction of the quantum wells with $M_z \approx 1.0\ kG$, while the existence of the pattern disturbs the uniformity of the magnetic field distribution and creates the minimum field point at an effective distance $d_{\text{min}} \approx 6\ \mu m$ from the bottom surface of the magnetic material beneath the slit pattern.

The number of trapped excitons $N_{\text{exc}}$ also depends on the magnetic trap width $\triangle_W$ and the trap depth, $\Lambda_{\text{depth}}$. This is a case of a harmonic potential well surrounded by magnetic barriers of the hight $\Delta B(\mathbf{x})$ where, depending on the magnetic depth, a tight confinement can be exhibited by milling narrow patters as shown in Figure 7.13(d-f). From these observations, we noticed that small slit sizes, 1 $\mu m \rightarrow$ 3.5 $\mu m$, generate lower magnetic field values and create by that deep magnetic potential wells and tight confinement which can be precisely allocated within the multiple quantum well system. For such trapping mechanism the magnetic field is approximated by

$$B \ll \frac{\hbar \triangle \eta}{\mu_B g_F m_F} \tag{7.11}$$

where the hyperfine splitting $\triangle \eta$ is larger than the Zeeman splitting.

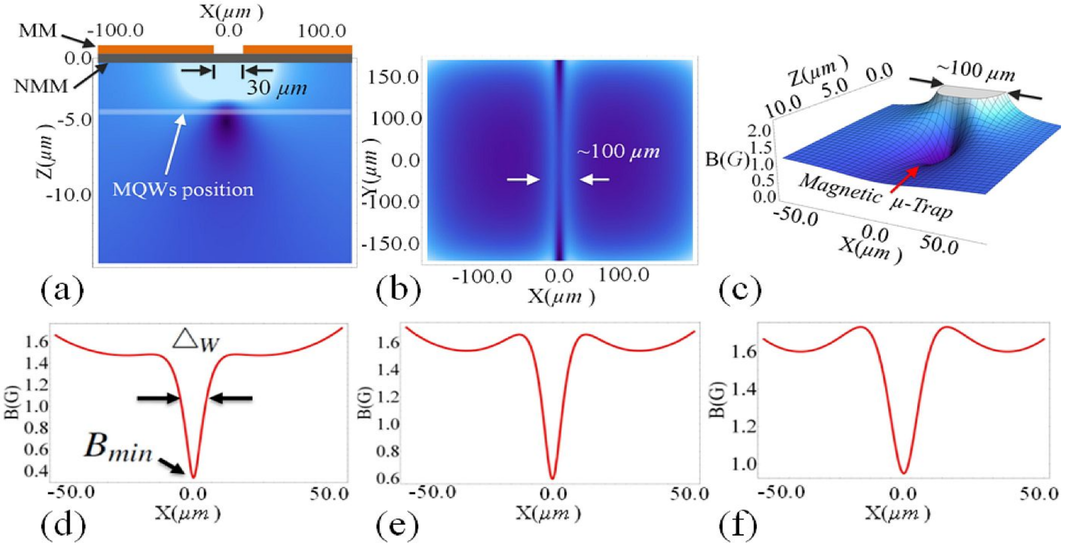

*Figure 7.13:* (a-b) Density plot of the simulated magnetic field local minima which is created at the location of the quantum wells. (c) 3D plot of the local minima showing the depth of the trap with respect to the slit width. (d-f) Plots showing simulation results of the width of the potential well $\triangle_W$ and the local minima values $B_{\text{min}}$ that depend on the slit size, (d) 1 $\mu m$, (e) 2 $\mu m$ and (f) 10 $\mu m$.

As the excitons composite particle internal motion exhibits a hydrogenlike nature, the energy spectrum of the composite (bounded electron-hole) shows full quantization and enhanced spin degeneracy, where it is believed that the interaction of excitons with external magnetic field can dramatically elevate the critical phase to a condensate level [170]. The ground state of the exciton's two-particle motion has a finite momentum and the optically active states are those for free excitons which recombine at a narrow radiative zone with a momentum close to zero [183]. The radiative zone is defined in the $k$-space by the intersection of the dispersion surface $E_{\text{exc}}(P)$ of the excitons with the excitation photon cone $E_{\text{ph}} = \frac{cP}{\sqrt{\epsilon}}$, where $\epsilon$ is the dielectric constant [133][184].

The inhomogeneity of the magnetic field, exhibited by local minima, causes the shift of the dispersion curve in the $k$-space (similar to that caused by a tilted magnetic field) with exciton energy defined as in equation (7.2). For excitons with a finite momentum close to zero, $P \sim 0$, the magnetic length $l_B$ is comparable to the Bohr radius $a_B$ in which case for $l_B < a_B$ the spin part, of the dominant exciton states wavefunction, is mainly deformed and causes the Zeeman splittings. Therefore, and due to the neutrality, excitons feel the gradient of the effective magnetic potential and get attracted to regions where the magnetic field strength is minimum. Thus, the excitons can be regarded as they are prepared in low magnetic field seeking-states similar to cold atoms.

It has been theoretically predicted that for excitons with $a_B \ll l_B$ in a magnetic filed the ground state of the system is due to the $e$-$h$ interaction which can lead to an excitonic condensate with sufficiently extended center-of-mass wavefunction in the confining space, while for $a_B \gg l_B$ the ground state is for incompressible Fermi liquid or Wigner crystal of electrons and holes which is due to the $e$-$e$ and $h$-$h$ interaction. In our experiment the interaction mainly belongs to excitons interacting with the inhomogeneous magnetic field and controlled by the difference in their effective mass where the effective mass of the exciton strongly depends on the perpendicularly applied magnetic field in which case it becomes much larger than the sum of $e$ and $h$ masses.

### 7.5.1 The integrated magnetic-quantum wells system

Similar to the first experiment, the integrated sample consists of three different layers deposited as follows, the first layer is the GaAs/$Al_{0.35}Ga_{0.65}As$ multiple quantum wells grown on a GaAs substrate using molecular beam epitaxy where the sample contains twenty periods of 9 $nm$ thick of GaAs quantum wells and 20 $nm$ thick of AlGaAs barriers. The second layer is the non magnetic material gadolinium gallium garnet, $Gd_3Ga_5O_{12}$, deposited on the surface of the GaAs/$Al_{0.35}Ga_{0.65}As$ and the third layer is the permanent magnetic material $Bi_2Dy_1Fe_4Ga_1O_{12}$ deposited on the top of the other two layers using rf-sputtering technique. Then the integrated system is annealed at 876.15 $K$ and magnetized along the $z$-direction.

The single-slit pattern is etched using a focused high-intensity femtosecond laser beam and a 320 $\mu m$ thick is removed from the GaAs substrate, using mechanical polishing, to allow measuring the photoluminescence signal when using the bottom side of the sample because the $Bi_2Dy_1Fe_4Ga_1O_{12}$ has a low transparency below 600 $nm$ which limits the excitation wavelengths to be above that point when using the magnetic material top side to measure the photoluminescence signal.

We again consider a scenario for the magnetic field direction to be $B_\perp$ field perpendicular to the growth direction of the quantum wells at the magnetic bottom of the local minima, and gradually changes to almost dominated $B_\|$ field elsewhere, causing the observed enhancement in the photoluminescence signal, at the position of the local minima, for the selected optically active state of the heavy-hole excitons.

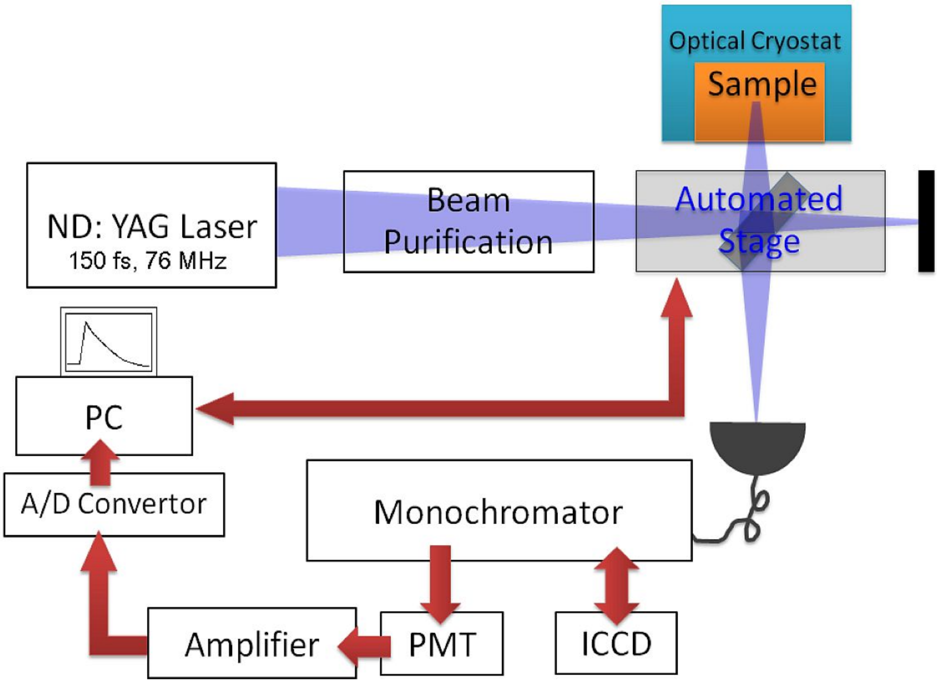

*Figure 7.14:* Setup of Experimental II which is similar to setup of Experiment but differs with the Intensified CCD part as explained in the text.

### 7.5.2 The experimental setup and results

The following experimental procedure is repeatedly mentioned in this section for a practical convenience.

- **The experiment**

*To suppress the phonon interaction, the integrated magnetic multiple quantum wells system is cooled down to 9 K using a helium path while mounted in an evacuated optical cryostat. A linearly polarized continuous wave (CW) Ti:sapphire pump laser of energy* $\sim 1.724\ eV$ *is used to excite the selected heavy-hole excitons (HH-exciton) state. The excitation signal is delivered to the mounted magnetic multiple quantum wells using an automated pump-scanning head that is integrated with a collimation system to collect the photoluminescence signal. Then, an optical fiber is used to transfer the collected photoluminescence photons to a monochromator integrated with a Peltier cooled ICCD camera.*
*The photoluminescence spectrum of HH-exciton state is then monitored after sweeping across the transition energy spectral region with the monochromator set to only read the energy of the desired optically active excitonic state,* $E = 1.547\ eV$*. The collected photoluminescence is converted to an electronic signal via a photomultiplier to be further amplified using a fast pre-amplifier.*
*The automated scanning head, with a pump laser focused down to a spot size of* $\sim 10\ \mu m$*, is used to spatially resolve the photoluminescence across the* $x/y$*-plane of the sample with step size of* $\sim 2\ \mu m$*. The experiment is repeated using right and left circularly polarized excitation waves,* $\sigma^+$ *and* $\sigma^-$*, respectively.*

- **The results and discussion**

Figure 7.15(b) shows high intensity values of a spatially resolved photoluminescence spectrum localized at the $B_{\text{min}}$ region beneath the single-slit at the effective distance $d_{\text{min}}$ within the multiple quantum wells system where similarly the photoluminescence signal is collected by scanning the $x/y$-plane along the $x$-direction. Due to the nonuniformity of both the deposited magnetic thin film and the nonmagnetic control layer, the local minima position is displaced along the confining $z$-direction which causes the modifications in the values of the $B_{\text{min}}$ and $\triangle B_{\text{min}}$ as the simulation results show in Figure 7.15(c) and as measured in Figure 7.15(d). $\triangle B_{\text{min}}$ is defined here as the difference between the actual $B_{\text{min}}$ value and the minimum value of the surrounding $magnetic\ valleys$[1].

We measured the thermal expansion of the confined cold excitons cloud by measuring the width of the spatially resolved energy peaks with respect to the temperature as shown in Figure (7.20). The effect of changing the polarization of excitation photons is shown in Figure (7.17) where right ($\sigma^+$) and left ($\sigma^-$) circularly polarized excitations pulses were used.

We also examined the effect of applying external magnetic bias fields along the $x$-axis ($B_{\parallel}$ parallel to the $x/y$-plane) and along the negative direction of the $z$-axis ($B_{\perp}$ perpendicular to the $x/y$-plane) as shown in Figure (7.20) in which case one can regard such behavior as a magnetically operated excitonic switch [187].

---

[1] We denote by magnetic valley the large regions that surround a single magnetic field local minima and acts as a reservoir that supplies the trap by th excitons.

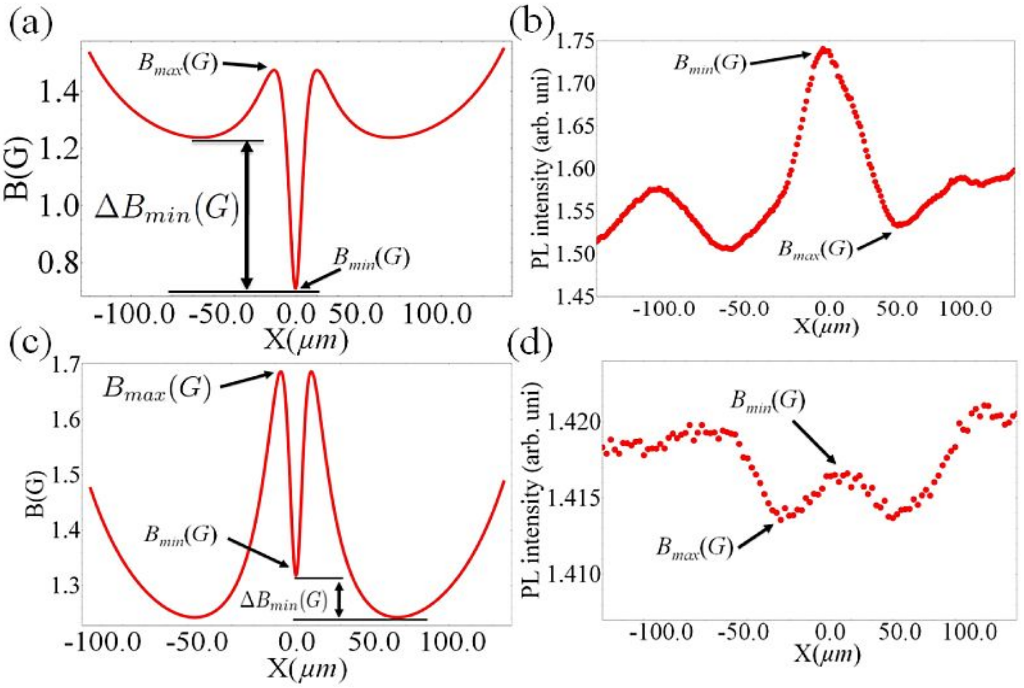

***Figure 7.15:*** (a) Simulated magnetic field local minima at the position of the multiple quantum wells, $d_{\text{min}} \approx 6\ \mu m$ and (b) the photoluminescence spectrum of the optically active state of the heavy-holes excitons at the energy peak of $E$ = 1.547 $eV$, spatially resolved at the quantum wells position below the single-slit. (c) Simulated magnetic field of a displaced minima and (d) the spatial distribution of the PL resolved across the displaced point. Simulation input: Thin film thickness $\tau \approx 2\ \mu m$, slit size $\sim 30\ \mu m \times 100\ \mu m$ and $M_z \approx 0.5\ kG$. Experimental parameters: CW excitation pump of $\sim$ 1.724 $eV$, $T \approx 9\ K$, and sample with the same parameters as used in the simulation.

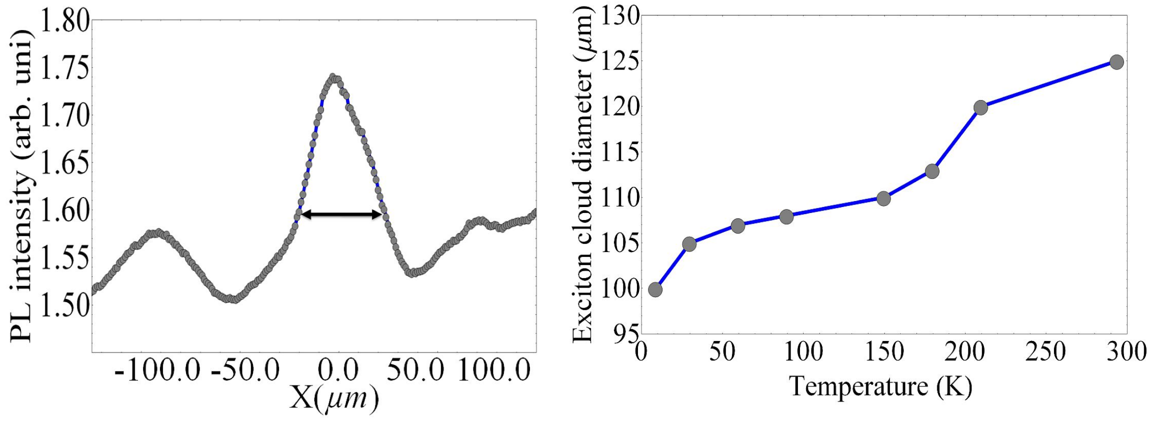

(a)

(b)

***Figure 7.16:*** (d) The thermal expansion of the excitonic cloud with respect to change in the background cooling temperature. The expansion also confirm that, since there is a room temperature excitons PL signal, the magnetic confinement can also work at room temperature.

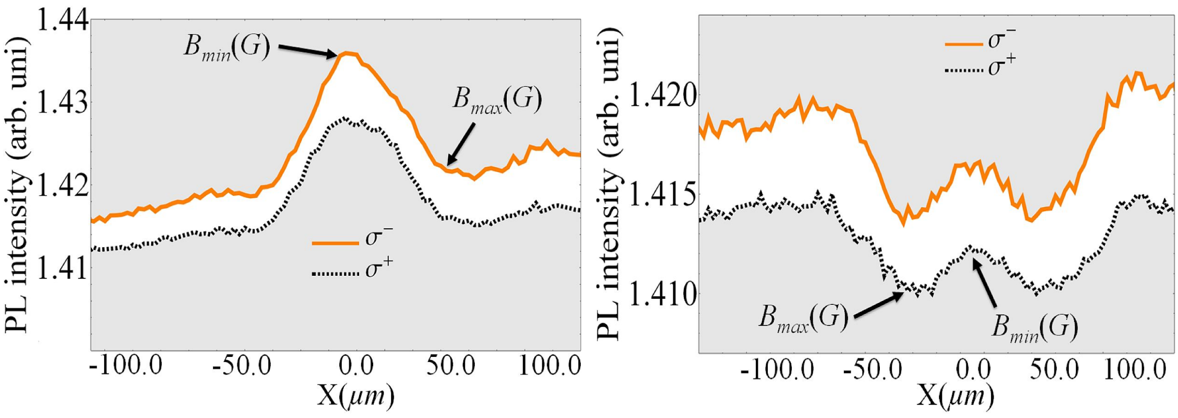

(a) (b)

***Figure 7.17:*** The effect of changing the polarity of the excitation photons using right ($\sigma^+$) and left ($\sigma^-$) circularly polarized pump.

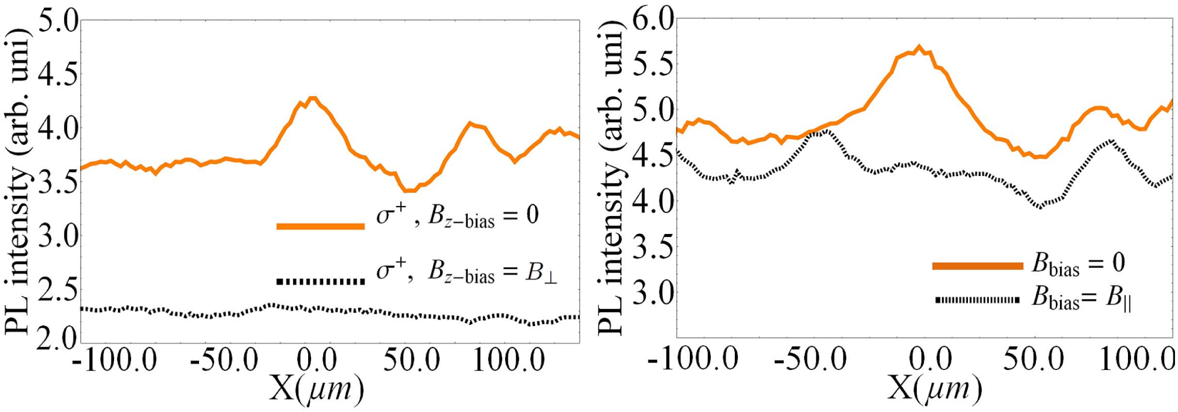

(a) (b)

***Figure 7.18:*** (a) The effect of applying external magnetic bias field along the negative direction of the $z$-axis where the cloud disappears because the application of the $z$-axis bias field elevates the trap bottom by several Gausses and hence less tightening the trap bottom and (b) the effect of applying magnetic bias field along the $x$-axis in which case the cloud is displaced along the axis of the applied magnetic bias field with slight change in the value of the trap bottom. The other maxima in the right side of Figure (b) is not due to the confinement and this is why it does not show any response to the external bias fields.

## 7.6 Experiment III: Magnetically Tunned Lifetime of Excitons

The lifetime of the excitonic particles in a relation to the temperature effect has been intensively investigated [183][188][189][190][191]. Considering the interaction between the excitons and the light in bulk materials we find that the excitons can not radiatively decay into photons due to the crystal momentum conservation. The exciton-photon interaction in bulk produces mixed modes, i.e. polaritons, which are stationary modes [191].

In quantum wells system, the breaking of the translational invariance along the growth direction changes the bulk picture. An exciton, which dresses in an in-plane momentum $\hbar k_{\|}$ state with the following condition, can interact with a one-dimensional continuous spectrum of electromagnetic mode

> *The exciton must have an in-plane momentum $\hbar k_{\|}$ that less than the resonant photon momentum $\hbar \boldsymbol{q}$.*

This results in an efficient radiative decay channel initialized by a macroscopic polarization that associated with the free exciton wavefunction. The recombination rates of the transverse and longitudinal excitonic modes can be estimated as

$$R(k_{\|}) = R_o \begin{cases} \frac{\mathbf{q}}{\sqrt{\mathbf{q}^2 - k_{\|}^2}} & \text{T-mode} \\ & \qquad (k_{\|} \leq \mathbf{q}) \\ \frac{\sqrt{\mathbf{q}^2 - k_{\|}^2}}{\mathbf{q}} & \text{L-mode} \end{cases} \tag{7.12}$$

where $R_o = \mathcal{S} \times 7.6 \times 10^8 \ \text{sec}^{-1}$ with $\mathcal{S} = 10^{-5}$ Å$^{-2}$ is the oscillator strength. Excitons with kinetic energy higher than the energy value $e = \frac{(\hbar \mathbf{q})^2}{2 m_{\text{exc}}}$ can not decay radiatively as long as the exciton-photon momentum mismatch in the above equation (7.12) is considered in which case only small fraction of the excitonic states are optically active with extremely short lifetime.

The acoustic phonon interaction with excitons is often considered to produce phonon-dressed excitons (not bar excitons) and the phonon-exciton scattering, with the assumption that the their scattering rate is larger than the recombination rate, it gives rise to the thermalization of the exciton population which reduces the coherence length making by that the phonon-exciton interaction less effective. The thermal equilibrium distribution of excitons states with different in-plane momenta produces an average decay time of the excitons population is given by

$$\langle R(\tau) \rangle = \frac{\int dE \rho(E) R(E) e^{-\frac{E}{k_B T}}}{\int dE \rho(E) e^{-\frac{E}{k_B T}}} \tag{7.13}$$

where $\rho(E)$ is the excitons density.

The relation between the temperature $T$ and lifetime of exciton $\tau(T)$ became significant at a bottleneck when increasingly small fraction of excitons become optically active, this bottleneck can read $\tau(T) = \frac{1}{R(T)}$. The following experimental results show the measured lifetime of the excitons under the above circumstances at a fixed temperature.

- **The experiment and results**

The setup of this experiment is basically the same as the previous two setups, however there are additional devices implemented in the setup for fast measurement. As shown in Figure 7.19(a), there is a microchannel plate photomultiplier (MCP-PMT) for detecting the

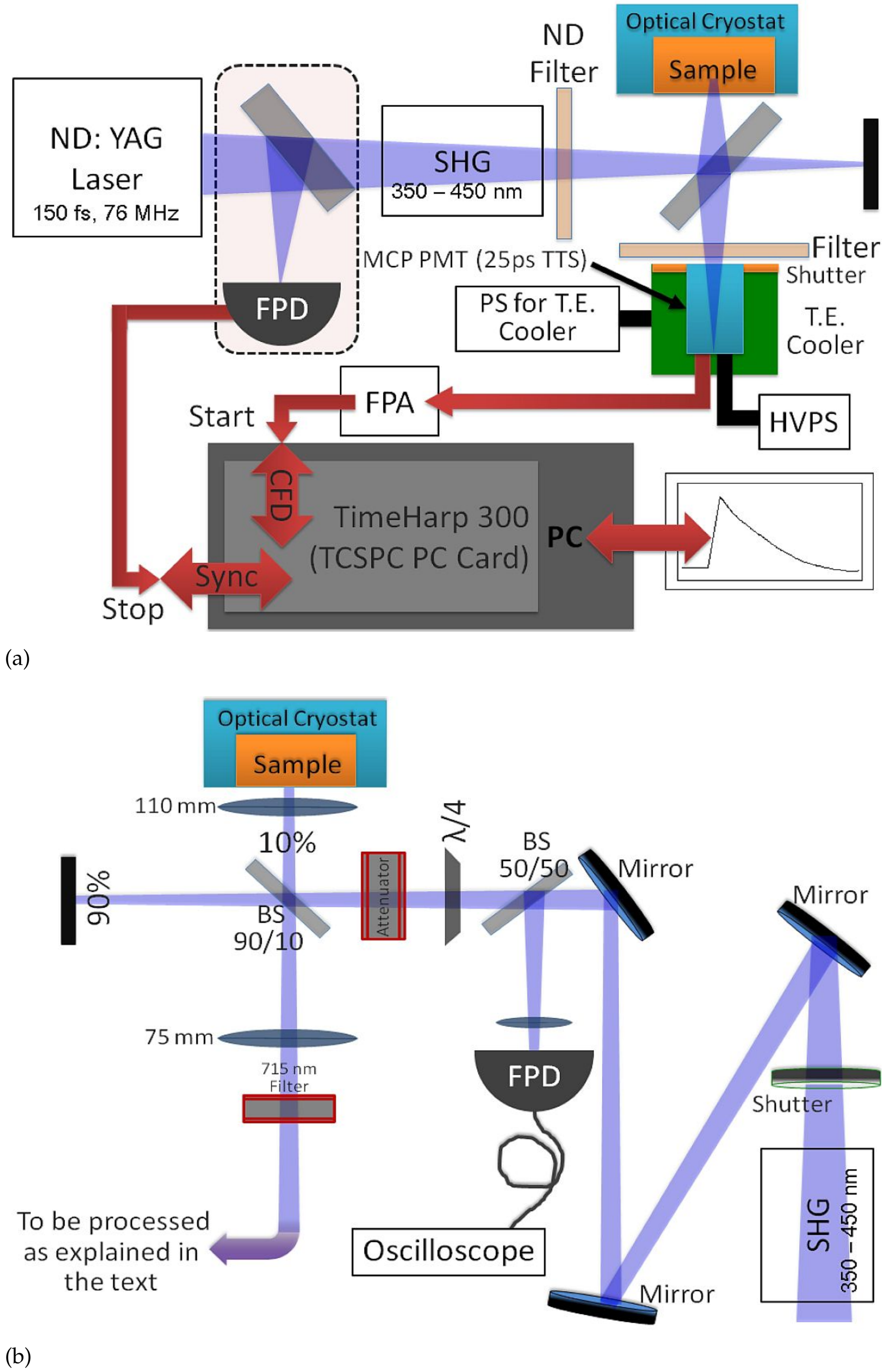

*Figure 7.19:* (a) The setup for Experiment III which is arranged to measure the lifetime of the excitonic particles using Time-Correlated Single-Photon scheme. (b) The detailed setup of the optical alignment where only 10% of the total beam is delivered to excite the electrons in the multiple quantum wells system.

photoluminescence emitted from the sample. The advantage of having the microchannels is to intensify single particles ( photons in this case) by the multiplication of electrons via secondary emission and more importantly is to provide a spatial resolution. The MCP-PMT is operated by a high voltage power supply operated at $\sim -3 \times 10^3 \ V$ and connected to a fast pre-amplifier which deliver the signal to a constant function discriminator (CFD). It is an electronic signal processing device that implemented to instantly carry the mathematical operation of finding the maximum value of a pulse by finding the zero of its slope. The MCP-PMT is also cooled down using a path of cold water.

The CFD is integrated in a computer system that contains a time-correlated single-photon counting (TCSPC) scheme which is a common technique in the field of ultrafast spectroscopy where it records very low level light signals with picosecond time resolution. On the other hand the whole setup is synchronized via a fast photodiode and monitored using an oscilloscope which shows a signal of synchronization stability with an amplitude of 50 mV.

The excitation pulse is produced by the femtosecond Ti:sapphire pump laser with a reputation rate of $7.6 \times 10^7$ ps $\sim$ 76 MHz which is adjusted using second harmonic generation to produce 400 nm pulse. When the second harmonic generation is not used a 700 nm pulse is used to illuminate the magnetic quantum wells system. The collimation and filtering setup is shown in Figure 7.19(b).

| Excitation Polarization | Position | Exciton Type | Delay Time $\tau_1$(ps) | Delay Time $\tau_2$(ns) |
|---|---|---|---|---|
| L. P. | Center | HH | $425 \pm 23$ | $3.024 \pm 0.074$ |
| | | LH | $419 \pm 159$ | $3.507 \pm 0.324$ |
| | Edge | HH | $468 \pm 10$ | $2.503 \pm 0.027$ |
| | | LH | $501 \pm 76$ | $3.302 \pm 0.112$ |
| R. C. P. $\sigma^+$ | Center | HH | $448 \pm 11$ | $3.297 \pm 0.024$ |
| | | LH | $469 \pm 36$ | $3.357 \pm 0.070$ |
| | Edge | HH | $560 \pm 6$ | $2.476 \pm 0.012$ |
| | | LH | $556 \pm 34$ | $3.337 \pm 0.041$ |

***Table 7.2:*** The delay time measured for heavy-hole (HH) excitons and light-hole (LH) excitons using linearly polarized light and circularly polarized light $\sigma^+$ with experimental conditions as specified in the text. L. P. and R. C. P. refer to linearly and right circularly polarized lasers, respectively.

We measured the lifetime of the light and heavy hole excitons under when the magnetic field cover is implemented within the multiple quantum wells system at a fixed temperature $T \approx 8 \ K$. Table (7.2) shows a comparison of the delay time measured at two different locations in the sample, namely center and edge, for both heavy-hole excitons and light-hole excitons. The photoluminescence decay curves in Figure (7.20) are fitted using the *PicoQuant FluoFit* software which uses the following intensity approximation

$$I(t) \sim \sum_{i=1}^{n} e^{-\frac{t}{\tau_i}} \tag{7.14}$$

with $n = 2$. As shown in the Figure (7.20), the photoluminescence decay processes slightly differ when measured at the two different radiative regions, the $B_\perp$ and $B_\parallel$ fields dominated zone. The results shown in these figures are generated using right circularly polarized $\sigma^+$ and linearly polarized excitation photons.

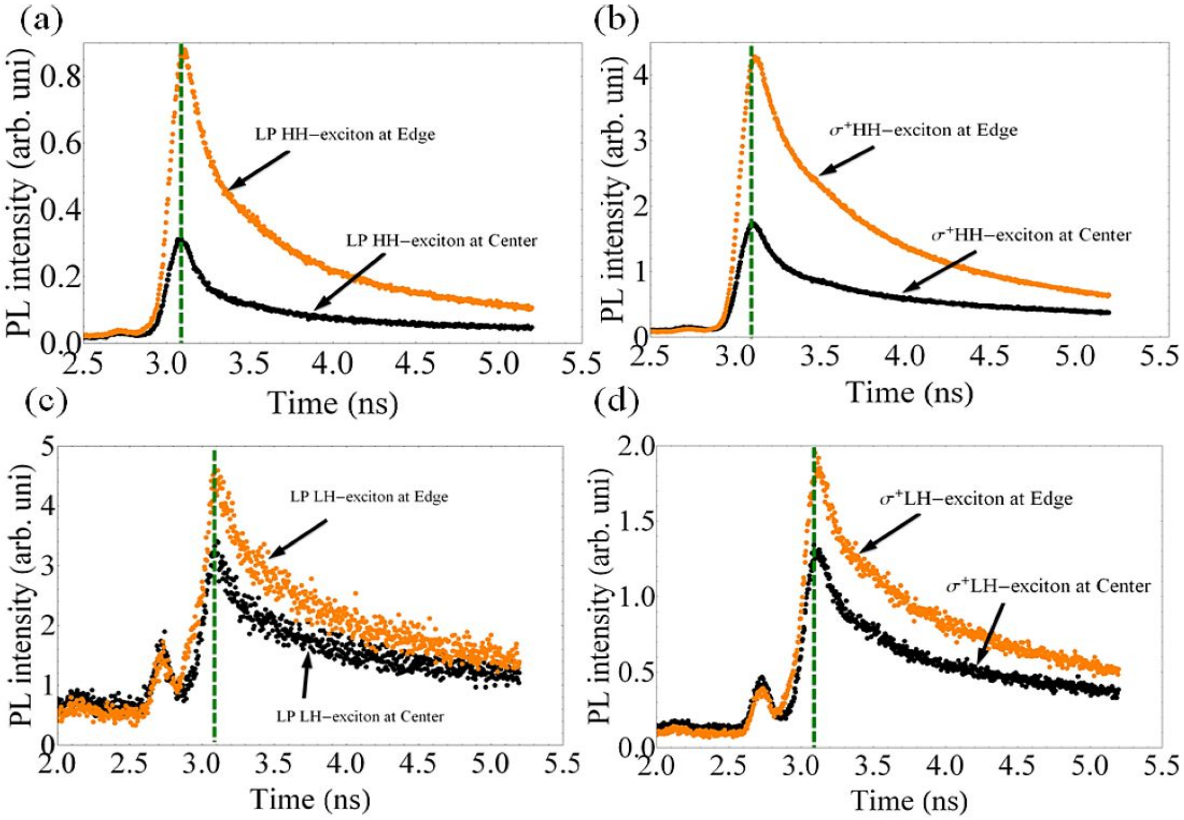

***Figure 7.20:*** Time correlated single photon counting (TCSC) measurements of the PL decay show a spatial dependence of the exciton radiative decay rate with respect to the localized inhomogeneous magnetic field. A linearly polarized pump (dotted line indicates the excitation pulse) is used to excite (a) the HH-excitons and (c) the LH-excitons at different locations within the $B_\perp$ and $B_\parallel$ regions, and a right circularly polarized $\sigma^+$ pump is also used to create (b) the HH-excitons and (d) the LH-excitons.

# Chapter 8

# Conclusion

## 8.1 Considering the Magnetic Micro-Confinement of Excitons as an Approach to Achieve the Excitons BEC

BY looking over the past thirty years, one finds that there have been many claims for observing the creation of Bose-Einstein condensation of excitons or maintaining a state of superfluidity. If we start by looking at the early claims for excitons in CuCl [216][217][218], $Cu_2O$ [219][220][221] and the condensation of excitons-polaritons coupled particles in microcavities [222] we find that they all have been followed by many disavowals and much debate [223][224][225]. The over all picture tells us that the primary objective is the experimental claims have been subject to multiple interpretation with inconsistent varies explanations, which has led all those who are pursuing theoretically or experimentally the fundamental questions regarding the creation of Bose-Einstein condensation of excitons to realize that it will be formidable to provide all the necessary details to explain the oddities in all the previous claims. We briefly cover in the following section some of the famous approaches to BEC of excitons.

The first claim relied on the observation of the temperature dependent photoluminescence linewidth in a system of coupled quantum wells [226]. The experiment encountered difficulties due the disorder of the substances interfaces for producing trapped excitons [227][228][229]. Recently, the indirect-excitons have been heavily investigated along with several claims of the formation of their condensation in systems of coupled quantum wells [130][133][230][231][232]. Stimulated bosonic scattering of excitons in highly statistically degenerate potential traps has been claimed by Butov et al. in which case their claim was based on the nonlinear dynamics of the photoluminescence [133][233][234]. But, it is later shown that the presence of the scattered photoluminescence, which comes from the substrate $n^+$-GaAs layers, is the reason for distorting the nonlinear photoluminescence dynamics when performing a spatially- and time-resolved photoluminescence measure on a system of coupled quantum wells. Also the observation of distant photoluminescence rings with an extended dark region between the ring and the excitation spot were reported [130][131] where they have been initially attributed to superfluid dark excitons or the macroscopically ordered excitonic coherent states. These observations were attributed to charge imbalance and in-plane charge transport [235] and the fragmented photoluminescence rings were interpreted as evidence of macroscopic ordered excitons states [236]. Extensive phase diagram of dense cold excitons confined in localized potential has also been reported [132][237].

The bright side of the previous claims is that the observations of the excitonic condensation always involves either exciton-polariton induced lasing [222], some selected resonant pumping, the spectral narrowing of excitonic luminescence [226][231] or fast expansion of the excitonic clouds [219]. These are particular cases and very useful in several application for understanding related fundamental science or some specific semiconductor industrial applications. However, they all were subject to plausible interpretations without resorting to a purely manifested Bose-Einstein condensation of excitons, the crucial evidence for such claim is to firmly demonstrate the coherence of the maintained states.

As mentioned early in the introduction and demonstrated through this dissertation, the magnetic micro-trapping of excitons relies on employing the confining mechanism that used in the field of ultracold atoms to trap excitons in solids. From the quantum particles prospective, it depends essentially on treating these particles as very little magnets prepared in low magnetic field seeking-states and interact literally with the external confining magnetic potential in such away that they seek the filed local minima. Although it is the first to propose the low magnetic field micro-trapping of excitons in this dissertation, it is still requires considerable theoretical and experimental efforts. If this mechanism is considered as an approach to achieve the Bose-Einstein condensate of excitons, it is then required to come up with an efficient cooling method to maintain the critical transition temperature of the trapped excitonic cloud towards the exciton BEC. Moreover, regardless we have experimentally presented an evidence for the magnetic confinement of excitons, we are still far from judging whether or not this approach is applicable for creating the exciton BEC. It is still in an initiative stage which requires to be handled by those who are experts and aware of the detailed aspects of such field. My believe is that these results have certainly triggered an interesting question

> *Can we consider the low magnetic field micro-confinement as an approach to achieve Bose-Einstein condensation of excitons in solids?*

## 8.2 Summary

We have developed a simplified method for realizing the magnetic confinement of quantum degenerate gases where we have analyzed the applicability of employing this method to confine two different species of quantum particles. Our first trial was to validate whether or not the new method can maintain a reliable degree of confinement to trap cold atoms and consequently to establish a practical simplified trapping mechanism for achieving the Bose-Einstein condensation of atomic gases.

The new method creates distributed magnetic micro-traps above a patterned surface of permanent magnetic thin film where we made use of the primary advantage of the stable magnetic trapping field exhibited by the permanent magnetic material. It is now well known that stable magnetic micro-traps for ultracold atoms are better manufactured from permanent magnetic material and not from current carrying wires due to the confining instability at the trap bottom generated by the phase fluctuation in the electrical current that used to produce the magnetic trapping field. This approach is also well known as the two-dimensional magnetic lattices and the micro-traps are regarded as the lattice sites .

One of the advantages realized in this type of magnetic micro-traps is the natural potential tilts exhibited a cross the distribution surface of the sites. Previously, the tilted potential is thought to be one of the disadvantages of the magnetic lattice where magnetic bias fields must be implemented externally as a crucial element in the setup of the experiment. However, our theoretical analysis has shown the opposite; the tilt in the confining magnetic potential is found to be of great interest when considering the tunneling of the trapped quantum particles between the lattice sites. Moreover, in the field of optical traps for cold atoms introducing potential tilts among the sites usually requires special experimental efforts while in the magnetic approach the tilt naturally exists as we demonstrated in the measured magnetic field of the trap. We thus denote a lattice in such configurations as the asymmetrical two-dimensional magnetic lattice.

We have also theoretically investigated the tunneling of the magnetically trapped ultracold quantum degenerate gases, namely ultracold atoms, under when the trapping potential fields are tilted. Our theoretical analysis has shown that it is possible to identify a macroscopic quantum phase transition in these systems in which case the transition can be adiabatically induced via external controls, such as bias magnetic fields or polarized lasers. Our calculations have shown that it is possible to adiabatically induce coherent oscillations for the Josephson atomic ac/dc currents so as to examine the existence of the macroscopic quantum phase transition.

To process quantum information, it is possible to consider the induced Josephson atomic current as a mechanism to transfer the entangled qubits across the magnetic lattice and hence to compute the quantum information in parallel[1]. Coherent Josephson oscillation maintained in such traps itself is a manifestation of simulating condensed matter system using trapped ultracold atoms. The overall spatial control of the distributed lattice sites made it simple to introduce a write/read mechanism or operational quantum gates based on the location of the write/read sites (qubits), for example one can consider the edge sites as read only sites after forming a long-range entanglement of multipartite in the asymmetrical two-dimensional magnetic lattice.

During the second phase of this research, we have experimentally investigated the low magnetic field confinement of excitonic particles. Excitons, which are the composite electron-hole particles, have been regarded as magnetic hydrogen-like quantum particles in which case their interaction with the external magnetic field potential has been carefully considered. The excitons have been formed in a system of multiple quantum wells created from GaAs/AlGaAs material where we employed the localized inhomogeneous magnetic fields, created by depositing permanent magnetic material at the surface of the GaAs/AlGaAs material, to lay within the confining plane of the quantum wells. We first analyzed the effect of the localized fields with low amplitudes on the Bohr radius of the excitonic particles where, to demonstrate such effect on the internal structure of the excitons, we spatially resolved the inhomogeneous depressions of the excitonic Zeeman splittings. These measurements have revealed that there is a magnetic induced shift of the excitons dispersion surface in the energy-momentum phase space, i.e the $k$-space. This is an important result because it reveals that an external magnetic weak/strong field can be used to control the migration of the dispersion surface (curve) across the excitonic phase space and hence drawing the important analogue of the evaporative cooling that used to induce the critical phase transition of cold atoms to their BEC transition phase point. We believe that the evaporative cooling is possible here because the distributed inhomogeneous magnetic fields across the the sample x/y-plane has revealed that there is an actual spatial excitonic migration from the initial quantum state towards the final quantum state with respect to the localized magnetic field values.

Based on the above observations we engineered a pronounced disturbance on the magnetic field cover, which lays within the confining plane of the quantum wells, to study whether the low magnetic field approach is applicable to confine the excitonic particles in a similar scenario to that of cold atoms. The disturbance has been created by micro-patterning the magnetic material and presented as magnetic field local minima projected into the same level of quantum well confinement. This configuration has allowed the creation of magnetic micro-trap allocated, via precise deposition, within the system of the multiple quantum wells

---

[1] Spatially transfered qubits are often known as flying qubits.

in which case the excitons behave according to their interaction with the gradient of the magnetic field toward its local minima. When excitons behave in such way they are known to be prepared in the so called low magnetic field seeking-state which is due to magnetic tunning of their Zeeman states as observed in the first experiment. A pronounce photoluminescence emission has been observed at the location of the field disturbance providing us with a clear evidence for the confinement of the excitonic particles. Moreover, the thermal expansion of the trapped cloud has indicated that this trapping mechanism can also work to confine excitonic quantum particles in solids.

Appendix A

# Special functions, integrals and related formulas

## A.1 Special functions, integrals and related formulas

### A.1.1 Gamma function

Gamma function integral is written as follows for the complex $z$-plane excluding the non-positive integers

$$\int_0^\infty e^{-x} x^{z-1} dx = \Gamma(z) \tag{A.1}$$

For integer values $z - 1 = n$, with $n \in \mathbb{R}$, we find that the Gamma function coincides with the fractional function

$$\int_0^\infty e^{-x} x^{n} dx = \Gamma(n+1) = n! \tag{A.2}$$

and the related integral can be derived from the following integral

$$\int_0^\infty e^{-lx^n} x^{m} dx = \frac{1}{l^{m+1}} \int_0^\infty e^{-x^n} x^{m} dx \tag{A.3}$$

For example

$$\int_0^\infty e^{-x^2} x^{2n+1} dx = \frac{1}{2} n! \tag{A.4}$$

$$\int_0^\infty e^{-x^2} x^{2n} dx = \frac{(2n-1)!!}{2^{n+1}} \sqrt{\pi} \tag{A.5}$$

### A.1.2 Bessel functions

The general solution of the Bessel function[1] is a linear combination of two particular solutions known as the regular and irregular solutions, i.e $j_l(x)$ at the origin which is known as the spherical Bessel of the first kind and $n_l(x)$ irregular at the origin of the second kind, respectively. Here are some special cases

- *Lowest orders*

---

[1] The Bessel differential equation can be found in any of the specialized mathematical text books.

$$j_o(x) = \frac{\sin x}{x}, \qquad n_o(x) = \frac{\cos x}{x} \tag{A.6}$$

$$j_1(x) = \frac{\sin x}{x^2} - \frac{\cos x}{x}, \qquad n_1(x) = \frac{\cos x}{x^2} + \frac{\sin x}{x} \tag{A.7}$$

- *Asymptotic forms for* $x \to \infty$

$$j_l(x) \underset{x\to\infty}{\sim} \frac{1}{x}\sin(x - \frac{1}{2}l\pi) \tag{A.8}$$

$$n_l(x) \underset{x\to\infty}{\sim} \frac{1}{x}\cos(x - \frac{1}{2}l\pi) \tag{A.9}$$

- *Asymptotic forms for* $x \to 0$

$$j_l(x) \underset{x\to 0}{\sim} \frac{x^l}{(2l+1)!!}\{1 - \frac{x^2}{2(2l+3)} + ...\} \tag{A.10}$$

$$n_l(x) \underset{x\to 0}{\sim} \frac{(2l+1)!!}{(2l+1)}(\frac{1}{x})^{l+1}\{1 + \frac{x^2}{2(2l-1)} + ...\} \tag{A.11}$$

### A.1.3 Digamma functions

The digamma function is given by the logarithmic derivative of the gamma function (or, depending on the definition, the logarithmic derivative of the factorial). There are two different notations for the digamma function, first it can be defined as the logarithmic derivative of the gamma function $\Gamma(z)$ as follows

$$\bar{\psi}(z) = \frac{d}{dz}\ln\Gamma(z) = \frac{\Gamma'(z)}{\Gamma(z)} \tag{A.12}$$

second it can also be defined as the logarithmic derivative of the factorial function

$$F(z) = \frac{d}{dz}\ln z! \tag{A.13}$$

where both definitions are related to each, such that

$$F(z) = \bar{\psi}(z+1) \tag{A.14}$$

The $n$-derivative of $\bar{\psi}(z)$ is called the polygamma function, see Figure (A.1) for the zero-derivative of function. Here are some identities for the digamma function

$$\frac{d\bar{\psi}_o(z)}{dz} = \sum_{n=0}^{\infty}\frac{1}{(z+n)^2} \tag{A.15}$$

$$\bar{\psi}_o(1-z) - \bar{\psi}_o(z) = \pi\cot(\pi z) \tag{A.16}$$

$$\bar{\psi}_o(1+z) - \bar{\psi}_o(z) = \frac{1}{z} \tag{A.17}$$

$$\bar{\psi}_o(2z) = \frac{1}{2}\bar{\psi}_o(z) + \frac{1}{2}\bar{\psi}_o(z+\frac{1}{2}) + \ln 2 \tag{A.18}$$

The logarithmic series is given by

$$\bar{\psi}_o(z) = \sum_{n=0}^{\infty} \frac{1}{(n+1)} \sum_{k=0}^{n} (-1)^k \binom{n}{k} \ln(z+k) \tag{A.19}$$

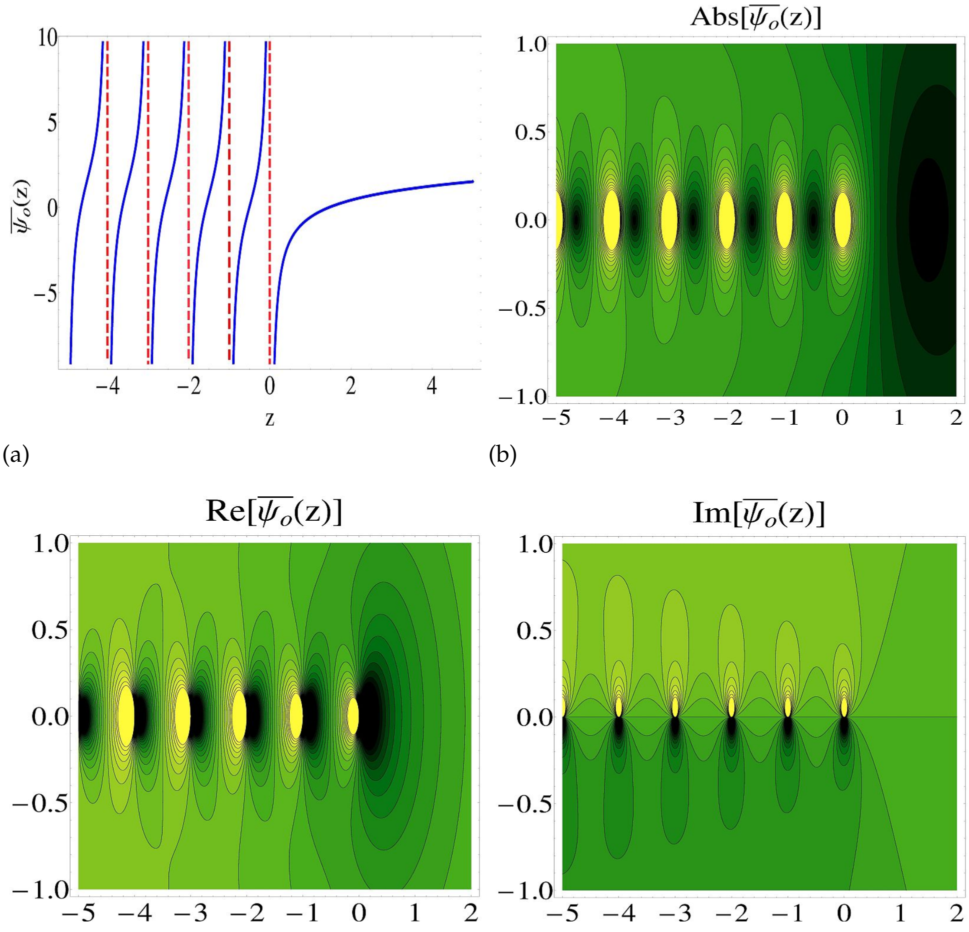

(a) (b) (c) (d)

***Figure A.1:*** (a) The amplitude of the digamma function $\bar{\psi}_o(z)$, (b-d) the amplitude of the absolute value Abs$[\bar{\psi}_o(z)]$ , the real part Re$[\bar{\psi}_o(z)]$ and the imaginary part Im$[\bar{\psi}_o(z)]$ across the $x/y$-plane, respectively.

### A.1.4 Riemann $\zeta$-function

The Riemann $\zeta$-function can be defined by the following integral for the real value of x, i.e. $x > 1$

$$\zeta(x) = \frac{1}{\Gamma(x)} \int_0^{\infty} \frac{u^{x-1}}{e^{u-1}} du \tag{A.20}$$

For $n$ integer values of $x$ we can evaluate the following identity

$$\begin{aligned}\frac{u^{n-1}}{e^{u-1}} &= \frac{e^{-u}u^{n-1}}{1-e^{-u}} \\ &= e^{-u}u^{n-1}\sum_{k=0}^{\infty}e^{-ku} \\ &= \sum_{k=1}^{\infty}e^{-ku}u^{n-1}\end{aligned} \tag{A.21}$$

such that

$$\int_0^{\infty}\frac{u^{n-1}}{e^{u-1}}du = \sum_{k=1}^{\infty}\int_0^{\infty}e^{-ku}u^{n-1}du \tag{A.22}$$

By making use of the $\Gamma(z)$ function, the integral in equation (A.20) can be evaluated to give the most common form of the Riemann $\zeta(z)$ function

$$\zeta(n) = \sum_{k=1}^{\infty}\frac{1}{k^n} \tag{A.23}$$

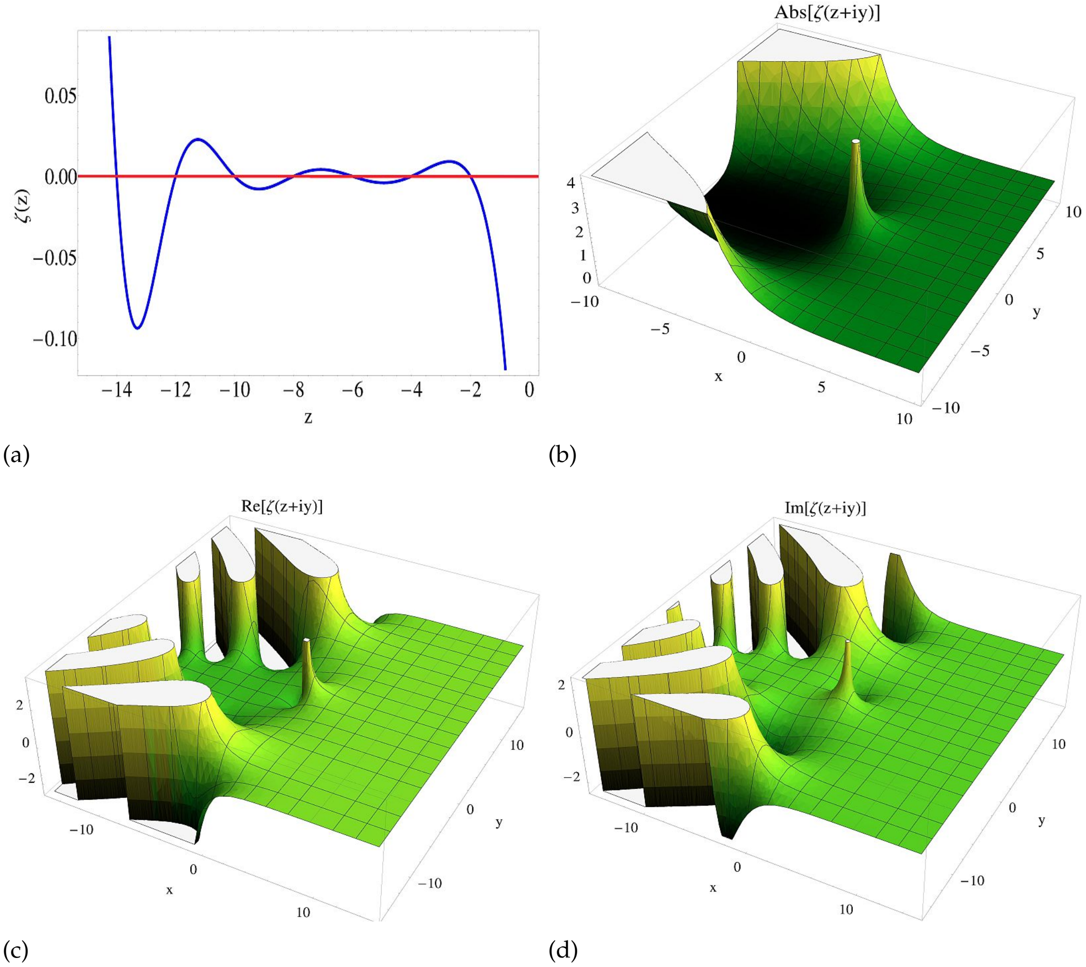

***Figure A.2:*** (a) The Riemann $\zeta(z)$ function, (b-d) the amplitude of the absolute value Abs$[\zeta(z+iy)]$ , the real part Re$[\zeta(z+iy)]$ and the imaginary part Im$[\zeta(z+iy)]$ across the $x/y$-plane, respectively, evaluated for $-10 < z < 10$ and $-10 < y < 10$.

# Bibliography

[1] P. Lett, R. Watts, C. Westbrook, W. Phillips, P. Gould, and H. Metcalf, *"Observation of atoms laser cooled below the Doppler limit,"* Phys. Rev. Lett. **61**, 169 (1988).

[2] S. Chu, *"The manipulation of neutral particles,"* Rev. Mod. Phys. **70**, 685 (1998).

[3] C. Cohen-Tannoudji, *"Manipulating atoms with photons,"* Rev. Mod. Phys. **70**, 707 (1998).

[4] W. Phillips, *"Laser cooling and trapping of neutral atoms,"* Rev. Mod. Phys. **70**, 721 (1998).

[5] H. Hess, *"Evaporative cooling of magnetically trapped and compressed spin-polarized hydrogen,"* Phys. Rev. B **34**, 3476 (1986).

[6] O. Luiten, M. Reynolds, and J. Walraven, *"Kinetic theory of the evaporative cooling of a trapped gas,"* Phys. Rev. A **53**, 381 (1996).

[7] W. Ketterle and N. van Druten, *"Evaporative cooling of trapped atoms,"* Adv. At. Mol. Opt. Phys. **37**, 181 (1996).

[8] W. Ketterle, "**Nobel Lecture**: *When atoms behave as waves: Bose Einstein condensation and the atom laser*," Rev. Mod. Phys. **261**,1131 (2002).

[9] E. Cornell and C. Wieman, "**Nobel Lecture**: *Bose Einstein condensation in a dilute gas; The first 70 years and some recent experiments*," Rev. Mod. Phys. **74**, 875 (2002).

[10] M. Anderson, J. Ensher, M. Matthews, C. Wieman and E. Cornell, *"Observation of Bose Einstein condensation in dilute atomic vapor,"* Science **269**, 198 (1995).

[11] K. Davis, M.-O Mewes, M. Andrews, N. van Druten, D. Durfee, D. Kurn and W. Ketterle, *"Bose Einstein condensation in a gas of sodium atoms,"* Phys. Rev. Lett. **75**, 3969 (1995).

[12] F. Santos, J. Léonard, J. Wang, C. Barrelet, F. Perales, E. Rasel, C. Unnikrishnan, M. Leduc, and C. Cohen-Tannoudji, *"Bose-Einstein condensation of metastable helium,"* Phys. Rev. Lett. **86**, 3459 (2001).

[13] A. Robert, O. Sirjean, A. Browaeys, J. Poupard, S. Nowak, D. Boiron, C. I. Westbrook, and A. Aspect, *"A Bose-Einstein condensate of metastable atoms,"* Science **292**, 463 (2001).

[14] T. Weber, J. Herbig, M. Mark, H.-C. Nägerl, and R. Grimm, *"Bose-Einstein condensation of cesium,"* Science **299**, 232 (2003).

[15] Y. Takasua, K. Maki, K. Komori, T. Takano, K. Honda, M. Kumakura, T. Yabuzaki, and Y. Takahashi, *"Spin-singlet Bose-Einstein condensation of two-electron atoms,"* Phys. Rev. Lett. **91**, 040404 (2003).

[16] J. T. M. Walraven, *"Elements of Quantum Gases: Thermodynamics and Collisional Properties of Trapped Atomic Gases,"* University of Amsterdam (2010).

[17] A. Griesmaier, J. Werner, S. Hensler, J. Stuhler, and T. Pfau, *"Bose-Einstein condensation of chromium,"* Phys. Rev. Lett. **94**, 160401 (2005).

[18] D. Fried, T. Killian, L. Willmann, D. Landhuis, S. Moss, D. Kleppner, and T. Greytak, *"Bose-Einstein condensation of atomic hydrogen,"* Phys. Rev. Lett. **81**, 3811 (1998).

[19] S. Jochim, M. Bartenstein, A. Altmeyer, G. Hendl, S. Riedl, C. Chin, J. Denschlag, and R. Grimm, *"Bose-Einstein condensation of molecules,"* Science **302**, 2101 (2003).

[20] M. Greiner, C. Regal, and D. Jin, *"Emergence of a molecular Bose-Einstein condensate from a Fermi gas,"* Nature **426**, 537 (2003).

[21] V. Bagnato, D. E. Pritchard and D. Kleppner, *"Bose-Einstein condensation in an external potential,"* Phys. Rev. A **35**, 4354 (1987).

[22] S. N. Bose, *"Plancks Gesetz und Lichtquantenhypothese,"* Zeitschrift für Physik **26**, 178 (1924).

[23] Einstein, *Quantentheorie des einatomigen idealen Gases - Erste Abhandlung*, Sitzungsber. Preuss. Akad. Wiss. 261 (1924).

[24] Einstein, *Quantentheorie des einatomigen idealen Gase - Zweite Abhandlung*, Sitzungsber.Preuss.Akad.Wiss. 3 (1925).

[25] J. Weiner, V.S. Bagnato, S. Zilio, and P.S. Julienne, *"Cold and Ultracold collisions,"* Rev. Mod. Phys. **71**, 1 (1999).

[26] M. Arndt, M. Ben Bahan, D. Guéry-Odelin, M. Reynolds and J. Dalibard, *"Observation of a Zero-Energy Resonance in Cs-Cs Collisions,"* Phys. Rev. Let. **79**, 625 (1997).

[27] N. F. Mott and H. S. W. Massey, *" The Theory of Atomic Collisions,"* **Oxford University Press**, London, (1965).

[28] J. L. Roberts, N. R. Claussen, J. P. Burke, Jr., C. H. Greene, E. A. Cornell, and C. E. Wieman , *"Resonant Magnetic Field Control of Elastic Scattering in Cold $^{85}$Rb,"* Phys. Rev. Lett. **81**, 5109 (1998).

[29] V. Bagnato and D. Kleppner, *"Bose-Einstein condensation in low-dimensional traps,"* Phys. Rev. A **44**, 7439 (1991)

[30] W. Ketterle and N. J. van Druten, *"Bose-Einstein condensation of a finite number of particles trapped in one or three dimensions,"* Phys. Rev. A **54**, 656 (1996)

[31] W. J. Mulli, *"A Study of Bose-Einstein Condensation in a Two-Dimensional Trapped Gas,"* J. Low Temp. Phys. **106**, 615 (1997)

[32] A. L. Migdall, J. V. Prodan, and W. D. Phillips, *"First Observation of Magnetically Trapped Neutral Atoms,"* Phys. Rev. Lett. **54**, 2596 (1985).

[33] W. Petrich, M. H. Anderson, J. R. Ensher, and E. A. Cornell, *"Stable, Tightly Confining Magnetic Trap for Evaporative Cooling of Neutral Atoms,"* Phys. Rev. Lett. **74**, 3352(1995).

[34] M. H. Anderson, J. R. Ensher, M. R. Matthews, C. E. Wieman, and E. A. Cornell, *"Observation of Bose-Einstein condensation in a dilute atomic vapor,"* Science **269**, 198 (1995).

[35] T. Bergeman, G. Erez, and H. J. Metcalf, *"Magnetostatic trapping fields for neutral atoms,"* Phys. Rev. A **35**, 1535 (1987).

[36] O. J. Luiten, *"Lyman-a Spectroscopy of Magnetically Trapped Atomic Hydrogen,"* **PhD thesis**, University of Amsterdam, (1993).

[37] P. Pinkse, A. Mosk, M. Weidemüller, M. W. Reynolds, T. W. Hijmans, and J. T. M. Walraven, *"Adiabatically changing the phase-space density of a trapped Bose gas,"* Phys. Rev. Lett., **78**, 990 (1997).

[38] W. Ketterle, D. S. Durfee, and D. M. Stamper-Kurn, *"Making probing and understanding Bose-Einstein condensates,"* In M. Inguscio, S. Stringari, and C. E. Wieman, editors, *"Bose-Einstein Condensation in Atomic Gases,"* Proceedings of the International School of Physics Enrico Fermi, Course CXL. IOS Press Ohmsha, (1999).

[39] H. Hess, G. P. Kochansky, J. M. Doyle, N. Masuhara, D. Kleppner, and T. J. Greytak, *"Magnetic trapping of spin-polarized atomic hydrogen,"* Phys. Rev. Lett. **59**, 672 (1987).

[40] W. Ketterle and N. J. van Druten, *" Evaporative cooling of trapped atoms,"* Advances in Atomic, Molecular, and Optical Physics **37**, 181 (1996).

[41] J. T. M. Walraven, *"Atomic hydrogen in magnetostatic traps,"* In G. L. Oppo, S. M. Barnett, E. Riis, and M. Wilkinson, editors, *"Quantum Dynamics of Simple Systems,"* **44** of SUSSP Proceedings. IOP, Bristol, (1996).

[42] O. J. Luiten, M. W. Reynolds, and J. T. M. Walraven, *"Kinetic theory of the evaporative cooling of a trapped gas,"* Phys. Rev. A **53**, 381 (1996).

[43] P. Valkering, *"Optimization of evaporative cooling of rubidium atoms in a magnetic trap,"* **Master's Thesis**, University of Utrecht, (1999).

[44] C. Zener, *"Non-adiabatic crossing of energy levels,"* Proceedings of the Royal Society of London Series A, **137**, 696 (1932).

[45] J. R. Rubbmark, M. M. Kash, M. G. Littman, and D. Kleppner, *"Dynamical effects at avoided level crossing: A study of the Landau-Zener effect using Rydberg atoms,"* Phys. Rev. A **23**, 3107 (1981).

[46] B. Desruelle, V. Boyer, S. G. Murdoch, G. Delannoy, P. Bouyer, and A. Aspect, *"Interrupted evaporative cooling of 87Rb atoms trapped in a high magnetic field,"* Phys. Rev. A **60**, R1759 (1999).

[47] S. Ghanbari, T. D. Kieu, A. Sidorov, and P. Hannaford, *"Permanent magnetic lattices for ultracold atoms and quantum degenerate gases,"* J. Phys. B: At. Mol. Opt. Phys. **39**, 847 (2006).

[48] M. Singh, M. Volk, A. Akulshin, A. Sidorov, R. McLean, and P. Hannaford, *"One dimensional lattice of permanent magnetic microtraps for ultracold atoms on an atom chip,"* J. Phys. B: At. Mol. Opt. Phys. **41**, 065301 (2008).

[49] Sidorov A, Lau D C, Opat G I,McLean R J, RowlandsWJ, and Hannaford P. *"Magnetostatic optical elements for laser-cooled atoms,"* Laser Physics, 8, 642 (1998).

[50] S. Ghanbari, *"Superfluid to Mott insulator quantum phase transition in permanent magnetic lattices,"* Center for Atom Optics & Ultrafast Spectroscopies, Swinburne University (http://www.swinburne.edu.au/engineering/caous/theses.htm), **PhD Thesis**, (2008).

[51] S. Ghanbari, T. Kieu and P. Hannaford, *" A class of permanent magnetic lattices for ultracold atoms,"* J. Phys. B: At. Mol. Opt. Phys. **40**, 1283 (2007).

[52] S. Ghanbari, T. Kieu, A. Sidorov and P. Hannaford, *"Permanent magnetic lattices for ultracold atoms and quantum degenerate gases,"* J. Phys. B: At. Mol. Opt. Phys. **39**, 847 (2006).

[53] A. Sidorov, J. McLean, F. Scharnberg, S. Gough, J. Davis, A. Sexton, I. Opat, and P. Hannaford, *"Permanent-magnet microstructures for atom optics,"* Acta Phys. Polon. B, **33**, 2137 (2002).

[54] M Singh, M Volk, A Akulshin, A Sidorov, R McLean and P Hannaford, *"One-dimensional lattice of permanent magnetic microtraps for ultracold atoms on an atom chip,"* J. Phys. B: At. Mol. Opt. Phys. **41**, 065301 (2008).

[55] I. Bloch, *"Ultracold quantum gases in optical lattices,"* Nature. Phys. **1**, 23 (2005).

[56] O. Mandel, M. Greiner, A. Widera, T. Rom, W. Hänsch, and I. Bloch, *"Coherent Transport of Neutral Atoms in Spin-Dependent Optical Lattice Potentials,"* Phys. Rev. Lett **91**, 010407 (2003).

[57] B. Paredes, A. Widera, V. Murg, O. Mandel, S. Fölling, I. Cirac, G. V. Shlyapnikov, T. W. Hänsch, and I. Bloch, *"Tonks-Girardeau gas of ultracold atoms in an optical lattice,"* Nature (London) **429**, 277 (2004).

[58] Z. Hadzibabic, P. Krüger, M. Cheneau, B. Battelier, and J. Dalibard, *"Berezinskii-Kosterlitz-Thouless Crossover in a Trapped Atomic Gas,"* Nature **441**, 118 (2006).

[59] I. Bloch, J. Dalibard, and W. Zwerger, *"Many-body physics with ultracold gases,"* Rev. Mod. Phys. **80**, 885 (2008).

[60] M. Greiner, O. Mandel, T. W. Hänsch, and I. Bloch, *"Collapse and revival of the matter wave field of a Bose-Einstein condensate ,"* Nature **51**, 419 (2002).

[61] R. Jördens, N. Strohmaier, K. Günter, H. Moritz, and T. Esslinger, *"A Mott insulator of fermionic atoms in an optical lattice,"* Nature **455**, 204 (2008).

[62] M. Köhl, H. Moritz, K. G. T. Stöferle, K. Günter and T. Esslinger, *"Fermionic Atoms in a Three Dimensional Optical Lattice: Observing Fermi Surfaces, Dynamics, and Interactions,"* Phys. Rev. Lett. **94**, 080403 (2005).

[63] D. DiVincenzo and Fortschr, *"The Physical Implementation of Quantum Computation"* Fortschritte der Physik **48**, 771 (2000).

[64] O. Mandel, M. Greiner, A. Widera, T. Rom, T. W. Hänsch, and I. Bloch, *"Controlled collisions for multi-particle entanglement of optically trapped atoms,"* Nature (London) **425**, 937 (2003).

[65] M. Riedel, P. Böhi, Y. Li, T. Hänsch, A. Sinatra, and P. Treutlein, *"Atom-chip-based generation of entanglement for quantum metrology ,"* Nature **464**, 1170 (2010).

[66] J. Reichel, *"Microchip traps and Bose-Einstein condensation,"* Appl. Phys. B **74**, 469 (2002).

[67] H. Ott, J. Fortágh, G. Schlotterbeck, A. Grossmann, and C. Zimmermann, *"Bose-Einstein Condensation in a Surface Microtrap,"* Phys. Rev. Lett. **87**, 230401 (2001).

[68] W. Hänsel, P. Hommelhoff, T. W. Hänsch, and J. Reichel, *"Bose-Einstein condensation on a microelectronic chip,"* Nature **413**, 498 (2001).

[69] J. Fortägh and C. Zimmermann, *"Magnetic microtraps for ultracold atoms,"* Rev. Mod. Phys. **79**, 235 (2007).

[70] J. Yin, W. Gao, J. Hu, and Y. Wang, *"Magnetic surface microtraps for realizing an array of alkali atomic Bose-Einstein condensates or Bose clusters,"* Opt. Commun **206**, 99 (2002).

[71] R. Gerritsma, S. Whitlock, T. Fernholz, T. Schlatter, J. Luigjes, J. Thiele, J. Goedkoop, and R. Spreeuw, *"Lattice of microtraps for ultracold atoms based on patterned magnetic films,"* Phys. Rev A **76**, 033408 (2007).

[72] T. Fernholz, R. Gerritsma, S. Whitlock, I. Barb, and R. J. C. Spreeuw, *"Fully permanent magnet atom chip for Bose-Einstein condensation,"* preprint arXiv: **0705.2569** [cond-mat.other], (2007).

[73] I. Teper, Y.-J. Lin, and V. Vuletić, *"Resonator-Aided Single-Atom Detection on a Microfabricated Chip,"* Phys. Rev. Lett. **97**, 023002 (2006).

[74] S. Whitlock, R. Gerritsma, T. Fernholz, and R. Spreeuw, *"Two-dimensional array of microtraps with atomic shift register on a chip ,"* New J. Phys. **11**, 023021 (2009).

[75] G. I. Opat, S. J. Wark, and A. Cimmino, *"Electric and magnetic mirrors and gratings for slowly moving neutral atoms and molecules,"* Appl. Phys. B **54**, 396 (1992).

[76] T. M. Roach, H. Abele, M. G. Boshier, H. L. Grossman, K. P. Zetie, and E. A. Hinds, *"Realization of a Magnetic Mirror for Cold Atoms,"* Phys. Rev. Lett. **75**, 629 (1995).

[77] A. I. Sidorov, R. J. McLean, W. J. Rowlands, D. C. Lau, J. E. Murphy, M. Walkiewicz, G. I. Opat, and P. Hannaford, *"Specular reflection of cold caesium atoms from a magnetostatic mirror,"* Quant. Semiclass. Opt. **8**, 713 (1996).

[78] M. Singh, R. McLean, A. Sidorov, and P. Hannaford, *"Dynamics of reflection of ultracold atoms from a periodic one-dimensional magnetic lattice potential,"* Phys. Rev. A **79**, 053407 (2009).

[79] P. Treutlein, P. Hommelhoff, T. Steinmetz, T. W. Hänsch, and J. Reichel, *"Coherence in Microchip Traps,"* Phys. Rev. Lett. **92**, 203005 (2004).

[80] C. Deutsch, F. Ramirez-Martinez, C. Lacroute, F. Reinhard, T. Schneider, J. N. Fuchs, F. Piéchon, F. Laloë, J. Reichel, and P. Rosenbusch, *"Spin Self-Rephasing and Very Long Coherence Times in a Trapped Atomic Ensemble,"* Phys. Rev. Lett. **105**, 020401 (2010).

[81] D. Jaksch, J. I. Cirac, P. Zoller, S. L. Rolston, and D. M. Lukin, *"Local Blockade of Rydberg Excitation in an Ultracold Gas,"* Phys. Rev. Lett. **93**, 063001 (2000).

[82] M. Lukin, M. Fleischhauer, R. Cote, L. Duan, D. Jaksch, J. Cirac, and P. Zoller, *"Dipole Blockade and Quantum Information Processing in Mesoscopic Atomic Ensembles,"* Phys. Rev. Lett. **87**, 037901 (2001).

[83] J. Cirac and P. Zoller, *"A scalable quantum computer with ions in an array of microtraps ,"* Nature **404**, 579 (2000).

[84] R. Raussendorf and H. Briegel, *"A One-Way Quantum Computer,"* Phys. Rev. Lett. **86**, 5188 (2001).

[85] D. Jakscha and P. Zoller, *"The cold atom Hubbard toolbox,"* Annals of Physics **315**, 52 (2005).

[86] S. Levy, E. Lahoud, I. Shomroni, and J. Steinhauer, *"The a.c. and d.c. Josephson effects in a Bose-Einstein condensate,"* Nature **449**, 579 (2007).

[87] F. Cataliotti, S. Burger, P. M. C. Fort, F. Minardi, A. Trombettoni, A. Smerzi, and M. Inguscio, *"Josephson Junction Arrays with Bose-Einstein Condensates,"* Science **293**, 843 (2001).

[88] W. Liu, W. Fan, W. Zheng, J. Liang, and S. Chui, *"Quantum Tunneling of Bose-Einstein Condensates in Optical Lattices under Gravity,"* Phys. Rev. Lett. **88**, 170408 (2002).

[89] A. L. Fetter and J. D. Walecka, *"Quantum Theory of Many-Particle System,"* Dover Publication Inc. Mineola, New York (2003).

[90] V. L. Ginzburg and L. P. Pitaevskii, Zh. Eksp. Teor. Fiz. **34**, 1240 (1958), Sov. Phys. JEPT **7**, 858 (1958); E. P. Gross, Nuovo Cimento **20**, 451 (1961); J. Math. Phys. **46**, 137 (1963).

[91] A. Griffin, *"Excitations in a Bose-Condensed Liquid,"* Cambridge Univ. Press, Cambridge, (1993).

[92] A. Smerzi, S. Fantoni and S. Giovanazzi, *"Macroscopic Quantum Coherence Phenomena in Bose-Einstein Condensates,"* Scuola Internazionale Superioredi Studi Avanzati (SISSA) Digital Library, **PhD Thesis** (1998).

[93] G. J. Milburn and J. Corney, *"Quantum dynamics of an atomic Bose-Einstein condensate in a double-well potential,"* Phys. Rev. Lett. **55**,4318 (1997).

[94] Y. Shin, G.-B. Jo, M. Saba, T. A. Pasquini, W. Ketterle, and D. E. Pritchard,*"Optical Weak Link between Two Spatially Separated Bose-Einstein Condensates,"* Phys. Rev. Lett. **95**, 170402 (2005).

[95] J. Javanainen, *"Oscillatory exchange of atoms between traps containing Bose condensates,"* Phys. Rev. Lett. **57**, 3164 (1986).

[96] B. J. Dalton, *"Two-Mode Theory of Bose-Einstein Condensate Interferometry,"* J. Mod Opt. **54**, 615 (2007).

[97] D. R. Dounas-Frazer, L. D. Carr, "Tunneling resonances and entanglement dynamics of cold bosons in the double well", preprint arXiv: **0610166** [quant-ph],(2006).

[98] S. Fölling, S. Trotzky, P. Cheinet, M. Feld, R. Saers, A. Widera1, T.Müller and I. Bloch, "Direct observation of second-order atom tunnelling", Natuer **448**, 1029 (2007).

[99] G. J. Milburn and J. Corney, *"Quantum dynamics of an atomic Bose-Einstein condensate in a double-well potential,"* Phys. Rev. Lett. **55**, 4318 (1997).

[100] A. Smerzi, S. Fantoni, S. Giovanazzi, and S. R. Shenoy, *"Quantum Coherent Atomic Tunneling between Two Trapped Bose-Einstein Condensates,"* Phys. Rev. Lett. **79**, 4950 (1997).

[101] A. Smerzi, A. Trombettoni, T. Lopez-Arias, C. Fort, P. Maddaloni, F. Minardi and M. Inguscio, *"Macroscopic oscillations between two weakly coupled Bose-Einstein condensates,"* Eur. Phys. J. B **31**, 457 (2003).

[102] H. Ott, J. Fortagh, G. Schlotterbeck, A. Grossmann, and C. Zimmermann, *"Bose-Einstein Condensation in a Surface Microtrap,"* Phys. Rev. Lett. **87**, 230401 (2001).

[103] M. Holthaus and S. Stenholm, *"Coherent control of the self-trapping transition,"* Eur. Phys. J. B **20**, 451 (2001).

[104] M. Albiez, R. Gati, J. Fölling, S. Hunsmann, M. Cristiani, and M. K. Oberthaler, *"Direct Observation of Tunneling and Nonlinear Self-Trapping in a Single Bosonic Josephson Junction,"* Phys. Rev. Lett. **95**, 010402 (2005).

[105] A. P. Tonel, J. Links, and A. Foerster, *"Quantum dynamics of a model for two Josephson-coupled Bose-Einstein condensates,"* J. Phys. A: Math. Gen. **38**, 1 (2005).

[106] A. Smerzi, S. Fantoni, S. Giovanazzi, and S. R. Shenoy, *"Quantum Coherent Atomic Tunneling between Two Trapped Bose-Einstein Condensates,"* Phys. Rev. Lett. **79**,4950 (1997).

[107] S. Raghavan, A. Smerzi, S. Fantoni, , and S. R. Shenoy, *"Coherent oscillations between two weakly coupled Bose-Einstein condensates: Josephson effects, $\pi$ oscillations, and macroscopic quantum self-trapping,"* Phys. Rev. A **59**, 620 (1999).

[108] J. Williams, R. Walser, J. Cooper, E. Cornell, and M. Holland, *"Nonlinear Josephson-type oscillations of a driven, two-component Bose-Einstein condensate,"* Phys. Rev. A **59**, R31 (1999).

[109] E. Sakellari, N. Proukakis, M. Leadbeater and C. Adams, *"Josephson tunnelling of a phase-imprinted Bose-Einstein condensate in a time-dependent double-well potential,"* New J. Phys. **6**, 42 (2004).

[110] S. Inouye, M. Andrews, J. Stenger, H. Miesner, D. Stamper-Kurn, and W. Ketterle, *"Observation of Feshbach resonances in a Bose-Einstein condensate,"* Nature **392**, 151 (1998).

[111] F. Cataliotti, S. Burger, C. Fort, P. Maddaloni, F. Minardi, A. Trombettoni, A. Smerzi, and M. Inguscio, *"Josephson Junction Arrays with Bose- Einstein Condensates,"* Science **293**, 843 (2001).

[112] I. Zapata, F. Sols, and A. Leggett, *"Adiabatic splitting, transport, and self-trapping of a Bose-Einstein condensate in a double-well potential,"* Phys. Rev. A **57**, R28 (1998).

[113] S. Giovanazzi, A. Smerzi, and S. Fantoni, *"Josephson Effects in Dilute Bose-Einstein Condensates,"* Phys. Rev. Lett. **84**, 4521 (2000).

[114] Zeng-Bing Chen and Yong-De Zhang, *"Possible realization of Josephson charge qubits in two coupled Bose-Einstein condensates,"* Phys. Rev. A. **65**, 022318 (2002).

[115] D. Kielpinski, C. Monroe, and D. J. Wineland, *"Architecture for a large-scale ion-trap quantum computer,"* Nature **417**, 709 (2002).

[116] J. Cirac and P. Zoller, *"A scalable quantum computer with ions in an array of microtraps,"* Nature **404**, 579 (2000).

[117] I. Deutsch, P. Jessen and R. Stock, *"Quantum Computing with Neutral Atoms,"* special issue of special issue of Quant. Inf. Proc. **3**, 15 (2004).

[118] L.-A. Wu, D. Lidar, and S. Schneider, *"Long-range entanglement generation via frequent measurements,"* Phys. Rev. A **70**, 032322 (2004).

[119] M. Plenio, *"Entanglement-area law for general bosonic harmonic lattice systems,"* Phys. Rev. Lett. **94**, 060503 (2005).

[120] Y. Makhlin, G. Schön, and A. Shnirman, *"Quantum-state engineering with Josephson-junction devices,"* Rev. Mod. Phys. **73**, 357 (2001).

[121] M. W. Zwierlein, C. A. Stan, C. H. Schunck, S. M. F. Raupach, A. J. Kerman, and W. Ketterle, *"Condensation of Pairs of Fermionic Atoms near a Feshbach Resonance,"* Phys. Rev. Lett. **92**, 120403 (2004).

[122] J. Werner, A. Griesmaier, S. Hensler, J. Stuhler, T. Pfau, A. Simoni and E. Tiesinga, *"Observation of Feshbach Resonances in an Ultracold Gas of* $^{52}$*Cr,"* Phys. Rev. Lett. **94**, 183201 (2005).

[123] C. Chin, T. Kraemer, M. Mark, J. Herbig, P. Waldburger, H.-C. Nägerl, and R. Grimm, *"Observation of Feshbach-Like Resonances in Collisions between Ultracold Molecules,"* Phys. Rev. Lett. **94**, 123201 (2005).

[124] S. Moskalenko, *"Reversible optico-hydrodynamic phenomena in a nonideal exciton gas,"* Fiz. Tverd. Tela **4**, 276 (1962).

[125] J. Blatt, W. Brandt, and K. Boer, *"Bose-einstein condensation of excitons,"* Phys. Rev. **126**, 1691 (1962).

[126] J. Wolfe, J. Lin, and D. Snoke, *"Bose-Einstein condensation of a nearly ideal gas: Excitons in* $Cu_2O$*,"* A.Griffin, D.W. Snoke and S. Stringari editors, In **Bose-Einstein Condensation**,(Cambridge University Press, 1995).

[127] J. Warren, K. O'Hara, and J. Wolfe, *"Two-body decay of thermalized excitons in* $CU_2O$*,"* Phys. Rev. B **61**, 8215 (2000).

[128] K. O'Hara, and J. Wolfe, *"Relaxation kinetics of excitons in cuprous oxide,"* Phys. Rev. B **62**, 12909 (2000).

[129] J. Jang, *"New perspectives on kinetics of excitons in* $CU_2O$*,"* Solid State Commun. **134**, 143 (2005).

[130] L. Butov, A. Gossard, and D. Chemla, *"Macroscopically ordered state in an exciton system,"* Nature **418**, 751 (2002).

[131] D. Snoke, S. Denev, Y. Liu, L. Pfeiffer, and K. West, *"Long-range transport in excitonic dark states in coupled quantum wells,"* Nature **418**, 754 (2002).

[132] L. Butov, C. Lai, A. Ivanov, A. Gossard and D. Chemla, *"Towards Bose-Einstein condensation of excitons in potential traps,"* Nature **417**, 47 (2002).

[133] L. Butov, A. Ivanov, A. Imamoglu, P. Littlewood A. Shashkin, V. Dolgopolov, K. Campman, and A. Gossard, *"Stimulated scattering of indirect excitons in coupled quantum wells: signature of a degenerate bose-gas of excitons,"* Phys. Rev. Lett. **86**, 5608 (2001).

[134] L. Keldysh and A. Kozlov, *"Collective properties of excitons in semiconductors,"* Sov. Phys. JETP **27**, 521 (1968).

[135] C. Weisbuch, M. Nishioka, A. Ishikawa and Y. Arakawa, *"Observation of the coupled exciton-photon mode splitting in a semiconductor quantum well microcavity,"* Phys. Rev. Lett. **69**, 3314 (1992).

[136] L. Dang, D. Heger, R. André, F. Boeuf and R. Romestain, *"Stimulation of polariton photoluminescence in semiconductor microcavity,"* Phys. Rev. Lett. **81**, 3920 (1998).

[137] P. Senellart and J. Bloch, *"Nonlinear emission of microcavity polaritons in the low density regime,"* Phys. Rev. Lett. **82**, 1233 (1999).

[138] P. Savvidis, J. Baumberg, R. Stevenson, M. Skolnick, D. Whittaker, and J. Roberts, *"Angle-resonant stimulated polariton amplifier,"* Phys. Rev. Lett. **84**, 1547 (2000).

[139] R. Huang, Y. Yamamoto, R. André, J. Bleuse, M. Muller and H. Ulmer-Tuffigo, *"Exciton-polariton lasing and amplification based on exciton-exciton scattering in a CdTe microcavity quantum wells,"* Phys. Rev. B. **65**, 165314 (2002).

[140] M. Richard, J. Kasprzak, R. Romestain, R. Andre and L. S. Dang, *"Spontaneous coherent phase transition of polaritons in CdTe microcavities,"* Phys. Rev. Lett. **94**, 187401 (2005).

[141] E. Hanamura, and H. Haug, *"Condensation effects of excitons,"* Physics Reports. Physics Letters Section C **33C**, 209 (1977).

[142] G. Wannier, *"The structure of electronic excitation levels in insulating crystals,"* Phys. Rev. **52**, 191 (1937).

[143] R. Leavitt and J. Little, *"Simple method for calculating exciton binding energies in quantum-confined semiconductor structures,"* Phys. Rev. B **42**, 11774 (1990).

[144] C. Priester, G. Allan and M. Lannoo, *"Wannier excitons in GaAs-*$Ga_{1-x}Al_xAs$ *quantum-well structures: influence of the effective-mass mismatch,"* Phys. Rev. B **30**, 7302 (1984).

[145] R. Greene, K. Bajaj and D. Phelps, *"Energy levels of Wannier excitons in GaAs-*$Ga_{1-x}Al_xAs$ *quantum-well structures,"* Phys. Rev. B **29**, 1807 (1984).

[146] T. Damen, J. Shah, D. Oberli, D. Chemla, J. Cunningham, and J. Kuo, *"Dynamics of exciton formation and relaxation in GaAs quantum wells,"* Phys. Rev. B **42**, 7434 (1990).

[147] S. Adachi, *"GaAs and related materials: Bulk semiconducting and superlattice properties,"* World Scientific, Singapore ; River Edge, NJ, (1994).

[148] R. Ferreira and G. Bastard, *"Tunneling and relaxation in semiconductor double quantum wells,"* Rep. Prog. Phys. **60**, 345 (1997).

[149] A. Alexandrou, J. Kash, E. Mendez, M. Zachau, JM. Hong, T. Fukuzawa, and Y. Hase, *"Electric-field effects on exciton lifetimes in symmetrical coupled gaas-al0.3ga0.7as double quantum wells,"* Phys. Rev. B **42**, 9225 (1990).

[150] R. Kaindl, M. Carnahan, D. Hagele, R. Lovenich and D. Chemla, *"Ultrafast terahertz probes of transient conducting and insulating phases in an electron-hole gas,"* Nature **423**, 734 (2003).

[151] A. Ivanov, P. Littlewood and H. Haug, *"Bose-einstein statistics in thermalization and photoluminescence of quantum-well excitons,"* Phys. Rev. B **59**, 5032 (1999).

[152] J. Feldmann, G. Peter, E. Göbel, P. Dawson, K. Moore, C. Foxon and R. Elliott, *"Linewidth dependence of radiative exciton lifetimes in quantum-wells,"* Phys. Rev. Lett. **59**, 2337 (1987).

[153] H. Bebb and E. Williams, *"Photoluminescence I: Theory in Semiconductors and semimetals,"* **8**, 181 Academic Press, New York, (1972).

[154] Lai, Chih-Wei Eddy, *"Spatially indirect excitons in coupled quantum wells"*. Lawrence Berkeley National Laboratory: Lawrence Berkeley National Laboratory. LBNL Paper LBNL-54356, (2004). Retrieved from: http://escholarship.org/uc/item/21c8t40t

[155] K. Bajaj, *"Use of excitons in materials characterization of semiconductor system,"* Mater. Sci. Eng. R-Rep. **34**, 59 (2001).

[156] L. Schultheis, A. Honold, J. Kuhl, K. Kohler and C. Tu, *"Optical dephasing of homogeneously broadened two-dimensional exciton-transitions in gaas quantumwells,"* Phys. Rev. B **34**, 9027 (1986).

[157] A. Parlangeli, P. C. M. Christianen, J. C. Maan, I. V. Tokatly, C. B. Soerensen and P. E. Lindelof, *"Optical observation of the energy-momentum dispersion of spatially indirect excitons,"* Phys. Rev. B **62**, 15323 (2000).

[158] L. Gorkov and Dzyalosh.Ie, *"Contribution to theory of mott exciton in a strong magnetic field,"* Sov. Phys. JETP **26**, 449 (1968).

[159] A. Gorbatsevich and I. Tokatly, *"Formation of k-space indirect magnetoexcitons in double-quantum-well direct-gap heterostructures,"* Semicond Sci. Tech. **13**, 288 (1998).

[160] S. Charbonneau, M. Thewalt, E. Koteles and B. Elman, *"Transformation of spatially direct to spatially indirect excitons in coupled double quantum wells,"* Phys. Rev. B **38**, 6287 (1988).

[161] Y. Lozovik, I. Ovchinnikov, S. Volkov, L. Butov and D. Chemla, *"Quasi-two-dimensional excitons in finite magnetic fields,"* Phys. Rev. B **65**, 235304 (2002).

[162] J. Davies, L. Smith, D. Wolverson, V. Kochereshko, J. Cibert, H. Mariette, H. Boukari, M. Wiater, G. Karczewski, T. Wojtowicz, A. Gust, C. Kruse, and D. Hommel, *"Excitons in motion in II-VI semiconductors,"* Phys. Stat. Sol. (b) 247, 1521 (2010).

[163] J. Davies, D. Wolverson, V. Kochereshko, A. Platonov, R. Cox, J. Cibert, H. Mariette, C. Bodin, C. Gourgon, E. Ubyivovk, Yu. Efimov, and S. Eliseev, *"Motional Enhancement of Exciton Magnetic Moments in Zinc Blende Semiconductors,"* Phys. Rev. Lett. **97**, 187403 (2006).

[164] L. Smith, J. Davies, D. Wolverson, S. Crampin, R. Cox, J. Cibert, H. Mariette, V. Kochereshko, M. Wiater, G. Karczewski, Yu. Efimov, S. Eliseev, *"Motion-dependent magnetic properties of excitons in CdTe,"* Phys. Rev. B **78**, 085204 (2008).

[165] L. Butov, C. Lai, D. Chemla, Y. Lozovik, K. Campman, and A. Gossard, *"Observation of magnetically induced effective mass enhancement of quasi 2D-excitons,"* Phys. Rev. Lett. **87**, 216804 (2001).

[166] J. Freire, F. Peeters, A. Matulis, V. Freire, and G. Farias, *"Fine structure of excitons in a quantum well in the presence of a nonhomogeneous magnetic field,"* Phys. Rev. B **62**, 7316 (2000).

[167] M. McCord and D. Awschalom, Appl. Phys. Lett. **57**, 2153 (1990).

[168] J. Freire, A. Matulis, F. Peeters, V. Freire, and G. Farias, *"Confinement of two-dimensional excitons in a nonhomogeneous magnetic field,"* Phys. Rev. B **61**, 2895 (2000).

[169] J. Levy, V. Nikitin, J. Kikkawa, A. Cohen, N. Samarth, R. Garcia, and D. Awschalom, *"Spatiotemporal Near-Field Spin Microscopy in Patterned Magnetic Heterostructures,"* Phys. Rev. Lett. **76**, 1948 (1996).

[170] Y. Kuramoto and C. Horie, *"Two-dimensional excitonic phase in strong magnetic fields,"* Solid State Commun. **25**, 713 (1978).

[171] C. Comte and P. Noziér, *"Exciton Bose condensation: the ground of an electron-hole gas I. Mean field description of a simplified model,"* J. Phys. **43**, 1069 (1982).

[172] E. Hanamura and H. Haug, *"Condensation effects of excitons,"* Phys. Rep. **33c**, 209 (1977).

[173] P. Noziér and C. Comte, *"Exciton Bose condensation: the ground of an electron-hole gas II. Spin states, screening and band structure effects,"* J. Phys. (Paris) **43**, 1083 (1982).

[174] S. Moskalenko and D. Snoke, ***"Bose-Einstein Condensation of Excitons and Biexcitons and Coherent Non-linear Optics with Excitons,"*** CAMBRIDGE University Press (2000).

[175] J. Kasprzak, M. Richard, S. Kundermann, A. Baas, P. Jeambrun, J. Keeling, F. Marchetti, M. Szymańska, R. André, J. Staehli, V. Savona, P. Littlewood, B. Deveaud and Le. Dang, *"Bose-Einstein condensation of exciton polaritons,"* Nature **443**, 05131 (2006).

[176] C. Lai, N. Kim, S. Utsunomiya, G. Roumpos, H. Deng, M. Fraser, T. Byrnes, P. Recher, N. Kumada, T. Fujisawa, and Y. Yamamoto, *"Coherent zero-state and $\pi$-state in an exciton-polariton condensate array,"* Nature **450**, 06334 (2007).

[177] M. Remeika, J. Graves, A. Hammack, A. Meyertholen, M. Fogler, L. Butov, M. Hanson, and A. Gossard, *"Localization-Delocalization Transition of Indirect Excitons in Lateral Electrostatic Lattices,"* Phys. Rev. Lett. **102**, 186803 (2009).

[178] S. Zimmermann, G. Schedelbeck, A. Govorov, A. Wixforth, J. Kotthaus, M. Bichler, W. Wegscheider, and G. Abstreiter, *"Spatially resolved exciton trapping in a voltage-controlled lateral superlattice,"* Appl. Phys. Lett. **73**, 154 (1998).

[179] A. High, A. Thomas, G. Grosso, M. Remeika, A. Hammack, A. Meyertholen, M. Fogler, L. Butov, M. Hanson, and A. Gossard, *"Trapping Indirect Excitons in a GaAs Quantum-Well Structure with a Diamond-Shaped Electrostatic Trap,"* Phys. Rev. Lett. **103**, 087403 (2009).

[180] Z. Koinov, G. Collins, and M. Mirassou, *"Confinement of magnetoexcitons in GaAs quantum well with a superconducting disk on top of the well,"* Phys. Stat. Sol. (b) **243**, 4046 (2006).

[181] D. Paquet, T. M. Rice, and K. Ueda, *"Two-dimensional electron-hole fluid in a strong perpendicular magnetic field: Exciton Bose condensate or maximum density two-dimensional droplet,"* Phys. Rev. B **32**, 5208 (1985).

[182] A. Imamoglu, *"Inhibition of spontaneous emission from quantum-well magnetoexcitons,"* Phys. Rev. B **54**, R14285 (1996).

[183] J. Feldmann, G. Peter, E. Göbel, P. Dawson, K. Moore, C. Foxon, and R. J. Elliott, *"Linewidth dependence of radiative exciton lifetimes in quantum wells,"* Phys. Rev. Lett. **59**, 2337 (1987).

[184] A. Parlangeli, P. C. M. Christianen, J. C. Maan, I. V. Tokatly, C. B. Soerensen, and P. E. Lindelof, *"Optical observation of the energy-momentum dispersion of spatially indirect excitons,"* Phys. Rev. B **62**, 15323 (2000).

[185] S. Charbonneau, M. Thewalt, E. Koteles, and B. Elman, *"Transformation of spatially direct to spatially indirect excitons in coupled double quantum wells,"* Phys. Rev. B **38**, 6287 (1988).

[186] A. Gorbatsevich and I. Tokatly, *"Formation of $k$-space indirect magnetoexcitons in double-quantum-well direct-gap heterostructures,"*Semicond. Sci. Tech. 13, 288 (1998).

[187] G. Grosso, J. Graves, A. Hammack, A. High, L. Butov, M. Hanson and A. Gossard, *"Excitonic switches operating at around 100 K,"* Nature Photonics **3**, 577 (2009).

[188] L. Andreani and A. Pasquarello, *"Accurate theory of excitons in GaAs/$Ga_{1-x}Al_xAs$ quantum wells,"* Phys. Rev. B **42**, 8928 (1990).

[189] M. Colocci, M. Gurioli, A. Vinattieri, F. Fermi, J. Massies and G. Neu, *"Temperature dependence of exciton lifetimes in GaAs/AlGaAs quantum well structures,"* Europhysics Letters **12**, 417 (1990).

[190] M. Colocci, M. Gurioli and A. Vinattieri, *"Dynamics of carrier recombination in GaAs/AlGaAs quantum well structures,"* Physica Scripta **T39**, 211 (1991).

[191] M. Colocci, M. Gurioli and J. Martinezpastor, *"Exciton relaxation dynamics in quantum well heterostructures,"* Journal De Physique IV **3**, 3 (1993).

[192] G. Brennen, C. Caves, P. Jessen, and I. Deutsch, *"Quantum Logic Gates in Optical Lattices,"* Phys. Rev. Lett. **82**, 1060 (1999).

[193] S. Ghanbari, P. Blakie, P. Hannaford and T. Kien, *"Superfluid to Mott insulator quantum phase transition in a 2D permanent magnetic lattice,"* Eur. Phys. J. B **70** 305 (2009).

[194] H. Zoubi and H. Ritsch, *"Bright and dark excitons in an atom-pairfilled optical lattice within a cavity,"* EPL **82**, 14001 (2008).

[195] H. Zoubi and H. Ritsch, *"Excitons and Cavity Polaritons for Cold-Atoms in an Optical Lattice,"* in Conference on Lasers and Electro-Optics/Quantum Electronics and Laser Science Conference and Photonic Applications Systems Technologies, OSA Technical Digest (CD) (Optical Society of America, 2008), paper QThE3.

[196] L. Perakis,*"Condensed-matter physics: Exciton developments,"* Nature **33**, 417 (2002).

[197] B. Josephson, *"Tunneling Into Superconductors,"* Phys. Lett. **1**, 251 (1962).

[198] S. Shapiro, *"Josephson Currents in Superconducting Tunneling: The Effect of Microwaves and Other Observations,"* Phys. Rev. Lett. **11**, 80 (1963).

[199] S. Ashhab and Carlos Lobo, *"External Josephson effect in Bose-Einstein condensates with a spin degree of freedom,"* Phys. Rev. A **66**, 013609 (2002).

[200] B. Juliá-Diaz, M. Guilleumas, M. Lewenstein, A. Polls, and A. Sanpera, *"Josephson oscillations in binary mixtures of F=1 spinor Bose-Einstein condensates,"* Phys. Rev. A **80**, 023616 (2009).

[201] R. Gati, M. Albiez, J. Fölling, B. Hemmerling, and M. Oberthaler, *"Realization of a single Josephson junction for Bose-Einstein condensates,"* Appl. Phys. B **82**, 207 (2006).

[202] B. Anderson and M. Kasevich, *"Macroscopic Quantum Interference from Atomic Tunnel Arrays,"* Science **282**, 1686 (1998).

[203] K. Mahmud, H. Perry, and W. Reinhardt, "*Quantum phase-space picture of Bose-Einstein condensates in a double well,"* Phys. Rev. A **71**, 023615 (2005).

[204] M. Andrews, C. Townsend, H. Miesner, D. Durfee, D. Kurn, and W. Ketterle, *"Observation of Interference Between Two Bose Condensates,"* Science **275**, 637 (1997).

[205] D. Hall, M. Matthews, C. Wieman, and E. Cornell, *"Measurements of Relative Phase in Two-Component Bose- Einstein Condensates,"* Phys. Rev. Lett. **81**, 1543 (1998).

[206] S. Papp, J. Pino, R. Wild, S. Ronen, C. Wieman, D. Jin, and E. A. Cornell, *"Bragg Spectroscopy of a Strongly Interacting $^{85}$Rb Bose-Einstein Condensate,"* Phys. Rev. Lett. **101**, 135301 (2008).

[207] N. Claussen, E. Donley, S. Thompson, and C. Wieman, *"Microscopic Dynamics in a Strongly Interacting Bose- Einstein Condensate,"* Phys. Rev. Lett. **89**, 010401 (2002).

[208] J. Estéve, C. Gross, A.Weller, S. Giovanazzi, and M. Oberthaler, *"Squeezing and entanglement in a Bose-Einstein condensate,"* Nature **455**, 1216 (2008).

[209] Q. Chena, J. Stajicb, S. Tanb, and K. Levinb, *"BCS-BEC crossover: From high temperature superconductors to ultracold superfluids,"* Physics Reports **412**, 1 (2005).

[210] A. Schirotzek, Y. Shin, C. Schunck, and W. Ketterle, *"Determination of the Superfluid Gap in Atomic Fermi Gases by Quasiparticle Spectroscopy,"* Phys. Rev. Lett. **101**, 140403 (2008).

[211] B. Josephson, *"Possible New Effects in Superconducting Tunnelling,"* Phys. Rev. Lett. **1**, 251 (1962).

[212] S. Levy, E. Lahoud, I. Shomroni, and J. Steinhauer, *"The a.c. and d.c. Josephson effects in a Bose-Einstein condensate,"* Nature **449**, 579 (2007).

[213] G. Milburn, J. Corney, E. Wright, and D. Walls, *"Quantum dynamics of an atomic Bose-Einstein condensate in a double-well potential,"* Phys. Rev. A **55**, 4318 (1997).

[214] R. Spekkens and J. Sipe, *"Spatial fragmentation of a Bose-Einstein condensate in a double-well potential,"* Phys. Rev. A **59**, 3868 (1999).

[215] S. Inouye, M. Andrews, J. Stenger, H. Miesner, D. Stamper-Kurn, and W. Ketterle, *"Observation of Feshbach resonances in a Bose-Einstein condensate,"* Nature **392**, 151 (1998).

[216] N. Peyghambarian, L. L. Chase and A. Mysyrowicz, *"Bose-Einstein statistical properties and condensation of excitonic molecules in CuCl,"* Phys. Rev. B **27**, 2325 (1983).

[217] L. Chase, N. Peyghambarian, G. Grynberg and A. Mysyrowicz, *"Evidence for Bose-Einstein condensation of biexcitons in CuCl,"* Phys. Rev. Lett. **42**, 1231 (1979).

[218] M. Hasuo, N. Nagasawa, T. Itoh and A. Mysyrowicz, *"Bose-Einstein condensation of biexciton system in CuCl,"* Journal of Luminescence **60-1**, 758 (1994).

[219] D. Snoke, J. Wolfe and A. Mysyrowicz, *"Evidence for Bose-Einstein condensation of excitons in* $Cu_2O$*,"* Phys. Rev. B **41**, 11171 (1990).

[220] J. Lin and J. Wolfe, *"Bose-Einstein condensation of paraexcitons in stressed* $Cu_2O$*,"* Phys. Rev. Lett. **71**, 1222 (1993).

[221] A. Mysyrowicz, E. Benson and E. Fortin, *"Directed beam of excitons produced by stimulated scattering,"* Phys. Rev. Lett. **77**, 896 (1996).

[222] S. Pau, H. Cao, J. Jacobson, G. Björk, and Y. Yamamoto, *"Observation of a laserlike transition in a microcavity exciton polariton system,"* Phys. Rev. A **54**, R1789 (1996).

[223] E. Benson, E. Fortin and A. Mysyrowicz, *"Anomalous exciton transport in* $Cu_2O$*: Excitonic superfluidity or phonon-wind effect?,"* Solid State Commun. **101**, 313 (1997).

[224] K. O'Hara and J. Wolfe, *"Relaxation kinetics of excitons in cuprous oxide,"* Phys. Rev. B **62**, 12909 (2000).

[225] A. Jolk, M. Jorger and C. Klingshirn, *"Exciton lifetime, auger recombination, and exciton transport by calibrated differential absorption spectroscopy in* $Cu_2O$*,"* Phys. Rev. B **65**, 245209 (2002).

[226] T. Fukuzawa, E. Mendez and J. Hong, *"Phase-transition of an exciton system in GaAs coupled quantum-wells,"* Phys. Rev. Lett. **64**, 3066 (1990).

[227] S. Baranovskii, R. Eichmann and P. Thomas, *"Temperature-dependent exciton luminescence in coupled quantum wells,"* Physica Status Solidi B-Basic Research **205**, R19 (1998).

[228] S. Baranovskii and P. Thomas, *"Phase-transition of an exciton system in GaAs coupled quantum-wells and on Fermi-Dirac distribution of excitons in coupled quantum-wells - comment,"* Phys. Rev. Lett. **69**, 993 (1992).

[229] S. Baranovskii, R. Eichmann and P. Thomas, *"Temperature-dependent exciton luminescence in quantum wells by computer simulation,"* Phys. Rev. B **58**, 13081 (1998).

[230] L. Butov, A. Zrenner, G. Abstreiter, G. Bohm and G. Weimann, *"Condensation of indirect excitons in coupled AlAs/GaAs quantum-wells,"* Phys. Rev. Lett. **73**, 304 (1994).

[231] A. Larionov and V. Timofeev, *"Condensation of interwell excitons in GaAs/AlGaAs double quantum wells,"* JETP Lett. **73**, 301 (2001).

[232] A. Dremin, V. Timofeev, A. Larionov, J. Hvam and K. Soerensen, *"Phase diagram of the Bose condensation of interwell excitons in GaAs/AlGaAs double quantum wells,"* JETP Lett. **76**, 450 (2002).

[233] L. Butov, A. Imamoglu, A. V. Mintsev, K. L. Campman and A. Gossard, *"Photoluminescence kinetics of indirect excitons in* $GaAs/Al_xGa_{1-x}As$ *coupled quantum wells,"* Phys. Rev. B **59**, 1625 (1999).

[234] L. Butov, A. Imamoglu, A. Shashkin, V. Dolgopolov, A. Mintsev, S. Feklisov, K. Campman and A. Gossard, *"Nonlinear photoluminescence kinetics of indirect excitons in coupled quantum wells,"* Phys. Status Solidi A **178**, 83 (2000).

[235] L. Butov, L. Levitov, A. Mintsev, B. Simons, A. Gossard, and D. Cheml, *"Charge transport and phase transition in exciton rings,"* preprint arXiv: **0308117** [cond-mat.other],(2003).

[236] R. Rapaport, Gang Chen, D. Snoke, Steve H. Simon, Loren Pfeiffer, Ken West, Y. Liu, and S. Denev , *"Mechanism of luminescence ring pattern formation in quantum well structures: Optically-induced in-plane charge separation,"* preprint arXiv: **0308150** [cond-mat.other], (2003).

[237] C. Lai, J. Zoch, A. Gossard and D. Chemla, *"Phase diagram of degenerate exciton systems,"* Science **303** (2004).